



HAL
open science

Biphoton Frequency-Correlations Engineering and Measurement with a Semiconductor Microcavity

Guillaume Boucher

► **To cite this version:**

Guillaume Boucher. Biphoton Frequency-Correlations Engineering and Measurement with a Semiconductor Microcavity. Quantum Physics [quant-ph]. Sorbonne Paris Cité; Université paris diderot, 2016. English. NNT: . tel-01467419

HAL Id: tel-01467419

<https://theses.hal.science/tel-01467419>

Submitted on 14 Feb 2017

HAL is a multi-disciplinary open access archive for the deposit and dissemination of scientific research documents, whether they are published or not. The documents may come from teaching and research institutions in France or abroad, or from public or private research centers.

L'archive ouverte pluridisciplinaire **HAL**, est destinée au dépôt et à la diffusion de documents scientifiques de niveau recherche, publiés ou non, émanant des établissements d'enseignement et de recherche français ou étrangers, des laboratoires publics ou privés.



Distributed under a Creative Commons Attribution 4.0 International License

UNIVERSITÉ PARIS DIDEROT - PARIS 7
SORBONNE PARIS CITÉ



LABORATOIRE
MATÉRIAUX ET PHÉNOMÈNES QUANTIQUES

ÉCOLE DOCTORALE 564 :
PHYSIQUE EN ÎLE-DE-FRANCE

UFR DE PHYSIQUE

THÈSE

présentée par

Guillaume BOUCHER

pour obtenir le grade de

Docteur en Sciences de l'Université Paris Diderot

Biphoton Frequency-Correlations Engineering and Measurement with a Semiconductor Microcavity

Soutenue publiquement le 9 mars 2016,
devant la commission d'examen composée de :

M.	Alberto BRAMATI,	Président du Jury
Mme	Eleni DIAMANTI,	Rapportrice
Mme	Sara DUCCI,	Directrice de thèse
M.	Jean-Pierre HERMIER,	Rapporteur
M.	Paolo MATALONI,	Examineur
Mme	Pérola MILMAN,	Invitée

Contents

Acknowledgements	v
List of Acronyms	ix
Introduction	1
I Photon pair generation by Spontaneous Parametric Down-Conversion in a semiconductor ridge microcavity	7
1 Working principle of the source	9
1.1 Phase-matching scheme for counter-propagating twin photons . . .	9
1.2 The pump beam microcavity	12
2 Theory of Cavity SPDC	17
2.1 Derivation of the state produced by SPDC	18
2.1.1 General considerations on the quantization of the electro- magnetic field	18
2.1.2 The electromagnetic field in the linear regime	19
2.1.3 The signal and idler fields	21
2.1.4 The Hamiltonian for the nonlinear interaction	22
2.1.5 The two-photon state	23
2.2 Engineering the JSA	25
2.2.1 The phase-mismatch along the guiding direction	25
2.2.2 The Joint Spectral Amplitude	27
2.2.3 The Joint Temporal Amplitude	34
2.2.4 Effect of the pump microcavity on the Joint Temporal Am- plitude	35
2.2.5 The Chronocyclic Wigner Function	37
2.3 Effects of the facets reflectivities on the JSA	41
2.4 Conclusion	45

II	Frequency-time correlations engineering	47
3	Joint Spectral Intensity Reconstruction with a Fiber Spectrograph	49
3.1	Characterization tools in frequency-time space	49
3.2	Single photon spectrograph – Working principle	50
3.3	Experimental implementation	51
3.3.1	Experimental set-up	52
3.3.2	Calibration of the spectrograph	53
3.3.3	Spectral resolution	56
3.3.4	Theoretical spectrogram	56
3.3.5	Spatial shaping	58
3.4	Experimental reconstruction	61
3.5	Conclusion	62
4	Joint Spectral Intensity reconstruction by “Stimulated” Parametric Down-Conversion	65
4.1	Working principle	65
4.2	Experimental setup	66
4.3	Joint Spectral Intensity measurements	67
4.3.1	Validation of the method	67
4.3.2	High-resolution frequency correlation engineering	70
4.4	Prospect for a phase sensitive measurement of the JSA with stimulated techniques	72
4.5	Conclusion	79
5	Biphoton state engineering in the frequency-time space	81
5.1	Hong Ou Mandel experiment	82
5.2	Generalization of the HOM experiment	86
5.3	Spatial shaping of the pump beam with a spatial light modulator	92
5.4	Conclusion	96
III	Controlling entanglement in polarization and frequency	97
6	Joint Spectral Amplitude engineering for maximal entanglement in polarization	99
6.1	Generation of Bell states in polarization	99
6.2	Characterization of the state	101
6.3	Optimizing the entanglement in polarization	104
6.4	Influence of the reflectivities of the facets	108
6.5	Conclusion	110

Perspectives	111
Conclusion	115
Appendix	119
A Source sample	119
B Characteristics of the Dispersion Compensating Fibers	121
C Concurrence and Joint Spectral overlap	123
D A note on softwares	125
E List of Publications and Conferences	127
Bibliography	157

Acknowledgements

En arrivant à MPQ à la recherche d'un stage, j'ai tout d'abord contacté Thomas Coudreau et Pérola Milman. Le sujet avait l'air passionnant, le courant passait bien entre nous. Toutefois la perspective d'une thèse uniquement théorique m'effrayait quelque peu. Ils ne m'en ont pas voulu de leur faire faux bond et Thomas m'a même présenté Sara Ducci, ma future encadrante. Mes remerciements vont donc vers eux, pour avoir rendu possible cette aventure.

J'ai ainsi eu la chance d'être dirigé pendant mon stage de master et ma thèse par Sara. Une chance en effet car tout en dirigeant mes travaux et en m'aidant à faire les choix difficiles, elle m'a donné les moyens de réaliser une multitude d'expériences (qui n'apparaissent pas toutes dans ce manuscrit). Tout en donnant un cadre à ma thèse, elle m'a surtout laissé la liberté dont j'avais besoin pour donner la couleur que je désirais à mes travaux, à cheval entre la théorie, les modèles, et les expériences qui les confirment. Merci encore pour la bière au bar de la station Lozère après la soutenance de stage M2 : la thèse se présentait sous les meilleurs auspices !

Mes remerciements vont ensuite à mes deux rapporteurs, Eleni Diamanti et Jean-Pierre Hermier pour leur lecture attentive du manuscrit. Je remercie également mes examinateurs Alberto Bramati (président) et Paolo Mataloni, ainsi que l'ensemble de mon jury pour leurs remarques, questions et écoute lors de ma soutenance.

Ma thèse a été l'occasion de tisser de nombreuses collaborations qui ont contribué à sa réussite. Je remercie les théoriciens du labo tout d'abord, Pérola et Thomas (une fois de plus), Tom Douce mais aussi Steve Walborn et Arne Keller. Un autre succès a été rendu possible grâce à l'interaction avec Marco Liscidini et John Sipe. Enfin je remercie les nombreuses personnes qui nous ont apportés des conseils sur les SLM, Nicolas Treps, Sylvain Gigan et tout particulièrement Ebrahim Karimi et Frédéric Bouchard même si l'application envisagée de cet appareil le sera pour un prochaine thèse.

Merci ensuite aux membres du laboratoire Matériaux et Phénomènes Quantiques. Mention spéciale à Anne Servouze pour son sourire et son grand professionnalisme. Merci aussi à Martial Nicolas et Patrick Lepert à la méca', Marc Apfel (et son voisin Alain Cangemi) à l'élec', Christophe Manquest, Pascal Filloux et Stefan Suffit de la salle blanche et enfin Joëlle Mercier, Jocelyne Moreau et Sandrine Di Concetto à la gestion. Et pour finir merci aux nombreux post-docs, stagiaires et doctorants qui ont croisé ma route, notamment : Benjamin Askenazi, Chérif Belacel, Charlotte Bessis, Roméo Bonnet, Ariane Calvar, Ana Chen, Djamal

Gacemi, Simon Huppert, Vishal Jagtap, Thibault Laurent, Pierre Massat, Julien Nadeo, Giulia Pegolotti, Philippe Petit, Hélène Prunier, Margaux Renaudat-St-Jean, Benjamin Szimansky, ...

J'en viens à l'équipe DON. Merci aux permanents, Laëtitia Doyennette, Giuseppe Leo, Ivan Favero, Alessio Andronico et Marco Ravaro. Aux post-docs, Eduardo Gil-Santos, Pierre Allain, Dac-Trung N'guyen et Oleksandr Stepanenko. Aux doctorants Alexandre Delga, Christophe Baker, Marc Savanier, David Parrain, Alice Bernard, Natalia Morais, Alok Barti, Valerio Gili, Mehdi Hamumi et la relève des photons jumeaux, Giorgio Maltese et Jonathan Belhassen (bon courage pour la thèse). Une pensée aux plantes vertes qui habitaient (et habitent encore pour certaines) le thésarium de manière permanente, Cosette le ficus, Vladimir le papyrus et Irina sa compagne. J'aimerais ensuite exprimer ma reconnaissance la plus profonde à ceux qui m'ont appris le métier et transmis leurs savoirs et savoir-faire : Adeline Orioux, Andreas Eckstein, Fabien Boitier, Yacine Halioua et Qifeng Yao. Enfin un énorme merci à mes camarades du quotidien, par ordre d'apparition : ma voisine permanente, Silvia Mariani. Merci pour les fous-rire, les nombreux memes partagés et tes regards gentiment moqueurs quand j'étais plus concentré sur Claire que sur la physique. Cécile Ozanam, mon X préférée et celle qui a suivi le même calendrier - stage et thèse - que moi (sauf pour la fin où je me suis fait coiffé au poteau). William Hease, pour les nombreuses discussions de physique ou non, et le tennis (sauf le matin qui n'est vraiment pas ton heure). Je ne te remercie en revanche pas pour ton choix d'aspirateur pour le labo ! Biswarup Guha pour les échanges sur le monde et la géopolitique et pour avoir accepté volontiers mon thé vert dont personne ne voulait en dépit de son alléchante odeur de soupe au chou. Et Claire bien sûr.

Les gens de l'extérieur ont aussi eu une importance considérable sur ce travail. Une pensée tout d'abord à ceux qui ont partagé mon expérience erasmus en L3 à Nottingham puis les potes du magistère d'Orsay (Vincent Gruson, Coline Bretz, JC Orain, Yohan 'Gro'Yo' Pageot, Tatiana Champetier, Zacharie Nolet, Rémi Chipon) et du M2 (Thibaut Karassouloff et Claire Lebouteiller).

En dehors du travail, un lieu très important est le logis. J'ai eu la chance de vivre en coloc' durant toute cette thèse et de rencontrer moult personnages. La première était formidable quoique courte et bien que j'ai refusé de dormir autre part que sur le canap' du salon. Un grand merci donc à JC, Yann, Blandine et Damien, ainsi qu'Ismaël et Louise pour les soirées, les raclettes, le Fernet pour le ping-pong et l'élaboration progressive du ping-bière-pong devenu après un travail d'orfèvre en terme de raffinement, un sport olympique orcéen (il a même eu droit à son logo et, de manière éphémère, à sa propre page wikipedia).

La seconde coloc' vitriote était catastrophique. Que des informaticiens (étudiants à epitech) avec des horaires décalés et des vies peu saines dont Mathieu le créateur du repaire de la chaussette. Il y eu toutefois quelques bons moments avec David, Gaël et Yannick notamment autour de nos collections de verres à Gueuze et à Rince-Cochon.

La dernière coloc' était la bonne puisqu'elle a permis de retrouver place d'it', mon ami de presque toujours, le sieur Pierrick Rancoeur. Il y aurait tant de choses

à évoquer, les petits soins que tu m'as prodigués quand je revenais épuisé de mes premiers enseignements alors que j'étais atteint par la MNI par exemple. Les pigeons qui se sont mis à nicher sur ma balconnière aussi. Les soirées avec les Illu'... Le temps est passé si vite et je me dis qu'on n'en a pas assez profité!

Merci aux amis de toujours justement : Pierrick et Antoine, Romain, Matthieu, Cindy, Bob et Julien. Je ne serais jamais allé aussi loin sans vous!

À ma famille, mes parents pour m'avoir incité à poursuivre mes études au delà du CP (sic!), et mes frère et soeur Gro'Da et Gross'Ma.

Enfin, pour avoir enchanté ma vie dans et hors du labo, merci à Claire.

List of Acronyms

Al	Aluminum
AlAs	Aluminium Arsenide
AlGaAs	Aluminum Gallium Arsenide
Al_xGa_{1-x}As	Aluminum Gallium Arsenide ($0 < x < 1$)
AOM	Acousto-Optic Modulator
BBO	β -Barium Borate
CAR	Coincidences to Accidentals Ratio
CCD	Charge-Coupled Device
CMOS	Complementary Metal-Oxide-Semiconductor
CW	Continuous Wave
CWF	Chronocyclic Wigner Function
DBR	Distributed Bragg Reflector
DCF	Dispersion Compensating Fiber
DFG	Difference Frequency Generation
EOM	Electro-Optic Modulator
ER	Extinction Ratio
FBG	Fiber Bragg Grating
FDFD	Finite-Difference Frequency-Domain
FROG	Frequency Resolved Optical Gating
FSR	Free Spectral Range
FTIR	Fourier-Transform Infra-Red
FWHM	Full Width at Half-Maximum

FWM	Four-Wave Mixing
GaAs	Gallium Arsenide
GVD	Group-Velocity Dispersion
HOM	Hong-Ou-Mandel
HWP	Half-Wave Plate
ICP-RIE	Inductively Coupled Plasma - Reactive-Ion Etching
InGaAs	Indium Gallium Arsenide
IR	Infrared
JSA	Joint Spectral Amplitude
JSI	Joint Spectral Intensity
JTA	Joint Temporal Amplitude
JTI	Joint Temporal Intensity
LiNbO₃	Lithium Niobate
MBE	Molecular Beam Epitaxy
MMI	Multi-Mode Interferometer
NA	Numerical Aperture
NIR	Near IR
OAM	Orbital Angular Momentum
OPA	Optical Parametric Amplifier
OPO	Optical Parametric Oscillator
OSA	Optical Spectrum Analyzer
PBS	Polarizing Beam Splitter
PPLN	Periodically Poled Lithium Niobate
PPKTP	Periodically Poled Potassium Titanyl Phosphate
QKD	Quantum Key Distribution
QPM	Quasi-Phase Matching
QWP	Quarter-Wave Plate

SEM	Scanning Electron Microscope
SESHG	Surface Emitting Second Harmonic Generation
SET	Stimulated Emission Tomography
SFG	Sum Frequency Generation
SHG	Second Harmonic Generation
SLM	Spatial Light Modulator
SNR	Signal to Noise Ratio
SNSPD	Superconducting Nanowire Single Photon Detector
SPAD	Single Photon Avalanche Photodiode
SPDC	Spontaneous Parametric Down-Conversion
SPIDER	Spectral Phase Interferometry for Direct Electric-field Reconstruction
SSPD	Superconducting Single Photon Detector
TDC	Time-to-Digital Converter
TE	Transverse Electric
TIR	Total Internal Reflection
TM	Transverse Magnetic
TWM	Three-Wave Mixing
VCSEL	Vertical-Cavity Surface-Emitting Laser
VECSEL	Vertical-External-Cavity Surface-Emitting Laser
WGM	Whispering Gallery Mode

Introduction

Among the peculiarities of quantum mechanics, entanglement is probably the most counterintuitive example: objects are said to be entangled when the state describing the full system cannot be factorized in a product of states characterizing the individual objects. This has some striking consequences: the characterization of two entangled particles (which may be in two very distant locations) reveals strong correlations on the outcomes on particles 1 and 2, even though the results of individual measurements on either particle are random [1]. This may appear as a *spooky action at a distance* [2] going against the fact that no information can be transmitted faster than the speed of light [3]. Nevertheless this striking feature was used to invalidate the existence of local hidden variables [4, 5, 6, 7, 8]. This was done through the violation of inequalities formulated by J.S. Bell [9, 10] which had formalized a debate going on for decades. Although these experiments are an indication of the non-local character of quantum mechanics, they are still in agreement with special relativity: a classical channel of communication is required to reveal the correlations preventing faster-than-light transmission of data.

Apart from these fundamental considerations on physics, it was suggested, by Feynman in particular [11], that these specificities offered by quantum mechanics could be exploited to perform quantum simulations and to build quantum computers. After this early proposal, several protocols have been proposed for which quantum computers would perform better than their ‘classical’ counterparts such as Shor’s algorithm [12] for the factorization into prime numbers or the Grover’s search algorithm [13]. Demonstrations of these protocols have followed using for example nuclear magnetic resonance [14] or superconducting qubits [15, 16]. The storage of qubits has also been done with cold atoms [17] and trapped ions [18]. In fact, the physical systems that can be used to implement quantum computation tasks are numerous [19].

Integrated Quantum Photonics In this context quantum photonics is an intense field of research: in [20], Knill, Laflamme and Milburn showed that optical quantum computation was achievable with linear optical elements and using single photon sources and detectors. In fact, the best achievements of quantum photonics have been obtained in the field of quantum communication: several protocols of Quantum Key Distribution (QKD) [21, 22], the transmission of a cryptographic key with a security against eavesdroppers guaranteed by quantum mechanics, have been successfully demonstrated [23, 24, 25]. Modules for QKD are now commercially available from companies such as IDQuantique or SeQureNet.

The strong advantages of the photons are the relative ease with which they can be produced and manipulated, their ability to be transported over long distances and their robustness against decoherence. This enabled the teleportation of quantum states [26, 27, 28] or even entanglement swapping from one system to another [29, 30], schemes that are at the basis of quantum repeaters, the analogs of classical amplifiers for quantum communications tasks. Photons have also been used to perform boson sampling, a task that is deemed harder to solve with classical rather than with quantum means [31, 32, 33, 34].

Integration of several “quantum” building blocks is a key issue on the way towards practical applications. After many important results obtained in quantum optics with bulk systems [35, 36, 26], we assist today to a real boom of quantum photonic technologies, a trend that is also followed by superconducting processors [37, 38] and cold atoms [39] and trapped ions [40] chips. A fully integrated photonic quantum device would thus gather into a single chip, sources of photons, optical circuits to manipulate them, and detectors with some electronics for feedback on the different elements of the device [20, 41, 42]. In that perspective, semiconductor materials are an attractive platform. The maturity of samples’ growth and processing techniques enables the fabrication of a great diversity of passive and active devices. Playing on the refractive index contrast between the materials in a heterostructure, light can be guided into channels [43]. Various techniques then allow to implement integrated beamsplitters [44, 45, 46] or to control the polarization of light within the waveguide [47, 48].

Among the semiconductor materials, the III-V platform has strong optoelectronic capabilities, for example the ability to implement laser diodes. In the perspective of building photonic circuits, the electro-optic Pockels effect in Gallium Arsenide (GaAs) can also be exploited to create integrated optical delay-lines [45, 46]. More specific to quantum photonics is the recent integration of superconducting nanowire single photon detectors on III-V waveguides [49, 50]. Finally, the strong second order nonlinearity of GaAs also enables the production of photon pairs.

Semiconductor Sources of Photon Pairs Two main processes are used today to produce photon pairs in semiconductor materials, namely the biexcitonic cascade in quantum dots and parametric processes in nonlinear media. In the first approach, the artificial atom constituted by the quantum dot is excited to form a double electron-hole pair (the biexciton). Two photons are then emitted in cascade with the de-excitation of the quantum dot. With this method, pairs of polarization entangled photons have been produced through optical [51, 52] or electrical pumping [53] of the quantum dots. The emission of photon pairs is deterministic, *i.e.* the excitation of the quantum dot is followed by the emission of a pair which is a strong advantage of this approach. However these sources must be cooled to cryogenic temperatures in order to extract the signal from the thermal noise.

Another possibility is offered by parametric processes relying on optical nonlinearities. This approach leads to a probabilistic emission but does not require cryogenic temperatures. On one hand, in centro-symmetric media, such as sili-

con, Four-Wave Mixing (FWM) is the most efficient nonlinear process. Pairs of photons can be spontaneously generated by absorption of two photons from the pump beam. Thanks to the compactness and the CMOS compatibility of the devices based on this approach, this is a hot research topic; different sources based on ridge waveguides [54, 55] or ring resonators [56] are under developments on silicon chips.

On the other hand, III-V semiconductor materials are non centro-symmetric and thus allow to access second order nonlinearities. In this case, the photon pairs are generated by Three-Wave Mixing (TWM) with a process called Spontaneous Parametric Down-Conversion (SPDC) in which the sum of the photons' energies corresponds to the energy of the pump photon. The pump beam is thus more easily separated from the photon pairs via spectral filtering than with FWM processes. The direct band-gap of GaAs allows also the integration of the pump laser within the nonlinear device [57, 58], dramatically reducing the footprint of the system. All these aspects have led us to adopt this strategy to develop our source.

A great diversity of devices have been demonstrated to satisfy both energy and momentum conservation in order to achieve an efficient generation of photon pairs. Indeed the usual strategy employed with SPDC in bulk crystals [36] which relies on birefringence to fulfill momentum conservation is not applicable to Aluminum Gallium Arsenide (AlGaAs) compounds due to the isotropy of the material. In waveguides, an artificial birefringence can be implemented by including aluminum-oxide layers in the heterostructure [59]. Another possibility is offered by modal phase-matching where the conservation of momentum is achieved by involving different spatial modes of ridge waveguides [60, 58]. We also mention the implementation of a Quasi-Phase Matching (QPM) through the periodic domain inversion; however AlGaAs QPM waveguides suffer from important optical losses [61, 62]. This is not the case for AlGaAs whispering-gallery mode micro-disk resonators for which no technological efforts is required in terms of domain inversion. Indeed, the QPM is automatically achieved with the crystal symmetry and the circular shape of the device [63, 64]. The strategy adopted in this thesis consists in a transverse pumping scheme with photons propagating in a waveguide in opposite directions and for which the phase-matching is automatically satisfied. This approach gives also a great flexibility in engineering the properties of the photons.

Degrees of freedom of the photon Among the degrees of freedom of the photon, polarization is probably the most investigated one. From the atomic radiative cascade [6] to type II SPDC [36], photon pairs with a given polarization state have been easily generated, manipulated and characterized. It is the most simple property of light on which to encode a qubit. However this Hilbert space is only two-dimensional and consequently the quantity of information contained in this degree of freedom is limited. To give one example, this imposes a limitation on the rate of QKD relying on polarization.

Spatial degrees of freedom for example provide a Hilbert space of higher dimension: using slits, multi-pixel detectors and adaptive optics, the transverse mo-

mentum and position of light can be discretized [65] to implement *qudits*, the counterparts of qubits in Hilbert spaces of dimension bigger than two. Quantum information can then be processed in free-space [66].

Another promising degree of freedom, especially for free-space communication [67], is the Orbital Angular Momentum (OAM) carried by light. In fact, the exploration of this property has begun only quite recently, even for classical light [68]. As opposed to polarization (the spin of light), OAM is an unbounded degree of freedom with a potentially unlimited Hilbert space. A recent QKD experiment has taken advantage of this space to transmit more than two bits per photon [69]. The qudits encoded in the OAM have also been used to test paradoxes of quantum mechanics [70], notably with the violation of Bell inequalities generalized for higher dimensions [71].

In the aim of realizing compact devices for long distance communications, the time-frequency properties of the photons are more suitable. For example, photons having a long coherence time (and thus a narrow spectrum) can be modulated with standard telecom components, such as electro-optic modulators [72, 73, 74], and coupled into optical fibers to carry the desired information with no deformation due to the dispersion and the nonlinearities of the fiber [75]. Photons with a rich time-frequency mode structure may also be used for quantum computing. Indeed, with the implementation of specialized beam-splitters called quantum pulse gates [76], which transmit or reflect specific time-frequency modes, linear optical quantum computing can be envisaged with these degrees of freedom [77].

Photon pairs produced by spontaneous TWM and FWM are generally entangled, sometimes in multiple degrees of freedom. These correlations between multiple degrees of freedom are potentially undesired if only one property of light is aimed to be entangled because they will give distinguishing information that may degrade this entanglement [78]. Moreover, some applications require single photon sources, which can be obtained with probabilistic sources of photon pairs using one photon of the pair to herald its twin. If correlations exist between the photons, the heralding operation will project the heralded photon into a mixed state, reducing its utility for most protocols [79]. For photons generated in waveguides, these detrimental correlations essentially concern the frequency-time degrees of freedom.

Frequency-time correlations engineering All these reasons motivate intense research on the control of the frequency-time properties of photon pairs in order either to remove any frequency correlation between them, or to engineer useful states for quantum technologies. With this wish for precise control of the biphoton also comes the necessity of accurately characterizing it. Depending on the bandwidth of the photons, the engineering is more easily done in the temporal or the spectral domain. The first manipulations were performed with techniques related to the shaping of ultrashort pulses: the frequency components of the photon's wavepacket were spatially separated with a dispersive element and a spectral phase was applied to them before their recombination in order to get a photon with engineered temporal properties [80]. The characterization was done with nonlinear

optical phenomena or with two-photon interferences at a beam-splitter [81]. Qudits in frequency can be implemented also, with a discretization of the continuous frequency space. In [82] for example, prisms have been used to perform a spatial separation of the photons' frequency components which could then be addressed independently with a programmable mask (spatial light modulator).

The operations mentioned above were done with devices external to the source of photon pairs, and on the photon pairs themselves. While one could generate a huge number of pairs and then perform a selection and filtering of the interesting photons, this is in fact very demanding in resource and done at the expense of the brightness of the source. Moreover such manipulation risks to degrade the “fragile” quantum state of the photon pairs. This has led to a strong effort in what is called *source engineering*, where the characteristics of the pump beam and the device are chosen in order to only emit photons with the desired properties, avoiding post-manipulation and unnecessary losses. With sources based on Periodically Poled Lithium Niobate (PPLN) waveguides for example, the poling periodicity can be chosen in order to achieve convenient dispersion properties which allow the control of the phase-matching. The engineering of the frequency correlations of the photons is then done by playing on the temporal characteristics of the pump beam affecting energy conservation in the SPDC process [83]. In fact, the first frequency engineering reported in [84] was performed in bulk crystals by adjusting the spatial properties of the pump beam which affect momentum conservation. However the variety of produced states has been limited by the dispersion properties of the crystal used in this first demonstration.

Outline of the thesis This work is focused on a semiconductor source made of AlGaAs: the device is transversally pumped and emits photons propagating in opposite directions. As we will see, this pump geometry renders the device very versatile for frequency correlations engineering. The automatic separation of the pump and the two photons is also a strong advantage, relieving the need for a pump filtering or a separation stage. To demonstrate the control of the frequency correlations, reliable characterization techniques are required. We compare the fiber spectrograph [85], the method at the state of the art at the beginning of this work, with a novel approach we introduced in this thesis. We also show how to go beyond with the frequency-time engineering of the photons and comment on complementary methods of characterization. A case where the frequency-time correlations of the photons can be detrimental is also treated and we present solutions to this problem.

The first part of this thesis is dedicated to the description of the source at the heart of this work. A first chapter summarizes the main features of this device emitting pairs of counterpropagating photons. In chapter 2, we give a theoretical analysis of the states produced by this source: the Joint Spectral Amplitude (JSA) or biphoton wavefunction describing the properties of the photons, and in particular their correlations in terms of frequency, is derived. The role played by the device, notably its facets and the microcavity, and the role of the pump beam on the biphoton state are highlighted. This allows to identify means to engineer

the spectral properties of the photons. We also introduce different functions to adequately describe the photons in the spectral and temporal domain and in a joint or separate manner.

In the second part, we present the experiments we have performed to engineer the time-energy properties of the two-photon state and the methods we have implemented to reconstruct the Joint Spectral Intensity describing them. We also suggest techniques to access the phase of the biphoton wavefunction. Chapter 3 begins with a review of the existing techniques for the measurements of the time-frequency properties of the photon pairs. We then detail one of these methods, the fiber spectrograph, and we show how the modification of the spatial profile of the pump beam can be used to control the degree of frequency correlation between the two photons. In chapter 4, we introduce a novel technique relying on the stimulation of the parametric process leading to a faster and more resolved reconstruction of the Joint Spectral Intensity. We also theoretically investigate a variation of this technique which would allow the full retrieval of the JSA. In chapter 5, we show how to go beyond simple modifications of the degree of frequency correlations to produce more exotic states. We revisit the two-photon interference at a beam-splitter with a generalized approach allowing to characterize these states in terms of their Wigner function.

The third part describes the production of states entangled in polarization. In chapter 6 we highlight the role played by the JSA on the quality of the entanglement and the influence of the facets of the waveguide. A new pumping scheme is proposed to improve the level of entanglement with respect to a first experiment performed in our team [86].

The manuscript ends with some conclusions and perspectives opened by this work.

Part I

Photon pair generation by Spontaneous Parametric Down-Conversion in a semiconductor ridge microcavity

Chapter 1

Working principle of the source

1.1 Phase-matching scheme for counter-propagating twin photons

Our source is a ridge waveguide consisting of an Aluminum Gallium Arsenide (AlGaAs) heterostructure (see Figures 1.1 and 1.2). Proposed by Berger and de Rossi [87], the general scheme for the production of pairs is the following: the pump beam, impinging on top of the ridge, generates by Spontaneous Parametric Down-Conversion (SPDC) signal and idler photons propagating in opposite directions into the waveguide. This guided regime is a strong advantage compared to non-collinear SPDC in bulk crystals [36, 84], since the direction of emission of the photons is degenerate for all frequencies. This greatly simplifies the collection of the generated photons with respect to bulk crystals. After the proof of principle of the source [88, 89], its conversion efficiency was enhanced [90, 91] with the integration of two Bragg mirrors, surrounding the core layers. Their role is to create a microcavity for the pump beam and to act as cladding layers for the signal and idler fields. The efficiency is thus improved by 2 orders of magnitude to reach 10^{-11} pairs per pump photon.

A distinctive feature of the source is the type II SPDC process due to the polarization of the incident pump beam and the form of the nonlinear susceptibility tensor imposing orthogonal signal and idler polarizations. Therefore, as shown in figure 1.1, two concurrent processes of photon pair generation occur: in the process we indicate as *interaction HV*, the signal photon is Transverse Electric (TE) polarized, *i.e.* its electric field is oriented parallel to the layers along the y -axis (H polarization); its twin, the idler photon, is Transverse Magnetic (TM) polarized with an electric field orthogonal to the layers along x (V polarization). In the concurrent process we indicate as *interaction VH*, the situation is reversed with a TM signal and a TE idler. In order to highlight the main features of our source, we express the conservation laws for efficient SPDC. Indeed, the energies and momenta of the emitted photons are given by:

$$\begin{cases} \hbar\omega_p = \hbar\omega_s + \hbar\omega_i \\ \mathbf{k}_p = \mathbf{k}_s + \mathbf{k}_i \end{cases} \quad (1.1)$$

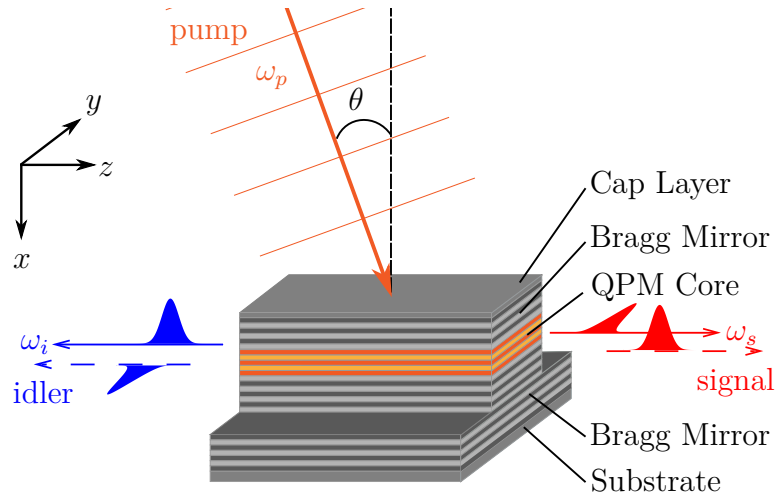


Figure 1.1 – Counterpropagating phase-matching scheme implemented in a semiconductor microcavity waveguide. The waveguide is etched from a AlGaAs layer heterostructure with alternating Al content, epitaxially grown on a GaAs chip (the substrate). The pump beam impinges on top of the waveguide with an angle θ and generates photons propagating in opposite directions with orthogonal polarization. The two possible down-converted pairs are represented in solid and dashed arrows, respectively. The Bragg mirrors create a microcavity for the pump beam and act as cladding layers for the signal and idler fields. The core layers are structured in order to achieve a Quasi-Phase Matching in the vertical direction. The cap layer on top of the sample protects the lower structures from chemical degradation due to contact with the environment.

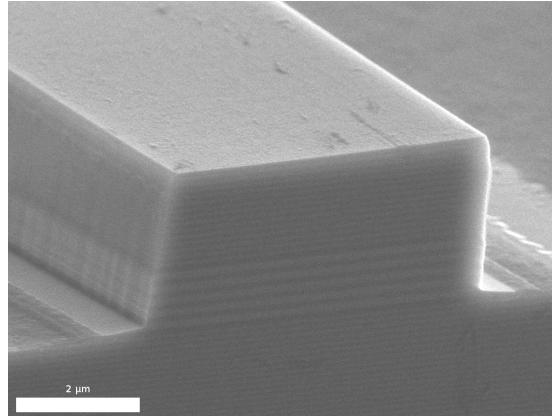


Figure 1.2 – Waveguide facet observed with a scanning electron microscope. The QPM can be clearly distinguished, surrounded by the asymmetric top and bottom Bragg mirrors. This particular sample was etched with Inductively Coupled Plasma - Reactive-Ion Etching.

where ω_p , ω_s and ω_i respectively represent the angular frequency of the pump, signal and idler fields and \mathbf{k}_p , \mathbf{k}_s , \mathbf{k}_i their wave-vectors. In the case of the counterpropagating phase-matching scheme sketched in Figure 1.3, the momentum

conservation can be projected along z and x . In this case (1.1) becomes:

$$\begin{cases} \omega_p = \omega_s + \omega_i \\ \frac{\omega_p}{c} \sin \theta = k_s - k_i \\ \frac{n_p \omega_p}{c} \cos \frac{\theta}{n_p} = k_{\text{QPM}} \end{cases} \quad (1.2)$$

where k_s and k_i are the norm of the photons' wavevectors within the sample and we have decomposed the pump wavevector along directions x and z with $n_p(\omega_p, x)$, the value of the refractive index at frequency ω_p and depth x in the heterostructure. To compensate the momentum of the pump beam in the vertical direction, a Quasi-Phase Matching (QPM) is implemented by alternating layers of different composition in the core of the waveguide. A detailed description is given in the next section. We now focus on the conservation of energy and the phase-matching along the propagation direction z :

$$\begin{cases} \omega_p = \omega_s + \omega_i \\ \omega_p \sin \theta = \omega_s n_s(\omega_s) - \omega_i n_i(\omega_i) \end{cases} \quad (1.3)$$

where $n_{s/i}$ are the effective indices of the guided signal and idler modes* and θ is the angle of incidence of the pump beam. We can then express the idler frequency ω_i as a function of the signal frequency ω_s :

$$\begin{cases} \omega_i = -\omega_s + \omega_p \\ \omega_i = \frac{n_s}{n_i} \omega_s - \frac{\omega_p}{n_i} \sin \theta \end{cases} \quad (1.4)$$

Figure 1.4 represents these two functions, allowing to identify the frequencies at which the photons are generated depending on the characteristics of the pump beam and the device. Over a large range of frequencies, the conservation of momentum is oriented in the positive diagonal and is almost orthogonal to the conservation of energy (anti-diagonal). Therefore, these two functions will always intersect, leading to a solution for efficient production of pairs. This scheme thus gives more flexibility with respect to collinear sources where these conditions can become parallel, preventing the emission of pairs above a certain pump wavelength for example [58].

The angle of incidence θ of the pump beam is a degree of freedom on which we can play to tune the signal and idler frequencies, as illustrated by Figure 1.5 where the wavelengths of the signal and the idler are represented for the two interactions HV and VH . We observe that the tuning curves are symmetric with respect to the axis $\theta = 0$: a specific pumping angle $\pm\theta_{\text{deg}} = \pm \arcsin\left(\frac{n_s - n_i}{2}\right)$ allows to obtain photons with degenerate frequencies for either interaction. The removal of the distinguishability in energy opens the possibility to generate polarization entangled photons as demonstrated by our group in [86]. More details on this experiment and on possible improvements to the level of entanglement will be given in chapter 6.

*Unless stated otherwise, the effective indices are determined throughout this work with the transfer matrix method [92]. The refractive indices are calculated following [93] as a function of temperature and the composition of the layers.

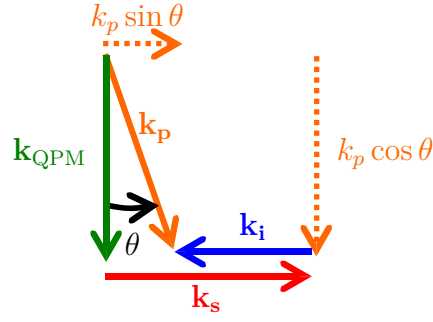


Figure 1.3 – Sketch of the phase-matching for counterpropagating photons.

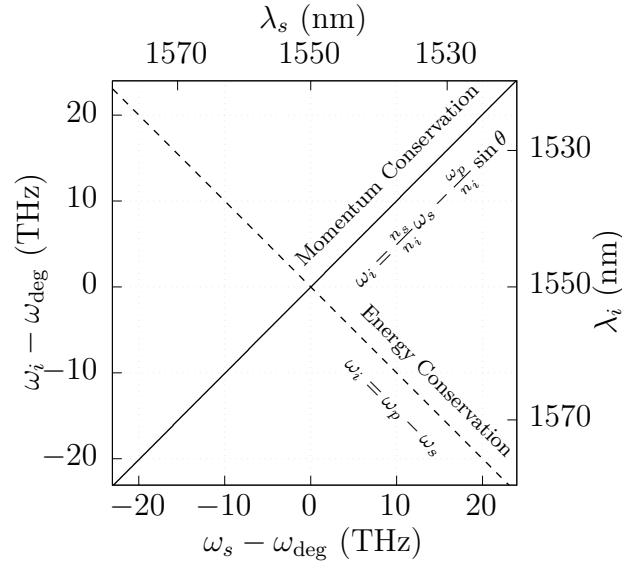


Figure 1.4 – Sketch representing the relationships imposed by energy and momentum conservation on the signal and idler frequencies ω_s and ω_i . The numerical simulation is performed for the nominal structure with a pump wavelength $\lambda_p = 2\pi c/\omega_p = 775$ nm and an angle of incidence $\theta = 0.349^\circ$, corresponding to the situation in which the down-converted photons are generated at the same frequency $\omega_{\text{deg}} = \omega_p/2$.

1.2 The pump beam microcavity

The previous section summarizes the working principle and the specific features of the counterpropagating phase-matching. A challenge with this scheme is to overcome the weak efficiency caused by the limited volume of interaction. Indeed in collinear geometries, the fields co-propagate over up to several centimeters while within this source, the interaction length is defined by the size of the pump beam on the ridge. Another issue is to avoid the penetration of the pump field into the substrate which was a source of noise (resulting in a limited Coincidences to Accidentals Ratio (CAR)) in the first generation of devices [88]. Indeed, the absorption of the pump within the substrate and the subsequent re-emission of incoherent photons over a wide range of frequencies was the cause of a broadband

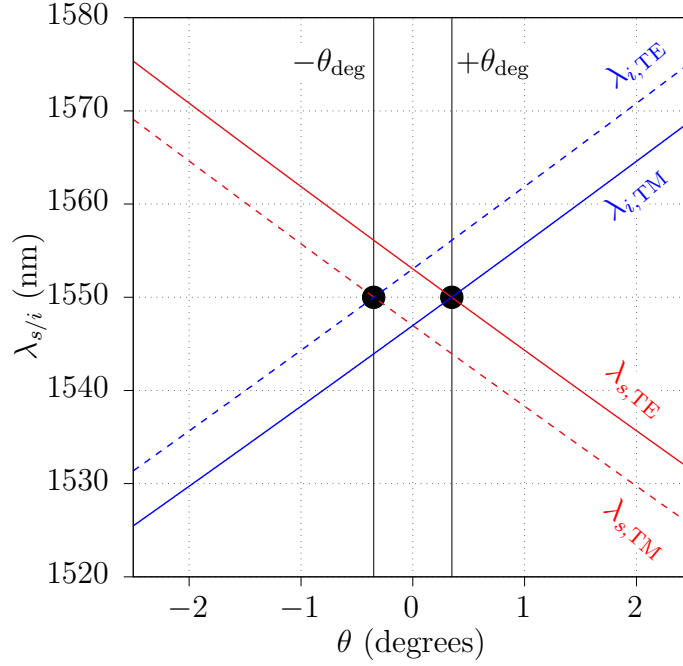


Figure 1.5 – Numerical simulation of the angular dependence of the signal (red) and idler (blue) wavelengths for interaction HV (solid lines) and interaction VH (dashed lines) for $\lambda_p = 775$ nm. The black lines correspond to the angles of incidence of pump beams for which each process generates a frequency degenerate photon pair (marked by a black circle).

optical noise.

These issues led to the current generation of devices where a microcavity is implemented for the pump beam. A design with two asymmetric Bragg mirrors was obtained after optimization. This work resulted in an enhancement of the conversion efficiency by two orders of magnitude and an improvement of the CAR while keeping a good compromise between the angular acceptance and the finesse of the device [90]. Figure 1.6 shows the amplitude distributions $E_s(x, y)$, $E_i(x, y)$ and $E_p(x, y)$ of the signal, idler and pump fields within the heterostructure. The Bragg mirrors confine the signal and idler fields and generate a standing wave pump field at resonance.

The oscillation of the pump beam within the structure requires a careful structuring of the nonlinear medium to ensure an efficient nonlinear interaction. Indeed, we will see in chapter 2 that the SPDC efficiency depends on the overlap integral between the transverse profile of the fields $E_s(x, y)$, $E_i(x, y)$ and $E_p(x, y)$, and the effective nonlinearity $d_{\text{eff}}(x)$ in the interaction volume as expressed by the quantity:

$$\chi_{\Gamma} \propto \iint dx dy d_{\text{eff}}(x) E_s(x, y) E_i(x, y) E_p(x, y) \quad (1.5)$$

We see that if $d_{\text{eff}}(x)$ is constant for all depths, this overlap integral would almost cancel due to the sign inversion of the pump amplitude every $\Lambda \approx \lambda_p/2n$, where the refractive index n depends on the aluminum content and the considered wave-

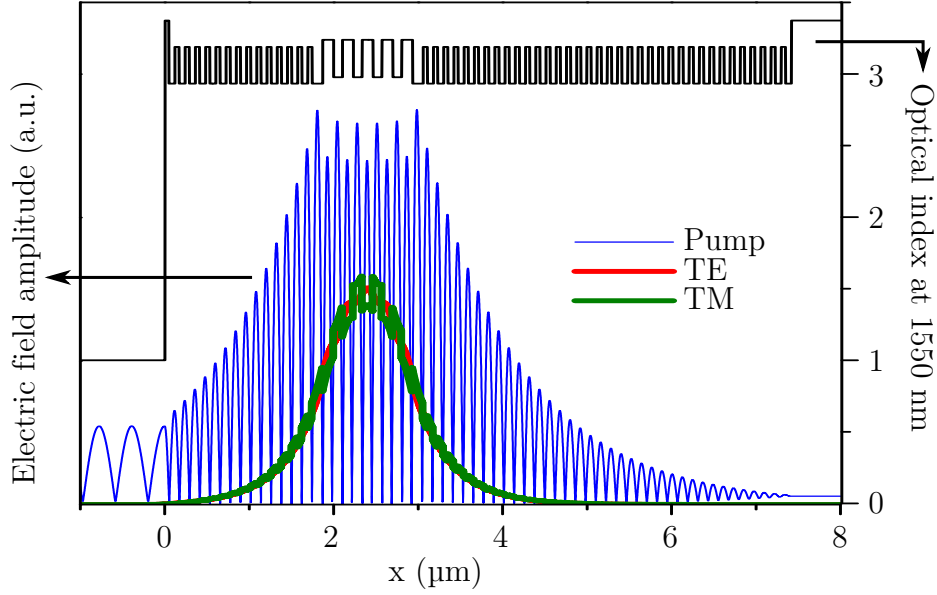


Figure 1.6 – Refractive index profile at 1550 nm structure and electric field amplitude for the three interacting modes within the heterostructure.

length*. The ideal solution would consist in a QPM by periodically poling the nonlinearity in the core layers, so that the interaction remains constructive at every depths. However periodic domain inversion of AlGaAs is a difficult technique to implement resulting in quite high optical losses [94], which are detrimental for quantum applications. The solution that we have chosen consists in alternating high second order susceptibility layers with low susceptibility ones having thicknesses Λ , matching their interfaces with the nodes of the intra-cavity pump field. Since the value of the nonlinear susceptibility is decreasing with increasing Aluminum content [95], a modification of the layers composition allows to obtain the QPM condition.

The addition of the microcavity has been therefore a strong improvement of the device. On the other hand its presence restricts the bandwidth of the pump field as far as the conversion efficiency is concerned. The reflectivity spectrum of Figure 1.7 shows the resonance wavelength $\lambda_{\mu\text{cav}} = 775$ nm of the nominal structure with a 280 pm theoretical bandwidth. This restriction on bandwidth is not a problem for pulses longer than a few picoseconds but prevents the use of shorter pulse. In the temporal domain, the intra-cavity pump pulse will not necessarily be Fourier-transform limited anymore. As an example, Figure 1.8 shows the temporal evolution of the intra-cavity pump field for a pulse of duration[†] 3.5 ps. We will see in section 2.2.4 how this mechanism impacts the time-energy properties of the biphoton state.

*we have neglected the influence of the angle of incidence of the pump beam. The correct formula is $\Lambda = \lambda_p / 2n \cos \theta$

[†]Full Width at Half-Maximum (FWHM) of the temporal intensity profile of the pulse.

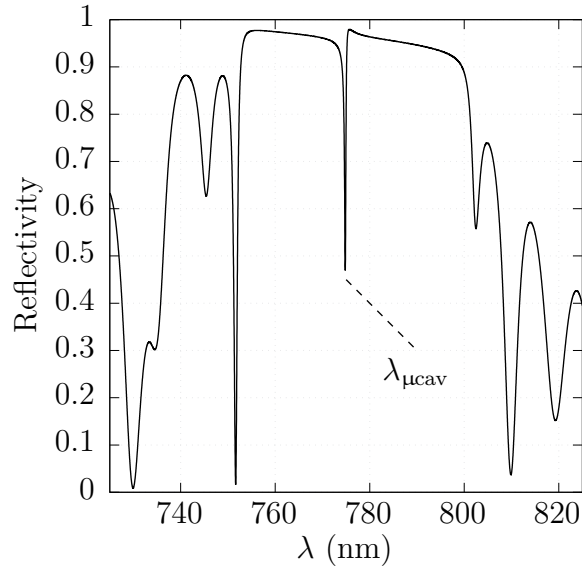


Figure 1.7 – Numerical simulation of the reflectivity of the nominal heterostructure for a pump beam at normal incidence. The pump beam resonates within the microcavity at a wavelength $\lambda_{\mu\text{cav}} = 775$ nm in the center of the stop-band.

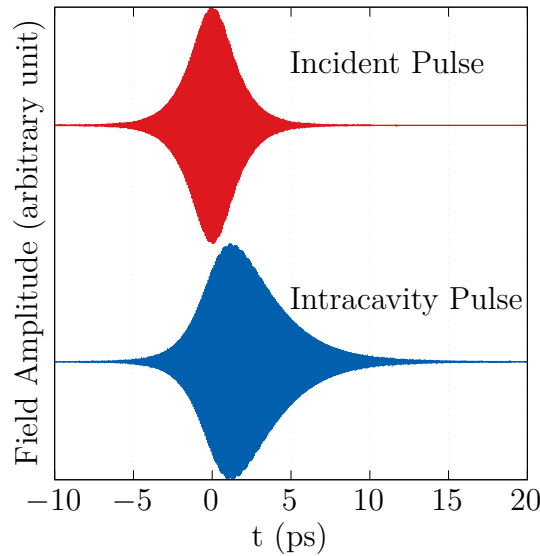


Figure 1.8 – Temporal amplitude profile of an incident pump pulse of duration 3.5 ps – FWHM of the intensity profile – (top red) with center wavelength $\lambda_p = 775$ nm and the corresponding intracavity pump field (bottom blue) simulated for the nominal structure at a temperature $T = 293.15$ K.

We should finally note that a tuning of the resonance point $\lambda_{\mu\text{cav}}$ can be achieved by heating or cooling the device. Indeed by changing the temperature, the size of the layers is altered through thermal expansion [96] and more importantly, the refractive indices are modified [93]. Figure 1.9 shows the position of the resonance $\lambda_{\mu\text{cav}}$ simulated for different temperatures. We see that this option

should be reserved for fine tuning as $\lambda_{\mu\text{cav}}$ is only shifted by two nanometers for a temperature variation of 40 °C.

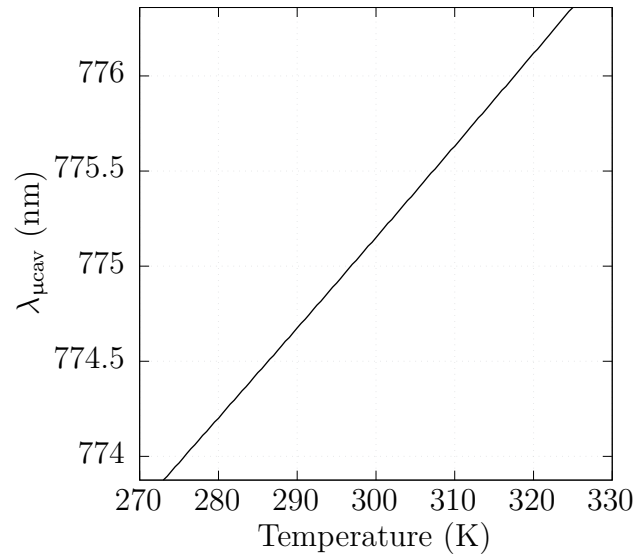


Figure 1.9 – Shift of the microcavity resonance wavelength $\lambda_{\mu\text{cav}}$ as a function of the temperature T of the device. This 1D numerical simulation takes into account both the variation of the refractive indices and the thermal expansion of the materials with temperature.

Chapter 2

Theory of Cavity SPDC

The versatility of sources based on a transverse pump configuration, in terms of frequency correlations engineering was first pointed out in [97]. In that reference, Walton *et al.* figured that the transverse pumping in waveguided counterpropagating phase matching geometries allowed to relax some constraints on the dispersion properties of the sample in the perspective of controlling the degree of correlations. In particular, they theoretically showed the possibility to generate states with positive frequency correlations, avoiding the problem of *group velocity matching* [98] which had prevented the production of such states in the first demonstrations of state engineering [84]. In a second work, the same authors discussed the extension of the technique to produce biphoton states with arbitrary frequency properties [42], notably frequency-uncorrelated states with different bandwidths for the signal and the idler by adjusting the spatial and temporal properties of the pump beam with a dispersive element. Another thorough analysis of the frequency properties of photon pairs generated in a counterpropagating geometry has been done in [99].

In this chapter, we perform a theoretical description of the time-frequency properties of the photon pairs produced with our device. In other words, we want to derive the Joint Spectral Amplitude (JSA) $\phi(\omega_s, \omega_i)$, a function giving the joint probability that the signal and idler photons are emitted at frequencies ω_s and ω_i , respectively. For photons generated in a waveguide, this function describes almost all properties of the pair and is thus sometimes called the biphoton wavefunction. Our goal is then to identify the parameters of the pump beam affecting the correlations between the constituents of the pair. The process we describe is sketched in figure 2.1 in which we focus on only one of the two possible interactions, the one in which the signal and the idler photons are emitted with a horizontal and vertical polarization, respectively. We thus refer to it as interaction *HV*. The results for the other interaction (interaction *VH*) and for higher-order guided modes are easily obtained by generalization. In the following, the x axis corresponds to the growth direction (oriented from the cap layer towards the substrate), the z axis is the propagation direction and the y axis is the direction orthogonal to the growth axis. The first section of this chapter is devoted to the derivation of the Hamiltonian describing the nonlinear interaction. In the second section, we dis-

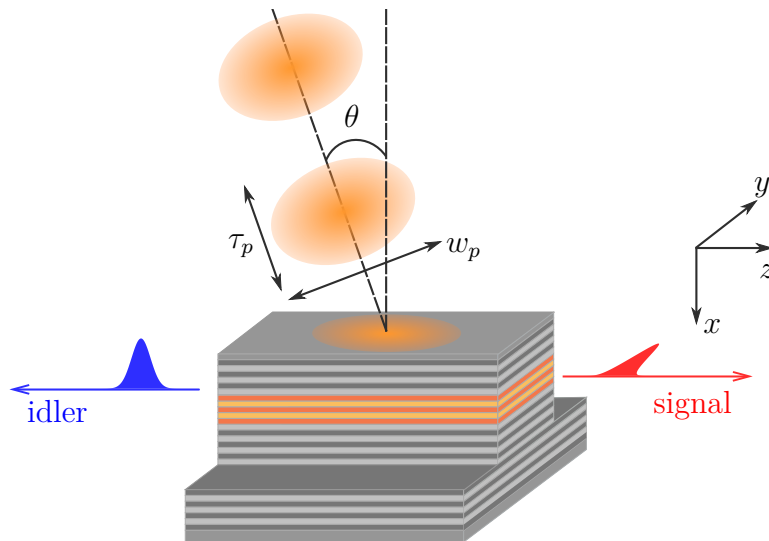


Figure 2.1 – Sketch of the process studied in this chapter: the pump beam is Gaussian with waist w_z and pulse duration τ_p , impinging with an angle of incidence θ . Although two interactions can occur, we will mostly focus on the one involving horizontally polarized signal photon and orthogonal idler photons (*HV*-process).

cuss the form of the JSA and the means to engineer it. Finally the influence of the reflectivities of the sample facets is discussed in the last section of this chapter.

2.1 Derivation of the state produced by SPDC

2.1.1 General considerations on the quantization of the electromagnetic field

The quantization procedure is exposed in many monographs [100, 101]: a Lagrangian formulation of the problem allows to find the conjugate canonical variables of the system [102]. These classical variables are then replaced by their quantum operators counterparts and the classical Poisson bracket by the corresponding canonical commutation relation.

Concerning the electromagnetic field, the scalar and vector potentials allow to derive the electric and magnetic fields. In vacuum, in the absence of free charges, a usual strategy is to adopt the Coulomb gauge in which the vector potential is transverse and the scalar potential can be canceled, which greatly simplifies the expression for the fields which are consequently purely transverse [103, 104]. An expansion in normal modes allows then to identify the conjugate canonical variables of the field and to obtain the quantized electromagnetic field. This approach can be extended to the case of the vacuum electromagnetic field in the presence of charges where the dynamics of the system is controlled by the Maxwell-Lorentz equations. The Coulomb gauge is again chosen to perform the canonical quanti-

zation*.

This approach is convenient to describe the interaction between light and matter when the latter is considered very dilute. The situation is less straightforward when dealing with optically dense matter which is the case for our device since the dispersion properties of the medium induce optical losses. An example of canonical quantization in a dense medium at the microscopic level can be found in [105]. The Lagrangian describing the system contains, in addition to terms describing matter and light, a part describing the interaction between them, and a reservoir term to take into account the energy lost by the field. Solving the problem by diagonalizing the full (linear) Hamiltonian allows to express the field operators and to find the dielectric constant of the medium, which is shown to satisfy the Kramers-Kronig relations. In particular, when losses are neglected, the derived field operators reduce to the ones obtained with a phenomenological approach [106] where the dielectric constant of the medium is assumed to be known *a priori* (from experiments). This justifies the “macroscopic” treatment we adopt in this thesis, since we will be interested in quantizing fields at frequencies away from any resonance *i.e.* where losses are negligible.

As a final remark, we note that other complications arise with complex photonic structures and cavities. The question of the electromagnetic field quantization in cavities is considered in details in the book of Dutra [107]. In an effort to describe nonlinear optical phenomena in non trivial structures [108, 109], Marco Liscidini, John Sipe and coworkers tackled this issue with a different approach based on quantum mechanics scattering theory [110]. In typical experiments light is coupled in and out an interaction region from a certain number of channels. Away from this interaction region, the channels are assumed to be isolated from each other. Therefore the problem consists in finding the part of an incident field that is scattered in every channels (asymptotic-in field) or conversely the incident fields in every channels that “scatters” in a wave outgoing in a single channel (asymptotic-out field). Doing so there is no need to define cavity quasi-modes [111] and their coupling with the external world since the effect of the structure on the field is completely considered in the solution to the scattering problem. This approach is convenient to describe SPDC or Four-Wave Mixing (FWM) since the nonlinear interaction is generally confined to a small volume and then light propagates away from it before being detected. This treatment was used by its authors to describe the links between spontaneous nonlinear phenomena, which can only be described in a quantum framework, and their stimulated counterparts for which a classical treatment exists [112, 113].

2.1.2 The electromagnetic field in the linear regime

The approach we follow for our treatment was introduced by Ghosh *et al.* in [114] and [115], where the derivation of the two-photon state produced by an SPDC source is derived with a first order perturbation of an interaction picture Hamilto-

*This gauge transformation is correct for low energy physics. However for relativistic systems, different transformations are more suitable [100].

nian. In transverse pumping geometries this approach was also followed by Booth *et al.* [116] and Peřina [99].

We first identify the modes of interest, those that will contribute to the nonlinear interaction Hamiltonian $\hat{H}_{\text{NL}}(t)$ and we choose the *interaction* or intermediate picture [117]. We remind that in the usual Schrödinger picture, the dependence in time is born by the wavefunction and the operators are constant in time. In the Heisenberg picture, the wavefunction is constant and the time evolution is contained in the operators so the fields better match their classical expression.

The interaction picture is a useful compromise in our case: the pump pulse represents a time dependent perturbation via the nonlinearity of the system. In its absence, the full Hamiltonian governing the radiation reduces to a linear term \hat{H}_{L} that has trivial consequences on the evolution of the electromagnetic field. With the adoption of the interaction picture, this evolution is contained in the operators allowing to capture all the physics due to the nonlinear interaction Hamiltonian $\hat{H}_{\text{NL}}(t)$ in the wavefunction. The final state (a long time after the pump pulse has left the medium) is then determined by solving a Schrödinger equation for the nonlinear term $\hat{H}_{\text{NL}}(t)$:

$$i\hbar \frac{d}{dt} |\Psi(t)\rangle = \hat{H}_{\text{NL}}(t) |\Psi(t)\rangle \quad (2.1)$$

Since the pump beam is very bright and the nonlinear interaction has a low efficiency, we assume that it is undepleted and we will thus adopt a classical description of the pump field. At this stage, we do not make any assumption on its spatio-temporal profile; we only impose a TE-polarization (*i.e.* with the electric field in the y direction of the waveguide), a choice that will be justified later. The pump beam is thus written as:

$$\hat{\mathbf{E}}_p(\mathbf{r}, t) \sim \mathbf{E}_p(\mathbf{r}, t) = \overbrace{(2\pi)^{-3/2} \int d\mathbf{k} \hat{\mathbf{u}}_y E_p(\mathbf{k}, t) e^{i(\mathbf{k}\cdot\mathbf{r} - \omega_{\mathbf{k}}t)}}^{\mathbf{E}_p^{(+)}(\mathbf{r}, t)} + \underbrace{\text{c.c.}}_{\mathbf{E}_p^{(-)}(\mathbf{r}, t)} \quad (2.2)$$

where $\hat{\mathbf{u}}_y$ is the unit vector indicating the polarization of the field and $E_p(\mathbf{k}, t)$ is the electric field amplitude at a given \mathbf{k} , whose expression will be specified later. The first integral $\mathbf{E}_p^{(+)}(\mathbf{r}, t)$ is then the analytic signal of the pump where $(+)$ indicates that positive frequencies are involved.

The parametric photons will be generated in the guided modes of the sample, propagating along the z -direction. The length L of the waveguide being much larger than the wavelengths in the range we will consider, we have a continuum of k -vectors aligned in the propagation direction. The confinement in the transverse plane (x, y) discretizes the number of allowed modes in those directions. Our waveguides are designed to be monomode in the growth direction, however the width of typical ridges is in the range $5 - 10 \mu\text{m}$. This allows higher order guided modes to exist in the y direction that we will identify with the label m . The polarization of the field is denoted with σ ; it can be either TE or TM. The modes are determined by solving the Maxwell equations for the heterostructure.

The quantization procedure is performed by expressing the classical fields in normal modes [103] and replacing their amplitudes by the corresponding creation - annihilation quantum operators. The electric field operator can thus be expressed under the form:

$$\hat{\mathbf{E}}(\mathbf{r}, t) = \sqrt{\frac{L}{2\pi}} \sum_{m,\sigma} \int dk \overbrace{\mathbf{E}_l(x, y) e^{i(kz - \omega_l t)} \hat{a}_l}^{\hat{\mathbf{E}}^{(+)}(\mathbf{r}, t)} + \underbrace{\text{h.c.}}_{\hat{\mathbf{E}}^{(-)}(\mathbf{r}, t)} \quad (2.3)$$

where \hat{a}_l is the annihilation operator of a photon in a given mode that we label $l = \{k, m, \sigma\}$ to keep a light notation and $\mathbf{E}_l(x, y)$ is the transverse profile of the mode in the waveguide. The \sqrt{L} factor appears because of the continuity of k . The creation and annihilation operators satisfy the usual commutation relations:

$$[\hat{a}_l, \hat{a}_l] = 0, \quad [\hat{a}_l, \hat{a}_l^\dagger] = \delta_{mm'} \delta_{\sigma\sigma'} \delta(k - k') \quad (2.4)$$

This is insured through a proper normalization of the modes [104, 108] which we detail hereafter. Given their guided nature, all the energy contained in the modes should pass through a plane transverse to the direction of propagation in the full course of time which is formally written:

$$\sum_{m,\sigma} \int dk \hbar \omega_l \hat{a}_l^\dagger \hat{a}_l = \int dt \iint dx dy \hat{\mathbf{I}}(\mathbf{r}, t) \quad (2.5)$$

where $\hat{\mathbf{I}}(\mathbf{r}, t) = \epsilon_0 c^2 [\hat{\mathbf{E}}^{(-)}(\mathbf{r}, t) \times \hat{\mathbf{B}}^{(+)}(\mathbf{r}, t) - \hat{\mathbf{B}}^{(-)}(\mathbf{r}, t) \times \hat{\mathbf{E}}^{(+)}(\mathbf{r}, t)]$ is the Poynting vector operator. This results in orthonormalization conditions on the transverse amplitudes $\mathbf{E}_l(x, y)$:

$$L \iint dx dy \epsilon_0 n^2(x, y; \omega_k) \mathbf{E}_{km\sigma}^*(x, y) \cdot \mathbf{E}_{km'\sigma'}(x, y) \frac{v_p(x, y; \omega_k)}{v_g(x, y; \omega_k)} = \frac{\hbar \omega_k}{2} \delta_{m,m'} \delta_{\sigma,\sigma'} \quad (2.6)$$

with $n(x, y; \omega_k)$ the local index of refraction and $v_p(x, y; \omega_k)$ and $v_g(x, y; \omega_k)$ the corresponding phase and group velocities [108]. The linear Hamiltonian governing the evolution of the guided fields is then:

$$\hat{H}_L = \sum_{m,\sigma} \int dk \hbar \omega_l \left(\hat{a}_l^\dagger \hat{a}_l + \frac{1}{2} \right) \quad (2.7)$$

2.1.3 The signal and idler fields

Our phase-matching scheme imposes counterpropagating photons. We will call *signal* the modes propagating in the forward direction, *i.e.* the terms with a positive k in the integral of equation (2.3) and *idler* those with a negative k (backward

propagation):

$$\hat{\mathbf{E}}(\mathbf{r}, t) = \underbrace{\sqrt{\frac{L}{2\pi}} \sum_{m,\sigma} \int_0^{+\infty} dk \mathbf{E}_l(x, y) e^{i(kz - \omega_l t)} \hat{\mathbf{a}}_l}_{\hat{\mathbf{E}}_s^{(+)}(\mathbf{r}, t)} + \underbrace{\sqrt{\frac{L}{2\pi}} \sum_{m,\sigma} \int_{-\infty}^0 dk \mathbf{E}_l(x, y) e^{i(kz - \omega_l t)} \hat{\mathbf{a}}_l}_{\hat{\mathbf{E}}_i^{(+)}(\mathbf{r}, t)} + \text{h.c.} \quad (2.8)$$

The guiding regime also implies a direct connection between the k vector and the frequency ω considered:

$$|k| = \frac{n_{m\sigma}(\omega) \omega}{c} \quad (2.9)$$

where $n_{m\sigma}(\omega)$ is the effective index of the mode. This allows to express the fields as an integral over frequencies [104], which will be more intuitive for the description of the frequency correlations between the photons. After the change of variables passing from k to ω , the fields read:

$$\hat{\mathbf{E}}_{s/i}^{(+)}(\mathbf{r}, t) = \sqrt{\frac{L}{2\pi}} \sum_{m,\sigma} \int_0^{+\infty} d\omega \frac{\mathbf{E}_{m\sigma}(x, y; \omega)}{\sqrt{v_g^{m\sigma}(\omega)}} e^{i(\pm|k_{m\sigma}(\omega)|z - \omega t)} \hat{\mathbf{a}}_{s/i, m\sigma}(\omega) \quad (2.10)$$

with $v_g^{m\sigma}(\omega)$ the effective group velocity of mode m, σ at frequency ω and $\hat{\mathbf{a}}_{s/i, m\sigma}(\omega)$ is the annihilation operator of a signal/idler photon of this mode. The exponential has a + sign for the signal field and a - for the idler. The fields being expressed, we must find the correct form of the nonlinear interaction Hamiltonian $\hat{H}_{\text{NL}}(t)$ before the formal derivation of the biphoton state.

2.1.4 The Hamiltonian for the nonlinear interaction

The nonlinear interaction Hamiltonian is the quantum equivalent of the classical nonlinear energy density representing the interaction of the three waves in the nonlinear medium [118], integrated over the whole interaction volume. Limiting our treatment to second order nonlinearities, this Hamiltonian reads:

$$\hat{H}_{\text{NL}}(t) = \frac{\epsilon_0}{3} \int d\mathbf{r} \chi_{ijk}^{(2)}(\mathbf{r}) \hat{\mathbf{E}}_i(\mathbf{r}, t) \hat{\mathbf{E}}_j(\mathbf{r}, t) \hat{\mathbf{E}}_k(\mathbf{r}, t) \quad (2.11)$$

where the summation over all repeated indices is implied and $\chi_{ijk}^{(2)}(\mathbf{r})$ represents the second order nonlinear susceptibility at the position \mathbf{r} in the medium. Being far from resonance, we neglect the dispersion of the nonlinear response. Taking into account the Kleinman's symmetry, all permutations of ijk are equivalent [118].

In the case of our device, the zincblende structure of $\text{Al}_x\text{Ga}_{1-x}\text{As}$ compounds imposes a cubic $\bar{4}3m$ symmetry of the crystal and thus a certain form of the nonlinear tensor [118]. Due to this fact and the phase matching being achieved for parametric fields propagating in opposite directions, only type II processes will

occur *i.e.* those involving signal and idler fields with orthogonal polarizations. In addition, SPDC can only take place if the pump is TE-polarized, justifying the choice made in the previous section. We do not give the full details of these calculations which can be found in appendix A of the PhD thesis of Xavier Caillet [91]. The nonlinear Hamiltonian thus simplifies to:

$$\begin{aligned} \hat{H}_{\text{NL}}(t) = & \epsilon_0 \int d\mathbf{r} \chi^{(2)}(\mathbf{r}) \hat{E}_p(\mathbf{r}, t) \hat{E}_{s,\text{TE}}(\mathbf{r}, t) \hat{E}_{i,\text{TM}}(\mathbf{r}, t) \\ & + \epsilon_0 \int d\mathbf{r} \chi^{(2)}(\mathbf{r}) \hat{E}_p(\mathbf{r}, t) \hat{E}_{s,\text{TM}}(\mathbf{r}, t) \hat{E}_{i,\text{TE}}(\mathbf{r}, t) \end{aligned} \quad (2.12)$$

with the factor $1/3$ gone because of the summation over all equivalent permutations. The condition of energy conservation will only become apparent after integration over time and over the pump spectrum. Nevertheless, for clarity, we now remove from the expression of $\hat{H}_{\text{NL}}(t)$ the terms that will not satisfy this condition. To do so, we remind that the fields can be separated into a positive frequency term $\hat{\mathbf{E}}^{(+)}(\mathbf{r}, t)$ (the analytic signal) which annihilates a photon in all modes and its hermitian conjugate with negative frequencies $\hat{\mathbf{E}}^{(-)}(\mathbf{r}, t)$ which creates a photon. Therefore the only terms of equation (2.12) that preserve energy are those involving the destruction of a photon in the pump mode and the creation of a photon in the signal and the idler (and their hermitian conjugates). Considering this, $\hat{H}_{\text{NL}}(t)$ reduces to:

$$\begin{aligned} \hat{H}_{\text{NL}}(t) = & \epsilon_0 \int d\mathbf{r} \chi^{(2)}(\mathbf{r}) \hat{E}_p^{(+)}(\mathbf{r}, t) \hat{E}_{s,\text{TE}}^{(-)}(\mathbf{r}, t) \hat{E}_{i,\text{TM}}^{(-)}(\mathbf{r}, t) + \text{h.c.} \\ & + \epsilon_0 \int d\mathbf{r} \chi^{(2)}(\mathbf{r}) \hat{E}_p^{(+)}(\mathbf{r}, t) \hat{E}_{s,\text{TM}}^{(-)}(\mathbf{r}, t) \hat{E}_{i,\text{TE}}^{(-)}(\mathbf{r}, t) + \text{h.c.} \end{aligned} \quad (2.13)$$

We have thus identified the nonlinear interaction Hamiltonian. In doing so we have also made it clear that two “interactions” can occur in the device with exchanged polarizations for the output photons. In the next section we derive the output state of the pair in the interaction picture.

2.1.5 The two-photon state

The output state of our source is retrieved by solving the Schrödinger equation (2.1) for $\hat{H}_{\text{NL}}(t)$. At a given time t , the state of the system reads:

$$|\Psi(t)\rangle = \hat{T} e^{\frac{1}{i\hbar} \int_{-\infty}^t \hat{H}_{\text{NL}}(t) dt} |\Psi(-\infty)\rangle \quad (2.14)$$

where \hat{T} is the time ordering operator*. In the low pump energy regime, where the probability to generate one pair (per pump pulse) is small, a valid expression for

*The expansion of the exponential will give multiple powers of the time integral of the Hamiltonian, which do not necessarily commute. In the regime where a high number of pairs is produced *i.e.* when the pump is very intense, the time ordering has the effect of taking into account pairs that are already produced which stimulate the production of pairs with identical characteristics bridging SPDC and DFG. An interesting discussion is found in section 5.4 of [119].

the output state is given by the first order approximation of the previous equation:

$$|\Psi(t)\rangle = |\text{vac}\rangle + \frac{1}{i\hbar} \int_{-\infty}^t dt \hat{H}_{\text{NL}}(t) |\text{vac}\rangle \quad (2.15)$$

where we have taken the vacuum $|\text{vac}\rangle$ as the initial state ($t \rightarrow -\infty$). The second term on the right hand side is the one describing the pair: writing $|\psi\rangle$ the two-photon state and β its generation probability amplitude, we have:

$$|\Psi(t)\rangle = |\text{vac}\rangle + \beta |\psi\rangle \quad (2.16)$$

Since we measure the state after the disappearance of the pump pulse (we measure the state away from the source), we can extend the time integration to $+\infty$. To simplify the demonstration, we focus only on the interaction where the signal photon is TE polarized. The results are readily extensible to the other interaction. We also neglect the interactions that can occur with guided modes of higher order and focus on the fundamental modes of the waveguide. Under these assumptions, the two-photon state is:

$$|\psi\rangle = \frac{\epsilon_0}{i\beta\hbar} \int dt \int d\mathbf{r} \chi^{(2)}(\mathbf{r}) \hat{E}_p^{(+)}(\mathbf{r}, t) \hat{E}_{s,\text{TE}}^{(-)}(\mathbf{r}, t) \hat{E}_{i,\text{TM}}^{(-)}(\mathbf{r}, t) |\text{vac}\rangle \quad (2.17)$$

Expanding the fields in terms of their integral over frequencies, we get:

$$\begin{aligned} |\psi\rangle = & \frac{\epsilon_0}{i\beta\hbar} \int dt \int d\mathbf{r} \iiint d\omega_p d\omega_s d\omega_i \chi^{(2)}(\mathbf{r}) E_p(\mathbf{r}, \omega_p) E_{\text{TE}}(x, y, \omega_s) E_{\text{TM}}(x, y, \omega_i) \\ & \times \frac{L}{2\pi \sqrt{v_g^{\text{TE}}(\omega_s) v_g^{\text{TM}}(\omega_i)}} e^{-i\Delta k z} e^{i\Delta\omega t} \hat{a}_{\text{TE}}^\dagger(\omega_s) \hat{a}_{\text{TM}}^\dagger(\omega_i) |\text{vac}\rangle \end{aligned} \quad (2.18)$$

with $\Delta\omega = (\omega_s + \omega_i) - \omega_p$ representing the energy difference between the three waves, and $\Delta k = k_{\text{TE}}(\omega_s) - k_{\text{TM}}(\omega_i)$ indicating the phase mismatch between the signal and the idler field. A first simplification is done by integrating this expression over time, which is essentially $\int dt \exp(i\Delta\omega t) = 2\pi\delta(\Delta\omega)$. This corresponds to the condition of energy conservation and justifies the removal of some terms from the nonlinear Hamiltonian. We can now integrate over the frequency ω_p to eliminate it from the expression of the state. This leads to an expression of the state as a double integration over the signal and idler frequencies:

$$\boxed{|\psi\rangle = \iint d\omega_s d\omega_i \phi(\omega_s, \omega_i) \hat{a}_{\text{TE}}^\dagger(\omega_s) \hat{a}_{\text{TM}}^\dagger(\omega_i) |\text{vac}\rangle} \quad (2.19)$$

with $\phi(\omega_s, \omega_i)$ the Joint Spectral Amplitude (JSA) or biphoton wavefunction :

$$\begin{aligned} \phi(\omega_s, \omega_i) = & \frac{\epsilon_0 L}{i\beta\hbar \sqrt{v_g^{\text{TE}}(\omega_s) v_g^{\text{TM}}(\omega_i)}} \\ & \times \int d\mathbf{r} \chi^{(2)}(\mathbf{r}) E_p(\mathbf{r}, \omega_s + \omega_i) E_{\text{TE}}(x, y, \omega_s) E_{\text{TM}}(x, y, \omega_i) e^{-i\Delta k z} \end{aligned} \quad (2.20)$$

Although an integral over \mathbf{r} is still present in the expression, once we will specify the form of the pump beam, its evaluation will give rise to a function of ω_s and ω_i corresponding to the phase-matching. Equations (2.19) and (2.20) can be generalized to the case in which both interactions occur and several spatial modes are involved:

$$|\psi\rangle = \iint d\omega_s d\omega_i \phi_\sigma^{mm'}(\omega_s, \omega_i) \hat{a}_{m\sigma}^\dagger(\omega_s) \hat{a}_{m'\sigma_\perp}^\dagger(\omega_i) |\text{vac}\rangle \quad (2.21)$$

with an implicit summation over the guided modes m and m' and the polarization σ (σ_\perp is the polarization orthogonal to σ). The JSA of a given process takes the form:

$$\begin{aligned} \phi_\sigma^{mm'}(\omega_s, \omega_i) = & \frac{\epsilon_0 L}{i\beta\hbar\sqrt{v_g^{m\sigma}(\omega_s)v_g^{m'\sigma_\perp}(\omega_i)}} \\ & \times \int d\mathbf{r} \chi^{(2)}(\mathbf{r}) E_p(\mathbf{r}, \omega_s + \omega_i) E_{m\sigma}(x, y, \omega_s) E_{m'\sigma_\perp}(x, y, \omega_i) e^{-i\Delta k z} \end{aligned} \quad (2.22)$$

the phase mismatch Δk depending on the modes involved and their frequencies. Having extracted the probability of generation β , the normalization of the biphoton wavefunction takes a simple form:

$$\langle\psi|\psi\rangle = \sum_{m,m',\sigma} \iint d\omega_s d\omega_i \left| \phi_\sigma^{mm'}(\omega_s, \omega_i) \right|^2 = 1 \quad (2.23)$$

The modulus square of the JSA, the Joint Spectral Intensity (JSI) or joint spectral density can thus be interpreted as the probability density of finding the biphoton in a given pair of modes and a given couple of frequencies, justifying the designation of $\phi_\sigma^{mm'}(\omega_s, \omega_i)$ as the biphoton wavefunction. Now that we have identified the general form of the biphoton state, it becomes necessary to specify a bit more the shape of the pump to understand how the control of its characteristics allows to engineer the emitted pairs.

2.2 Engineering the JSA

After the derivation of the state in the previous section, we now comment on the engineering of the biphoton time-frequency correlations in our device. In doing so, we will also introduce different ways to visualize the characteristics of the state that, depending on the situation, can be more convenient than the most usual JSI.

2.2.1 The phase-mismatch along the guiding direction

To simplify the following discussions, we first analyze the term of phase mismatch $c\Delta k(\omega_s, \omega_i) = \omega_s n_{\text{TE}}(\omega_s) - \omega_i n_{\text{TM}}(\omega_i)$ with $n_{\text{TE/TM}}$ the effective index of the TE/TM mode, for the case of the first interaction (see figure 2.1) and limit our treatment to fundamental modes. To do so, we expand the effective indices of the

signal and idler modes around the degenerate frequency $\omega_{\text{deg}} = \omega_p/2$, to second order in $\delta\omega = \frac{\omega_s - \omega_i}{2}$:

$$\begin{aligned} n_{\text{TE}}(\omega_s = \omega_{\text{deg}} + \delta\omega) &= n_{\text{TE}}(\omega_{\text{deg}}) + \delta\omega \left. \frac{dn_{\text{TE}}}{d\omega} \right|_{\omega_{\text{deg}}} + \frac{(\delta\omega)^2}{2} \left. \frac{d^2n_{\text{TE}}}{d\omega^2} \right|_{\omega_{\text{deg}}} \\ n_{\text{TM}}(\omega_i = \omega_{\text{deg}} - \delta\omega) &= n_{\text{TM}}(\omega_{\text{deg}}) - \delta\omega \left. \frac{dn_{\text{TM}}}{d\omega} \right|_{\omega_{\text{deg}}} + \frac{(\delta\omega)^2}{2} \left. \frac{d^2n_{\text{TM}}}{d\omega^2} \right|_{\omega_{\text{deg}}} \end{aligned} \quad (2.24)$$

Using these expansions we can re-express the phase mismatch:

$$\Delta k = k_{\text{deg}}(\omega_p) + \frac{\omega_-}{\bar{v}_g} + \left(\frac{\omega_-}{2} \right)^2 \delta_{\text{GVD}} \quad (2.25)$$

where $\omega_- = \omega_s - \omega_i$. The first term in this expansion correspond to the wavevector the pump should have (projected along the z -axis) in order to produce frequency-degenerate photon pairs. Its full expression is:

$$k_{\text{deg}}(\omega_p) = \frac{\omega_p \left(\frac{n_{\text{TE}} - n_{\text{TM}}}{2} \right)}{c} = \sin \theta_{\text{deg}} \frac{\omega_p}{c} \quad (2.26)$$

This term is linked to the birefringence of the device: the pump beam should impinge with an angle θ_{deg} to obtain degenerate photons (see figure 1.3). Even though bulk GaAs is not birefringent, the structuration implies a small index mismatch between the two polarizations and therefore the angle of incidence for degeneracy is slightly offset from normal incidence.

The second term in equation (2.25) depends on \bar{v}_g , the harmonic mean of the group velocities defined by:

$$\begin{aligned} \bar{v}_g^{-1} &= \frac{v_g^{\text{TE}-1} + v_g^{\text{TM}-1}}{2} \\ &= \frac{1}{c} \left[\frac{n_{\text{TE}} + n_{\text{TM}}}{2} + \frac{\omega_{\text{deg}}}{2} \frac{d(n_{\text{TE}} + n_{\text{TM}})}{d\omega} \right] \end{aligned} \quad (2.27)$$

This is one of the main features of the counterpropagating phase-matching playing a strong role in the control of the frequency correlations. Indeed \bar{v}_g will act as a proportionality coefficient between the spatial profile of the pump beam and the spectral width of the JSA along the axis defined by the ω_- variable.

The third term of (2.25) is controlled by the difference between the Group-Velocity Dispersions (GVDs) of the two photons:

$$\begin{aligned} \delta_{\text{GVD}} &= \frac{1}{2} \left(\frac{d^2k_{\text{TE}}}{d\omega^2} - \frac{d^2k_{\text{TM}}}{d\omega^2} \right) \\ &= \frac{1}{2c} \left[2 \frac{d(n_{\text{TE}} - n_{\text{TM}})}{d\omega} + \omega_{\text{deg}} \frac{d^2(n_{\text{TE}} - n_{\text{TM}})}{d\omega^2} \right] \end{aligned} \quad (2.28)$$

The GVD is rather small for our waveguides, at least for the low order modes, and its value being close for TE and TM modes, we will neglect this third term in the rest of the discussion*:

$$\Delta k = k_{\text{deg}}(\omega_p) + \frac{\omega_-}{v_g} \quad (2.29)$$

Having identified and commented the different contributions to the phase-mismatch along the propagation direction, we start the analysis of the impact of the pump profile on the biphoton state.

2.2.2 The Joint Spectral Amplitude

In order to analyze the influence of the spatial profile of the pump beam on the biphoton, we make some assumptions: we restrict the pump beam propagation to the (x, z) plane so that its wavevector k_p has no y -component (see figure 2.1). We also assume that the transverse profile $\phi_p(y, z)$ of the pump is separable along the y and z axis, *i.e.* we can express it as a product $\phi_p(y) \times \phi_p(z)$. The amplitude of the pump beam thus reads:

$$E_p(\mathbf{r}, \omega_p \equiv \omega_+) = \mathcal{E}_p^{(0)} f_{\text{ucav}}(x, \omega_+) f_{\text{spectrum}}(\omega_+) \phi_p(y, \omega_+) \phi_p(z, \omega_+) \quad (2.30)$$

Here $\omega_+ = \omega_p = \omega_s + \omega_i$ and $f_{\text{ucav}}(x, \omega_p)$ is a function describing the effect of the microcavity on the spectrum and the shape of the pump beam along x ; $f_{\text{spectrum}}(\omega_+)$ is the spectrum of the pump field; $\phi_p(y, \omega_+)$ and $\phi_p(z, \omega_+)$ are the spatial profile of the beam along the y and z -direction with a possible dependence on ω_+ . $\mathcal{E}_p^{(0)}$ is a normalization constant. With this expression for the pump beam, we can decompose the integral over \mathbf{r} in equation (2.22) for the JSA along x , y and z . In order to do so, we introduce the explicit expression of $\chi^{(2)}(\mathbf{r})$, the quantity describing the nonlinear medium:

$$\chi^{(2)}(\mathbf{r}) = \chi^{(2)}(x) \times \Pi_W(y) \times \Pi_L(z) \quad (2.31)$$

where $\Pi_W(y)$ and $\Pi_L(z)$ are rectangular gate functions ($\Pi_L(z) = 1$ if $|z| \leq L/2$ and 0 elsewhere) giving the extent of the nonlinear medium along the length L and the width W of the waveguide, directions along which the nonlinearity is constant. $\chi^{(2)}(x)$ is the value of the nonlinearity along the x -axis, given by the composition of the layers in the heterostructure[†]. With this considered, the general expression

*We do however take into account the full (calculated) chromatic dispersion in our numerical simulations.

[†]To estimate the value of the second order nonlinear coefficient, we use the value obtained for GaAs at telecom wavelengths in [120] and the dependence on the Aluminum content from [95].

of the JSA is:

$$\begin{aligned}
\phi_{\sigma}^{mm'}(\omega_s, \omega_i) &= \frac{\epsilon_0 L}{i\beta\hbar\sqrt{v_g^{m\sigma}(\omega_s)v_g^{m'\sigma_{\perp}}(\omega_i)}} \mathcal{E}_p^{(0)} f_{\text{spectrum}}(\omega_+) \\
&\times \int dx \chi^{(2)}(x) f_{\mu\text{cav}}(x, \omega_+) E_{m\sigma}(x, \omega_s) E_{m'\sigma_{\perp}}(x, \omega_i) \\
&\times \int dy \Pi_W(y) \phi_p(y, \omega_+) E_{m\sigma}(y, \omega_s) E_{m'\sigma_{\perp}}(y, \omega_i) \\
&\times \int dz \Pi_L(z) \phi_p(z, \omega_+) e^{-i\Delta k z}
\end{aligned} \tag{2.32}$$

The first and second integrals represent the overlap of the three fields in the cross-section of the waveguide. The second integral along y in particular determines the pairs of modes m and m' which can interact depending on their overlap with the profile $\phi_p(y, \omega_+)$ of the pump beam. Focusing on the third integral which corresponds to the phase-matching, we introduce the quantity:

$$\phi_{\text{PM}}(\omega_s, \omega_i) = \int dz \Pi_L(z) \phi_p(z, \omega_+) e^{-i\Delta k(\omega_s, \omega_i)z} \tag{2.33}$$

where $\Delta k(\omega_s, \omega_i)$ is the phase-mismatch whose expression is given by equation (2.29). If the pump spot-size is small with respect to the length of the waveguide, *this expression corresponds approximately to the Fourier transform of $\varphi(z, \omega_+) = \phi_p(z, \omega_+) e^{-ik_{\text{deg}}z}$:*

$$\phi_{\text{PM}}(\omega_s, \omega_i) = \int_{-L/2}^{+L/2} dz \varphi(z, \omega_+) e^{-i(\omega_s - \omega_i)z/\bar{v}_g} \sim \sqrt{2\pi} \tilde{\varphi}\left(\frac{\omega_-}{\bar{v}_g}, \omega_+\right) \tag{2.34}$$

To illustrate this result, we take the simple example of a pulsed gaussian beam of waist w_y along direction y and w_z along direction z located at the core of the source so that we consider a flat wavefront, with a pulse duration $\tau_p \propto \Delta\omega_p$ and central frequency $\omega_p^{(0)}$ matching the resonance frequency of the microcavity. The typical output pulse of a Ti:sapphire laser has a hyperbolic secant temporal profile rather than a Gaussian. This function is its own Fourier Transform so we choose this for $f_{\text{spectrum}}(\omega_+)$. The beam is impinging with an angle θ with respect to the vertical direction. We are in the absence of chirp and there is no frequency dependence in the angular spectrum (θ is independent of ω_p). We finally assume that we can decouple the spatial effect of the microcavity on the pump beam, *i.e.* its amplitude distribution in the growth direction (see figure 1.6) from the spectral filtering effect. This is indeed a correct approximation since the amplitude distribution can be considered constant over the spectral acceptance of the microcavity (see figure 1.7 and 2.6). Therefore we can write $f_{\mu\text{cav}}(x, \omega_+) = f_{\mu\text{cav}}(x) \times f_{\mu\text{cav}}(\omega_+)$. With these considerations, the amplitude of the pump reads:

$$\begin{aligned}
E_p(\mathbf{r}, \omega_+) &= \mathcal{E}_p^{(0)} f_{\text{ucav}}(x) \\
&\times \exp\left(-\frac{y^2}{w_y^2}\right) \\
&\times \exp\left(-\frac{z^2}{w_z^2}\right) e^{i\frac{\omega_+ \sin \theta}{c} z} \\
&\times \text{sech}\left(\frac{\omega_+ - \omega_p^{(0)}}{\Delta\omega_p}\right) f_{\text{ucav}}(\omega_+)
\end{aligned} \tag{2.35}$$

Focusing on fundamental signal and idler modes and interaction HV , the JSA corresponding to this form of pump can be fully identified by simplifying equation (2.20):

$$\boxed{\phi(\omega_s, \omega_i) = \chi_\Gamma \phi_{\text{PM}}(\omega_-) \phi_{\text{spectral}}(\omega_+)} \tag{2.36}$$

The term χ_Γ is the overlap integral between the interacting fields and the nonlinear medium, including multiplicative constants:

$$\begin{aligned}
\chi_\Gamma(\omega_s, \omega_i) &= \frac{\epsilon_0 L \mathcal{E}_p^{(0)}}{i\beta\hbar\sqrt{v_g^{\text{TE}}(\omega_s)v_g^{\text{TM}}(\omega_i)}} \\
&\times \iint dx dy \chi^{(2)}(x) \Pi_W(y) f_{\text{ucav}}(x) \exp\left(-\frac{y^2}{w_y^2}\right) E_{\text{TE}}(x, y, \omega_s) E_{\text{TM}}(x, y, \omega_i)
\end{aligned} \tag{2.37}$$

It corresponds to the quantity that has been optimized during the design of the source [91] since the efficiency of the source is directly linked to its value. The GVD of the modes is weak so the effective group velocities can be considered constant. The JSIs we study in this thesis will not exceed a few nanometers in width and will remain the telecom band. For such frequency ranges, the profiles of the guided modes do not vary significantly, which is also the case for the distribution of the pump beam in the heterostructure within the acceptance bandwidth of the microcavity. Therefore χ_Γ has just a marginal effect on the shape of the JSA. For this analytic discussion we can thus consider it as frequency-independent and it will just represent a multiplicative constant.

Since there is no angular dispersion in the pump beam, the phase-matching term $\phi_{\text{PM}}(\omega_-)$ depends only on ω_- , *i.e.* on the difference between the signal and the idler frequency. The pump frequency will just act as a parameter, setting the center of ϕ_{PM} in the (ω_s, ω_i) plane but will play no role in the shape of this function. For a Gaussian pump beam, with a waist that is small with respect to the waveguide length *i.e.* $w_z \ll L$, we have:

$$\phi_{\text{PM}}(\omega_-) = \sqrt{\pi} w_z \exp\left[-\left(\frac{\omega_- - \omega_-^{(0)}}{\Delta\omega_-}\right)^2\right] \tag{2.38}$$

A representation of this function is given in figures 2.2(a), (b) and (c). We see that the phase-matching condition together with our choice of pump beam sets a

distribution along the anti-diagonal of the (ω_s, ω_i) plane, *i.e.* along the ω_- axis. This function is Gaussian of width $\Delta\omega_- = 2\bar{v}_g/w_z$ and it is shifted from degeneracy by an amount $\omega_-^{(0)} = \omega_p(\sin\theta - \sin\theta_{\text{deg}})\bar{v}_g/c$. We can see that at the small angles approximation, $\omega_-^{(0)} \approx \omega_p(\theta - \theta_{\text{deg}})\bar{v}_g/c$, we retrieve the linear dependence of the frequencies of the photons with the angle of incidence θ (see figure 1.5). As shown in figure 2.2, by varying the size of the pump beam, we can engineer the degree of frequency-correlation between the signal and the idler along the antidiagonal of the JSA. Note that in the limiting case where $w_z \gg L$, depicted in figure 2.2(c), we pump the whole waveguide and ϕ_{PM} is just the Fourier Transform of $\Pi_L(z)$:

$$\phi_{\text{PM}}(\omega_-) = L \operatorname{sinc}\left(\frac{\omega_- - \omega_-^{(0)}}{\Delta\omega_-}\right) \quad (2.39)$$

with $\operatorname{sinc}(x) = \sin(x)/x$ and where $\Delta\omega_- = 2\bar{v}_g/L$ is the smallest width we are able to achieve with a given sample. In intermediate situations ($w_z \approx L$), ϕ_{PM} is given by the convolution of the Gaussian corresponding to the incident beam and the cardinal sine corresponding to the waveguide.

The control of the spatial properties of the pump beam allows us to engineer the part of the JSA that depends on the phase-matching and we have seen that this corresponds to the antidiagonal (ω_- axis) in the case of the counterpropagating scheme. The control on the positive diagonal, namely the ω_+ axis, is related to the conservation of energy and is thus allowed by the modification of the spectro-temporal properties of the pump beam:

$$\phi_{\text{spectral}}(\omega_+) = \operatorname{sech}\left(\frac{\omega_+ - \omega_p^{(0)}}{\Delta\omega_p}\right) f_{\text{ucav}}(\omega_+) \quad (2.40)$$

We see from this expression that the pump spectrum directly defines a function that is orthogonal to that defined by the phase-matching condition (see figures 2.2(d), (e) and (f)) and thus a modification of the bandwidth $\Delta\omega_p$ of the pump laser will affect the width $\Delta\omega_+$ of the function that defines the JSA in the ω_+ direction. Here we have chosen a hyperbolic secant to match the characteristics of our laser but a Continuous Wave (CW) laser could be chosen as well, in which case ϕ_{spectral} will take the linewidth of the laser and we will obtain an anticorrelated state, such as the one depicted in figure 2.2(g) but with an even thinner width along ω_+ . More sophisticated engineering of the pump beam can be done, for example using a 4f-line [83] to pulse-shape the beam. We note that even though the first demonstrations of frequency engineering of the biphoton were done with the spatial shaping of the pump beam [84], modifying the spectro-temporal properties of the pump beam is, in collinear geometries, the only option once the sample has been processed. This is a strong advantage of the counterpropagating scheme which has the versatility of playing on the two aspects. With our device, this flexibility will be limited by the presence of the microcavity whose constraints on the resonance wavelength and the acceptable bandwidth are described by $f_{\text{ucav}}(\omega_+)$.

We note the special case for which the phase-matching and the energy conservation impose distributions of identical widths *i.e.* $\sqrt{\ln(2)}\Delta\omega_- = \operatorname{sech}^{-1}(1/2)\Delta\omega_+$

for a Gaussian spatial profile and a hyperbolic secant temporal profile or, in terms of experimental parameters:

$$\begin{aligned}
 w_z &= \frac{2\sqrt{\ln(2)}\bar{v}_g}{\operatorname{sech}^{-1}(1/2)\Delta\omega_p} \\
 &= \frac{\pi\sqrt{\ln(2)}\bar{v}_g}{2\operatorname{sech}^{-1}(1/2)\operatorname{sech}^{-1}(\sqrt{1/2})}\tau_p
 \end{aligned} \tag{2.41}$$

with $\Delta\omega_p$ the FWHM of the spectral amplitude and τ_p the FWHM of the temporal pulse intensity. For these specific conditions (neglecting the phase imposed by the microcavity and limiting the pump bandwidth to its spectral acceptance), the frequency state of the pair will be uncorrelated as in figure 2.2(h), which is a situation of paramount importance for heralded single photon sources [79].

Changing the spectral and spatial properties of the pump beam thus allows to tune the JSA along two orthogonal axis as illustrated in figure 2.2. However since these axis correspond to $\omega_+ = \omega_s + \omega_i$ and $\omega_- = \omega_s - \omega_i$, the simple Gaussian pump we have proposed does not allow to control the bandwidths of the photons individually. Fortunately, using a dispersive element like a prism or a grating, one can correlate the wavevector with the individual frequency components of the pulse so that $\mathbf{k}_p \cdot \hat{\mathbf{u}}_z = f(\omega_p)\omega_p/c$ with f a function describing the effect of the dispersive element on the k -distribution. This has the consequence to rotate $\phi_{\text{PM}}(\omega_-, \omega_+)$ which now depends on ω_+ . The dispersion can be chosen [42] so that the state is uncorrelated (no information on ω_s is gained by measuring ω_i and vice versa) but with different bandwidths for the photons. For example if a horizontal JSA is desired (with degenerate central wavelengths), *i.e.* a biphoton state with a bigger bandwidth for the signal rather than the idler, the distribution $\phi_{\text{PM}}(\omega_-, \omega_+)$ corresponding to the phase-matching should be horizontal as well. In the frame (ω_+, ω_-) , the center of ϕ_{PM} , labeled $\omega_-^{(0)}$ (see the definitions in equation (2.38)), must thus evolve as $\omega_-^{(0)} = \omega_+ - \omega_p^{(0)}$. The orthogonal situation corresponds to $\omega_-^{(0)} = -(\omega_+ - \omega_p^{(0)})$ so that the angle of incidence $\theta(\omega_+)$ obeys the following relation:

$$\sin [\theta(\omega_+)] = \sin \theta_{\text{deg}} \pm \frac{c}{\bar{v}_g} \left(1 - \frac{\omega_p^{(0)}}{\omega_+} \right) \tag{2.42}$$

with + or - for a horizontal or a vertical JSA respectively. The two situations are illustrated in figure 2.3. The angle θ_{deg} in equation (2.42) is the central angle in the dispersed beam (corresponding to the central frequency $\omega_p^{(0)}$). For this choice of central angle, the central frequencies of the photons will be degenerate. Choosing a different central angle in the above expression gives even more latitude, allowing to choose non degenerate central wavelengths for the photons as in figures 2.3(b), (d) and (f).

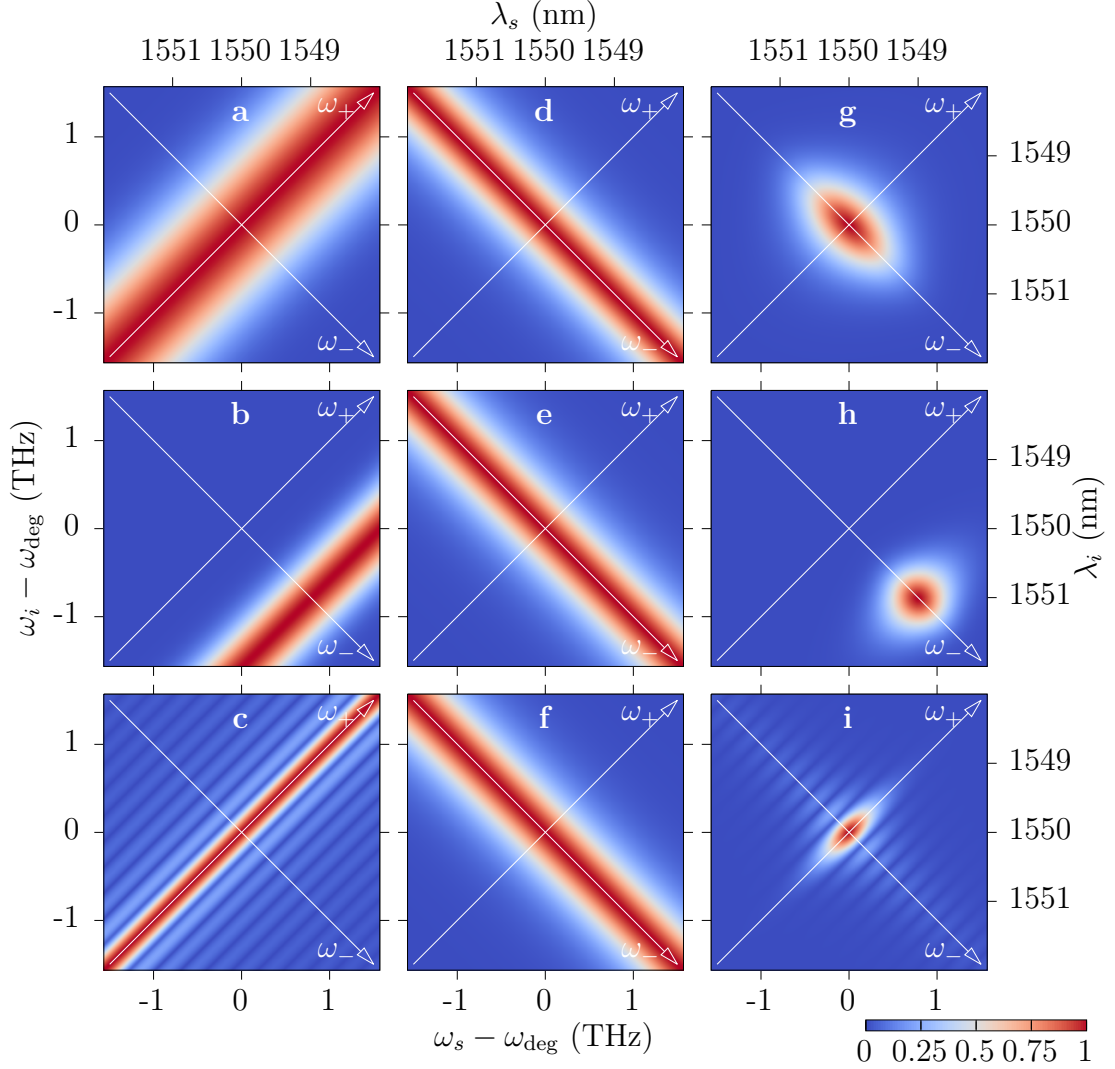


Figure 2.2 – Norm of the phase-matching function $\phi_{\text{PM}}(\omega_s, \omega_i)$ (left column), of the spectral function $\phi_{\text{spectral}}(\omega_s, \omega_i)$ (central column) and of the JSA $\phi(\omega_s, \omega_i)$ (right column). In all simulations, the pulse duration amounts to $\tau_p = 3.5$ ps, the pump has a central wavelength $\lambda_p = 775$ nm and we consider the nominal heterostructure with a length $L = 2$ mm. The first row corresponds to a waist $w_z = 200$ μm leading to a frequency anticorrelated state. The device is pumped at the degeneracy angle θ_{deg} . In the second row, $w_z = 377$ μm is chosen to match τ_p according to equation (2.41) in order to obtain an uncorrelated state. The angle of incidence is slightly different from θ_{deg} . In the third row a correlated state is obtained by pumping the device at θ_{deg} with $w_z = 4$ mm. $\phi_{\text{PM}}(\omega_s, \omega_i)$ takes a sinc shape, as testified by the sidelobes in the JSA. The effect of the microcavity has been removed in these numerical simulations (it slightly reduces the width of $\phi_{\text{spectral}}(\omega_s, \omega_i)$).

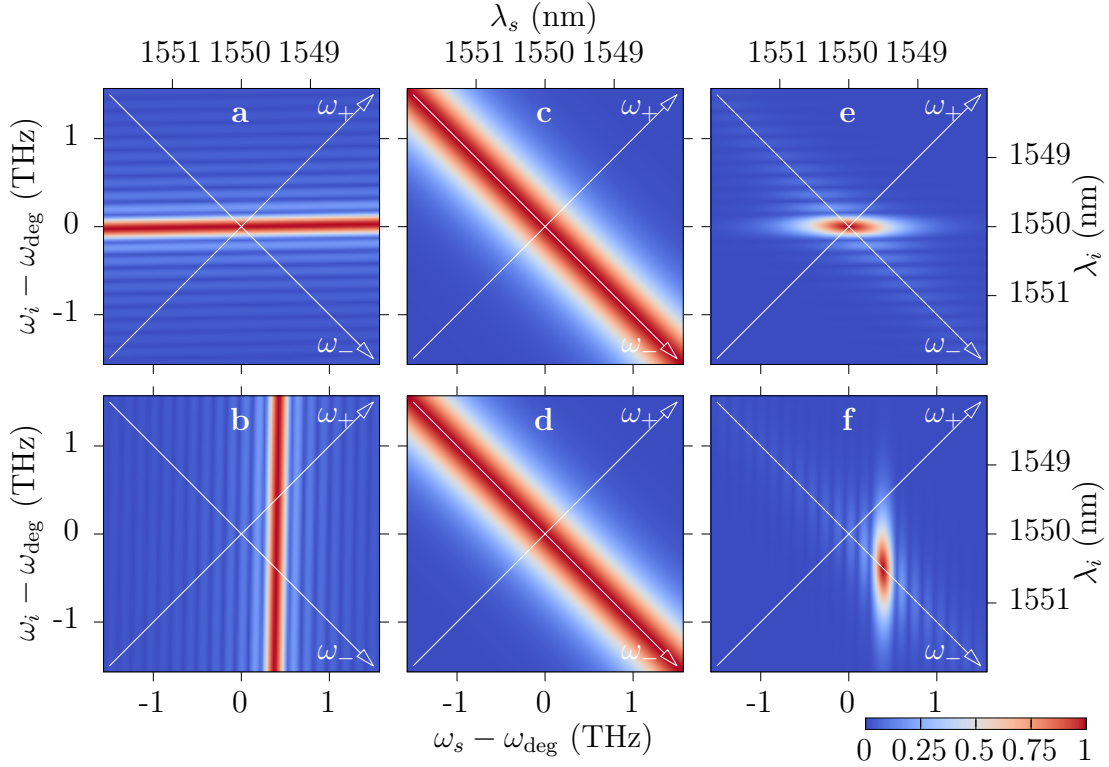


Figure 2.3 – Norm of the phase-matching function $\phi_{\text{PM}}(\omega_s, \omega_i)$ (left column), of the spectral function $\phi_{\text{spectral}}(\omega_s, \omega_i)$ (central column) and of the JSA $\phi(\omega_s, \omega_i)$ (right column). With a pump frequency dependent angle of incidence $\theta(\omega_p)$, ϕ_{PM} gets a ω_+ -dependency and can thus be tilted arbitrarily in order to obtain frequency-uncorrelated biphoton states with independent bandwidths for the signal and the idler. Top row: the angular dispersion is chosen to get a broader signal photon. Bottom row: the idler photon is broader with the opposite choice of dispersion. The central angle $\theta(\omega_p^{(0)})$ is different from θ_{deg} . For both numerical simulations, $w_z = 2$ mm, $\tau_p = 3.5$ ps, $\lambda_p = 775$ nm, $L = 2$ mm and we do not consider the effect of the microcavity.

2.2.3 The Joint Temporal Amplitude

To further study the joint properties of the photons we introduce a new tool: the Joint Temporal Amplitude (JTA) $\tilde{\phi}(t_s, t_i)$ which gives the joint probability amplitude of detecting the photons of the pairs at given times t_s and t_i [121, 98, 122, 99]. Although the JSA is strictly defined for positive frequencies, taking into account the relatively narrow bandwidths of the fields, we can safely calculate the JTA as the Fourier transform of the JSA [104]:

$$\tilde{\phi}(t_s, t_i) = \frac{1}{2\pi} \iint d\omega_s d\omega_i \phi(\omega_s, \omega_i) e^{-i\omega_s t_s} e^{-i\omega_i t_i} \quad (2.43)$$

where the domain of integration over ω_s and ω_i extends from $-\infty$ to $+\infty$.

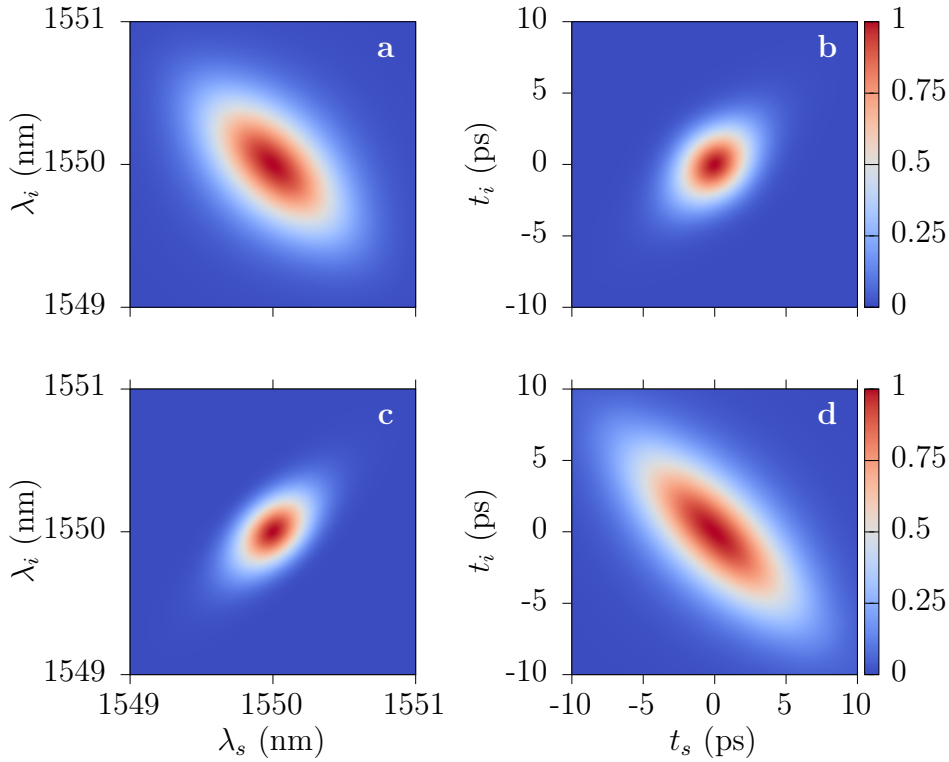


Figure 2.4 – Examples of JSIs (left column) and the corresponding JTIs (right column). (a) and (b): the waist of the pump beam is $w_z = 200 \mu\text{m}$. (c) and (d): the waist is $w_z = 700 \mu\text{m}$. The JTIs show opposite correlations to the JSIs because of the Fourier Transformation. In all situations, the effect of the microcavity is ignored and $\tau_p = 3.5 \text{ ps}$, $\lambda_p = 775 \text{ nm}$, $L = 2 \text{ mm}$.

To illustrate the meaning of this new function, we consider the frequency-anticorrelated two-photon state represented in figure 2.4(a) which is the typical state generated by SPDC sources with a (quasi-)CW pump. By computing the JTA (sketched in figure 2.4(b)), we see that the photons are positively correlated in time *i.e.* they will tend to be detected with the same delay with respect to each other. In the case of a frequency correlated state, the photons are anticorrelated

in time (figures 2.4(c) and (d)). This situation is easily illustrated with our source: it is as if the pair being “generated” on one edge of the source, one photon would directly exit and arrive earlier at the detector while the other would have to travel throughout the whole sample and be detected later, the duration of the pump pulse being shorter than this delay [97].

2.2.4 Effect of the pump microcavity on the Joint Temporal Amplitude

So far we have deliberately neglected the effect of the microcavity in order to focus on the specific features of the counterpropagating phase-matching. Coming back to our device, we must specify the form of $f_{\mu\text{cav}}$, the function describing the influence of the microcavity on the pump beam and consequently on the biphoton. Scattering matrix methods [123] (more stable against numerical instabilities compared to the standard transfer matrix approach [92]) allow to simulate the pump field within the heterostructure thus taking into account the presence of the microcavity. In order to get an analytic expression, we model the microcavity as a standard Fabry-Perot cavity, sketched in figure 2.5 and show its general agreement with the numerical simulations. To simplify the discussion we also assume that the beam impinges with normal incidence.

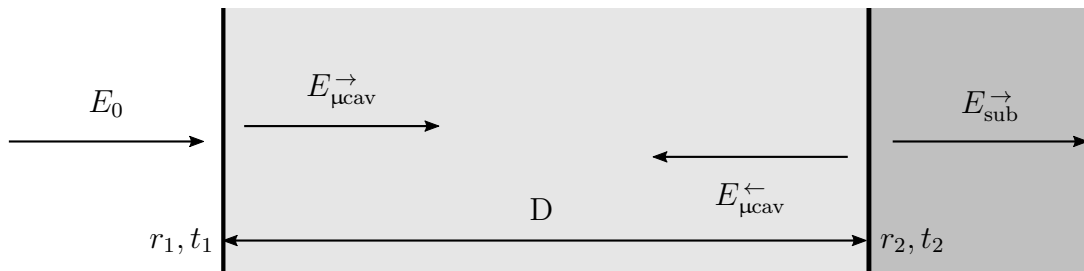


Figure 2.5 – Fabry-Perot model of the microcavity with the Bragg mirrors as beamsplitters with reflection and transmission coefficients r_1, t_1 for the top mirror (left on this sketch) and r_2, t_2 for the bottom mirror. The medium has an effective depth D . The incident field is E_0 and intracavity fields are labeled $E_{\mu\text{cav}}^{\rightarrow}$ and $E_{\mu\text{cav}}^{\leftarrow}$. The field that penetrates in the substrate (with negligible amplitude) is noted $E_{\text{sub}}^{\rightarrow}$.

We consider a monochromatic plane wave beam of frequency ω and amplitude E_0 impinging on the device. The Bragg mirrors are modeled by thin beam splitters with reflection and transmission coefficients r_1, r_2 and t_1, t_2 . They delimit a cavity filled with a lossless medium of effective optical length $n_p D$ with n_p an effective index representing the average refractive index in the central layers of the structure. We note that the length D does not exactly correspond to the distance between the Bragg mirrors in the real structure, given that the field is penetrating the mirrors [124, 125]. The field inside the cavity is the result of multiple transmissions and reflections within the structure. The small fraction of light reaching the substrate will get absorbed there and we do not expect any energy to enter

the microcavity from this side. Labeling $E_{\mu\text{cav}}^{\rightarrow}$ the intracavity field propagating in the forward direction, and $E_{\mu\text{cav}}^{\leftarrow}$ the field propagating in the opposite direction within the microcavity, we have:

$$\begin{aligned} E_{\mu\text{cav}}^{\rightarrow}(x, \omega) &= t_1 E_0 e^{ikx} \left(1 + r_1 r_2 e^{ik2D} + (r_1 r_2)^2 e^{ik4D} + (r_1 r_2)^3 e^{ik6D} + \dots \right) \\ &= t_1 E_0 e^{ikx} \left(\frac{1}{1 - r_1 r_2 e^{ik2D}} \right) \\ E_{\mu\text{cav}}^{\leftarrow}(x, \omega) &= t_1 r_2 E_0 e^{ik(2D-x)} \left(\frac{1}{1 - r_1 r_2 e^{ik2D}} \right) \end{aligned} \quad (2.44)$$

We can thus deduce the total intracavity pump field:

$$E_{\mu\text{cav}}^{\rightarrow}(x, \omega_+) + E_{\mu\text{cav}}^{\leftarrow}(x, \omega_+) = \overbrace{t_1 E_0 (e^{ikx} + r_2 e^{ik(2L-x)})}^{f_{\mu\text{cav}}(x)} \times \underbrace{\frac{1}{1 - r_1 r_2 e^{ik2D}}}_{f_{\mu\text{cav}}(\omega_+)} \quad (2.45)$$

where $f_{\mu\text{cav}}(x)$ describes the distribution of the field in the cavity along the x -direction and $f_{\mu\text{cav}}(\omega_+)$ gives the overall spectral transmission function of the microcavity. The dependence of this function on the pump wavelength is given in figure 2.6 for both the analytic model and the numerical simulation of the nominal structure. We recognize the Lorentzian profile, characteristic of the resonance, and the associated phase shift. The most obvious effect of the microcavity on the JSA

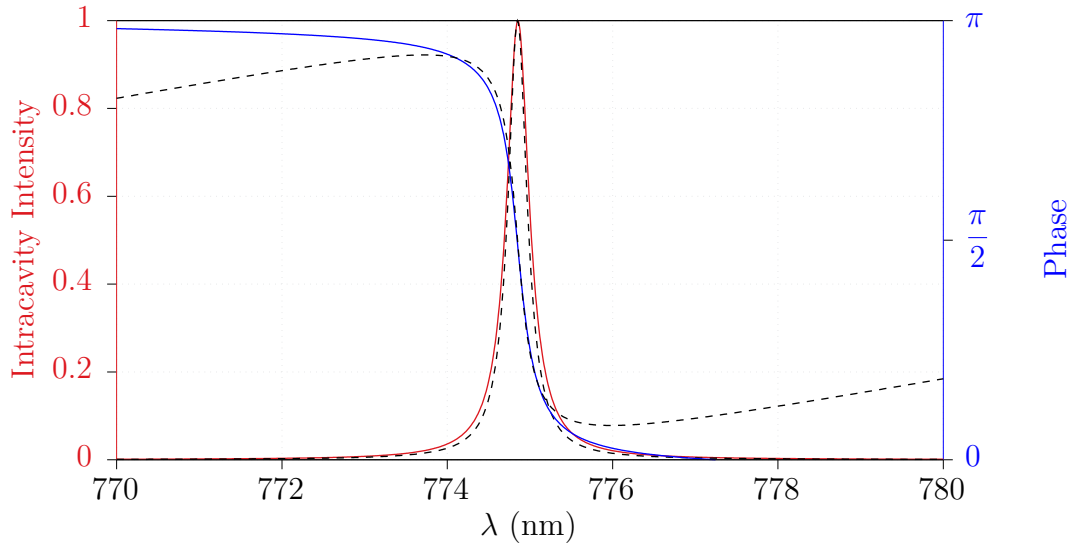


Figure 2.6 – Curves representing the dependence of $|f_{\mu\text{cav}}(\omega_+)|^2$ and of the phase of $f_{\mu\text{cav}}(\omega_+)$ with λ . Solid lines: numerical simulations done with a scattering matrix method on the nominal structure. Dashed lines: analytic model developed in this section with $R_1 = |r_1|^2 = 0.9435$ and $R_2 = |r_2|^2 = 0.9974$ and the central phase adjusted to match the resonance.

is a limitation of the pump bandwidth that the device can accept. This results in

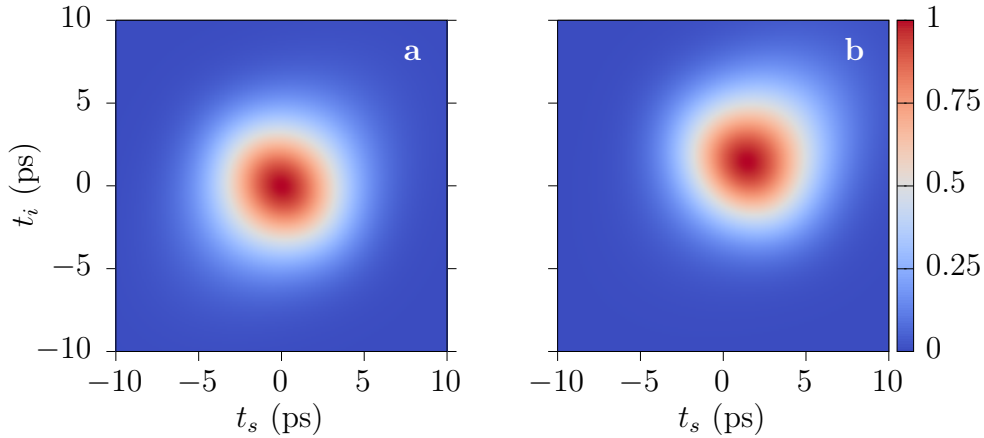


Figure 2.7 – JTIs illustrating the effect of the microcavity on the joint temporal profiles of the photons. (a): JTI corresponding to a frequency uncorrelated state with the phase of the corresponding JSA being flat. As expected, the JTI shows no temporal correlation between the photons. (b): the effect of the microcavity is added to the previous state. The photons wavepackets are slightly delayed and present some temporal asymmetry in the positive diagonal due to the pump pulse resonance inside the microcavity. For these simulations, $\tau_p = 3.5$ ps, $\lambda_p = 775$ nm, $w_z = 377$ μm and $L = 2$ mm.

a band-pass filtering of the pump spectrum at a central frequency $\omega_{\mu\text{cav}}$ with a bandwidth $\Delta\omega_{\mu\text{cav}}$.

The microcavity also affects the phase since the pulse dwells a certain amount of time in the microcavity. This is more easily seen by looking at the JTA $\tilde{\phi}(\omega_s, \omega_i)$ of the biphoton. Adding the resonance of the pump beam with no initial chirp to the frequency-uncorrelated case, we see in figure 2.7(b) that we end up with a JTI which is elongated along the diagonal $t_i = t_s$ compared to the case where the phase of the JSA is set to zero (figure 2.7(a)). This reflects the fact that the pulse dwells a longer time in the cavity than its initial duration.

2.2.5 The Chronocyclic Wigner Function

The simultaneous visualization of the spectral and temporal properties of the photons is not easy since the JSA and JTA are complex valued. Indeed the phase profile of these functions can be very rich and contains critical features for the degree of correlation. The pump beam can also be chirped, which means that the frequency components of the pulse arrive at different times. This impacts the JSA and correlates temporal and spectral properties of the biphoton [126]. This information is lost if we simply look at the JSI and the JTI.

The quasiprobability Wigner function used in quantum mechanics [127] has been adopted by the ultrafast optics community to describe the characteristics of ultrashort pulses. In this context, the function is called Chronocyclic Wigner Function (CWF) and the usual \hat{X} and \hat{P} operators are replaced by the time t and its

conjugate variable, the frequency ω [128]. This tool is now largely employed to describe the results of pulse characterization techniques such as Frequency Resolved Optical Gating (FROG) or Spectral Phase Interferometry for Direct Electric-field Reconstruction (SPIDER) methods [129]. Indeed it allows to easily distinguish the important features of the pulse, *i.e.* its temporal and spectral widths and the possible chirp. Writing $E(t)$ the analytic signal of the electromagnetic field or $E(\omega)$ its representation in the spectral domain, the corresponding CWF reads:

$$\begin{aligned} W(t, \omega) &= \frac{1}{\sqrt{2\pi}} \int dt' \langle E(t + t'/2) E^*(t - t'/2) \rangle e^{i\omega t'} \\ &= \frac{1}{\sqrt{2\pi}} \int d\omega' \langle E(\omega + \omega'/2) E^*(\omega - \omega'/2) \rangle e^{-i\omega' t} \end{aligned} \quad (2.46)$$

This function represents the quasi-probability of measuring a pulse at a frequency ω and a time t . The field quantities that are usually measured with a spectrometer or an autocorrelator *i.e.* the spectral and temporal intensities $I(\omega) = |E(\omega)|^2$ and $I(t) = |E(t)|^2$ are easily retrieved as the marginals of the CWF:

$$\begin{aligned} I(t) &= \frac{1}{\sqrt{2\pi}} \int d\omega W(t, \omega) \\ I(\omega) &= \frac{1}{\sqrt{2\pi}} \int dt W(t, \omega) \end{aligned} \quad (2.47)$$

This formalism was readopted by Grice and Walmsley [122] for the full description of the time-energy properties of the biphoton, both for pure and mixed states. To describe the state with a real quantity, they extended the definition of the CWF to cover the joint time-frequency properties of both signal and idler photons. The Joint Chronocyclic Wigner Function is thus a four dimensional (real) quantity that depends on the frequencies ω_s , ω_i and detection times t_s , t_i and which can be derived from the (complex) density matrix of the state $\hat{\rho}$:

$$\begin{aligned} W(\omega_s, t_s, \omega_i, t_i) &= \frac{1}{2\pi} \iint d\omega'_s d\omega'_i e^{-i(\omega'_s t_s + \omega'_i t_i)} \\ &\quad \times \left\langle \omega_s + \frac{\omega'_s}{2}, \omega_i + \frac{\omega'_i}{2} \left| \hat{\rho} \right| \omega_s - \frac{\omega'_s}{2}, \omega_i - \frac{\omega'_i}{2} \right\rangle \end{aligned} \quad (2.48)$$

In the case of a pure state, W can be expressed as a function of the JSA ϕ since $\hat{\rho} = |\psi\rangle \langle\psi|$. A few simplifications of the previous expression give us:

$$\boxed{W(\omega_s, t_s, \omega_i, t_i) = \frac{1}{2\pi} \iint d\omega'_s d\omega'_i e^{-i(\omega'_s t_s + \omega'_i t_i)} \times \phi \left(\omega_s + \frac{\omega'_s}{2}, \omega_i + \frac{\omega'_i}{2} \right) \phi^* \left(\omega_s - \frac{\omega'_s}{2}, \omega_i - \frac{\omega'_i}{2} \right)} \quad (2.49)$$

The representation of this four-variables function is not evident. Fortunately, the characteristics of our source allow us to factorize it into a phase-matching dependent part and a term depending on the spectrum of the pump beam (and the

transfer function of the microcavity f_{micav}). We will develop this in deeper details in chapter 5. For the moment, we use this formalism to describe the frequency-time properties of individual photons of the pair [126, 130]. Taking the partial trace over the frequencies of one photon allows to retrieve the single photon CWF of its twin:

$$W_s(\omega_s, t_s) = \frac{1}{2\pi} \int d\omega_i \int dt_i W(\omega_s, t_s, \omega_i, t_i) \quad (2.50)$$

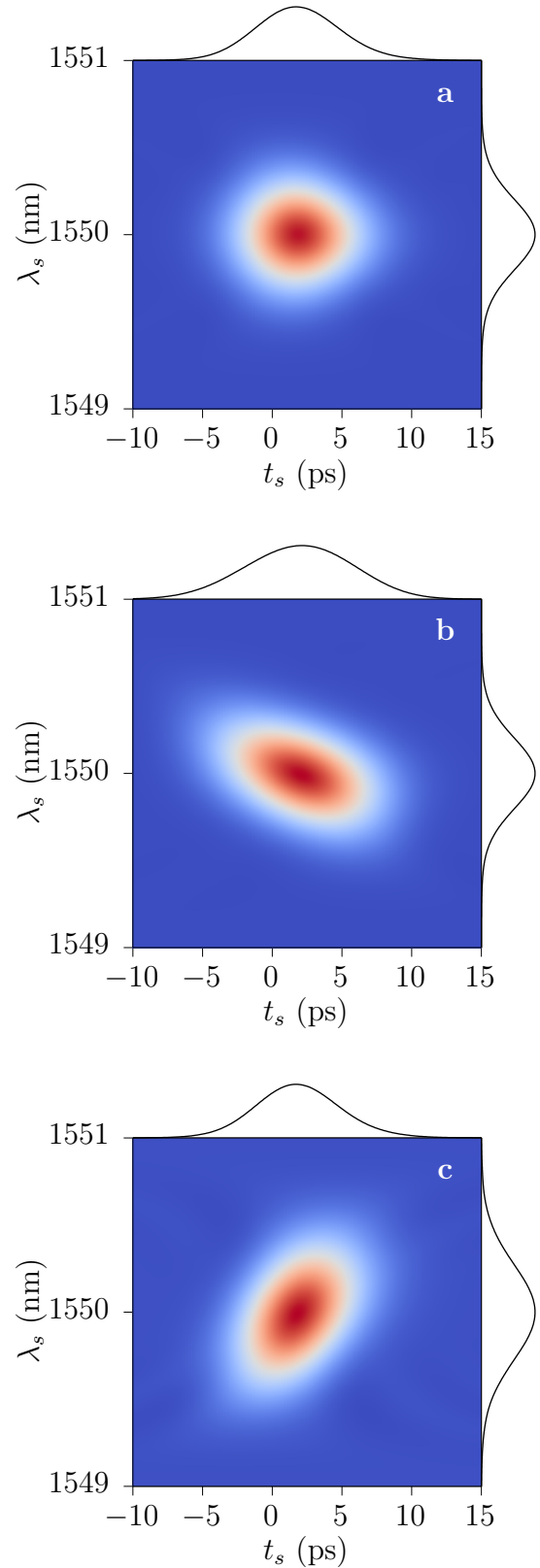
with an analogous formula for the idler. As with ultrashort pulses, the integration of W_s along the temporal or the spectral axis allows to project the distribution over the conjugate quantity and thus to recover the spectrum of the photon or its temporal profile respectively:

$$\begin{aligned} I_s(\omega_s) &= \frac{1}{\sqrt{2\pi}} \int dt_s W_s(\omega_s, t_s) \\ I_s(t_s) &= \frac{1}{\sqrt{2\pi}} \int d\omega_s W_s(\omega_s, t_s) \end{aligned} \quad (2.51)$$

Taking the example of a frequency-uncorrelated state, we represent in figure 2.9(a) the CWF of the signal photon, with the projection of the spectral and temporal intensities along their respective axis. The spectral width is the one we expect by looking at the JSI and, as we have already seen with the JTI (figure 2.7(b)), the temporal profile presents some asymmetry due to the resonance of the pump in the microcavity.

Other spatial and temporal characteristics of the pump beam may create correlations between the temporal and spectral properties of the single photons. Because of energy conservation, the chirp of the pump beam itself is transferred to the photons. For example the presence quadratic chirp in the pump beam implies that $\phi_{\text{spectral}}(\omega_+) \rightarrow \phi_{\text{spectral}}(\omega_+) e^{i\beta(\omega_+ - \omega_+^{(0)})^2}$ and induces a chirp on the signal photon (figure 2.9(b)). The chirp in figure 2.9(c) on the other hand is due to a curvature of the wavefront of the Gaussian pump beam as a result of momentum conservation.

Figure 2.8 – Chronocyclic Wigner Functions of the signal photon. On the sides of the map are the projection of the Wigner function representing $I_s(t_s)$ and $I_s(\omega_s)$. (a): signal CWF for a frequency uncorrelated biphoton state. (b): signal CWF for a pump beam having a quadratic chirp $\beta = 5 \times 10^{-24} \text{ s}^2/\text{rad}$. (c): signal CWF for a pump beam having a curved wavefront (radius of curvature $R = -0.5 \text{ m}$). In all simulations: the pump has a central wavelength $\lambda_p = 775 \text{ nm}$, a pulse duration $\tau_p = 3.5 \text{ ps}$, the waist is $w_z = 377 \text{ }\mu\text{m}$ and the incidence angle is the degeneracy angle θ_{deg} . The simulated device has a length $L = 2 \text{ mm}$.



2.3 Effects of the facets reflectivities on the JSA

The refractive index contrast between the air and the $\text{Al}_x\text{Ga}_{1-x}\text{As}$ compounds induces a partial reflectivity at the facets of the waveguide. Finite-Difference Frequency-Domain (FDFD) numerical simulations allow us to estimate the modal reflectivities $R_{\text{TE}} = 26.7\%$ and $R_{\text{TM}} = 24.7\%$ for the TE and TM fundamental modes, respectively. The simulations have been done for $\lambda \approx 1550$ nm and for ridges of typical width $W = 5$ μm [90]. Thus, the two facets create a cavity for the signal and the idler modes which has a non negligible impact on the photons. Indeed in the experiment done with our source to prove the generation of indistinguishable photons [131], the team attributed the non ideal visibility of the photons interference to the reflections of the photons at the facets and we shall see in chapter 5 that the analysis of the experiment in terms of the biphoton wavefunction can shed light on this issue.

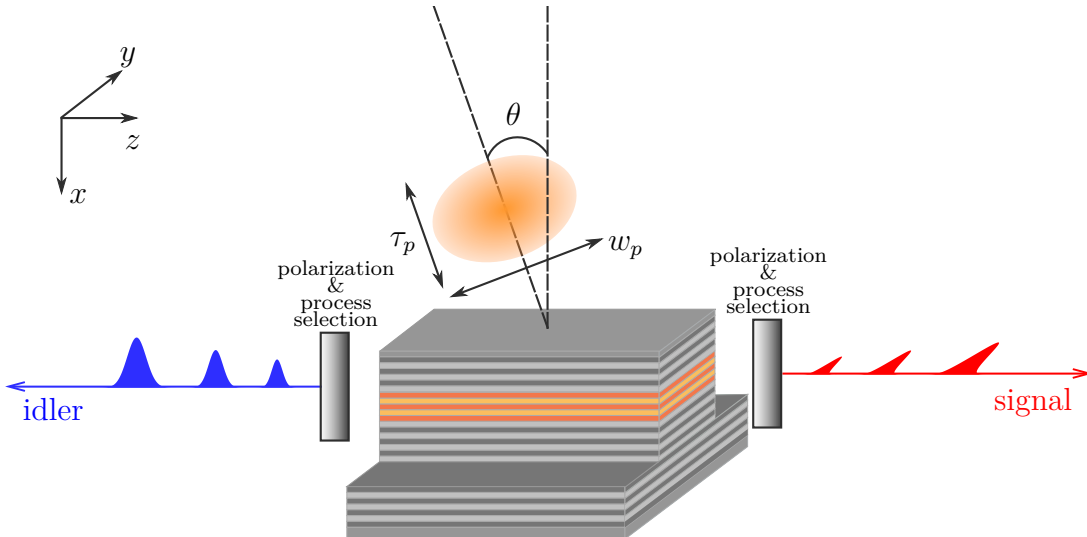


Figure 2.10 – Sketch of the situation studied in this section: photon pairs are produced and can make round-trips in the sample because of the facets’ reflectivities. A suitable filtering is assumed in order to only study the process HV in which signal (idler) photons are horizontally (vertically) polarized.

The influence of the reflectivities of the facets on the time-frequency properties of the generated photons is taken into account by following the approach of Jeronimo-Moreno *et al.* [132]. Unfolding the Fabry-Perot cavity and considering the facets as beamsplitters with creation and annihilation operators for intra-cavity and free-space external modes, the authors show that the effect of the cavity reduces to the multiplication of the original JSA by transfer functions describing the Fabry-Perot transmission for the signal and the idler frequencies, as long as the source remains in the spontaneous regime, *i.e.* that the generated photons do not stimulate the emission of other photons. To simplify the analysis of the counterpropagating scheme, as sketched in figure 2.10, we assume that polarizers are present on both sides of the sample so that only one polarization

will be selected on each arm. We also suppose that we can select only one of the two possible interactions, with frequency filtering for example in addition to the polarizers*. This is verified for all the experiments we comment in this manuscript, except for the notable case of polarization Bell states where both polarizations must be considered on each side of the source (the corresponding analysis is given in section 6.4).

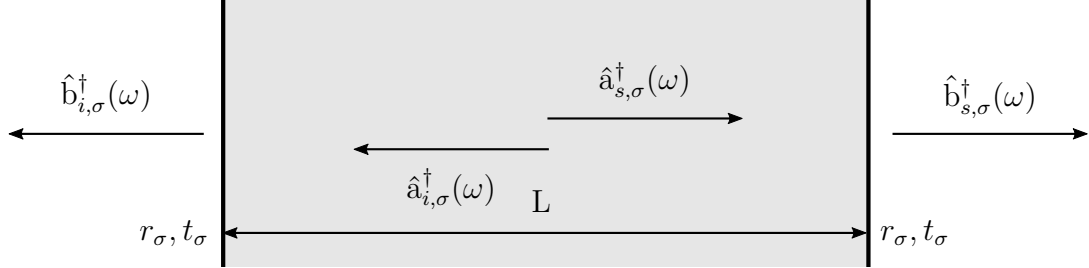


Figure 2.11 – Sketch of the sample with the facets considered as identical beamsplitters with polarization-dependent reflection and transmission coefficients r_σ , t_σ . The medium has a length L .

Figure 2.11 presents a sketch of the situation we study with $\hat{a}_{s/i,\sigma}^\dagger(\omega)$ and $\hat{b}_{s/i,\sigma}^\dagger(\omega)$ the creation operator of a signal/idler photon with polarization σ and frequency ω in the intra-cavity mode and free-space mode respectively. The left and right facets are represented by polarization-dependent beamsplitters of (complex) amplitude reflection and transmission coefficients r_σ and t_σ which fulfill $R_\sigma = |r_\sigma|^2 = \sqrt{1 - |t_\sigma|^2}$. The sample has a length L . Since we set the origin of the z -axis at the center of the device, the first term we have to consider is the propagation phase from the center to the edge of the waveguide:

$$\hat{a}_{s,\sigma}^\dagger(\omega) \rightarrow e^{ik_\sigma L/2} \hat{a}_{s\sigma}^\dagger(\omega) \quad (2.52)$$

with $k_\sigma = n_\sigma(\omega)\omega/c$ and where we chose the signal photon as a starting point. This term is not strictly important here since it almost exclusively represents a temporal offset because of the nearly frequency-independent group velocity. Nevertheless in the case of polarization Bell states, it must be considered to account for the birefringence of the sample. The photon reaching the forward facet is then either reflected in the backward internal mode $\hat{a}_{i,\sigma}^\dagger$ or transmitted in the forward external mode $\hat{b}_{s,\sigma}^\dagger(\omega)$:

$$\hat{a}_{s,\sigma}^\dagger(\omega) \rightarrow e^{ik_\sigma L/2} \left(r_\sigma \hat{a}_{i\sigma}^\dagger(\omega) + t_\sigma \hat{b}_{s,\sigma}^\dagger(\omega) \right) \quad (2.53)$$

At the opposite facet, the same scenario happens with the addition of a phase corresponding to the propagation over the length of the waveguide. As mentioned earlier, we suppose for simplicity that the photons transmitted at this facet will

*Without this precaution, an idler TE photon emitted via interaction VH can be reflected by the left facet, then transmitted by the right one and can thus contribute to detection events where we would expect only the signal TE photon from interaction HV .

not contribute to the detection events on the idler side thanks to the polarizer which will either absorb them or send them to a different path. We can essentially discard the terms $\hat{b}_{i,\sigma}^\dagger(\omega)$ originating from $\hat{a}_{s,\sigma}^\dagger(\omega)$. The reflected energy reaches again the first facet with a phase corresponding to the round trip inside the cavity and is subjected to a new beamsplitter transformation:

$$\hat{a}_{s,\sigma}^\dagger(\omega) \rightarrow e^{ik_\sigma L/2} \left(r_\sigma^3 e^{ik_\sigma 2L} \hat{a}_{i,\sigma}^\dagger(\omega) + t_\sigma \left[1 + r_\sigma^2 e^{ik_\sigma 2L} \right] \hat{b}_{s,\sigma}^\dagger(\omega) \right) \quad (2.54)$$

Consequently, after n round-trips in the sample, the creation operator of the signal mode is transformed into:

$$\hat{a}_{s,\sigma}^\dagger(\omega) \rightarrow e^{ik_\sigma L/2} \left(r_\sigma^{2n+1} e^{ik_\sigma 2nL} \hat{a}_{i,\sigma}^\dagger(\omega) + t_\sigma \sum_{j=0}^n \left[r_\sigma^2 e^{ik_\sigma 2L} \right]^j \hat{b}_{s,\sigma}^\dagger(\omega) \right) \quad (2.55)$$

For $n \rightarrow \infty$, all the energy is extracted from the cavity, *i.e.* the term in $\hat{a}_{i,\sigma}^\dagger(\omega)$ in equation (2.55) is negligible and the original creation operator reads $\hat{a}_{s,\sigma}^\dagger(\omega) = f_\sigma(\omega) \hat{b}_{s,\sigma}^\dagger(\omega)$ with:

$$f_\sigma(\omega) = e^{ik_\sigma L/2} \frac{t_\sigma}{1 - r_\sigma^2 e^{ik_\sigma 2L}} \quad (2.56)$$

which is, up to the half-length propagation phase factor, the usual Fabry-Perot transmission function. The JSA with reflective facets is then:

$$\boxed{\phi_{\text{FP}}(\omega_s, \omega_i) = f_{\text{TE}}(\omega_s) f_{\text{TM}}(\omega_i) \phi(\omega_s, \omega_i)} \quad (2.57)$$

for the HV interaction (with an analogous expression for the VH interaction). We illustrate this in figure 2.12 where the JSI for non-reflective facets represented in (a) is transformed into the JSI (b) considering the facets reflectivity. Specific frequencies for the signal and the idler are selected leading to a checkerboard pattern on top of the original JSI*. Although this additional feature may be undesirable for some applications, it will be an interesting benchmark to test the resolution of techniques of reconstruction of the joint spectra.

In figure 2.12(c), we illustrate the effect of the Fabry-Perot on the norm of the JTA, for the state of figure 2.12(b). As expected we see several peaks along the signal and idler frequency axis. The main one corresponds to the direct transmission of both photons, and the others to a given number of round-trips of either

*The length of the sample is known to be $L = 2.1$ mm however the accuracy of our cleavage method prevents us from knowing it at a subwavelength precision. When simulating the Fabry-Perot pattern due to the facets' reflectivity, we will obtain the correct free spectral range *i.e.* the spacing between the Fabry-Perot peaks which is approximately 180 pm for both polarizations with this sample length. We note however that the absolute position of the peaks is very sensitive to the sample length and we thus have to resort to direct measurements of the Fabry-Perot pattern [133] to fix this.

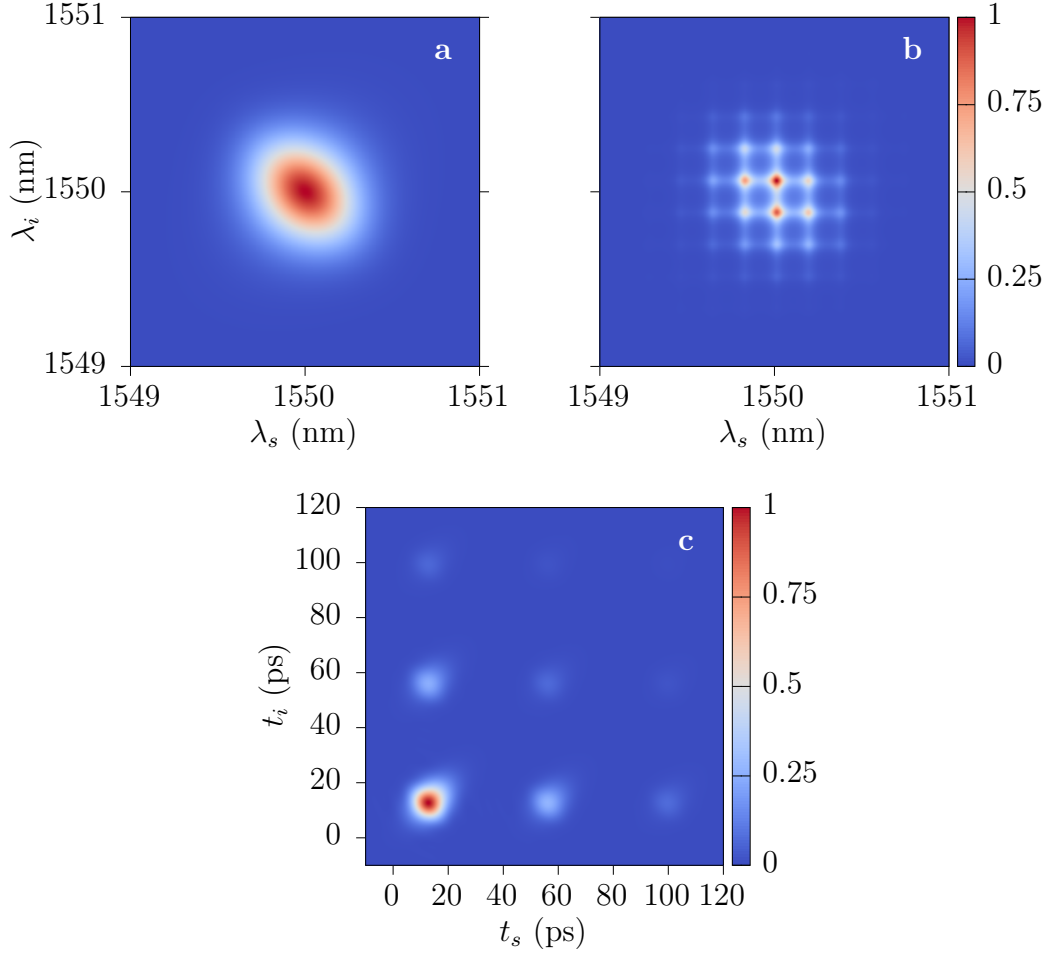


Figure 2.12 – (a) and (b): numerical simulation of the JSI for non reflective facets (a), and for facets having reflectivities $R_{TE} = 26.7\%$ and $R_{TM} = 24.7\%$ (b). In both cases, the pump has a central wavelength $\lambda_p = 775$ nm, a pulse duration $\tau_p = 3.5$ ps, a waist $w_z = 377$ μm and an incidence angle θ_{deg} . The simulated device has a length $L = 2.1$ mm. A slight anticorrelation is due to the frequency filtering of the microcavity (theoretical FWHM 280 pm). (c): norm of the JTA corresponding to the state represented in (b). The main peak is identical to the one in figure 2.7(b) and the lateral peaks are replica due to the double reflections of any photon of the pair. The main pulse is offset from the time origin (the arrival of the pump pulse into the sample) because of the time required to exit the sample.

or both photons, separated by the round trip time $\tau_\sigma = 2L/v_g^\sigma \approx 44$ ps, with an exponentially decaying amplitude (cavity ring-down). The CWF for the signal photon is represented in figure 2.13 for the same biphoton state. We see that the Wigner function takes negative values between the round trip times but once integrated along the time or the frequency axis, these interference terms washes out: the spectrum is modulated by the Fabry-Perot pattern and the temporal profile shows the peaks due to the round-trips.

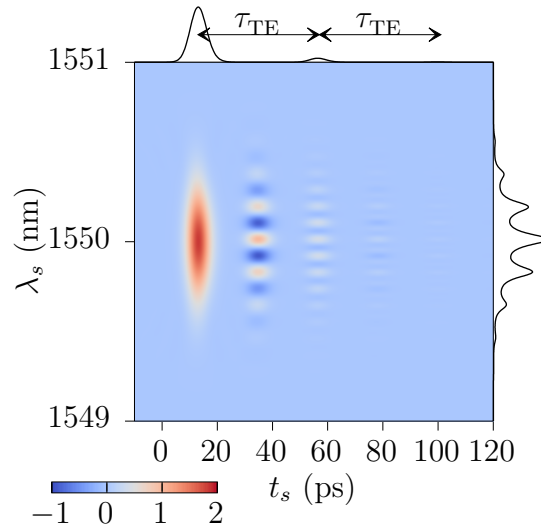


Figure 2.13 – Chronocyclic Wigner Function of the signal photon of the biphoton state whose JSI is depicted in figure 2.12(b). The Wigner function takes some negative values because of the coherence that exists between the subsequent pulses. On top of the map, the integration of W_s along the frequency axis leads to the temporal intensity $I_s(t_s)$. The main pulse (the photon is directly transmitted) is followed by a pulse of lower amplitude after a time corresponding to a round trip in the waveguide. The third pulse is barely visible. Integration along the λ_s axis gives the signal spectrum $I_s(\omega_s)$ which is represented at the right side of the map.

2.4 Conclusion

In this chapter we have given a theoretical description of the two-photon state produced by our source. This state is completely characterized by the biphoton wavefunction or Joint Spectral Amplitude (JSA) $\phi(\omega_s, \omega_i)$, which gives the joint probability that the signal and idler photons are emitted at frequencies ω_s and ω_i .

With the counterpropagating phase-matching, the characteristics of our source and convenient properties of the pump beam, the JSA takes a simple form: it can be written as a product of a function ϕ_{PM} related to momentum conservation and depending only on the frequency difference $\omega_- \equiv \omega_s - \omega_i$ of the photons, and a function ϕ_{spectral} related to energy conservation which only depends on the sum of their frequencies $\omega_+ \equiv \omega_s + \omega_i$.

This allows to identify means to engineer the degree of frequency correlations between the photons. On one hand, the control of the spatial properties of the pump beam acts on ϕ_{PM} and modifies the extent of the JSA along the anti-diagonal axis $\omega_i = -\omega_s + \omega_p^{(0)}$ corresponding to variable ω_- . On the other hand, the spectral properties of the pump beam acts on ϕ_{spectral} and changes the extent of the JSA along the diagonal axis $\omega_i = \omega_s$ corresponding to variable ω_+ . The source is thus very versatile thanks to the control of the JSA along these two orthogonal axis.

The spectral and temporal contributions of the pump beam microcavity and of the reflectivities of the facets have also been studied. To better describe their

effects on the biphoton wavefunction, we introduced alternative descriptions of the biphoton state: the Joint Temporal Amplitude (JTA) allows to visualize in the temporal domain the effect of the resonance of the pump beam on the photon pair; the Chronocyclic Wigner Functions (CWFs) show both spectral and temporal aspects and are useful in describing the individual photons of the pair.

Part II

Frequency-time correlations engineering

Chapter 3

Joint Spectral Intensity Reconstruction with a Fiber Spectrograph

3.1 Characterization tools in frequency-time space

Reconstructing the full biphoton wavefunction, *i.e.* the Joint Spectral Amplitude (JSA) in waveguided regime is a formidable task. Indeed, the characterization of ultra-short pulses is still an intense subject of research for classical electromagnetic fields [129]. With photon pairs the task of reconstructing the full spectral and temporal properties is complicated by the fact that the photons can be correlated in those degrees of freedom and the characterization technique must thus be able to resolve this. Moreover, detection in the single photon regime is an additional difficulty. Single photon detectors suffer from low detection efficiencies and poor temporal resolution. Dark counts can also be easily mistaken for genuine photons. The techniques developed by the ultrafast community are thus not directly transposable for our needs.

To our knowledge, a full tomography of the JSA has not yet been reported for sources producing photons with a rich chromocyclic structure. In fact most characterization techniques are limited to the modulus square of the biphoton wavefunction, *i.e.* the Joint Spectral Intensity (JSI). The most obvious strategy in that respect is to send each photon of the pair to a monochromator (which will select a specific “pixel” in the JSI by filtering the signal and the idler at given wavelengths) and record, for a sufficient time, the number of coincidences at the output of the monochromators [84, 134, 135]. This approach require very long integration times depending on the size of the JSI and the desired sampling.

Measurements of the Joint Temporal Intensity (JTI) have also been reported, which is only achievable when the photons are sufficiently narrow, *i.e.* their coherence time must exceed the temporal resolution of the detection chain. With spontaneous Four-Wave Mixing (FWM) in cold atomic ensemble, Cho *et al.* generated pairs of photons with coherence time between 10 ns and 200 ns, well above the timing jitter of their detectors [136].

In [137], Polycarpou *et al.* managed to reconstruct the full waveform of one photon of the pair. To do so, they heralded the photon to be characterized with the detection of its twin. A homodyne detection with a pulse-shaped local oscillator allowed to infer the full spectro-temporal form of the heralded photon. Although this result is remarkable, it requires a source for the local oscillator, which is not accessible for all sources of photon pairs. This technique also does not capture all the richness of the biphoton state since it measures the properties of a single photon. Indeed the heralding procedure requires a tight spectral filtering of the heralding photon to avoid the projection of the photon to characterize in a mixed state.

Two-photon interferences at beam-splitters [138] are also sensitive to a part of the biphoton wavefunction. The central frequencies of the photons must remain close to maintain a good interference visibility. Moreover they cannot distinguish a frequency-anticorrelated state from an uncorrelated state having the same width in the ω_- axis. A theoretical proposal to solve this problem was made recently [139]. We will introduce in chapter 5 a generalization [140] of the famous Hong-Ou-Mandel (HOM) interferometer [35].

A promising scheme for the characterization of photon pairs is the two-photon counting interferometry introduced by Boitier *et al.* in [141]. The technique relies on two-photon absorption in a semiconductor detector. Unfortunately this technique is not sensitive enough to work at the single photon regime yet.

In the next section we describe our implementation of the single-photon fiber spectrograph. With this technique of reconstruction of the JSI, which was the state of the art at the beginning of this work, we finish our overview of photon pairs characterization methods.

3.2 Single photon spectrograph – Working principle

As an optical pulse propagates through a given medium, *e.g.* an optical fiber, it is subject to the chromatic dispersion of the material. Its temporal shape can be greatly altered as it travels, which is a major concern for telecommunications together with losses. The effect of propagation over a length l of the medium corresponds to adding a frequency dependent phase $\phi(\omega) = k(\omega)l$ to the pulse spectrum $E(\omega)$, where chromatic dispersion of the wave-vector $k(\omega)$ can be Taylor expanded to identify different contributions [142]:

$$k(\omega) = \underbrace{k_0}_{\text{constant phase}} + \overbrace{\frac{\partial k}{\partial \omega}(\omega - \omega_0)}^{\text{time delay}} + \underbrace{\frac{1}{2} \frac{\partial^2 k}{\partial \omega^2}(\omega - \omega_0)^2 + \dots}_{\text{chirp}} \quad (3.1)$$

While the first two terms of this expansion have no effect on the temporal profile of the pulse $|E(t)|^2 = \left| \int d\omega E(\omega) e^{i\phi} e^{-i\omega t} \right|^2$, this is not the case for higher order terms.

For example the second order one is responsible for the Group-Velocity Dispersion (GVD): the frequency components of the pulse propagate at different speeds with respect to each others and arrive at different times to the end receiver. This (and effects associated to higher order terms of chromatic dispersion) results in a modification of the shape of the pulse called *chirp*, illustrated in Figure 3.1. This “frequency-to-time translation” is the principle used by the fiber spectrograph to reconstruct the JSI.

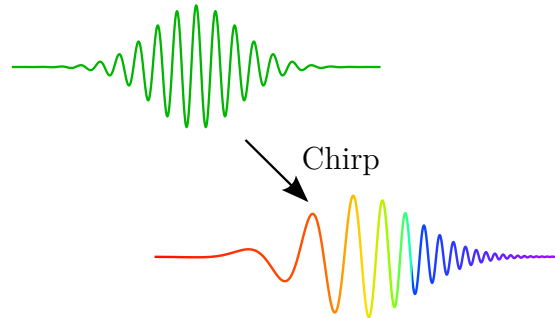


Figure 3.1 – Sketch illustrating the chirp of a pulse. A Fourier-transform limited pulse experiencing chirp exhibits a modified temporal profile so that its instantaneous frequency changes with time.

At the single photon level, the propagation of a biphoton state generated by a Continuous Wave (CW) pump in a medium exhibiting GVD was studied in [143]. It was shown in particular that for long distance propagation, the temporal shape of the two-photon state (JTI) is stretched and corresponds to the JSI, in an analogous way a lens perform a Fourier transformation of an electromagnetic field in its focal plane. It is a sort of *far-field condition* [144]. The experimental demonstration of this temporal stretching was done in [145] through the measurement of the second order correlation function. The first reconstruction of a JSI was performed in [85] for a biphoton state generated by a pulsed pump. In that work, Dispersion Compensating Fibers (DCFs) were used to translate the frequency information into arrival time information with an acceptable level of loss. This kind of fiber is used in telecommunications for its GVD of greater magnitude and opposite in sign compared to standard fibers so that a short length of DCF can compensate the chirp due to a propagation over long distance with very low additional losses. The chirped photon wavepackets were detected with free-running single photon detectors and their arrival times recorded by a Time-to-Digital Converter (TDC). A calibration of the spectrograph with independent sources allowed to reconstruct the JSI by recording the JTI “Fourier transformed” by the DCF.

3.3 Experimental implementation

This section describes the experimental set-up that we have implemented in our laboratory. The goal is to have a tool to measure the frequency correlations of the biphoton and to reconstruct the associated JSI.

3.3.1 Experimental set-up

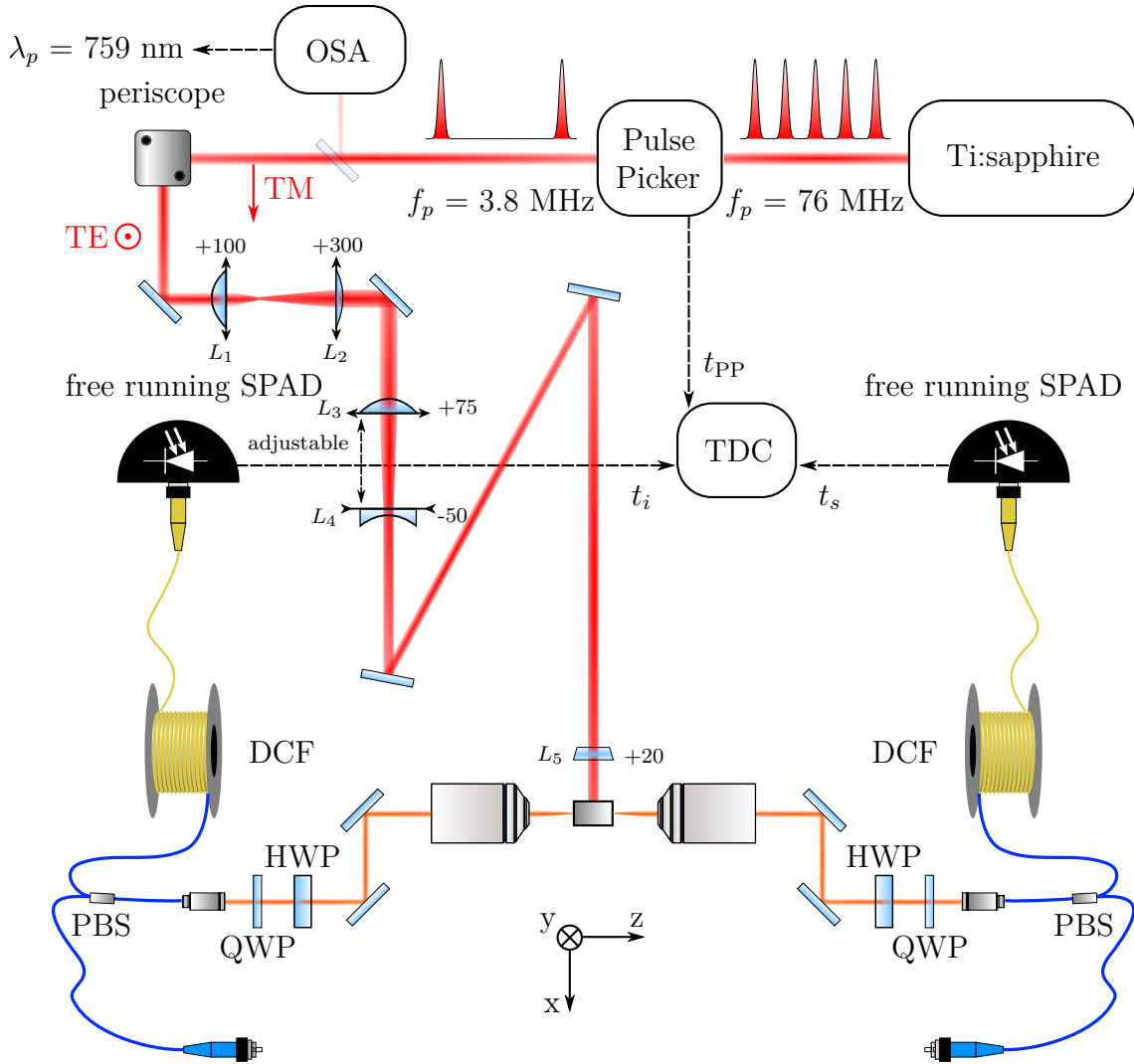


Figure 3.2 – Experimental set-up for the reconstruction of the JSI with the fiber spectrograph (see text for description). Focal lengths are given in millimeters.

The experimental set-up we have implemented is represented in Figure 3.2. A mode-locked Ti:sapphire laser (Coherent MiraTM) provides pump pulses of duration $\tau_p = 3.5$ ps centered at wavelength $\lambda_p = \lambda_{\mu\text{cav}} = 759$ nm (corresponding to the microcavity resonance) with a repetition rate $f_p = 76$ MHz. A pulse-picker (APETM) based on acousto-optic modulation reduces this repetition rate to a suitable level for the detection chain, with $f_p = 3.8$ MHz as a maximum value. Indeed this has to be set in conjunction with the dead time of the detectors and the detection efficiency of the whole chain to avoid its saturation. The pulse-picker also provides a trigger signal t_{PP} for the spectrograph. Optionally, a small fraction of the pump beam is sent to an Optical Spectrum Analyzer (OSA) in order to monitor λ_p . A periscope is used to set the pump beam at a suitable height for

the sample and to adjust its polarization in order to have an efficient nonlinear conversion. A first telescope made of two spherical lenses L_1 and L_2 magnifies the beam and allows in conjunction with the last cylindrical lens L_5 of the optical path to focus the pump beam onto the ridge waveguide of width $W \approx 6 - 10 \mu\text{m}$. The spatial shape of the pump beam is subsequently controlled with a second telescope made of two cylindrical lenses L_3 and L_4 to adjust the size of the beam along the z -axis. A full description of this part of the set-up is given in section 3.3.5. A set of dielectric mirrors with a broadband coating is used all along the optical path.

The collection of the photons is done with two microscope objectives ($\times 40$, NA= 0.65). Two pairs of silver coated mirrors couple the signal and idler photons into single-mode polarization-maintaining telecom fibers equipped with collimators. A Half-Wave Plate (HWP) and a Quarter-Wave Plate (QWP) enable to set the polarization of the photon to a given orientation. In conjunction with a fibered-Polarizing Beam Splitter (PBS) from OzOpticsTM, this configuration allows to select the interaction we want to study (signal Transverse Electric (TE) - idler Transverse Magnetic (TM) or the opposite). Each photon is then launched into a DCF module from DrakaTM where it experiences a delay depending on its frequency. Two free-running InGaAs Single Photon Avalanche Photodiodes (SPADs) id220 from idQuantiqueTM detect the photons with efficiency 20% and a dead time set to 10 μs . Their arrival times t_s and t_i is then recorded by a TDC (QuTools from QuTauTM). The trigger t_{PP} from the pulse-picker is also recorded by the TDC which allows to obtain the delays between the pump pulses and the detection of the photons $\tau_{s/i} = t_{s/i} - t_{\text{PP}}$. An appropriate calibration of the spectrograph provides the conversion between $\tau_{s/i}$ and the corresponding photons wavelengths $\lambda_{s/i}$, allowing to reconstruct their marginal spectra. The detection of events in coincidence within one pump pulse sequence enables the reconstruction of the JSI $|\phi(\omega_s, \omega_i)|^2$.

3.3.2 Calibration of the spectrograph

To retrieve the absolute wavelengths values, the photon spectrograph must be properly calibrated. Different procedures can be followed to solve this issue. In [85], the calibration was performed using an independent reference consisting in an Optical Parametric Amplifier (OPA) reference. A small fraction of the OPA light was sent into the fiber spectrograph, while the rest was measured with an Optical Spectrum Analyzer (OSA). The comparison of the two independently recorded spectra allowed the calibration.

Another solution consists in using the generated photons themselves for the calibration, which is useful since it does not require an additional source. Photons from one arm are injected into a monochromator and detected with a SPAD. A marginal spectrum is thus recorded by sweeping a given range of wavelengths with the monochromator. The calibration is then performed by recording the corresponding spectrogram with the fiber spectrograph.

Along with the previous strategies, in the case of our sample we can also take advantage of the reflectivities of the facets. Indeed if no selection on polarization

54 Joint Spectral Intensity Reconstruction with a Fiber Spectrograph

is imposed at the collection stage, we can detect the signal and idler photons of both interactions at the same time and record a marginal spectrum. In our case, this can be simply done by rotating the QWP by 45° so that no optics needs to be removed. Figures 3.3(a) and 3.3(b) show the recorded marginal spectra for the left and right arms. The photon which gives rise to a given peak is used to label it (signal/idler, directly transmitted/reflected once). We can identify a central wavelength in the graph which marks the point at which the photons would be degenerate *i.e.* $\lambda_{s/i} = 2\lambda_p$: this point is at the same distance from the peak associated to photons that are directly transmitted through the facet and the corresponding peak associated to photons which are reflected on the opposite facet and then transmitted. The temporal delay $\tau_{\text{Left/Right}}^{(0)}$ corresponding to degenerate photons is therefore identified for both DCFs giving the following relations for the calibration:

$$\begin{cases} \lambda_{\text{Left}} = \frac{\tau_{\text{Left}} - \tau_{\text{Left}}^{(0)}}{D_{\text{Left}}} + 2\lambda_p \\ \lambda_{\text{Right}} = \frac{\tau_{\text{Right}} - \tau_{\text{Right}}^{(0)}}{D_{\text{Right}}} + 2\lambda_p \end{cases} \quad (3.2)$$

where $\tau_{\text{Left/Right}} = t_{\text{Left/Right}} - t_{\text{PP}}$ is the temporal delay between the detection time $t_{\text{Left/Right}}$ of one photon on the Left/Right arm and the trigger signal t_{PP} originating from the pulse picker. $D_{\text{Left/Right}}$ is the dispersion of the DCF module. Figure 3.3(c) represents the calibrated marginal spectra obtained with this procedure showing a perfect agreement between them while figure 3.3(d) depicts the experimental situation in the tuning curves of the device.

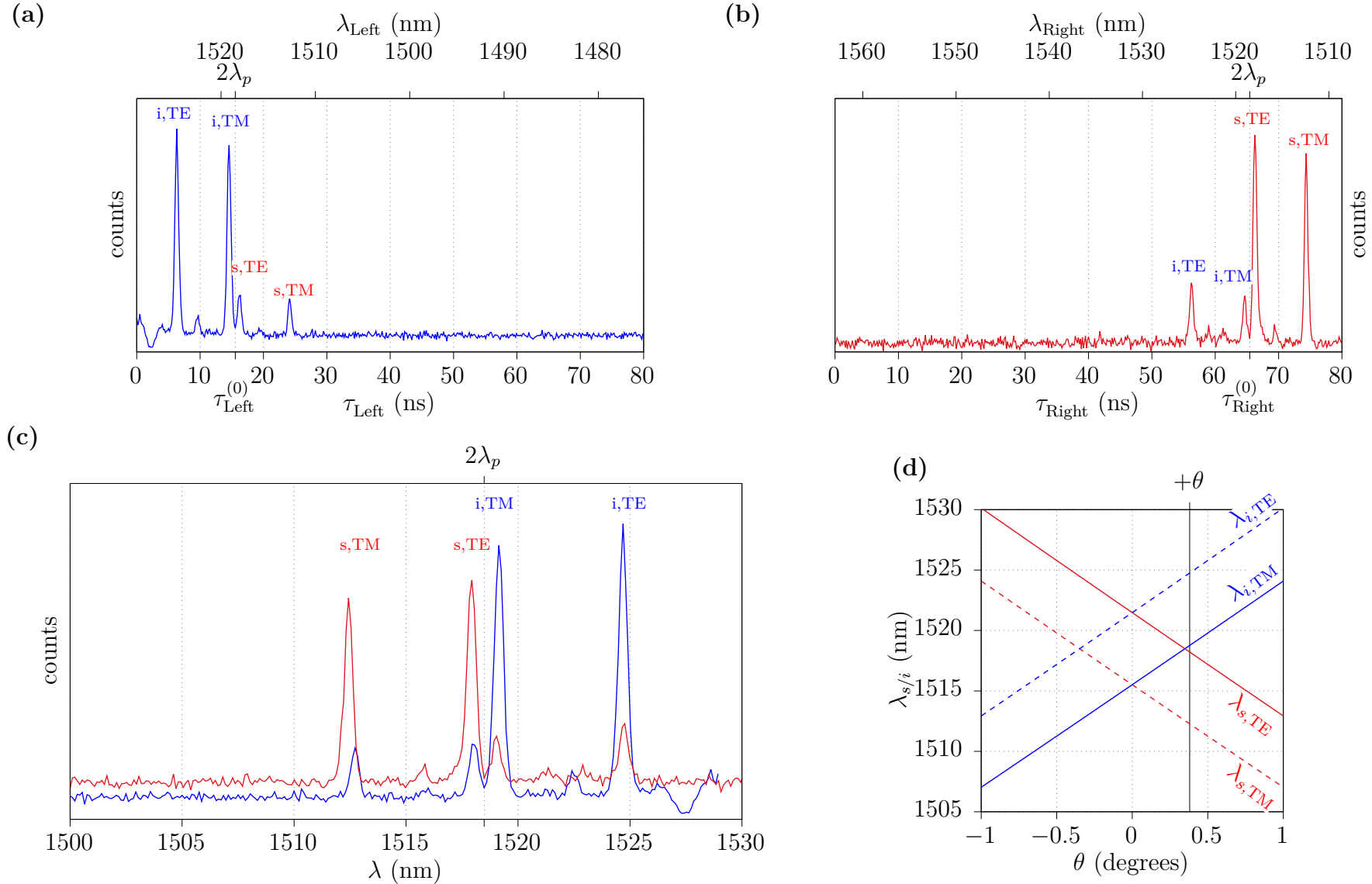


Figure 3.3 – Marginal spectra recorded with the fiber spectrograph by collecting photons respectively from the left (idler) (a) and the right (signal) side (b) of the source. With a proper setting of the QWPs, both interactions appear in the spectrograph. The main peaks correspond to photons that are directly transmitted by the facet, while smaller ones correspond to photons that are reflected by the opposite facet, then transmitted. Photons are labeled according to their polarization and initial propagation direction. The degeneracy point $2\lambda_p$ can be identified from the graph and the knowledge of the pump wavelength $\lambda_p = 759.245$ nm and the dispersion of the DCF allows the wavelength calibration. The superposition of the calibrated marginal spectra is reported in figure (c). (d): angular tuning curves simulated for the real device, with a vertical line indicating the pumping angle λ and the central wavelengths of the photons.

3.3.3 Spectral resolution

The choice of the length of the DCF is a compromise between the resolution we want to achieve and the level of losses of the apparatus. Indeed since frequencies are now related to temporal delays, the resolution we can reach depends on the dispersion parameter $D = -\frac{2\pi c}{\lambda^2} \frac{\partial^2 k}{\partial \omega^2} \times l$ of the “frequency to time translator” and on the accuracy with which we can measure the photon detection time. The timing resolution is limited by the electronics of the devices involved in the measurements, *i.e.* by the jitter of the pulse picker δt_{PP} , the temporal resolution $\delta t_{s/i}$ of the SPADs and the temporal size δt_{TDC} of the time bins of the TDC. Taking all this into account, we can express the wavelength resolution that we can achieve:

$$\Delta\lambda = \frac{\sqrt{\delta t_{\text{PP}}^2 + \delta t_{s/i}^2 + \delta t_{\text{TDC}}^2}}{|D|} \quad (3.3)$$

Obviously the stronger the dispersion, the better the wavelength resolution will be. For DCFs, the spool length can be increased to improve this figure of merit, however this is at the cost of higher losses. Furthermore, the pump power must remain sufficiently low to limit the generation of double pairs. This is necessary in order to correctly interpret the experimental results as the measurements of the characteristics of a two-photon state*. The chain of collection and detection therefore has to be as efficient as possible and the losses due to the translator must be limited to an acceptable value. Alternatives to DCF include solutions based on Fiber Bragg Gratings (FBGs) such as chromatic dispersion emulators or pulse stretchers [147]. For a similar level of losses, the dispersion achieved can be one order of magnitude higher compared to DCFs. However the operational bandwidth of such devices is limited to hundreds of GigaHertz around a specific wavelength. This lack of flexibility and the cost of such apparatus are the reasons for the choice of DCFs in a large majority of groups.

We now estimate the resolution of our spectrograph by putting in (3.3) the typical values of our detection chain. The timing jitter of the pulse picker can reach $\delta t_{\text{PP}} = 200$ ps while the temporal resolution of our SPADs is $\delta t_{s/i} = 250$ ps. The TDC bin size is $\delta t_{\text{TDC}} = 81$ ps. In the range of wavelengths we wish to measure, the dispersion of the DCFs is $D \approx -1475$ ps/nm (for insertion losses around 7.3 dB). We finally obtain the following resolution for the spectrograph:

$$\Delta\lambda(\delta t_{s/i} = 250 \text{ ps}) = 224 \text{ pm} \quad (3.4)$$

3.3.4 Theoretical spectrogram

To verify the good functioning of the fiber spectrograph, we have taken into account the dispersion properties of the DCF spools to simulate the expected spectrogram. The faithful reconstruction of a JSI with the single photon spectrograph will depend on the ability to reach the *far-field condition* (by using a sufficient length of fiber) so that, *e.g.*, the photons’ temporal elongation due the

*see Section 5.6 of [146] for a thorough discussion of this issue.

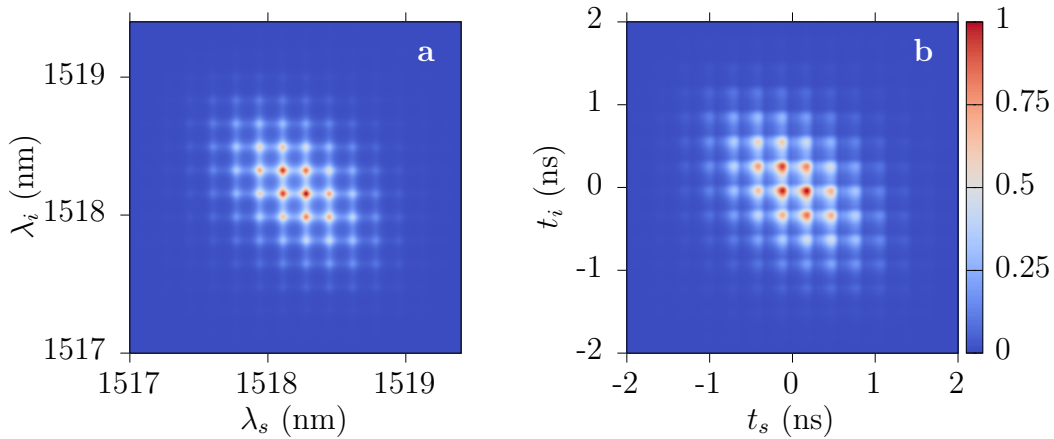


Figure 3.4 – (a): numerical simulations of a JSI. (b): numerical simulations of the JTI resulting from the propagation of the photons into the DCFs. The parameters are a ridge waveguide of length $L = 2.1$ mm, pump waist $w_p = 222$ μm , pumping angle $\theta = \theta_{\text{deg}} = 0.349^\circ$, pulse duration $\tau_p = 3.2$ ps and central wavelength $\lambda_p = 759.1$ nm.

resonance of the pump within the microcavity is not an issue (an effect encoded in the phase of the JSI). Figure 3.4 shows the comparison between the JSI calculated for our device and the expected reconstruction given the characteristics of the DCFs. Figure 3.4(a) represents the calculated JSI of a state generated for a ridge waveguide of length $L = 2.1$ mm, pump waist $w_p = 222$ μm , pumping angle $\theta = \theta_{\text{deg}} = 0.349^\circ$, pulse duration $\tau_p = 3.2$ ps and central wavelength $\lambda_p = 759.1$ nm. The phases of the Fabry-Perot are the same as set in [148].

This state being fixed, we use the characteristics of the DCFs (details can be found in appendix B) to deduce the Joint Temporal Amplitude (JTA) which can be measured with the spectrograph according to:

$$\tilde{\phi}(t_s, t_i) = \mathcal{F} \left[\phi(\omega_s, \omega_i) \times e^{-i \frac{l k''(\omega_s)}{2} (\omega_s - \omega_p/2)^2} \times e^{-i \frac{l k''(\omega_i)}{2} (\omega_i - \omega_p/2)^2} \right] (t_s, t_i) \quad (3.5)$$

where l is the length of the fiber and $k''(\omega) = \frac{\partial^2 k}{\partial \omega^2}$ is the frequency-dependent second order derivative of the wave-vector inside the DCF. Figure 3.4(b) presents a numerical simulation of the JTI corresponding to the previous parameters. We see that the correlation of the JTI is similar to that of the JSI. Oscillations corresponding to the Fabry-Perot are also present. In fact, the wavepackets corresponding to photons making a certain number of round trips before being transmitted by the facet do not necessarily overlap at its output. However the stretching due to the DCF allows this overlap to occur and results in the interference pattern shown in figure 3.4(b). The resonance of the pump within the microcavity has a completely negligible effect on the reconstructed spectrogram with such a stretching. We note a blurring of the peaks along the diagonal $t_i = t_s$: this is due to the non negligible third order of dispersion in the DCFs. We also point that the Free Spectral

Range (FSR) *i.e.* the spacing between the fringes is below or almost equal to the resolution of our spectrograph, we will thus experience difficulties to resolve them in the experiment.

3.3.5 Spatial shaping

The modification of the frequency correlations in this experiment is done via the control of the spatial shape of the pump beam. The output beam from the Ti:sapphire is a TEM₀₀ Hermite-Gaussian beam. For consistency, we note x the direction of epitaxy of the waveguide corresponding to the propagation direction of the pump beam. The pump transverse coordinates z and y correspond to the direction of propagation of the signal and idler photons and to the transverse direction of the waveguide, respectively. Writing $r^2 = y^2 + z^2$, the spatial shape of the pump beam can then be described with the following expression:

$$E_p(x, y, z) = E_0 \frac{w_0}{w_p(x)} \exp\left(-\frac{r^2}{w_p^2(x)}\right) e^{ik_p\left(x + \frac{r^2}{2R(x)}\right)} e^{i\varphi_G} \quad (3.6)$$

where E_0 is the amplitude of the field at the position x_0 of the waist w_0 , $w_p(x)$ is the beam radius ($1/e^2$ maximum intensity) at the position x , $R(x)$ the radius of curvature of the beam and φ_G the Gouy phase.

As indicated in figure 3.2, a first telescope made of two spherical plano-convex lenses L_1 and L_2 of respective focal lengths $f_1 = +100$ mm and $f_2 = +300$ mm enables the magnification of the beam by a factor 3. In conjunction with the last cylindrical lens L_5 of focal length $f_5 = 20$ mm, this allows to focus the pump beam along the y -axis onto the ridge. A second telescope consists of two cylindrical lenses L_3 and L_4 of focal lengths $f_3 = +75$ mm and $f_4 = -50$ mm whose separation can be accurately adjusted with the help of a translation stage with micrometric precision. This configuration allows a very convenient frequency engineering because a simple modification of the distance between the lenses of the second telescope changes the extension of the pump beam (and its radius of curvature) along the guiding direction, giving the possibility to generate a great diversity of states.

The distance between the two lenses of the cylindrical telescope is a parameter that must be calibrated to link the graduation of the screw with a particular profile of the pump beam. To calibrate the telescope, we first perform a knife-edge measurement in its absence at two distant locations along the beam path. This consists in progressively cutting the beam with a sharp and opaque object (a black painted razor blade in our case) while recording the transmitted beam power. This allows to estimate the size of the beam at the location $x = x_{KE}$ of the blade. Since we give a specific shape to the beam along the z axis and cut it along the same direction, we can disregard the other transverse direction y , so that:

$$E_p(x_{KE}, z) \propto E_0 \frac{w_0}{w_p} \exp\left(-\frac{(z - z_0)^2}{w_p^2}\right) e^{ik_p\left(x_{KE} + \frac{(z - z_0)^2}{2R}\right)} \quad (3.7)$$

where we now consider that w_p and R represent the waist and the radius of curvature, respectively, at x_{KE} along axis z only. Assuming that the beam is

centered at a position $z_0 \gg w_p(x)$, the power that we measure as the blade cuts the beam is:

$$P_{x_{\text{KE}}}(z) = P_{\text{total}} - P_{\text{blocked}} \quad (3.8)$$

$$P_{x_{\text{KE}}}(z) \propto \int_{-\infty}^{+\infty} \exp\left(-\frac{2(z-z_0)^2}{w_p^2}\right) dz - \int_0^z \exp\left(-\frac{2(\zeta-z_0)^2}{w_p^2}\right) d\zeta \quad (3.9)$$

The change of variables $\zeta \rightarrow \frac{\sqrt{2}\zeta}{w_p}$ and writing $Z_{(0)} = \frac{\sqrt{2}z_{(0)}}{w_p}$ allow us to express $P_{x_{\text{KE}}}$ as a function of the error function erf:

$$P_{x_{\text{KE}}}(z) \propto \sqrt{\pi} \frac{w_p}{\sqrt{2}} - \frac{w_p}{\sqrt{2}} \int_{Z_{(0)}}^{Z-z_{(0)}} e^{-\zeta^2} d\zeta \quad (3.10)$$

$$P_{x_{\text{KE}}}(z) \propto \sqrt{\pi} - \left[\int_{-Z_{(0)}}^0 e^{-\zeta^2} d\zeta + \int_0^{Z-z_{(0)}} e^{-\zeta^2} d\zeta \right] \quad (3.11)$$

Using the parity of $e^{-\zeta^2}$, $\int_{-Z_{(0)}}^0 e^{-\zeta^2} d\zeta = \int_0^{Z_{(0)}} e^{-\zeta^2} d\zeta$ and since $\int_0^z e^{-\zeta^2} d\zeta = \frac{\sqrt{\pi}}{2} \text{erf}(z)$, we obtain:

$$P_{x_{\text{KE}}}(z) \propto 1 - \left[\text{erf}\left(\frac{z_0\sqrt{2}}{w_p}\right) + \text{erf}\left(\frac{(z-z_0)\sqrt{2}}{w_p}\right) \right] \quad (3.12)$$

an expression which allows to deduce the beam radius w_p from the knife-edge experiment.

By performing the measurements at two different positions along the axis of propagation x of the pump beam, we can also estimate the radius of curvature according to the propagation of Gaussian beams, since w_p and R are linked in the complex beam parameter:

$$q(x) = \left(\frac{1}{R(x)} - i \frac{\lambda_p}{\pi w_p^2(x)} \right)^{-1} \quad (3.13)$$

In our experiment, these measurements allowed to estimate the waist and radius of curvature after the first telescope to be $w_p \approx 2$ mm and $R \approx 6.5$ m, respectively. Knowing this we would in principle be able to estimate the spatial properties of the pump beam at the location of the source and for different settings of the cylindrical telescope using Gaussian beam propagation [142]. However the graduation of the micrometer screw does not give directly the absolute distance between the two lenses L_3 and L_4 in the telescope. We must therefore perform additional knife-edge measurements for different settings of the micrometer screw, as shown in figure 3.5. We can then estimate the distance between the lenses by fitting the results thanks to Gaussian beam propagation, which consists here in matching the setting giving the minimal waist for both experiment and simulation (see figure 3.5). The discrepancy between the simulation and the experiment when the beam is focused can be attributed to the degradation of the beam quality inside

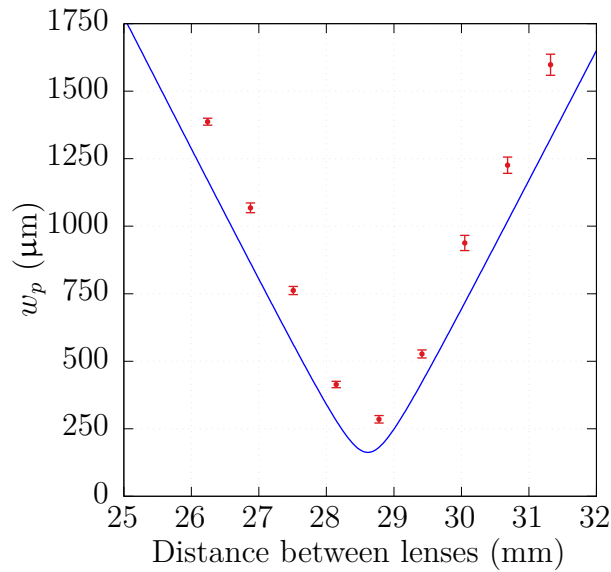


Figure 3.5 – Waist w_p measured with the knife-edge technique for different distances between the cylindrical lenses of the telescope. The blue line represents the simulated radius given the parameters of the beam deduced without the telescope.

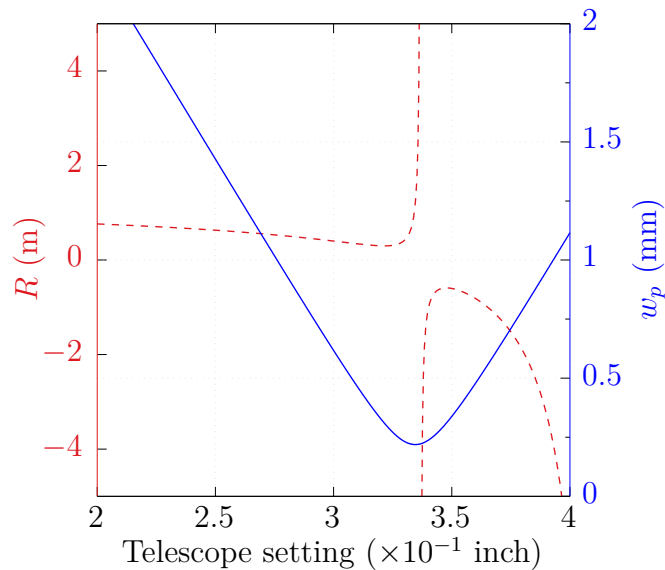


Figure 3.6 – Simulation of the $1/e^2$ intensity radius w_p (solid blue) and the radius of curvature R (dashed red) of the pump beam at the location of the sample for different settings of the telescope.

the pulse-picker. Imperfect orientation of the cylindrical lenses can also impair the spatial shaping.

The knowledge of all these parameters, allows us to plot the spatial size and curvature radius of the pump beam at the position of the source as a function of the settings of the telescope (figure 3.6). From our numerical simulations, we know that frequency-uncorrelated pairs can be produced for a pump beam with

a flat wavefront ($R \rightarrow \infty$) and a waist $w_p \approx 400 \mu\text{m}$. This value is accessible by setting the telescope close to 0.36 inch. A wide range of other parameters for the pump beam can then be explored to obtain biphoton states with different levels of frequency correlations.

3.4 Experimental reconstruction

In this section, we present the typical experimental results obtained with the fiber spectrograph. Examples of reconstructed JSIs are shown in figure 3.7. In this experiment, the level of frequency correlations is changed, as described in section 3.3.5, by a simple modification of the distance between the cylindrical lenses of the tunable telescope. The corresponding beam size w_p and radius of curvature R are indicated for each numerical simulations of the JSIs expected for these parameters. The pump beam central wavelength is $\lambda_p = 759.150 \text{ nm}$. The signal and idler photons are TM and TE-polarized, respectively. Rather than trying to measure the very small angle of incidence θ , we rely on the marginal spectra and the knowledge of the pump wavelength to deduce it:

$$\theta = \sin^{-1} \left[\lambda_p \left(\frac{n_{\text{TM}}(\lambda_s^{(0)})}{\lambda_s^{(0)}} - \frac{n_{\text{TE}}(\lambda_i^{(0)})}{\lambda_i^{(0)}} \right) \right] \quad (3.14)$$

with $\lambda_{s/i}^{(0)}$, the central signal and idler wavelengths obtained from the marginal spectra. In this particular experiment, the angle is $\theta = 0.43^\circ$.

We notice that we retrieve the expected correlations with a good agreement. A strong advantage over methods where monochromators or tunable filters are used for the JSI measurement is that the spectrograph itself does not reject any pair. The integration time (approximately one hour for each experiment) is thus reduced compared to those methods which would require longer integration especially for spectrally broad photons as in Fig. 3.7(e). Even though the JSIs seem to show some structuring, the resolution of our spectrograph is not sufficient to resolve the Fabry-Perot fringes due to the facets reflectivity that clearly appear in the numerical simulations. A slight offset along the positive diagonal can be attributed to a modification of the pump wavelength during the experiment.

We note that due to the different temporal sizes of the odd and even bins of the TDC, a data analysis is necessary. The following procedure was chosen to solve this issue: artificial temporal bins of equal size are built at the corner shared by four neighboring raw bins by taking the mean of the counts recorded in those four bins. For example, reconstructing the value of the JSI at a point located between bins m and $m + 1$ along the signal time axis and n and $n + 1$ on the idler side, thus corresponding to signal wavelengths $\lambda_s^{(m)}$ and $\lambda_s^{(m+1)}$ and idler wavelengths $\lambda_i^{(n)}$ and $\lambda_i^{(n+1)}$ amounts to:

$$|\phi|^2 \left(\frac{\lambda_s^{(m)} + \lambda_s^{(m+1)}}{2}, \frac{\lambda_i^{(n)} + \lambda_i^{(n+1)}}{2} \right) = \frac{|\phi|_{m,n}^2 + |\phi|_{m+1,n}^2 + |\phi|_{m,n+1}^2 + |\phi|_{m+1,n+1}^2}{4} \quad (3.15)$$

where $|\phi|_{i,j}^2$ corresponds to the number of coincidences recorded during the experiment at signal bin i and idler bin j . With this straightforward procedure, we obtain consistent temporal bin sizes (corresponding to the average bin size $\delta t_{\text{TDC}} = 81$ ps) while maintaining a good resolution.

The resolution in the experiment could be improved by using Superconducting Single Photon Detectors (SSPDs) instead of InGaAs SPADs. Indeed while avalanche photodiodes have quantum efficiencies of 25% at most, detectors based on superconductors can reach more than 90% with a slightly reduced timing jitter and an extremely low dark counts rate [149]. Superconducting Single Photon Detectors (SSPDs) would allow to afford greater losses from the fibers, so a longer DCF spool could be used, increasing the magnitude of the dispersion D . In our case the resolution would be improved by at least a factor 3.5.

3.5 Conclusion

This chapter has begun with an overview of experimental techniques to reconstruct the time-frequency properties of the two-photon state. It is then devoted to the description of the two-photon fiber-spectrograph we have implemented in this perspective. The group velocity dispersion of optical fibers is used to convert the frequency components of the photons into temporal delays. Recording the arrival times of the photons with free-running single photon detectors enables then the reconstruction of the Joint Spectral Intensity (JSI).

After the description of the calibration of this tool we have shown how it enables the demonstration of frequency-correlation engineering with our source. The advantages and limitations of this technique have also been identified.

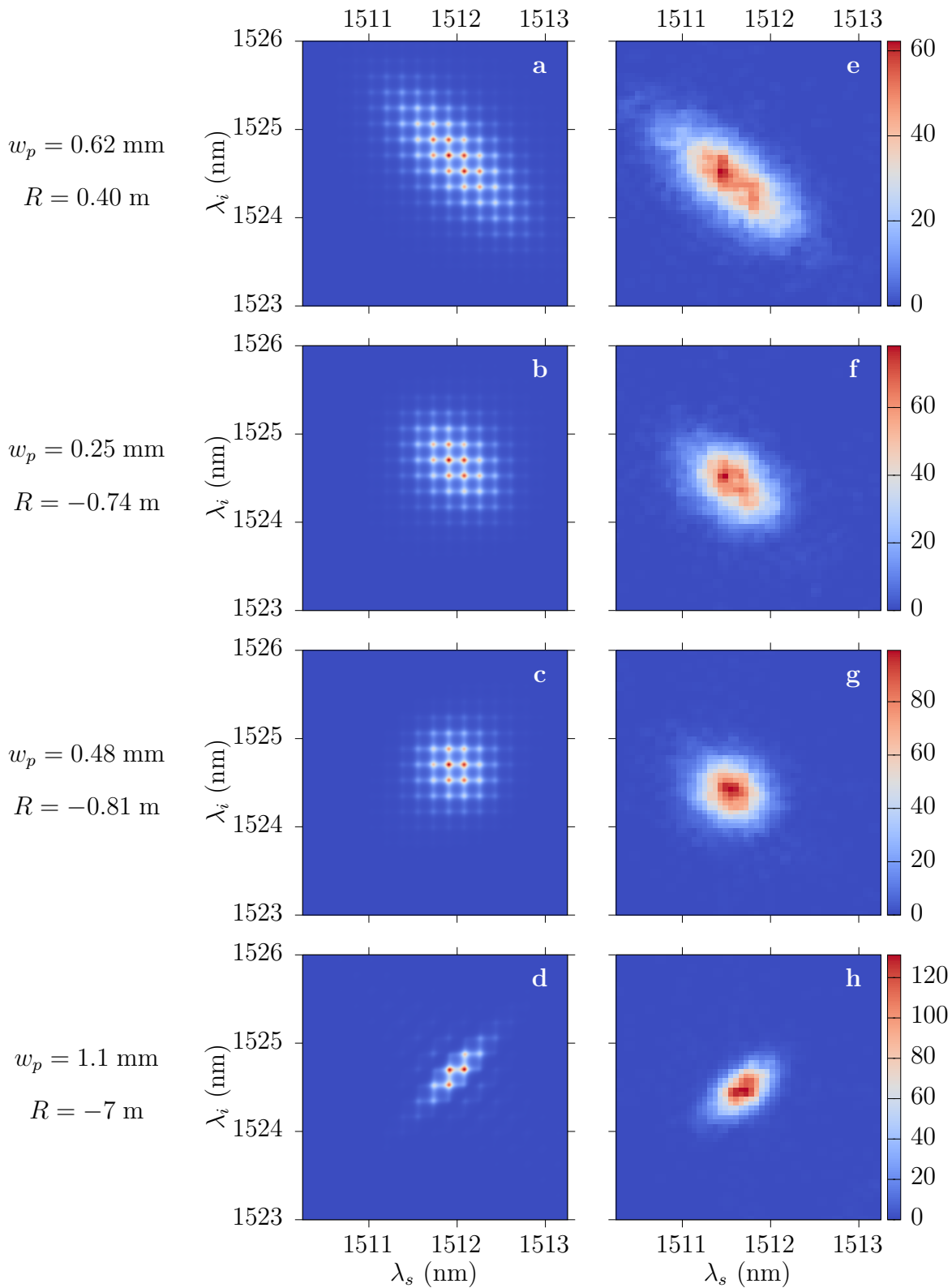


Figure 3.7 – Example of frequency correlations engineering. (a)-(d): numerical simulations of the JSIs for different pump beam radius of curvature R and transverse size w_p . (e)-(h): experimental JSIs reconstructed with the fiber spectrograph. The color scale indicates the number of coincidences recorded per temporal bin for an experimental integration of one hour.

Chapter 4

Joint Spectral Intensity reconstruction by “Stimulated” Parametric Down-Conversion

4.1 Working principle

The spontaneous processes of SPDC and FWM have a stimulated counterpart, Difference Frequency Generation (DFG), which can be described with a classical treatment (see figure 4.1). In this process the nonlinear medium is illuminated with two beams: the pump beam and the signal. Depending on their characteristics in terms of momentum and energy, a third field (idler) can be generated at the frequency difference. In [113], Liscidini and Sipe pointed out that, since the pump spectrum and the phase-matching are identical in the spontaneous and the stimulated processes, the biphoton wavefunction serves as a response function for the generation of the idler field. They thus suggested a novel approach to realize the tomography of biphoton states using these classical fields, calling this technique Stimulated Emission Tomography (SET).

This method is very appealing for the characterization of the JSI: in the case a coherent signal field $B_\nu(\omega_s)$ in the mode ν with central frequency ω_s and spectral width $\delta\omega_s$ is used to stimulate the DFG process, the average number of idler photons generated in mode η in a spectral window $\delta\omega_i$ around ω_i is:

$$\langle \hat{a}_\eta^\dagger(\omega_i) \hat{a}_\eta(\omega_i) \rangle_{B_\nu(\omega_s)} \delta\omega_i \approx 2 |B_\nu(\omega_s)|^2 |\beta|^2 |\phi(\omega_s, \omega_i)|^2 \delta\omega_s \delta\omega_i \quad (4.1)$$

with $|B_\nu(\omega_s)|^2$, the average number of photons in the stimulating field and $|\beta|^2$, a normalization constant giving the probability that a pair is emitted by SPDC. We see that the number of stimulated idler photons is proportional to the intensity of the signal field. This means that the field produced via DFG can be intense enough to be detected and characterized with “classical” detectors, *i.e.* other detectors than SPADs, and can still give information about the JSI, $|\phi(\omega_s, \omega_i)|^2$ [†], allowing its reconstruction as shown in figure 4.2.

[†]as long as the stimulating field does not deplete the pump beam

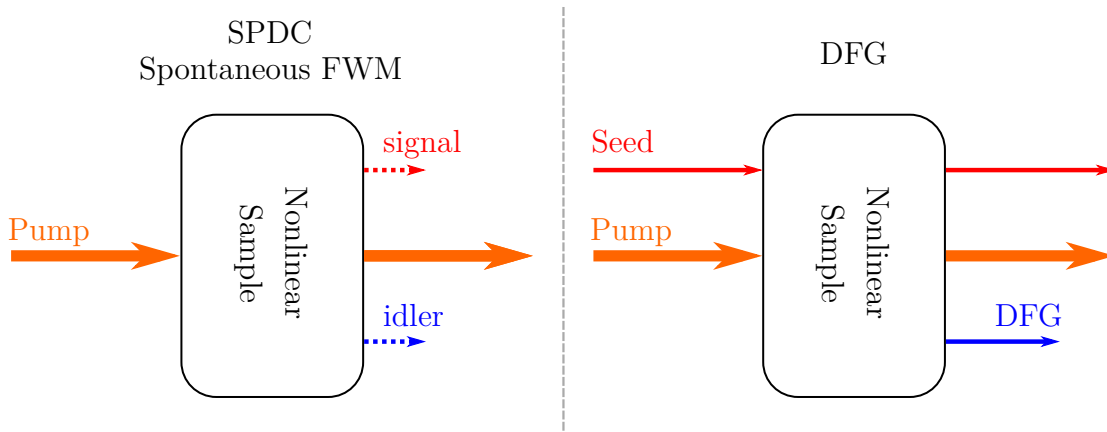


Figure 4.1 – Sketch showing the link between spontaneous nonlinear processes (left panel) and their stimulated equivalents (right panel). In the spontaneous cases, only the pump field is injected into the nonlinear material and generates signal and idler photons in pairs starting from vacuum fluctuations. In the stimulated case, a second field, corresponding to the signal in this sketch, is injected along with the pump. It stimulates the emission of the corresponding idler field by Difference Frequency Generation (DFG).

4.2 Experimental setup

Starting from these ideas, in collaboration with Liscidini and Sipe, we decided to implement a set-up to validate their proposal and to use it for the frequency state engineering of our source. Figure 4.3 depicts the experimental set-up developed to implement the stimulated reconstruction of the JSI. It was designed to keep the flexibility to switch from the SPDC-based experiment to the DFG one. The use of fibered elements also allows to easily replace or to remove them without having to worry about modification of the optical path.

The pumping scheme of the source is similar to the one used for the experiment with the fiber spectrograph described in section 3.3.1. A tunable infrared CW laser (Tunics-Plus™) provides the seed beam with a linewidth $\delta\omega_s = 100$ kHz and an optical power between 1 and 10 mW. Despite the quality of the laser, some sidebands are present around the main peak. A tunable fibered Fabry-Perot filter from OzOptics™ with a bandwidth 1.2 nm is used to avoid the presence of these lines in the spectral range where the DFG occurs. A fibered polarization controller is used to set the polarization of the seed beam which is injected into a polarization maintaining fibered PBS used as a polarization circulator. The seed beam is then sent into free space via a fiber collimator and coupled to the source with a microscope objective ($\times 40$, NA= 0.65). The polarization of the seed is aligned with respect to the TE and TM axis of the waveguide via the orientation of the QWP and HWP. These waveplates also allow to switch from one interaction to the other. The transmitted part of the seed is collected with another microscope objective (same characteristics) and measured with a powermeter. This allows to renormalize the experimental data by taking into account the gaussian transmission profile of the Fabry-Perot filter.

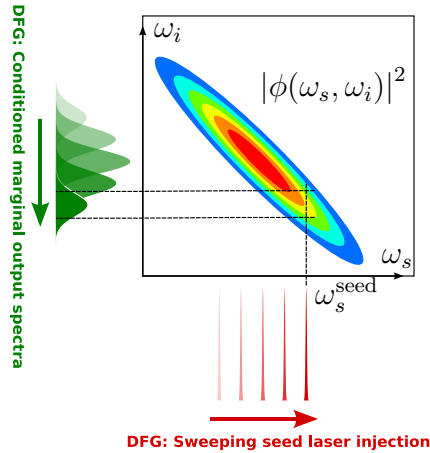


Figure 4.2 – Reconstruction scheme of a JSI, shared by the SPDC and the DFG process for the same nonlinear sample and the same pump configuration. In the DFG case, a narrow-band seed laser beam at frequency ω_s^{seed} stimulates the emission of a spectrally pre-conditioned coherent output beam in the idler mode. This spectrum is proportional to a “slice” of the JSI corresponding to the injected wavelength. Sweeping the seed wavelength allows the reconstruction of the JSI.

The idler beam generated by DFG propagates in the opposite direction and with orthogonal polarization with respect to the seed beam. The injection objective of the signal thus serves as a collection objective for the idler which is coupled into the PBS via the collimator. The orthogonal polarizations of the two beams allow an easy separation between them. The idler beam is then sent to an Optical Spectrum Analyzer (OSA) (Yokogawa™ 6730C). This instrument can reach a resolution of 20 pm with a sufficient sensitivity to detect idler photons in the telecom band.

Once the seed wavelength $\lambda_s^{(0)}$ is chosen, the DFG emission is analyzed with the OSA by measuring the optical power at different idler wavelengths λ_i , so that a slice $|\phi(\lambda_s^{(0)}, \lambda_i)|^2$ of the JSI is reconstructed. By sweeping the seed laser, the JSI can be deduced on a given wavelength range (figure 4.2).

4.3 Joint Spectral Intensity measurements

4.3.1 Validation of the method

To demonstrate the technique and its advantages, we have performed a measurement of the JSI both with the fiber spectrograph and the stimulated technique in the same pumping conditions. In this experiment, the Ti:sapphire laser wavelength is centered at 759.1 nm with a spectral Full Width at Half-Maximum (FWHM) of 400 pm. Only the adjustable cylindrical telescope is present in this experiment and set so that the waist $w_p = 240 \mu\text{m}$ of the pump beam is located at the position of the source (we thus assume the wavefront to be flat). As in the previous

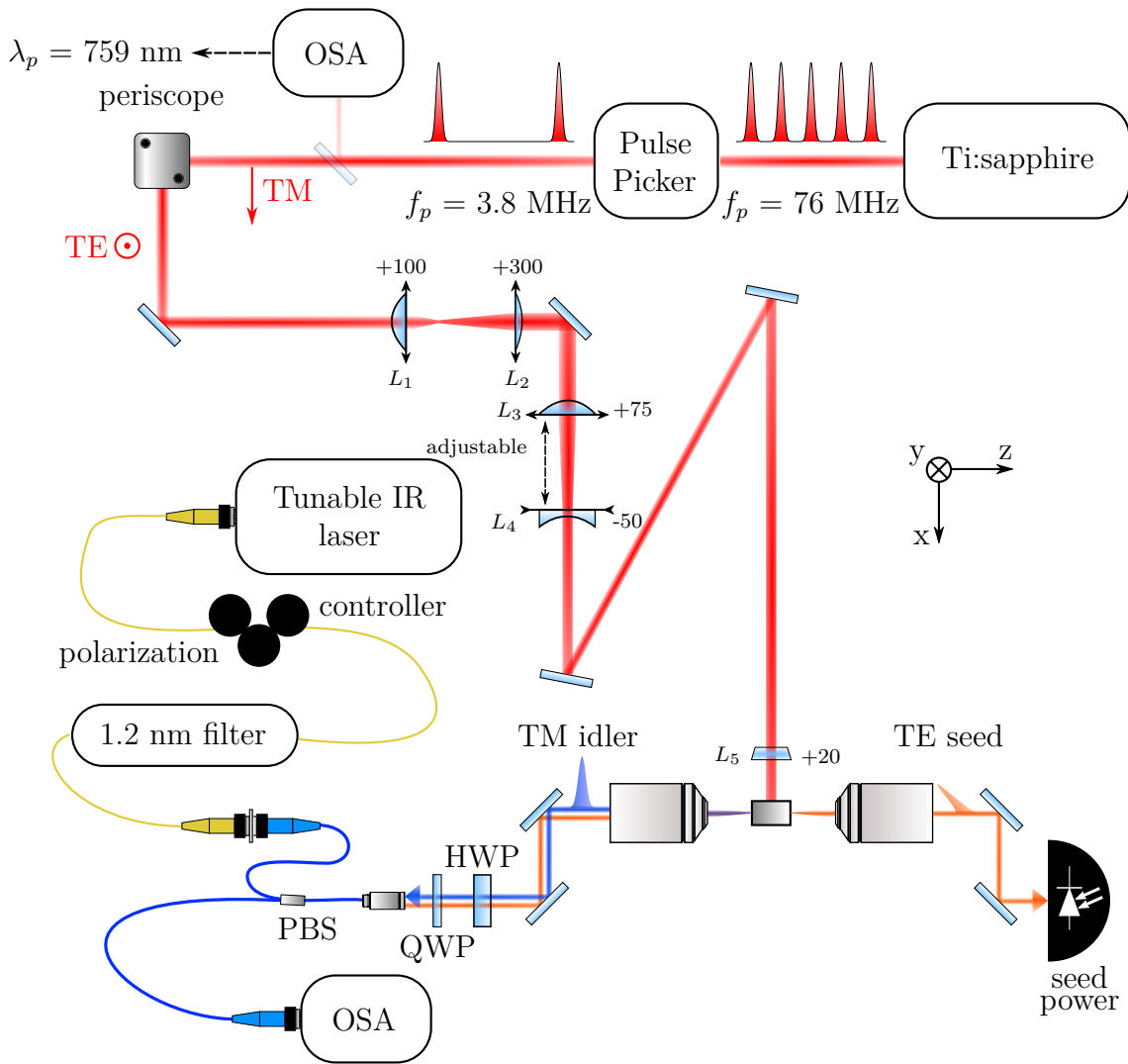


Figure 4.3 – Experimental set-up for the reconstruction of the JSI with the DFG-based method (see text for description). Focal lengths are given in millimeters.

experiment, the repetition rate of the laser is lowered from 76 MHz to 3.8 MHz in order to avoid the saturation of the SPADs. For consistency, we keep the same conditions in the stimulated experiment. In front of the waveguide the pump beam average power is 46 mW.

The characteristics of the spectrograph for the experiment based on SPDC are identical to the ones described in chapter 3. Concerning the DFG-based experiment, the seed is TE-polarized with an optical power of 8 mW. The Fabry-Perot filter is centered at the central wavelength of the window to be investigated, 1512.1 nm. The OSA is set to its best wavelength resolution, namely 20 pm and at the maximal sensitivity. The wavelength scanning speed is thus slowed down but on the other hand power level down to -100 dBm (*i.e.* 0.1 pW) can be detected.

Figures 4.4(a) and 4.4(b) represent the results of the experiments with the fiber spectrograph and the stimulated technique, respectively, along with the numeri-

cal simulation of the expected JSI (figure 4.4(c)). A remarkable improvement in resolution is obtained with the stimulated technique with 20 pm for both the idler (limited by the OSA) and the seed directions (10 pm sampling), to be compared to a resolution of 224 pm with the fiber spectrograph. The integration time is also reduced: in the spectrograph experiment, coincidences are counted for 2 hours while with the DFG method only 45 minutes are required for the reconstruction. Note that we could arbitrarily reduce the integration time in the “spontaneous” experiment, but this would necessarily jeopardize the quality of the reconstruction. The maximal values have been normalized to 1 in all graphs. In the fiber spectrograph experiment, the peak pixel contains 100 coincidences. In the DFG experiment, the maximum detected idler power is 290 nW.

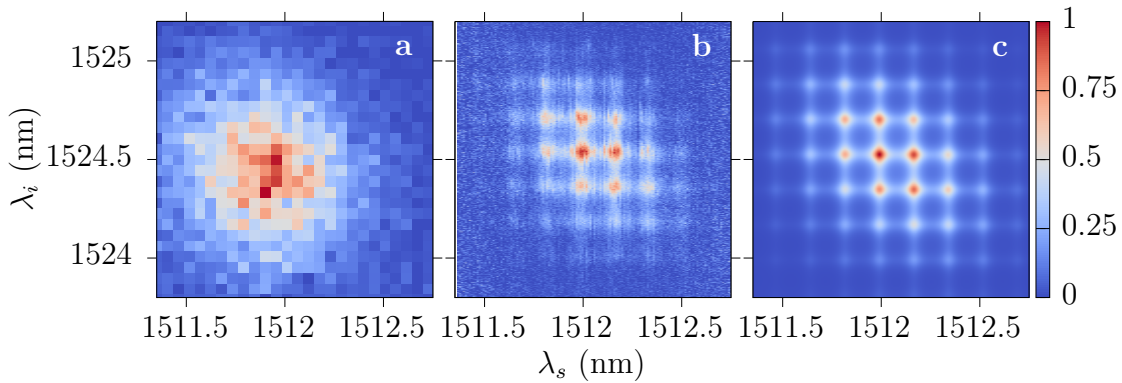


Figure 4.4 – Comparison between the spontaneous and stimulated reconstruction of the JSI. (a) Experimental JSI measured with the fiber spectrograph in 120 min with a 224 pm spectral resolution along both wavelength axis. (b) Experimental JSI reconstructed with the DFG-based method with a 20 pm resolution for both axis in 45 min. (c) Numerical simulation of the JSI for the corresponding experimental parameters.

For the numerical simulation, apart from the angle of incidence and the phase of the Fabry-Perot, all the other experimental parameters are independently determined. By measuring the spectrum of the pump beam, we get knowledge of its central wavelength λ_p and its spectral width. The determination of the spatial properties of the pump beam is described in section 3.3.5. The effective indices n_{TE} and n_{TM} of the guided modes within the sample are simulated with the transfer matrix method [92] and from the knowledge of the actual structure of the sample (see Appendix A). The length of the waveguide $L = 2.1$ mm has been determined from observations with an optical microscope. For the microcavity resonance width, we use the theoretical value $\Delta\lambda_{\mu\text{cav}} = 280$ pm [90].

The improvement in resolution and speed of acquisition offered by this technique is remarkable and should prove very useful in the perspective of characterizing complex photonic circuitry with multiple nondeterministic sources. This method has indeed been adopted by other groups to characterize their sources [150,

151, 55, 152]. In [150], stimulation was used to characterize the JSI of pairs produced by spontaneous FWM in polarization-maintaining optical fibers. The side-lobes of the sinc phase-matching part of the JSI are clearly reconstructed. In the case of spontaneous FWM in silicon micro-ring resonators, the same method was adopted in [152] to measure the JSI. In that experiment, the resonances of the fields in the device are responsible for a very narrow joint spectrum, below 100 pm. A home-made actively stabilized Fabry-Perot filter was thus used instead of an OSA to analyze the idler field. The achieved resolution is 4 pm in the idler direction and 2 pm for the seed.

With our current implementation, it is not yet possible to study the frequency correlations at the degeneracy point. This is due to the poor Extinction Ratio (ER) of the fibered PBS which amounts approximately to 20 dB. A significant part of the stimulating beam would thus pollute the idler beam and we cannot perform a frequency filtering in that case. A solution to this issue would consist in using a free space plate PBS whose ER can reach up to 40 dB. An increase of the energy of the pump pulses would also allow to decrease the seed power required for a given number of idler photons and solve this issue.

4.3.2 High-resolution frequency correlation engineering

This tool opens the way to the investigation of the frequency correlation engineering with our devices. The simplest engineering can be obtained by adjusting the cylindrical telescope at different settings as in section 3.4. Using the DFG method, the corresponding modifications of the JSI are investigated. For this experiment, both spherical and cylindrical telescopes are used and the signal seed is TM polarized (a TE idler field is thus characterized). Figure 4.5 shows the results of the reconstruction for different waists w_p and radii of curvature R (right column) along with numerical simulations for the corresponding parameters (left column). Depending on the overall efficiency of the DFG process, the sensitivity of the OSA and the investigated spectral window, the time required for the reconstruction may vary. The pump wavelength for experiments (e) and (h) is $\lambda_p = 759.256$ nm and the reconstruction takes 25 minutes. For experiments (f) and (g), we measure $\lambda_p = 759.145$ nm and the acquisition is done in 1 hour. Note that the stripes of noise in the experimental maps come from the technical noise of the OSA. In figure (h), the instrument automatically removed all values below a certain threshold. On one hand this has clearly reduced the presence of noise but on the other hand, the edges of the JSI have been suppressed.

As appears in figure 4.5, the obtained level of resolution allows to reconstruct the fine details predicted by the numerical simulations which were not resolved with the fiber spectrograph. Note that in the simulations we have neglected the losses since we know them to be low for this kind of waveguides ($\alpha \approx 0.1$ cm⁻¹). However the aging of the sample could have induced losses due to oxidation and may explain why the Fabry-Perot peaks are slightly larger than expected.

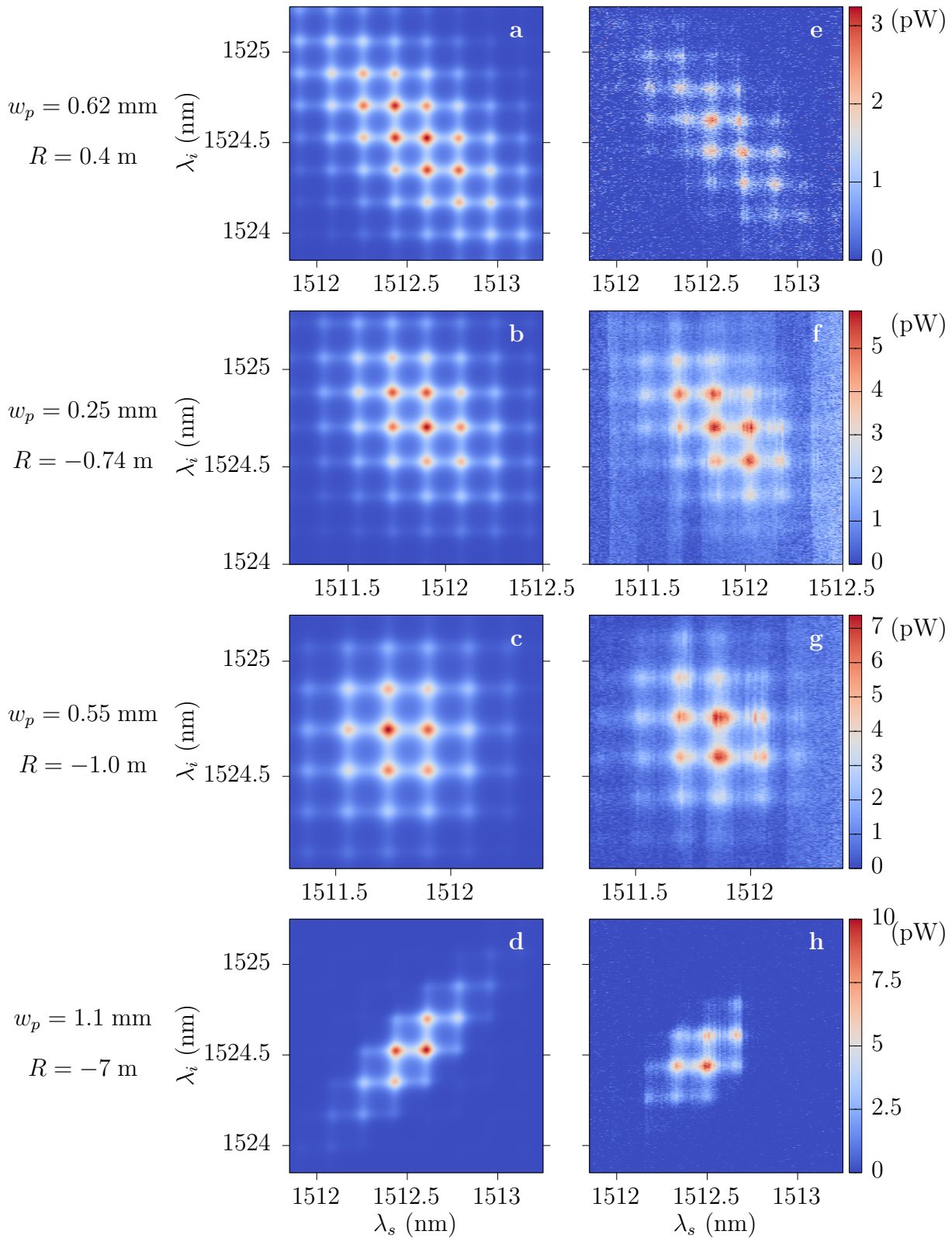


Figure 4.5 – Example of frequency correlations engineering. (a)-(d): numerical simulations of the JSIs corresponding to the indicated radius of curvature R and pump beam transverse size w_p . (e)-(h): experimental JSIs reconstructed using DFG.

4.4 Prospect for a phase sensitive measurement of the JSA with stimulated techniques

The results we have just described were limited to the measurement of the JSI and thus lacks the phase sensitivity required for a full reconstruction of the JSA. Nevertheless, they do not take full advantage of the Stimulated Emission Tomography (SET) proposal [113] since we only use a CW stimulating beam rather than a pulsed seed. Indeed the response of the source to a pulsed stimulation would consist in idler pulses with characteristics dependent on the the seed beam and more importantly on the timing information contained in the phase of the biphoton wavefunction. One could then try to reconstruct the full JSA by stimulating the device with known signal pulses and then characterize the generated idler beam with standard techniques for ultrashort pulses reconstruction [129, 153] such as Frequency Resolved Optical Gating (FROG) or Spectral Phase Interferometry for Direct Electric-field Reconstruction (SPIDER), tools that are now commercially available. Unfortunately those devices demand high input powers. We cannot afford to stimulate the source with too energetic pulses otherwise we would risk to deplete the pump. Even the increase of the pump repetition rate to the 76 MHz value of the Ti:sapphire laser will not provide enough mean power to operate commercial pulse profilers. The need for a controllable source of pulsed light around 1550 nm that we must synchronize with the pump pulses is an additional complication to the set-up. These reasons lead us to look for an alternative method.

Injecting both the pump and the seed beams in the source, we recall that the idler DFG intensity we measure with the OSA is:

$$I_{\omega_s}(\omega_i) = |\phi(\omega_s, \omega_i)|^2 \quad (4.2)$$

with ω_s the frequency of the seed and ω_i the idler frequency measured at the OSA and where we dropped multiplicative constants to keep a light notation. As stated above this measurement is insensitive to the phase $\xi(\omega_s, \omega_i)$ of the JSA. The main idea of our proposal is to inject two seeds detuned with respect to each other instead of a single one. Indeed with a fundamental seed at ω_s , a sideband at $\omega_s + \Omega$ and a control phase ψ between them, the intensity that will be measured at a spectrometer or the OSA reads:

$$I_{\omega_s, \Omega, \psi}(\omega_i) = |\phi(\omega_s, \omega_i) + e^{i\psi} \phi(\omega_s + \Omega, \omega_i)|^2 \quad (4.3)$$

where we assume that the seeds have equal intensities. The measurement is now sensitive to the phase thanks to the interference between the two terms on the right hand side of the previous equation. This is clearer if we decompose the JSA as $\phi(\omega_s, \omega_i) = |\phi(\omega_s, \omega_i)| e^{i\xi(\omega_s, \omega_i)}$ with its explicit norm and phase and we transform the former expression for the DFG intensity into:

$$\begin{aligned} I_{\omega_s, \Omega, \psi}(\omega_i) = & |\phi(\omega_s, \omega_i)|^2 + |\phi(\omega_s + \Omega, \omega_i)|^2 \\ & + 2|\phi(\omega_s, \omega_i)||\phi(\omega_s + \Omega, \omega_i)| \cos(\psi + \xi(\omega_s, \omega_i) - \xi(\omega_s + \Omega, \omega_i)) \end{aligned} \quad (4.4)$$

By adjusting the control phase ψ to 0 and $-\pi/2$, we can estimate the cosine and the sine of the phase difference $\delta\xi = \xi(\omega_s, \omega_i) - \xi(\omega_s + \Omega, \omega_i)$ between two points in the JSA:

$$\cos(\delta\xi) = \frac{I_{\omega_s, \Omega, \psi=0} - 1/2[I_{\omega_s} + I_{\omega_s + \Omega}]}{\sqrt{I_{\omega_s} I_{\omega_s + \Omega}}} \quad (4.5)$$

$$\sin(\delta\xi) = \frac{I_{\omega_s, \Omega, \psi=-\pi/2} - 1/2[I_{\omega_s} + I_{\omega_s + \Omega}]}{\sqrt{I_{\omega_s} I_{\omega_s + \Omega}}} \quad (4.6)$$

where the dependence of all the terms with ω_i is implied and $I_{\omega_s, \Omega, \psi}$ is the intensity measured in the presence of the two seeds while I_{ω_s} is the intensity measured with our standard stimulation technique (a single seed). We thus see that the method will involve the comparison of intensities measured with or without the interference pattern. The phase difference is then retrieved:

$$\delta\xi = \arg [\cos(\delta\xi) + i \sin(\delta\xi)] \quad (4.7)$$

This is only a relative phase between two points $\xi(\omega_s, \omega_i)$ and $\xi(\omega_s + \Omega, \omega_i)$ in the JSA. To reconstruct the actual phase, we need to select one point $\xi(\omega_s^{(0)}, \omega_i^{(0)})$ which will serve as a reference for the mapping, setting a global phase that we will choose to match our theoretical prediction (this choice has no physical consequence). Increasing the detuning Ω between the two seeds and seeding in both directions ω_s and ω_i would allow, in principle to reconstruct the full phase distribution of the state. Our proposal is in fact related to the spectral shearing technique [154] for ultrashort pulse analysis where shearing relates to the spectral separation Ω between the original pulse carrier frequency and the shifted frequency of the pulse replica generated for the analysis.

To actually implement this scheme, we need an efficient method for generating a sideband to the seed and we thus have to optically modulate the beam. Acousto-Optic Modulators (AOMs) allow to achieve this, however the sideband will be spatially separated from the carrier beam which is not practical for our method. The range of shearing frequency is also limited with those devices compared to Electro-Optic Modulators (EOMs). State of the art EOMs can now achieve frequency modulation of the order 40 GHz and are usually fully integrated into fibered components. Generally, the modulation (in phase or in amplitude) of those devices generates several sidebands offset from the original carrier by a integer multiple of the modulation frequency Ω . Even though the technique would still be sensitive to the phase of the JSA, the algorithm to retrieve the actual phase would be overwhelmingly complicated. Fortunately some tricks exist to circumvent this issue. Indeed, amplitude EOM are usually two phase EOMs arranged in a Mach-Zehnder interferometer configuration. By modulating them in quadrature and balancing the interferometer properly, a single sideband can be selected along with the carrier frequency [155]. Extinction Ratio of at least 35 dB between the sideband of interest and the others have been achieved. Some solutions are also commercially available that allow to keep only the sideband with the possibility

to suppress the carrier [156]. We also note that arrangements combining an amplitude and a phase EOM in series [157] or in a Mach-Zehnder arrangement [158] allow to obtain a single sideband that is orthogonally polarized with respect to the original seed. Indeed, with a convenient initial polarization state, the EOM behaves as a variable waveplate thus allowing the modulation to be perceived in the polarization. In both cases the Extinction Ratio reached 20 dB. It is nevertheless interesting for our scheme since an additional Pockels cell combined with a polarizer would allow, while keeping the modulation on, to switch between the original seed at ω_s alone, to the sideband at $\omega_s + \Omega$ alone and to the double seed. With no modification of the setup or of the setting of the EOM, we would be able to measure the terms in equations (4.5) and (4.6) in a minimum amount of time, avoiding the issue of modifications of these intensities because of thermal fluctuations for example, in the span of time required for an otherwise long acquisition. This would however requires an additional free-space part to perform the adjustment and filtering of the polarization.

The use of an electro-optic modulator would nevertheless be insufficient to cover the full range of our JSA. Figure 4.6 shows a sketch of the algorithm we propose; we combine the adjustment of the shearing frequency and the sweeping of the frequency of the seed laser to solve this issue. The seed laser would be set at $\omega_s = \omega_s^{(0)}$, typically at a point where the intensity of the reconstructed JSI is maximal to optimize the Signal to Noise Ratio (SNR). The first shearing would then be performed between $\omega_s^{(0)}$ and $\omega_s^{(0)} + \delta\omega_s$ followed by a shearing between $\omega_s^{(0)}$ and $\omega_s^{(0)} + 2\delta\omega_s$... until the maximum shearing the modulator can achieve is reached: $\omega_s^{(0)} + \Omega^{\max}$. The seed laser would then be set for the next iteration at $\omega_s = \omega_s^{(1)} = \omega_s^{(0)} + \Omega^{\max}$ and we would resume the shearing measurements with $\omega_s^{(1)} + m\delta\omega_s$ (with $m = 1 \dots \Omega^{\max}/\delta\omega_s$) until the range of interest has been fully probed. For all these shearings, the intensity would be measured with the OSA at different ω_i , yielding $I_{\omega_s, \Omega, \psi}(\omega_i)$ with $\omega_s = \omega_s^{(n)} = \omega_s^{(0)} + n\Omega^{\max}$, $\Omega = m\delta\omega_s$ and $\psi = 0$ or $-\pi/2$.

Doing so, we would get the following relation:

$$\xi(\omega_s^{(n)} + m\delta\omega_s, \omega_i) = \xi(\omega_s^{(n)}, \omega_i) - \delta\xi(\omega_s^{(n)} + m\delta\omega_s, \omega_i) \quad (4.8)$$

To solve this recurrence relation, we need the phase at the starting point, namely $\xi(\omega_s^{(0)}, \omega_i)$. An additional shearing along the idler direction and for a DFG intensity measured at a single frequency $\omega_s^{(0)}$ (we thus do not need the OSA for this measurement since no sweeping is required) would provide this value up to a global offset phase $\xi(\omega_s^{(0)}, \omega_i^{(0)})$ that we could set to an arbitrary value in order to match the simulated phase and reconstruct $\xi(\omega_s, \omega_i)$.

To estimate the feasibility of the technique, we take into account the noise of the OSA in simulating both the measurement of the JSI and the reconstruction of the phase. Studying the technical noise of the OSA shows that it is Gaussian, with a standard deviation $\sigma \approx 0.2$ pW and centered at a maximum mean value $\bar{p} \approx 0.5$ pW in the range of detection we normally use. The minimal detectable value is $p_{\min} = 1$ fW. Note that \bar{p} and p_{\min} can slightly change between experiments: in our simulations, we have chosen the worst case scenario. We simulate

the measurement $I_{\omega_s}(\omega_i)$ of the JSI and the shearing measurement $I_{\omega_s, \Omega, \psi}(\omega_i)$ with two uncorrelated noises and combine the two to retrieve an estimate of the JSA $\phi_{\text{est}}(\omega_s, \omega_i)$. The fidelity \mathcal{F} is then computed as our figure of merit to compare the simulated reconstruction $\phi_{\text{est}}(\omega_s, \omega_i)$ against the theoretical JSA $\phi(\omega_s, \omega_i)$:

$$\mathcal{F} = \left| \iint d\omega_s d\omega_i \phi(\omega_s, \omega_i) \phi_{\text{est}}^*(\omega_s, \omega_i) \right| \quad (4.9)$$

A shearing $\Omega = 20$ GHz is chosen for the simulations, corresponding to commercially available EOMs. We assume that we manage to select only one sideband of the modulated signal and recombine it with the original seed at the same intensity. In the experiments presented in this thesis, a pulse-picker was used to generate a clock signal. The repetition rate of the pump laser was reduced to 3.8 MHz with this device to avoid the saturation of the single photon detectors. For phase-sensitive reconstructions, this choice is not a good one since we would get a fidelity of only 50% (figure 4.7). The reduction of the repetition rate is actually not necessary for the stimulated experiment and we can assume that the source is pumped at the full repetition rate of 76 MHz. The intensity measured with the OSA as well as the SNR should therefore be improved by a factor 20. Figure 4.8 shows the result of these simulations in terms of predicted state and expected measurement. In this case, the fidelity reaches 97%. The improvement in SNR is actually so beneficial that a shearing of 1 GHz may suffice for the measurement. We also note that $\delta\xi$ can be rather small so a better fidelity may be obtained by approximating $\delta\xi \approx \sin(\delta\xi)$. This has to be investigated on a case by case basis.

Additional errors in the experiment may come from the inaccuracy with which the shearing is done, namely the fluctuation $\delta\Omega$ of the shearing frequency should remain below the spacing $\delta\omega_s$ between our data points. The control phase ψ which in fact represents the synchronization between the pump repetition rate and the modulation of the seed also plays an important role and should be controlled as precisely as possible.

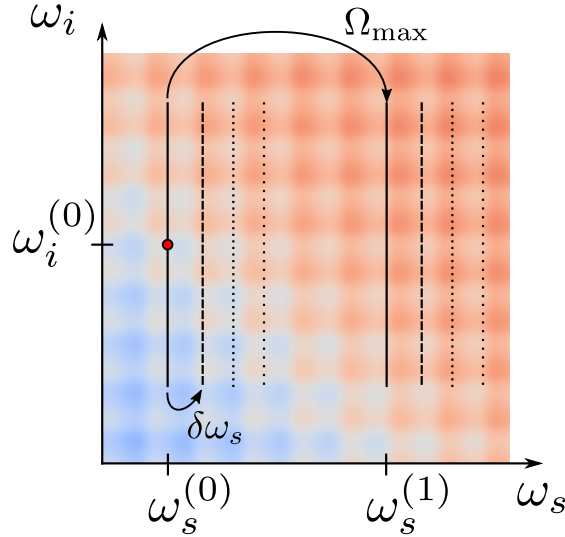


Figure 4.6 – Experimental protocol proposed for the reconstruction of $\xi(\omega_s, \omega_i)$. The seed laser centered at $\omega_s^{(0)}$ is modulated in order to generate a sideband detuned by a frequency $\Omega = m\delta\omega_s$. The comparison of the idler intensities produced by the modulated and un-modulated seed beams and measured with an OSA at different frequencies ω_i allows to establish a relationship between the phases at frequencies $\omega_s^{(0)}$ and $\omega_s^{(0)} + \Omega$. The maximum shearing Ω^{\max} achievable by current modulators is likely not sufficient to cover the full range of interest. It is thus necessary to tune the seed at $\omega_s^{(1)} = \omega_s^{(0)} + \Omega^{\max}$ and resume the shearing until the full window has been scanned. This first shearing being done for the signal, we gain information on the signal phase and the phase correlations between signal and idler. However all phase information belonging to the idler only is lost. A shearing experiment must be performed along the idler direction to circumvent this. With this additional measurement, the phase profile $\xi(\omega_s, \omega_i)$ can be reconstructed up to a phase $\xi(\omega_s^{(0)}, \omega_i^{(0)})$, marked by a red dot on the graph, which can be set to an arbitrary value. (The map represents a portion of the numerically simulated phase profile $\xi(\omega_s, \omega_i)$ for the example source.)

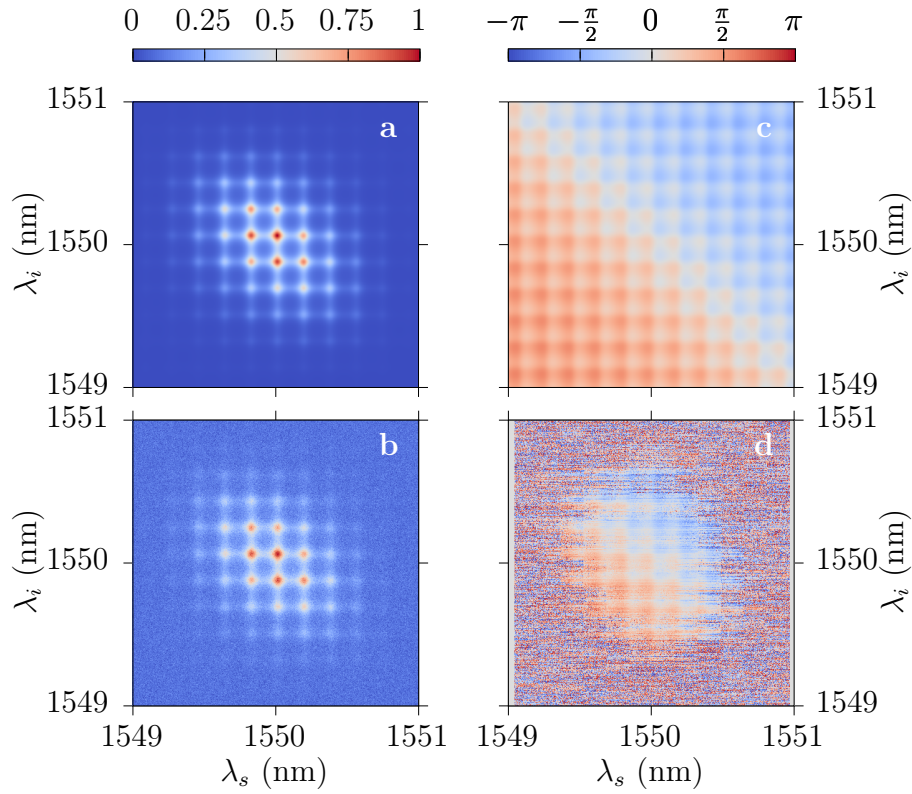


Figure 4.7 – Numerical simulations of the expected and “reconstructed” JSI and phase. JSI (a) and phase profile (c) generated by the device. Simulation of the expected outcome from the reconstruction of the JSI (b) and phase profile (d) taking into account the noise level in our set-up. The pump laser has a repetition rate of 3.8 MHz. The non trivial shape of the phase profile in (c) is due to the resonance of the pump beam in the microcavity and to the reflective facets of the sample.

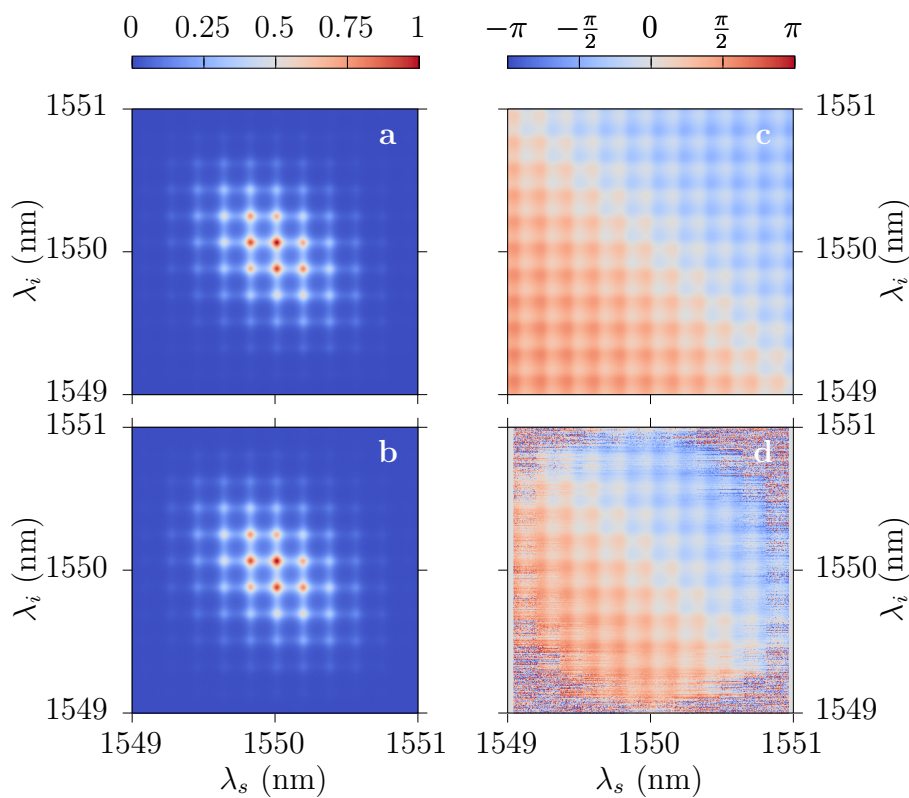


Figure 4.8 – Numerical simulations of the expected and “reconstructed” JSI and phase. JSI (a) and phase profile (c) generated by the device. Simulation of the expected outcome from the reconstruction of the JSI (b) and phase profile (d) taking into account the noise level in our set-up. The pump laser has a repetition rate of 76 MHz.

4.5 Conclusion

This chapter has described the demonstration of a novel technique for the reconstruction of the Joint Spectral Intensity (JSI). Proposed by our collaborators Marco Liscidini and John Sipe, it is based on the fact that the Joint Spectral Amplitude (JSA) acts as a response function not only for SPDC but also for Difference Frequency Generation (DFG), the corresponding stimulated nonlinear process. Indeed for the same pumping condition, the injection of a seed laser beam, corresponding to specific vacuum fluctuations in the signal mode for the spontaneous process, is responsible for the production of light in the idler mode. The spectral properties of the idler beam reflects the form of the JSI, allowing its reconstruction. Moreover, the intensity of the DFG light is proportional to the power of the seed and can thus be detected and characterized with “classical” instruments giving more flexibility than single photon detectors. With this advantage, this method allows a faster and more resolved reconstruction of the JSI in comparison to other techniques, a reason for its widespread adoption by the community.

The technique has been limited to the characterization of the JSI. However we have made a proposal to extend it to the measurement of the JSA using electro-optic modulation.

A part of the work presented in this chapter has been published in [148].

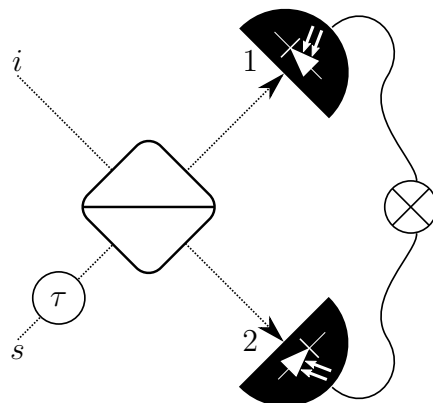
Chapter 5

Biphoton state engineering in the frequency-time space

The methods described so far (with the exception of the technique presented in 4.4) are limited to the measurement of the JSI. The phase information contained in the JSA, which is non trivial for our source, is lost in the measurement. Moreover, methods to reconstruct the JSI do not allow to distinguish between a pure and a mixed state. They thus do not constitute complete tomographies. In this chapter we revisit the two-photon interference on a beamsplitter, famously known as the experiment of Hong, Ou and Mandel [35]. In particular we show that a partial information on the phase of the biphoton wavefunction can be inferred from this type of experiment.

We first describe the original Hong-Ou-Mandel (HOM) experiment and some examples of two-photon interferences obtainable with our source. We then discuss a modified experiment which gives access to more information on the biphoton wavefunction and in particular, allows to reconstruct the antisymmetric part of the chronocyclic Wigner function of the state. We finally show examples of Schrödinger-cat like states that can be generated with our source and measured with this technique.

Figure 5.1 – General principle of the HOM interferometer. Single photons coming from input paths s and i impinge on a 50/50 beamsplitter. The interference is observed by recording the coincidences in output paths 1 and 2 as a function of the delay τ between the two input arms.



5.1 Hong Ou Mandel experiment

The original experiment of Hong, Ou and Mandel [35] consists in sending the photons of the pair into two input ports of a 50/50 beamsplitter with the possibility to delay the arrival of one of them with respect to the other with an optical delay line, or equivalently to set the respective arrival times of the photons with a convenient translation of the beamsplitter (see figure 5.1). If the photons are indistinguishable from each other and their wavepackets are superimposed at the beamsplitter, the scenarios in which both photons are transmitted or reflected cannot be distinguished and interfere destructively. In this situation two detectors located in the output arms of the beamsplitter will never click in coincidence, giving rise to a dip in the coincidence counts.

To understand this effect and its dependence on the input state, we start by assuming a 50/50-beamsplitter with input arms s and i and output arms 1 and 2 as sketched in figure 5.1 and, considering the phase-shift when the beam is reflected, the signal and idler creation operators are transformed into:

$$\begin{aligned}\hat{a}_s^\dagger(\omega_s) &= \frac{\hat{a}_1^\dagger(\omega_s) + i\hat{a}_2^\dagger(\omega_s)}{\sqrt{2}} e^{-i\omega_s\tau} \\ \hat{a}_i^\dagger(\omega_i) &= \frac{i\hat{a}_1^\dagger(\omega_i) + \hat{a}_2^\dagger(\omega_i)}{\sqrt{2}} e^{i\omega_i\tau}\end{aligned}\quad (5.1)$$

where 2τ represents the optical path delay between the two input arms. The transformation of the initial biphoton state $|\psi\rangle = \iint d\omega_s d\omega_i \phi(\omega_s, \omega_i) \hat{a}_s^\dagger(\omega_s) \hat{a}_i^\dagger(\omega_i) |\text{vac}\rangle$ is thus:

$$\begin{aligned}|\psi\rangle &= \frac{1}{2} \iint d\omega_s d\omega_i \phi(\omega_s, \omega_i) e^{-i(\omega_s - \omega_i)\tau} \left(i\hat{a}_1^\dagger(\omega_s) \hat{a}_1^\dagger(\omega_i) + i\hat{a}_2^\dagger(\omega_s) \hat{a}_2^\dagger(\omega_i) \right. \\ &\quad \left. + \hat{a}_1^\dagger(\omega_s) \hat{a}_2^\dagger(\omega_i) - \hat{a}_1^\dagger(\omega_i) \hat{a}_2^\dagger(\omega_s) \right) |\text{vac}\rangle\end{aligned}\quad (5.2)$$

The first two terms correspond to scenarios in which both photons leave the beamsplitter in the same output port while the last two terms correspond to the situation where the two photons take different output ports. The opposite signs between the last two terms in the sum is the cause of the interference that will occur when recording the coincidences at the detectors located in the two output arms. The probability of coincidence is proportional to the joint-photocurrent of the detectors [104]:

$$P(t, t'; \tau) = \langle \psi | \hat{E}_1^{(-)}(t) \hat{E}_2^{(-)}(t') \hat{E}_1^{(+)}(t) \hat{E}_2^{(+)}(t') | \psi \rangle \quad (5.3)$$

with $\hat{E}_{1(2)}^{(+)}(t)$ the positive frequency part of the electric field operator in the output arm 1 (2, respectively). Since we are in the interaction picture, we remind that the field operators have an explicit time dependence $\hat{E}^{(+)}(t) = \frac{\mathcal{E}(\omega^{(0)})}{\sqrt{2\pi}} \int d\omega e^{-i\omega t} \hat{a}(\omega)$ and we have used the slowly varying envelope approximation ($\omega^{(0)} \gg \Delta\omega$) to

extract all the frequency-dependent normalization term from the integral. The normalized coincidence rate thus reads:

$$P(t, t'; \tau) = \left\| \iint d\omega_1 d\omega_2 \hat{a}_1(\omega_1) \hat{a}_2(\omega_2) e^{-i\omega_1 t} e^{-i\omega_2 t'} |\psi\rangle \right\|^2 \quad (5.4)$$

The first two terms of equation (5.2) will obviously not contribute to the coincidence counts. Applying the creation and annihilation operators to the vacuum and integrating over ω_s and ω_i , we obtain:

$$P(t, t'; \tau) = \frac{1}{4} \left\| \iint d\omega_1 d\omega_2 e^{-i\omega_1 t} e^{-i\omega_2 t'} \left(\phi(\omega_1, \omega_2) e^{-i(\omega_1 - \omega_2)\tau} - \phi(\omega_2, \omega_1) e^{-i(\omega_2 - \omega_1)\tau} \right) |\text{vac}\rangle \right\|^2 \quad (5.5)$$

In a real experiment we would integrate the joint-detection events over time for each pump pulse. In fact because of their jitter, the detectors have a timing resolution of 200 ps and thus perform a time integration of the photon pulses whose maximal temporal duration is of the order $L/v_g = 22$ ps. Even if we take into account the possible reflections of the wavepackets in the sample, we can see from figure 2.12(c) that almost all events are comprised in a 100 ps temporal window. Integrating over times t and t' allows thus to simplify expression (5.5). Indeed the modulus squared term involves a double integral over ω_1 and ω_2 and an additional double integral over ω'_1 and ω'_2 because of the hermitian conjugate in the product, which simplifies because of the time integration of the terms $e^{-i(\omega_1 - \omega'_1)t}$ and $e^{-i(\omega_2 - \omega'_2)t'}$:

$$P(\tau) = \frac{1}{4} \iint d\omega_1 d\omega_2 \left(\phi^*(\omega_1, \omega_2) e^{i(\omega_1 - \omega_2)\tau} - \phi^*(\omega_2, \omega_1) e^{i(\omega_2 - \omega_1)\tau} \right) \times \left(\phi(\omega_1, \omega_2) e^{-i(\omega_1 - \omega_2)\tau} - \phi(\omega_2, \omega_1) e^{-i(\omega_2 - \omega_1)\tau} \right) \quad (5.6)$$

Multiplying these terms and swapping the dummy variables of integration when necessary, we get:

$$P(\tau) = \frac{1}{2} \left[\iint d\omega_1 d\omega_2 \left| \phi(\omega_1, \omega_2) \right|^2 - \iint d\omega_1 d\omega_2 \phi(\omega_1, \omega_2) \phi^*(\omega_2, \omega_1) e^{-i(\omega_1 - \omega_2)2\tau} \right] \quad (5.7)$$

Taking into account the normalization of the biphoton wavefunction (given by equation (2.23)), we obtain the general expression for the coincidence count rate in a HOM experiment:

$$P(\tau) = \frac{1}{2} - \frac{1}{2} \iint d\omega_1 d\omega_2 \phi(\omega_1, \omega_2) \phi^*(\omega_2, \omega_1) e^{-i(\omega_1 - \omega_2)2\tau} \quad (5.8)$$

The rate of coincidences is the difference between the constant term $\frac{1}{2}$, giving the probability that the photons go into different ports and an interference term which is controlled by the relative delay τ accumulated by the photons before the beamsplitter. This term is the autoconvolution of the antidiagonal part of the Joint Temporal Amplitude (JTA). This is more clear if we express the JSA of our

source as in equation (2.36) with $\phi(\omega_s, \omega_i) = \chi_\Gamma \phi_{\text{PM}}(\omega_-) \phi_{\text{spectral}}(\omega_+)$ and do a change of variables from ω_1, ω_2 to ω_+, ω_- :

$$P(\tau) = \frac{1}{2} - \frac{|\chi_\Gamma|^2}{2} \int d\omega_+ |\phi_{\text{spectral}}(\omega_+)|^2 \int d\omega_- \phi_{\text{PM}}(\omega_-) \phi_{\text{PM}}^*(-\omega_-) e^{-i\omega_- 2\tau} \quad (5.9)$$

We see that ϕ_{spectral} , the part of the JSA which depends on the chronocyclic properties of the pump beam will not contribute to the shape of the interference pattern in the HOM experiment. The two-photon interference is described by the last integral which corresponds to the autoconvolution $(\tilde{\phi}_{\text{PM}} * \tilde{\phi}_{\text{PM}}^*)(2\tau)$. $\tilde{\phi}_{\text{PM}}(2\tau)$ is the Fourier transform of $\phi_{\text{PM}}(\omega_-)$ and corresponds to the antidiagonal part of the JTA $\tilde{\phi}_{\text{PM}}(2\tau)$. Using the normalization condition (2.23) we have:

$$P(\tau) = \frac{1}{2} \left(1 - \frac{\int d\omega_- \phi_{\text{PM}}(\omega_-) \phi_{\text{PM}}^*(-\omega_-) e^{-i\omega_- 2\tau}}{\int d\omega_- |\phi_{\text{PM}}(\omega_-)|^2} \right) \quad (5.10)$$

In order to illustrate this result, we take the example of a Gaussian pump beam as in equation (2.38) with waist w_z and incidence angle θ . In this case, (5.10) becomes:

$$P(\tau) = \frac{1}{2} \left(1 - \exp \left[-2 \left(\frac{\omega_-^{(0)}}{\Delta\omega_-} \right)^2 \right] \exp \left[-2 \left(\frac{\tau}{\Delta t_-} \right)^2 \right] \right) \quad (5.11)$$

where $\Delta\omega_- = 2\bar{v}_g/w_p$ with \bar{v}_g the harmonic mean of the group velocities of the TE and TM modes defined at equation (2.27), $\omega_-^{(0)} = (k \sin \theta - k_{\text{deg}}) \bar{v}_g$ and $\Delta t_- = 2/\Delta\omega_- = w_p/\bar{v}_g$. With degenerate photons, the frequency difference offset $\omega_-^{(0)}$ vanishes and the coincidence rate is fully characterized by the second exponential which describes the HOM dip. Indeed, for $\tau = 0$ both photons arrive at the beamsplitter at the same time and will bunch together, so the coincidence rate drops from 50% to zero. In our particular case, the dip takes a Gaussian form with a width Δt_- controlled by the size of the beam on the device (see figure 5.2(a)). If the central frequency of the photons differ, *i.e.* $\omega_-^{(0)} \neq 0$, the shape of the dip is preserved but with a reduced visibility as $|\omega_-^{(0)}|$ increases.

We note that the shape of the dip is not necessarily Gaussian. For example when the whole waveguide is illuminated, ϕ_{PM} takes a sinc shape, as indicated in equation (2.39). Consequently the convolution of its Fourier Transform and thus the dip, takes a triangular shape (see figure 5.2(a)) [159]. On the other hand, when a square band-pass frequency filter is applied to a strongly anticorrelated biphoton state, ϕ_{PM} has the form of the filter and the dip thus takes a sinc shape [160].

In these examples ϕ_{PM} is an even function of ω_- , but we can imagine different situations. In [161], a BBO crystal was pumped with first-order Hermite-Gaussian beams. The odd profile of the pump beam resulted in an antisymmetric biphoton state. Consequently the coincidence count rate took a bump shape instead of the usual dip (the photons always left the beamsplitter from different ports). Figure 5.2(b) reports the numerical simulation of the two-photon interference when

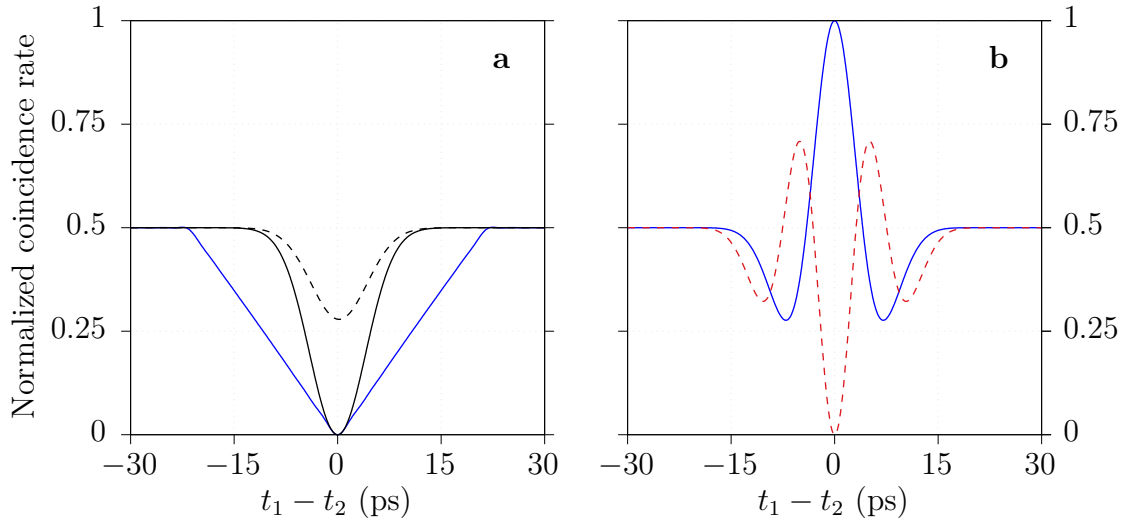


Figure 5.2 – Examples of simulated HOM interferences for our source. The facets are assumed totally transmissive. (a): the pump beam is a fundamental Gaussian beam. The solid black line depicts the Gaussian dip obtained with a beam of waist $w_z = 377 \mu\text{m}$ impinging at the degeneracy angle θ_{deg} . The dashed black line is obtained with the same waist but with an angle of incidence imposing a 400 pm offset between the central wavelengths of the signal and the idler. The dip has an identical shape but a reduced visibility because $\omega_-^{(0)} \neq 0$. The solid blue line is the triangular dip obtained when the whole length of the waveguide is pumped at the degeneracy angle. (b): interferences obtained for a HG₁₀ beam (solid blue line) and a HG₂₀ (dashed red line).

our source is illuminated with a HG₁₀ and a HG₂₀ pump. These different forms of the interference pattern indicate that the HOM experiment is a sensitive technique to probe the biphoton state. We will discuss this in details in the next section.

In this discussion, we have ignored so far the influence of the facets. As mentioned earlier, the HOM experiment done with our source in 2010 [131] resulted in a Gaussian dip as expected since the waveguide was not fully illuminated. However the visibility of the dip was limited to 85%. This was attributed to the reflection of the photons at the facets. Figure 5.3 shows the shape of the dip calculated taking into account the reflectivity of the facets. Satellite dips appear in addition to the main dip due to the interference between a doubly reflected photon with a directly transmitted one. The probability of further reflections being low, satellite dips that are further apart are not distinguished. The double reflection of both photons will contribute to the main dip. We notice that the visibility of the dip is not necessarily decreased by the facets' reflectivity. Indeed if the resonance phases for the TE and TM modes are identical, then the photons remain indistinguishable and the theoretical visibility is still 100%. Nevertheless, we have already mentioned that the control of the relative phase between the TE and TM modes is not possible and they do not coincide in general. For example, if we perform the simulation with the TE/TM phases measured in the experiment reported in [148]

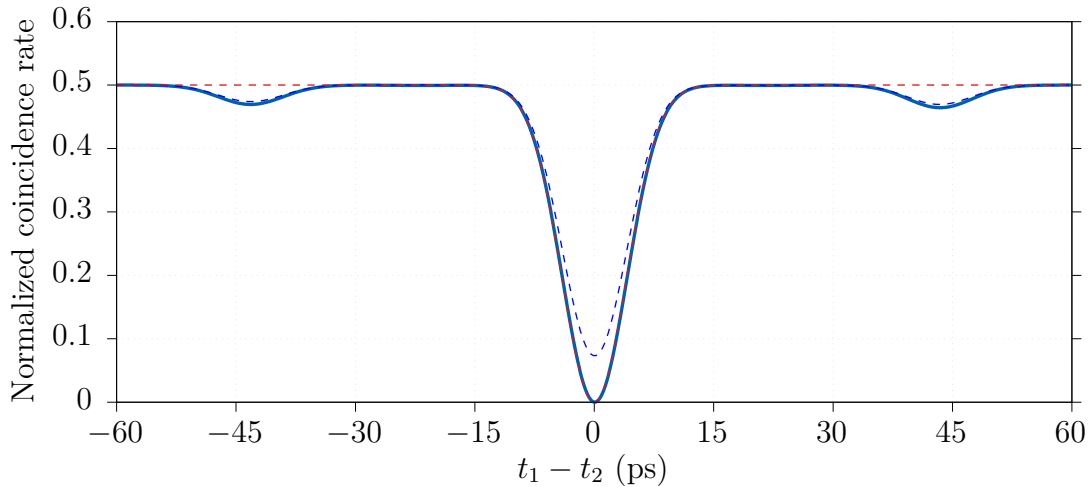


Figure 5.3 – Two-photon interference simulated for a source of length $L = 2.1$ mm, a pump beam of waist $w_p = 377$ μm impinging at the degeneracy angle θ_{deg} . Red dashed line: dip simulated with perfectly transmissive facets. Solid blue line: dip obtained with partially reflective facets with $R_{\text{TE}} = 26.7\%$ and $R_{\text{TM}} = 24.7\%$. The phase of the Fabry-Perot resonances is set so that they coincide for the TE and TM modes at the wavelengths of interest. Dashed blue line: dip simulated with the typical Fabry-Perot phases of our sample measured at room temperature.

instead of identical phases, we get a reduction of the dip visibility, still with the presence of the satellite dips (see figure 5.3).

5.2 Generalization of the HOM experiment

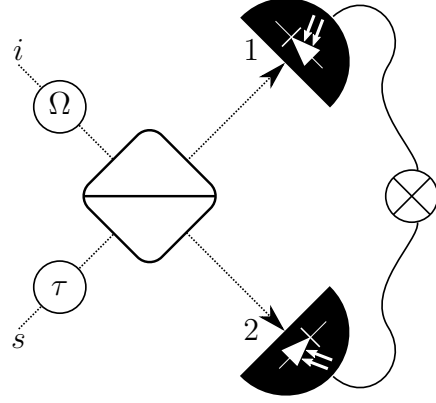
A collaboration with our colleagues of the theory team (T. Douce, T. Coudreau, P. Milman, A. Keller and S.P. Walborn) has led to a generalization of the HOM experiment allowing to open new perspectives for state measurement and engineering [140]: in this modified version of the HOM experiment, a frequency shifting device, such as an optical modulator, is inserted into one of the input arms in addition to the standard delay line in the other arm (see figure 5.4). This gives access to another degree of freedom in the analysis of the biphoton state, namely the frequency difference between the signal and the idler photons that we have labeled ω_- . Our colleagues showed that the quantity that is reconstructed by performing the modified HOM experiment is in fact a Wigner function.

Indeed, neglecting the reflection at the facets of the waveguide and using equation (2.36) where we have expressed the JSA as a product of a function of ω_+ and a function of ω_- , we can simplify the expression (2.49) of the joint Chronocyclic Wigner Function (CWF) of the biphoton state:

$$W(\omega_s, t_s, \omega_i, t_i) = \chi_{\Gamma} W_+(\omega_+, t_+) \times W_-(\omega_-, t_-) \quad (5.12)$$

with $\omega_{\pm} = \omega_s \pm \omega_i$ and $t_{\pm} = \frac{t_s \pm t_i}{2}$ and two-dimensional chronocyclic Wigner

Figure 5.4 – Modified HOM interferometer. The addition of a frequency shift Ω in (at least) one of the input arms allows to probe more properties of the biphoton state.



functions defined thanks to the separability of the state as:

$$\begin{aligned}
 W_+(\omega_+, t_+) &= \frac{1}{\sqrt{2\pi}} \int d\omega'_+ \phi_{\text{spectral}} \left(\omega_+ + \frac{\omega'_+}{2} \right) \phi_{\text{spectral}}^* \left(\omega_+ - \frac{\omega'_+}{2} \right) e^{-i\omega'_+ t_+} \\
 W_-(\omega_-, t_-) &= \frac{1}{\sqrt{2\pi}} \int d\omega'_- \phi_{\text{PM}} \left(\omega_- + \frac{\omega'_-}{2} \right) \phi_{\text{PM}}^* \left(\omega_- - \frac{\omega'_-}{2} \right) e^{-i\omega'_- t_-}
 \end{aligned} \tag{5.13}$$

We can already notice some similarities between the expression of W_- and the HOM coincidence rate given in equation (5.10). The introduction of a frequency shift Ω modifies the equation (5.1) for the creation operators before the beam splitter in the following manner:

$$\begin{aligned}
 \hat{a}_s^\dagger(\omega_s) &= \frac{\hat{a}_1^\dagger(\omega_s + \Omega/2) + i\hat{a}_2^\dagger(\omega_s + \Omega/2)}{\sqrt{2}} e^{-i\omega_s \tau} \\
 \hat{a}_i^\dagger(\omega_i) &= \frac{i\hat{a}_1^\dagger(\omega_i - \Omega/2) + \hat{a}_2^\dagger(\omega_i - \Omega/2)}{\sqrt{2}} e^{i\omega_i \tau}
 \end{aligned} \tag{5.14}$$

and further calculations show that equation (5.10) for the coincidence rate is transformed into:

$$P(\Omega, \tau) = \frac{1}{2} \left(1 - \frac{\int d\omega_- \phi_{\text{PM}}(\Omega + \omega_-/2) \phi_{\text{PM}}^*(\Omega - \omega_-/2) e^{-i\omega_- \tau}}{\int d\omega_- |\phi_{\text{PM}}(\omega_-/2)|^2} \right) \tag{5.15}$$

With the normalization $\int d\omega_- |\phi_{\text{PM}}(\omega_-/2)|^2 = 1$, the chronocyclic Wigner function W_- is thus directly retrieved from the generalized HOM measurement:

$$W_-(\omega_-, t_-) = \frac{1 - 2P(\omega_-, t_-)}{\sqrt{2\pi}} \tag{5.16}$$

To illustrate this, we take the example of a Gaussian pump beam with a waist w_p , small with respect to the length L of the waveguide arriving with an incidence angle θ . We allow the beam to impinge at a location z_0 which may be different

from the center of the sample. Starting from equation (2.38), the phase-matching dependent part ϕ_{PM} of the JSA reads:

$$\phi_{\text{PM}}(\omega_-) = \sqrt{\pi} w_z \exp \left[- \left(\frac{\omega_- - \omega_-^{(0)}}{\Delta\omega_-} \right)^2 \right] e^{i\omega_- t_-^{(0)}} \quad (5.17)$$

with $t_-^{(0)} = z_0/\bar{v}_g$. We assume the angle of incidence small enough to approximate $w_z = w_p \cos\theta \approx w_p$ so that the width of the function is $\Delta\omega_- = 2\bar{v}_g/w_p$ and it is centered at $\omega_-^{(0)} = (k \sin\theta - k_{\text{deg}})\bar{v}_g \approx (\theta - \theta_{\text{deg}})\bar{v}_g \omega_p/c$. With this choice of pump beam, the W_- Wigner function can be drastically simplified to:

$$W_-(\omega_-, t_-) = \pi w_p^2 \exp \left[- 2 \left(\frac{\omega_- - \omega_-^{(0)}}{\Delta\omega_-} \right)^2 \right] \exp \left[- 2 \left(\frac{t_- - t_-^{(0)}}{\Delta t_-} \right)^2 \right] \quad (5.18)$$

with $\Delta t_- = 2/\Delta\omega_- = w_p/\bar{v}_g$. We see that this is a Gaussian Wigner function centered at point $t_-^{(0)}$ and $\omega_-^{(0)}$, of widths $\Delta\omega_-$ and Δt_- that corresponds to the representation of a coherent state (see Fig. 5.5).

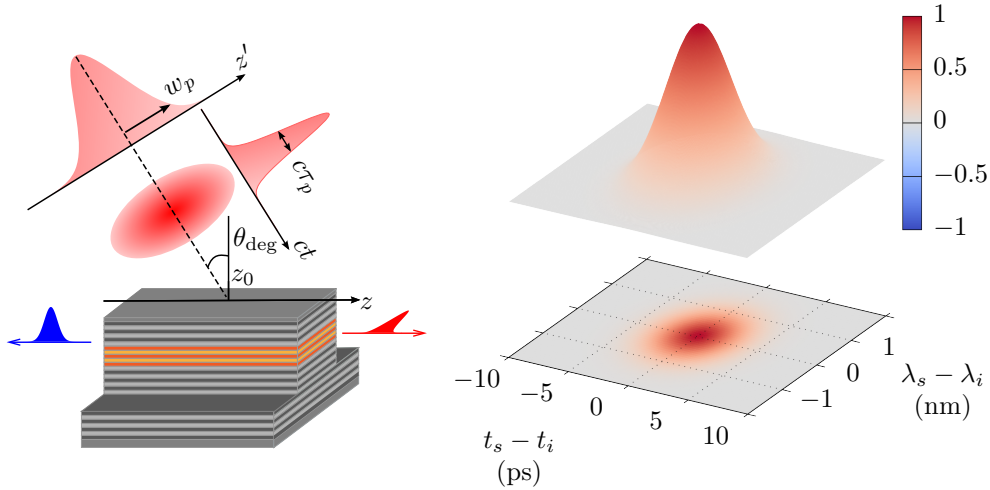


Figure 5.5 – Pumping scheme (left) and CWF W_- (right) corresponding to a ‘Gaussian’ state. The pump beam impinging at $z_0 = 0$, the center of the waveguide, with the angle $\theta = \theta_{\text{deg}}$, the state is centered at $t_- = 0$ and $\omega_- = 0$. The widths along both axis are related to the waist w_p of the pump beam. As long as $W(\omega_s, \omega_i, t_s, t_i)$ can be factorized according to equation (5.12), the pulse duration plays no role in the form of $W_-(\omega_-, t_-)$. The usual HOM interference curve corresponds to the slice along the axis $t_s - t_i$ at degeneracy ($\lambda_s - \lambda_i = 0$). We plot $\sqrt{2\pi}W_-$ to easily identify the value 1 as a dip of full depth (bunching at the beamsplitter) and -1 as a full bump (antibunching) - see equation (5.16). In this simulation $w_p = 200 \mu\text{m}$, $L = 2 \text{ mm}$, $\lambda_p = 775 \text{ nm}$ and $\tau_p = 3.5 \text{ ps}$.

Thus, in this situation, a shift of the pump spot z_0 is equivalent to a displacement along the t_- axis of the phase space while a change in the angle of incidence θ of the pump beam corresponds to a shift of the state along the Ω axis. *The*

original HOM experiment in fact corresponds to measuring the slice of W_- along the axis t_- at the zero frequency offset $\omega_- = 0$. Even though the birefringence of the device may offset the arrival time of one photon with respect to the other, for our sample and the typical lengths we are dealing with ($L = 2$ mm) this effect is negligible as demonstrated by the central position of W_- in figure 5.5. If the angle of incidence of the pump beam is different from θ_{deg} , the center of state will be offset from $\omega_- = 0$ and the usual HOM experiment will exhibit a dip of reduced visibility, as we have already commented in the previous section and illustrated in figure 5.2(a).

This technique thus offers new perspectives to engineer and characterize more exotic states than the ones we showed in chapters 3 and 4. For example with two identical beams impinging at z_a and z_b a superposition of 2 coherent states displaced along the τ axis is obtained. In the limit $|t_-^{(a)} - t_-^{(b)}| \gg \Delta t_-$, *i.e.* $|z_a - z_b| \gg w_p$, such states are almost orthogonal, representing a superposition of two distinct coherent states (Schrödinger cat-like states). This situation is depicted in figure 5.6. In the right figure, the two peaks correspond to the effect of the individual beams at z_a and z_b , while the fringes between them indicate the existence of a well defined coherence. Indeed, if the pump beams are generated with two independent lasers with no phase relation, this fringes would not exist, and we would get the representation of a statistical mixture of the two coherent states. If a decoherence mechanism is present, these fringes would blur, resulting in a state of reduced purity [162, 163]. The technique is thus very general and can be used to characterize states that are mixed although the origin of the decoherence can be due to the environment or from a lack of separability in terms of ω_- and ω_+ variables*. In the latter case, the state can still be decomposed as a sum over separable states $W(\omega_s, t_s, \omega_i, t_i) = \sum_k c_k W_+^k(\omega_+, t_+) \times W_-^k(\omega_-, t_-)$, just like the Schmidt decomposition usually performed for the JSA with ω_s and ω_i [165]. The interference will be the results of the different contributions in the superposition.

The link we have made between the HOM experiment and the W_- function is a very good illustration that two-photon experiments cannot be simply considered as an interference between two photons as discussed *e.g.* in reference [166][†]. Indeed in the usual HOM experiment (see the slice at $\omega_- = 0$ in figure 5.6), if only one of the two beams is present, we would observe a dip of full visibility, offset from $t_- = 0$, because we do not pump at the center of the waveguide. However, when both pump beams impinge, the former dips have a depth reduced by two and an additional dip of full visibility arises between them, even though no pair is 'generated' in the center of the waveguide.

Figure 5.7 illustrates another example of state that can be generated. In this case a superposition of states along the axis ω_- is obtained by pumping the device with 2 different angles of incidence θ_a and θ_b , impinging at the same point z_0 . In this case quasi-orthogonality is obtained for $|\omega_-^{(a)} - \omega_-^{(b)}| \gg \Delta\omega_-$, *i.e.* $|\theta_a -$

*An example of non-trivial HOM interference for such non separable states can be found in the experiment reported in [164].

[†]In this reference, an interference is observed even though the optical path delay between the photons is compensated only after the beamsplitter.

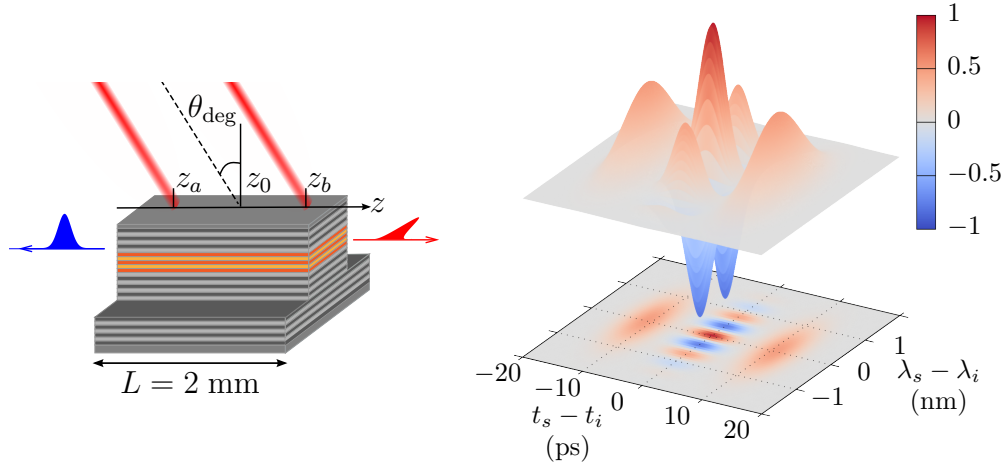


Figure 5.6 – Left: pumping scheme to obtain a Schrödinger cat-like state along t_- . Right: CWF W_- of the corresponding biphoton state. In this example the sample is pumped at two different locations z_a and z_b separated by the same distance ($500 \mu\text{m}$) from the center z_0 of the waveguide. The two beams have $w_p = 200 \mu\text{m}$, $\lambda_p = 775 \text{ nm}$ and $\tau_p = 3.5 \text{ ps}$.

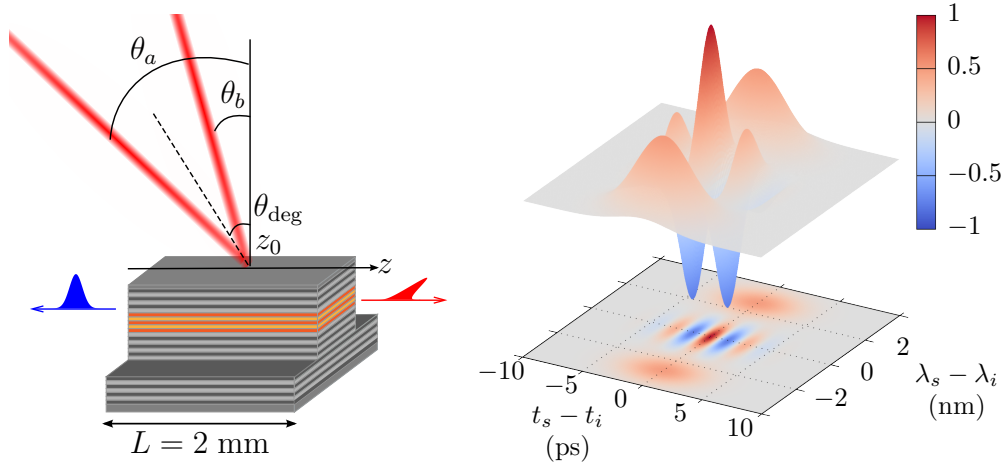


Figure 5.7 – Left: pumping scheme to produce a Schrödinger cat-like state along ω_- with two beams impinging at the same location but with different angles of incidence. Right: CWF W_- of the corresponding biphoton state. The pump beams are tilted symmetrically with respect to the degeneracy angle ($\theta_{a,b} = \theta_{\text{deg}} \mp \delta\theta$) so that $\lambda_-^{(a,b)} = -\frac{8\pi c}{\omega_p^2} \omega_-^{(a,b)} = \pm 2615 \text{ pm}$. The two beams have $w_p = 200 \mu\text{m}$, $\lambda_p = 775 \text{ nm}$ and $\tau_p = 3.5 \text{ ps}$.

$|\theta_b| \gg \frac{2c}{\omega_p w_p}$ (for small angles). While the cat state in time introduced in the previous paragraph has never been observed (to our knowledge), the state encoded along ω_- we are describing here has already been produced and sent to a HOM interferometer where fringes analogous to the ones we show in figure 5.7 along the axis t_- at $\omega_- = 0$ have been measured by Ou and Mandel themselves [167].

We can imagine the engineering of more exotic states using complex configurations of pump beams. As an illustration, we choose a so-called compass state (see figure 5.8), a superposition of four coherent states presenting interesting applications in quantum metrology, as pointed out in [168, 169]. In order to obtain such state, a set of four different pump beams is required, combining the pumping schemes previously described. Two pairs of beams impinge at two different points separated by a distance $|z_a - z_b|$, each pair consisting in two beams symmetrically tilted with respect to the degeneracy angle as shown in figure 5.8.

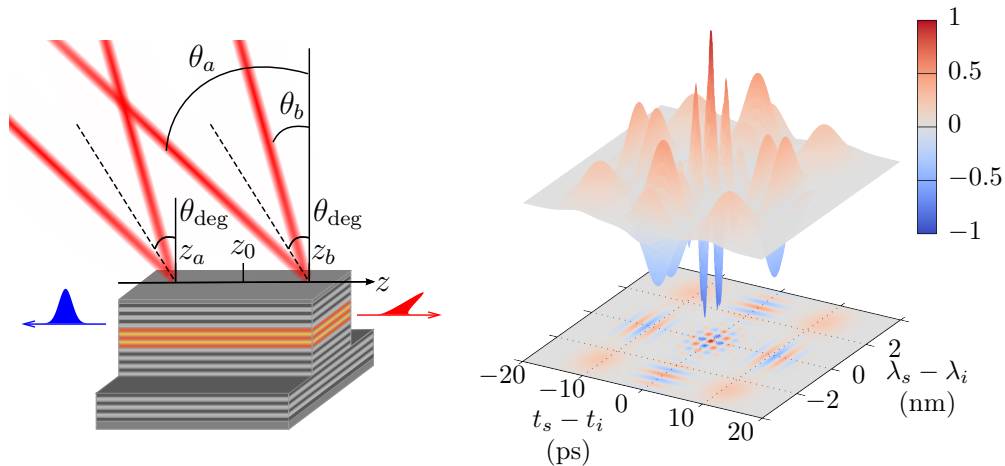


Figure 5.8 – Left: pumping scheme to generate a compass state. Right: CWF W_- of the corresponding biphoton state. Two pairs of beams are used, impinging at two different locations z_a and z_b separated by the same distance ($500 \mu\text{m}$) from the center z_0 of the waveguide. In each pair, the pump beams are tilted symmetrically with respect to the degeneracy angle ($\theta_{a,b} = \theta_{\text{deg}} \pm \delta\theta$) so that $\lambda_-^{(a,b)} = -\frac{8\pi c}{\omega_p^2} \omega_-^{(a,b)} = \mp 2615 \text{ pm}$. In this simulation $w_p = 200 \mu\text{m}$, $L = 2 \text{ mm}$, $\lambda_p = 775 \text{ nm}$ and $\tau_p = 3.5 \text{ ps}$.

Although the measurement of the state along the t_- axis is already a well established technique [170, 171, 134, 172, 164], the characterization of the state along the orthogonal axis ω_- is still an open issue. We can mention the work of Olislager *et al.* where EOMs are used to implement the manipulation of the state in the frequency domain [73, 74]. For the frequency range relevant for our device, state of the art EOMs in the telecom-band could work if the state is not too broad. Indeed, a modulation of 40 GHz correspond to a wavelength shift of 360 pm, which would allow a partial characterization of the simple state at degeneracy pictured in figure 5.5 or of the central fringes of the compass state in figure 5.8. In situations where the state is broader, the measurement will demand a displacement of the state itself along ω_- as a coarse frequency shift and a fine control would be provided by optical modulation.

The development of techniques to probe the time-energy properties of the biphoton is a subject of intense research. Indeed the implementation of the generalized HOM interferometer for the reconstruction of a Wigner function [140] has

been recently implemented in an experiment [173]. In this reference a CW beam is used to pump a Periodically Poled Potassium Titanyl Phosphate (PPKTP) crystal for the generation of the biphoton state. The monochromaticity of the pump allows to simplify the experimental scheme, since the issue of shifting the frequency over a large range can be overcome by changing the frequency of the pump. In fact, in their implementation, heating or cooling the crystal modifies the phase-matching conditions and is tantamount to changing the frequency difference between the photons of the pair. This first proof-of-principle is encouraging for our own implementation in pulsed regime.

5.3 Spatial shaping of the pump beam with a spatial light modulator

In order to get a full flexibility for the biphoton state engineering we have decided to implement a shaping of the pump beam with a Spatial Light Modulator (SLM). This has also been the occasion to start a collaboration with the team of Robert Boyd and Ebrahim Karimi in Ottawa (Canada). This type of device consists in a matrix of liquid crystals whose orientation can be set pixel by pixel and reprogrammed on demand. The orientation of the crystals affects the local birefringence thus providing a tool to control the phase and/or intensity distributions of the impinging beam [174]. Applications of SLM include the generation of optical tweezers [175] or adaptive optics [176]. In the spectral domain, they are used for pulse shaping [177] where a pulse is dispersed, modified with the SLM and recombined with a dispersive element, thus allowing to control its chronocyclic properties and to correct potential anomalies such as chirp.

In our case, we are interested in the spatial shaping of the beam. The approach we adopt consists in imaging the SLM onto the device as sketched in figure 5.9, performing a simultaneous phase and intensity masking [174]. The polarization direction of the pump beam and its intensity are controlled by a half-wave plate and a polarizer. Indeed to modulate the beam, the polarization has to be linear and oriented along the plane containing the incident and reflected beams. The beam is then expanded by a telescope (lenses L_1 and L_2) to cover the whole active surface of the modulator. The model we have chosen is a LetoTM from the company Holoeye for its excellent resolution, namely 1920×1080 pixels of size $6.4 \times 6.4 \mu\text{m}^2$. It is a reflective, phase-only modulator based on the LCoS technology (Liquid Crystals on Silicon). Since a non negligible part of the beam energy is unaltered by the SLM, we superimpose to the modulation mask, the phase of a prism (or blazed grating) in order to deflect the interesting part of the reflected beam into the first order of diffraction. This also allows to modulate the intensity of the beam: since we image the SLM, we can remove some areas by simply not applying the prism phase at these locations so the corresponding energy will remain in the zeroth order (see figure 5.10). The selection of the first order is done with a 4f-line: a first lens L_3 allows the spatial filtering of the modulated beam in the Fourier plane with an adjustable iris. In order to maximize the efficiency, the separation

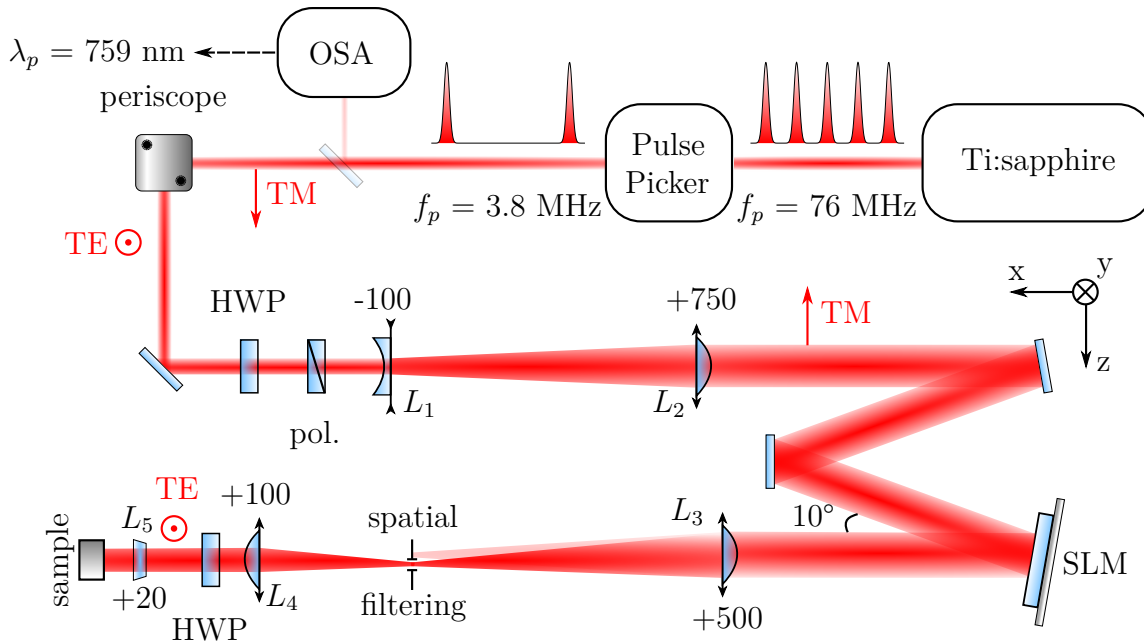


Figure 5.9 – Setup for the spatial shaping of the pump beam with an SLM (simultaneous phase and intensity masking). See the text for details. Focal lengths are given in millimeters.

between the zeroth and first orders must be as small as possible. The second lens L_4 allows the imaging of the selected intensity onto the waveguide. The telescope which is formed by these two lenses also allows to adjust the size of the beam to the length of the waveguide. An additional half-wave plate allows to set the polarization of the beam to TE in order to maximize the photon pair production. Finally, a cylindrical lens L_5 is still present to focus the beam on the ridge in the transverse direction y .

Several precautions must be taken to ensure the correct behavior of the device. We have already mentioned the correct orientation of the polarization. The amount of aberrations must also be kept to a minimum by using lenses with not too short focal lengths. To maintain a high modulation efficiency and avoid astigmatism, the angle between the incident and the reflected beams at the SLM must be below 20° . Concerning the SLM itself, the display is addressed with eight bits allowing 256 different settings for each pixel. The voltage control value that has to be applied to obtain a given phase retardance depends on various parameters, such as the central wavelength of the beam or the temperature of the room. A correct calibration of the device allows to obtain a linear phase response as testified by the Ronchi test [178] shown in figure 5.11. This graph is obtained by measuring the power in the first order (or in order -1) when applying a mask with pairs of stripes of alternating values, each pair consisting of one stripe with a constant zero value (no phase added to the beam) and the other addressed with a varying gray level value (G.L.) – see figure 5.12. The power $P_1(\text{G.L.})$ that is measured in the first order allows to retrieve the actual phase retardance $\Phi(\text{G.L.})$ applied by

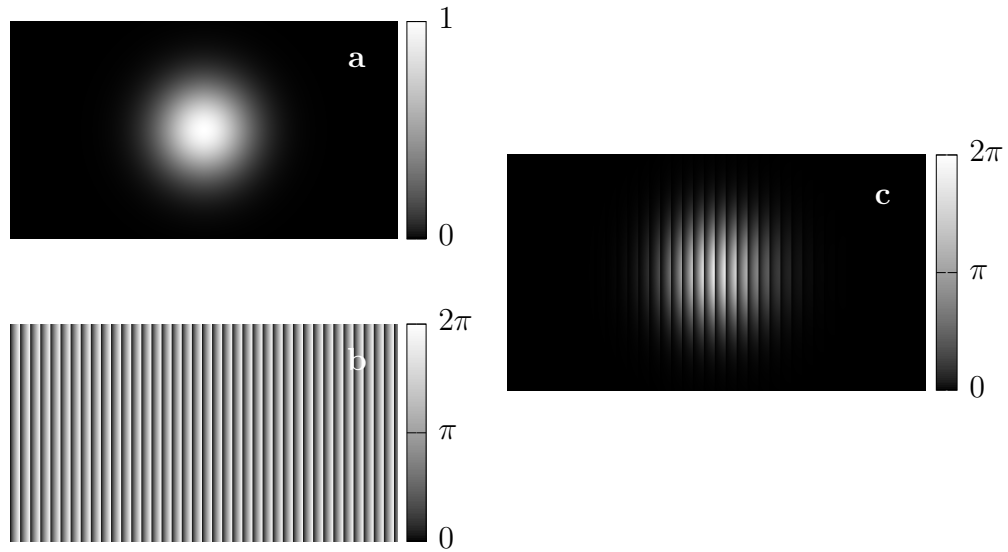


Figure 5.10 – Principle of phase and intensity masking with a phase-only SLM. (a): desired intensity profile (Hermite-Gaussian beam). (b): blazed phase grating (prism) applied to the SLM to deflect the impinging intensity into the first order of diffraction. (c): phase mask applied to the SLM to obtain the Hermite-Gaussian beam after spatial filtering of the first order of diffraction. The exact encryption procedure of the mask is detailed in reference [174].

the whole device to the beam according to:

$$P_1(\text{G.L.}) \propto [1 - \cos \Phi(\text{G.L.})] \quad (5.19)$$

We also see from figure 5.11 that if the stripes have a width of only one pixel, the cross-talk between them prevents the phase from reaching 2π . Therefore the phase encoded with a mask having high spatial frequencies will not be faithful. Other characterization procedures can be applied in order to make sure that the phase is correctly encoded locally and to compensate for any defect of flatness of the display [179, 180].

The efficiency of the device is limited by two factors: the pixelation of the device with 200 nm of interpixel gap, leading to a 93% fill-factor, is responsible for the diffraction of the beam into higher orders, even when the device is not addressed. This, along with the reflectivity of the back mirror is limiting the usable power to 75% of its initial value. The resolution and the possible cross-talk between the pixels on the other hand limit the diffraction efficiency *i.e.* the ability to send all the energy in the first order with a mask corresponding to a phase blazed grating (a prism) and more generally to give the correct phase to the beam with an arbitrary mask. According to the specifications of the manufacturer, our SLM is supposedly the best in class with almost 85% of the usable power sent into the first order of diffraction with a blazed grating of 16 levels and less than

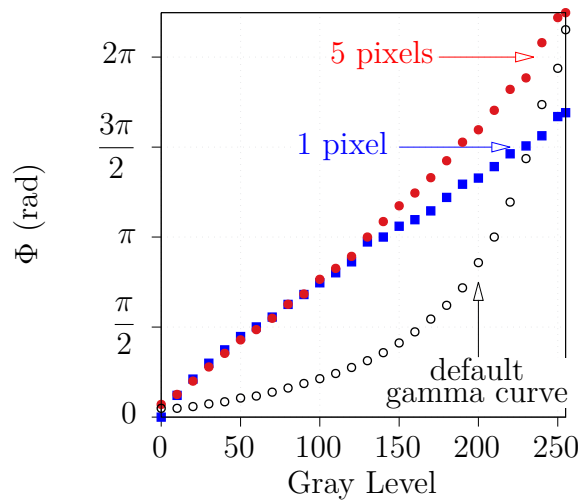


Figure 5.11 – Phase retardance Φ obtained at $\lambda_p = 760$ nm as a function of the gray level applied to the SLM. This result is obtained via a Ronchi test with stripes 1-pixel and 5-pixels wide. The lower slope with the 1 pixel experiment is due to the cross-talk between the liquid-crystals. An almost linear modulation is obtained compared to the default calibration which is adapted for 633 nm (measured with stripes of 5 pixels width).

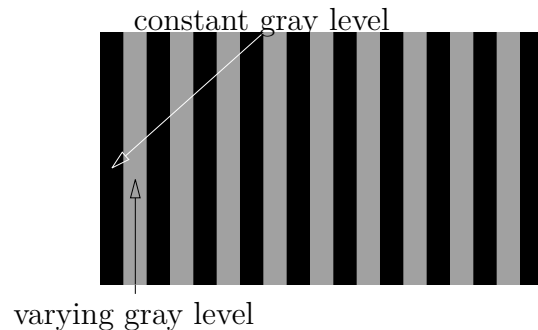


Figure 5.12 – Phase mask applied to the SLM to perform a Ronchi test. Stripes with a constant gray level value alternate with stripes whose gray level is varied while the intensity diffracted in the first order is measured. This allows the calibration of the phase applied by the SLM for a given gray level.

1% in the other orders at a 633 nm central wavelength. These performances would lead to a total light utilization efficiency, *i.e.* the ratio between the power before the SLM and the power selected after the SLM, of almost 64%. Even though the beam shape is well controlled (see figure 5.13), the total efficiency obtained up to now is limited to 16.6%. Work is in progress to improve this figure of merit in order to be able to measure the biphoton state with this pumping scheme.

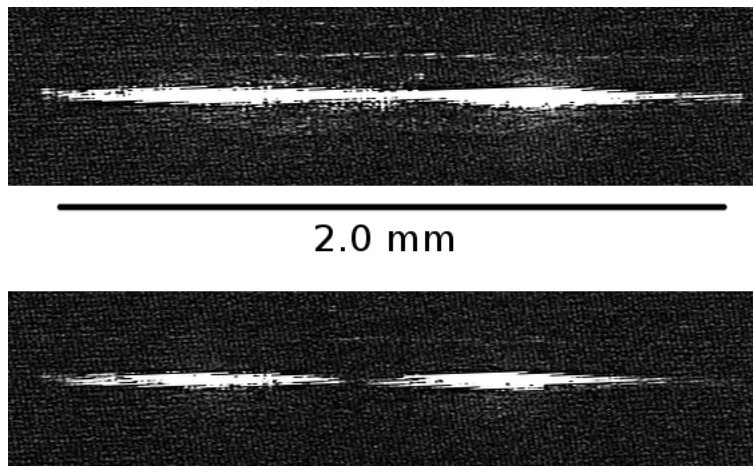


Figure 5.13 – CCD pictures of the sample illuminated by the Ti:sapphire laser beam spatially shaped by the SLM. Top: Laguerre-Gaussian LG_{01} beam focused by the cylindrical lens on the waveguide. Bottom: Hermite-Gaussian HG_{10} beam.

5.4 Conclusion

In this chapter, the two-photon interference at a beam-splitter has been theoretically treated, with examples of interferences that we have linked to the form of the JSA. With our colleagues from the theory team, we have introduced a generalization of the Hong-Ou-Mandel interferometer with a frequency displacement in addition to the temporal displacement, opening the way to the generation and characterization of more exotic two-photon states with our source, for example Schrödinger cat-like and compass states.

For the production and engineering of these states, we are implementing a new pumping scheme with a Spatial Light Modulator to control the spatial phase and amplitude of the pump beam.

A part of the work presented in this chapter has been published in [181].

Part III

Controlling entanglement in polarization and frequency

Chapter 6

Joint Spectral Amplitude engineering for maximal entanglement in polarization

So far we have focused on only one of the two possible interactions which can occur in our device. In fact, as described in chapter 1, for a given angle of incidence, two concurrent phase-matching conditions can be fulfilled: one in which the photon emitted towards the positive z (the signal) is Transverse Electric (TE)-polarized (with its idler twin Transverse Magnetic (TM)-polarized) and one in which it is TM-polarized (with its twin TE-polarized). We have named these two processes interaction HV and VH , respectively. This feature of our source enables the production of Bell states in polarization, a result which has been experimentally demonstrated by our team in [86]. Starting from this demonstration, we present a theoretical model taking into account the pertinent physical parameters having an impact on the entanglement in polarization. In particular we link the level of generated entanglement to the Joint Spectral Amplitude (JSA) of the biphoton state and we show how to optimize the pumping scheme to get the maximum entanglement in polarization.

6.1 Generation of Bell states in polarization

The debate between Einstein, Podolsky, Rosen [182] and Bohr [183] on the completeness of quantum mechanics and the possible existence of local hidden variables was formalized by Bell [9] and Clauser, Horne, Shimony and Holt [10]. These works allowed to identify an inequality that could be checked through experiments to settle the debate [6, 7, 8]. For two qubits, a maximal violation of the Bell-CHSH inequality is provided by the Bell states [184]:

$$\begin{aligned} |\Psi^\pm\rangle &= \frac{|HV\rangle \pm |VH\rangle}{\sqrt{2}} \\ |\Phi^\pm\rangle &= \frac{|HH\rangle \pm |VV\rangle}{\sqrt{2}} \end{aligned} \tag{6.1}$$

where H and V stand for horizontal or vertical polarization respectively and where the first and second members of each ket represent the property of particle 1 and 2, respectively. Such states, after being used to test the foundations of quantum mechanics, constitute today one of the major building blocks for quantum information and communication [185, 12, 1, 26].

Coming back to our device and considering only fundamental spatial modes, the general biphoton state, *i.e.* in the absence of spectral filtering and selection on polarization, reads:

$$|\psi\rangle = \frac{1}{\sqrt{2}} \iint d\omega_s d\omega_i \phi_{HV}(\omega_s, \omega_i) |\omega_s, H\rangle |\omega_i, V\rangle + \frac{1}{\sqrt{2}} \iint d\omega_s d\omega_i \phi_{VH}(\omega_s, \omega_i) |\omega_s, V\rangle |\omega_i, H\rangle \quad (6.2)$$

where $\phi_{HV}(\omega_s, \omega_i)$ and $\phi_{VH}(\omega_s, \omega_i)$ are the JSAs of the HV and VH process, respectively, and where we have explicitly extracted the $1/\sqrt{2}$ factor from the normalization of the JSAs. Assuming a plane wave and a monochromatic pump beam impinging with an angle θ , the previous expression simplifies into:

$$|\psi\rangle = \frac{|\omega_s, H\rangle |\omega_i, V\rangle + e^{i\varphi} |\omega'_s, V\rangle |\omega'_i, H\rangle}{\sqrt{2}} \quad (6.3)$$

with φ a possible phase offset between $\phi_{HV}^\theta(\omega_s, \omega_i)$ and $\phi_{VH}^\theta(\omega'_s, \omega'_i)$. In this state the frequency degree of freedom is labeling the process introducing a *which-path* information. This information must be removed in order to obtain a maximal entanglement. In other words, we want:

$$|\psi\rangle = |\omega_s \omega_i\rangle \otimes \frac{|HV\rangle + e^{i\varphi} |VH\rangle}{\sqrt{2}} \quad (6.4)$$

Such state cannot be obtained by pumping the device with a beam impinging with a single angle of incidence θ due to the residual birefringence of the waveguide. Having $\omega_s = \omega'_s$ and $\omega_i = \omega'_i$ is equivalent to $\omega_+^{HV} = \omega_+^{VH} = \omega_p$, which is satisfied by energy conservation, and $\omega_-^{HV} \equiv \omega_s - \omega_i = \omega_-^{VH} \equiv \omega'_s - \omega'_i$ which is achievable with an adaptation of the phase-matching. Indeed, we recall that for the HV interaction, $\omega_-^{(0)} = \omega_p(\sin \theta - \sin \theta_{\text{deg}}) \bar{v}_g / c$ and the degeneracy angle has been defined in equation (2.26) to be $\theta_{\text{deg}} = \sin^{-1}(\frac{n_{\text{TE}} - n_{\text{TM}}}{2})$. For the VH interaction, the polarization of the signal and the idler are exchanged and degeneracy is therefore achieved with the opposite angle $-\theta_{\text{deg}}$. Thus, pumping interaction HV with an angle θ_{HV} and interaction VH with an angle θ_{VH} , the condition to produce a Bell state reduces to:

$$\underbrace{\omega_-^{HV}}_{\omega_p(\sin \theta_{HV} - \sin \theta_{\text{deg}}) \frac{\bar{v}_g}{c}} - \underbrace{\omega_-^{VH}}_{\omega_p(\sin \theta_{VH} + \sin \theta_{\text{deg}}) \frac{\bar{v}_g}{c}} = 0 \quad (6.5)$$

which simplifies into $\sin \theta_{HV} - \sin \theta_{VH} = 2 \sin \theta_{\text{deg}}$. All the angles involved in our study being small this condition can be approximated to:

$$\theta_{HV} - \theta_{VH} = 2\theta_{\text{deg}} \quad (6.6)$$

Therefore, pumping the device with two different angles with a separation $2\theta_{\text{deg}}$ between them allows to remove the correlation between the spectral and polarization degrees of freedom, as shown in figure 6.1(d). In other words, we render the two processes indistinguishable, except for the polarization of the photons. We must however apply a spectral filtering to remove the photons that are produced, for example, with the HV process but with the θ_{VH} angle and vice-versa. We illustrate this scheme in figure 6.1 in the more general situation of a pulsed Gaussian beam choosing the simple case of degeneracy angles *i.e.* $\theta_{HV} = \theta_{\text{deg}}$ and $\theta_{VH} = -\theta_{\text{deg}}$. We see that this choice of angles allows to overlap the Joint Spectral Intensities (JSIs) of the two processes of interest and to obtain a frequency degenerate $|\Psi^+\rangle$ Bell state. We also identify the photons that must be removed by spectral filtering. Changing the angles while keeping the $2\theta_{\text{deg}}$ separation between them allows to maintain the overlap since the JSIs will only be shifted along the ω_- axis. With this more general case, we would obtain frequency non-degenerate Bell states $|\Psi^+\rangle$. We note that the other Bell states can be obtained with the addition and a convenient adjustment of a half-waveplate on one of the output arms for the Φ^\pm states, or with a suitable birefringent element for the Ψ^- state [36].

6.2 Characterization of the state

We have identified the general scheme to generate a Bell state in polarization which consists in pumping the device with two angles and applying a frequency filtering. The automatic separation of the photons eases their characterization with respect to the case of collinear sources. In this geometry, we can easily perform the polarization tomography of the state to reconstruct its density matrix $\hat{\rho}$ by placing polarization analyzers in each output arm [186]. The single counts and the coincidences between the two detectors are recorded for 16 different settings of these analyzers. Indeed with two polarization qubits, the Hilbert space is described by the basis $\{|HH\rangle, |HV\rangle, |VH\rangle, |VV\rangle\}$, and therefore the density matrix has 16 components. The sets of coincidence measurements allows, in principle, to reconstruct it via an inversion procedure. Nevertheless, like any inversion algorithm, the sensitivity to the noise can be problematic, leading to reconstructed density matrices that are not even physical, with purity $\text{Tr}(\hat{\rho}^2)$ above 1 for example. To circumvent this problem, different methods can be applied such as the maximum likelihood technique where the physical density matrix that resembles the most to the matrix obtained by inversion is identified. Debates are still ongoing regarding the best methods to use [187] and on the errors that can arise from the quantities derived from the reconstructed matrices [188]. During the PhD thesis of Adeline Orioux [189] and in the experiment reported in [86] demonstrating the generation of Bell states with the source, the maximum likelihood technique was used to reconstruct the density matrix from the polarization tomography measurements.

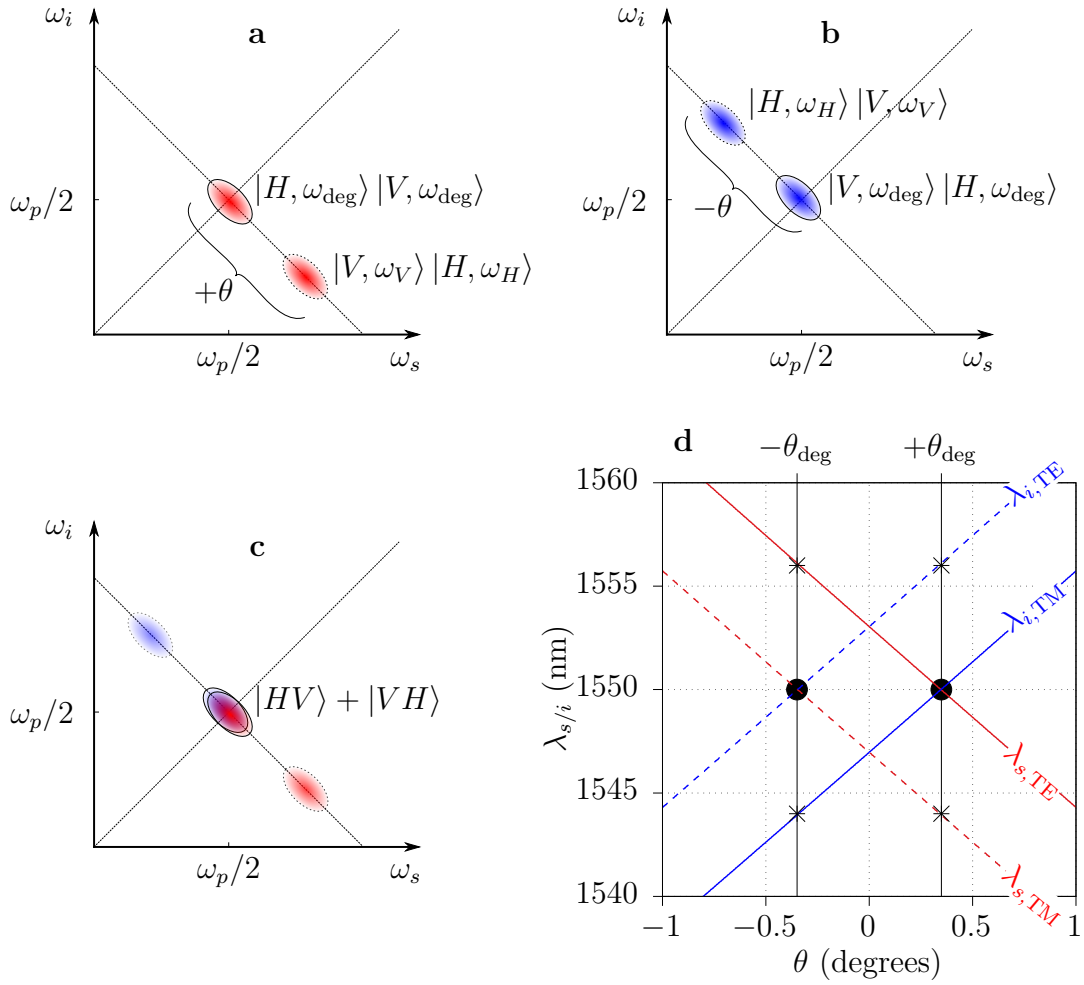


Figure 6.1 – Sketch of the JSIs illustrating the scheme to obtain biphoton states that are maximally entangled in polarization. (a) and (b): JSIs describing the spectral properties of the pairs emitted by the two processes for a pump beam with an angle of incidence $+\theta_{\text{deg}}$ and $-\theta_{\text{deg}}$, respectively. (c): pumping the device with both angles and removing the non-degenerate pairs allows to obtain a Ψ^+ Bell state, since the two processes are now indistinguishable from a spectral point of view. (d): Tuning curves of the photons as a function of the angle of incidence θ , describing the same situation. The black disks and the crosses indicate the photons we select and the ones we remove, respectively.

Pumping the device with two angles θ_{deg} and $-\theta_{\text{deg}}$, filtering out the frequency non-degenerate pairs, the output state can be written:

$$\begin{aligned}
 |\psi\rangle = \frac{1}{\sqrt{2}} \iint d\omega_s d\omega_i & \left[\phi_{HV}^{+\theta_{\text{deg}}}(\omega_s, \omega_i) \hat{a}_H^\dagger(\omega_s) \hat{a}_V^\dagger(\omega_i) \right. \\
 & \left. + \phi_{VH}^{-\theta_{\text{deg}}}(\omega_s, \omega_i) \hat{a}_V^\dagger(\omega_s) \hat{a}_H^\dagger(\omega_i) \right] |\text{vac}\rangle
 \end{aligned} \tag{6.7}$$

where $\phi_{HV}^{+\theta_{\text{deg}}}$ ($\phi_{VH}^{-\theta_{\text{deg}}}$, respectively) is the JSAs of the HV (VH) process pumped with the angle $+\theta_{\text{deg}}$ ($-\theta_{\text{deg}}$). We have not yet made any assumption on the form

of the pump beam with the exception of the angles of incidence. Since only polarization measurements are performed in the tomography, the density matrix that is reconstructed is not, in fact, the full density matrix $|\psi\rangle\langle\psi|$ of our biphoton but the reduced density matrix $\hat{\rho}$ expressed in the basis $\{|HH\rangle, |HV\rangle, |VH\rangle, |VV\rangle\}$. This is obtained by taking the trace of $|\psi\rangle\langle\psi|$ over the frequency degrees of freedom. Starting from the expression (6.7), this amounts to:

$$\hat{\rho} = \frac{1}{2} \begin{pmatrix} |HH\rangle & |HV\rangle & |VH\rangle & |VV\rangle \\ 0 & \dots & \dots & 0 \\ \vdots & \alpha_{+\theta_{\text{deg}}} & \beta & \vdots \\ \vdots & \beta^* & \alpha_{-\theta_{\text{deg}}} & \vdots \\ 0 & \dots & \dots & 0 \end{pmatrix} \quad (6.8)$$

where the diagonal elements $\alpha_{+\theta_{\text{deg}}}$ and $\alpha_{-\theta_{\text{deg}}}$ represent the relative efficiencies of the two processes and the antidiagonal element β indicates the overlap between them:

$$\alpha_{+\theta_{\text{deg}}} = \iint d\omega_s d\omega_i \left| \phi_{HV}^{+\theta_{\text{deg}}}(\omega_s, \omega_i) \right|^2 \quad (6.9)$$

$$\alpha_{-\theta_{\text{deg}}} = \iint d\omega_s d\omega_i \left| \phi_{VH}^{-\theta_{\text{deg}}}(\omega_s, \omega_i) \right|^2 \quad (6.10)$$

$$\beta = \iint d\omega_s d\omega_i \phi_{HV}^{+\theta_{\text{deg}}}(\omega_s, \omega_i) \phi_{VH}^{-\theta_{\text{deg}}}{}^*(\omega_s, \omega_i) \quad (6.11)$$

The purity of the state is given by $\text{Tr}[\hat{\rho}^2] = (\alpha_{+\theta_{\text{deg}}}^2 + \alpha_{-\theta_{\text{deg}}}^2 + 2|\beta|^2)/4$. Making use of the fact that $\alpha_{+\theta_{\text{deg}}} + \alpha_{-\theta_{\text{deg}}} = 2$, a pure state is obtained with $\alpha_{+\theta_{\text{deg}}} \alpha_{-\theta_{\text{deg}}} = |\beta|^2$. Of course if we were to use two pump beams from independent lasers with the same power, the overlap term β would vanish because of the independent phase fluctuations which would be reflected in $\phi_{HV}^{+\theta_{\text{deg}}}$ and $\phi_{VH}^{-\theta_{\text{deg}}}$, leading to a mixed state. Our target state is obtained when all the terms have equal weights, namely:

$$\alpha_{+\theta_{\text{deg}}} = \alpha_{-\theta_{\text{deg}}} = |\beta| = 1 \quad (6.12)$$

In fact, if the two processes have the same strength, *i.e.* $\alpha_{+\theta_{\text{deg}}} = \alpha_{-\theta_{\text{deg}}} = 1$, then the joint spectrum overlap $|\beta|$ corresponds to the *concurrence* $\mathcal{C} = |\beta|$, a commonly used entanglement estimator [190, 191, 192]*. The phase of β , corresponding to φ in equation (6.4), does not feature in \mathcal{C} because it does not contribute to nor does it degrade the entanglement of the state. For example if this phase is 0, we obtain the $|\Psi^+\rangle$ Bell state while with a π -phase, we get the $|\Psi^-\rangle$ state, both states being maximally entangled. In fact in many experiments, this phase is not well controlled which results in a reduced fidelity to the $|\Psi^+\rangle$ state, even though the state is strongly entangled, a reason to discourage the use of the fidelity to estimate the quality of the state that is obtained. In our scheme, φ is set by the position of the pump beams on the waveguide. Indeed if the beam is offset from the center of the sample, the signal and the idler photons will not travel through the same length before escaping the waveguide, which will result in a non zero φ

*A demonstration is given in appendix C.

because of the birefringence of the sample. This is indeed equivalent to placing a birefringent element in one of the output arms. As long as the position of the spot of the pump beam is not moving during the course of the experiment, φ will not fluctuate and the entanglement will be preserved.

In conclusion, to obtain a maximally entangled state in polarization, we need to set up the two laser pumps such that $\alpha_{+\theta_{\text{deg}}} = \alpha_{-\theta_{\text{deg}}}$ in order to excite the two processes with the same strength, and at the same time make them as indistinguishable as possible to maximize the value of $\mathcal{C} = |\beta|$. We note that the existence of spectral correlations between signal and idler does not necessarily result in a degradation of the produced entanglement as long as they are identical for both processes, as can be seen in the definition of β .

6.3 Optimizing the entanglement in polarization

A very simple way to produce two coherent pump beams impinging at $\pm\theta_{\text{deg}}$ consists in passing the pump beam through the center of a Fresnel bi-prism (see Fig. 6.2). The angle of each prism can be chosen such that it deviates the pump beam entering the first face with a normal incidence by θ_{deg} . This is the solution which has been adopted in the experiment reported in [86].

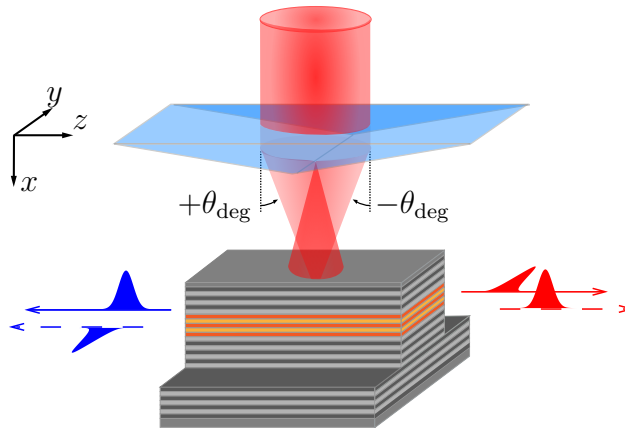


Figure 6.2 – Scheme to produce pairs of photons entangled in polarization at degenerate frequencies. A Fresnel bi-prism is used to obtain two coherent beams impinging on the source at the degeneracy angles.

Unfortunately, if the initial beam is Gaussian, the two beams emerging from the bi-prism will have opposite half-Gaussian shapes. Beams of this form will never overlap perfectly because of chirality. This has an impact on the JSAs of the two processes. Figures 6.3(a) and (c) report the the JSIs $|\phi_{HV}^{+\theta_{\text{deg}}}|^2$ and $|\phi_{VH}^{-\theta_{\text{deg}}}|^2$ of the two processes with the bi-prism located at the optimal distance from the source. For a beam of waist $w_p = 600 \mu\text{m}$ at the location of the biprism and a degeneracy angle at $\lambda_p = 759.4 \text{ nm}$ amounting to $\theta_{\text{deg}} = 0.349^\circ$, this distance is 4 cm. We see that the JSIs overlap almost perfectly. However their phase distributions do not exactly correspond, which is revealed when looking at the Joint Temporal

Intensities (JTIs) $|\tilde{\phi}_{HV}^{+\theta_{\text{deg}}}|^2$ and $|\tilde{\phi}_{VH}^{-\theta_{\text{deg}}}|^2$ represented in figures 6.3(b) and (d). The shape of each JTI corresponds to the refracted half-Gaussian with oscillations due to the diffraction at the junction of the prisms. A which-path information is present due to the non-optimal overlap of the two beams resulting in a degradation of the entanglement.

Here we propose an alternative solution which consists in shearing the incident pump beam into two replicas with a specific type of grating (see Fig. 6.4), designed to diffract the incident intensity only into its first order with an angle $\pm\theta_{\text{deg}}$. This is possible if the grating transmission function $t_d(z)$ is:

$$t_d(z) = \cos\left(\frac{2\pi z}{d}\right) \quad (6.13)$$

where $d \sim \frac{\lambda}{\theta_{\text{deg}}}$ is the period of the grating. In this case a normally incident Gaussian beam with amplitude $S(z, \theta = 0)$ and waist w_p is transformed into two beams

$$S^\pm(x, z) = \frac{1}{2}S(z - z_\pm, \pm\theta_{\text{deg}}) \quad (6.14)$$

with

$$z_\pm = \pm \tan \theta_{\text{deg}} (x - x_G) = \pm \frac{\lambda}{d} (x - x_G) \quad (6.15)$$

where x_G is the position of the grating. We thus create two copies of the incident Gaussian beam impinging onto the waveguide with opposite angles $\pm\theta_{\text{deg}}$. In this case, the optimal overlap is obtained if the grating is as close as possible to the waveguide. This kind of grating can be realized with an intensity mask corresponding to the absolute value of the sinusoidal transmission factor and a phase mask to account for the alternating sign. They are at the basis of lateral shearing interferometry, a technique of wavefront reconstruction which consists in interfering replicas of the initial beam [193].

For a quantitative analysis, figure 6.5 reports the value of the concurrence $\mathcal{C} = |\beta|$ obtained in the two cases as a function of the distance between the optical element producing the two pumping beams and the waveguide. In the case of the bi-prism, the concurrence saturates at 84%, corresponding to the optimal overlap between the 2 *half-Gaussians* emerging from it. The situation is different with the grating since we can obtain almost unity concurrence when its distance from the samples tends to zero. Even if in the present experimental set-up it may be difficult to reduce the distance to less than 1 cm, this already results in a photon pair concurrence of 98%, corresponding to an improvement of 17% with respect to the bi-prism configuration. We assumed a spectral filtering over a ± 2.95 nm spectral window corresponding to half the separation between the degenerated and non-degenerated JSAs. We note that tighter filtering conditions also allow to increase the value of the concurrence but at the expense of the brightness of the source. Another possibility would consist in using the bi-prism with an initial beam that is shaped to adopt a top-hat profile. In this case we would not suffer from an asymmetry and the experimental difficulty would consist, just as with the bi-prism alone, in finding the position which maximizes the overlap between the beams.

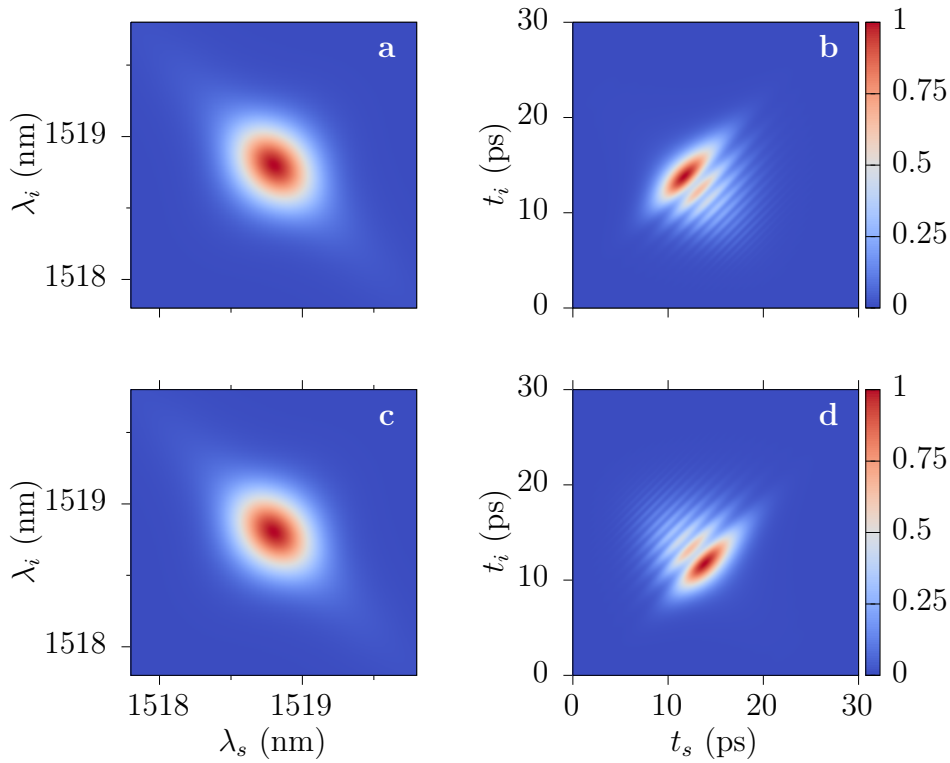


Figure 6.3 – Frequency-time properties of the photon pairs obtained with the bi-prism scheme for the production of polarization Bell states. The biprism is placed at the optimal distance from the waveguide to maximize the entanglement of the state. (a): JSI of the HV process obtained by pumping the device at $+\theta_{\text{deg}}$. (b): corresponding JTI. (c): JSI of the VH process pumped with the angle $-\theta_{\text{deg}}$. (d): corresponding JTI.

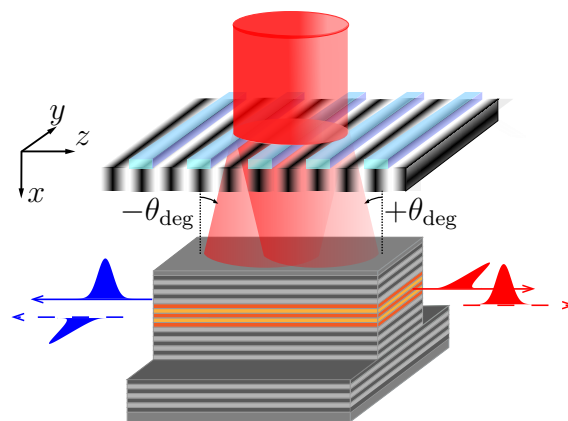


Figure 6.4 – Scheme to produce pairs of photons entangled in polarization at degenerate frequencies with a grating. In this case, the pump beam is sheared into two beams impinging onto the sample at the degeneracy angles.

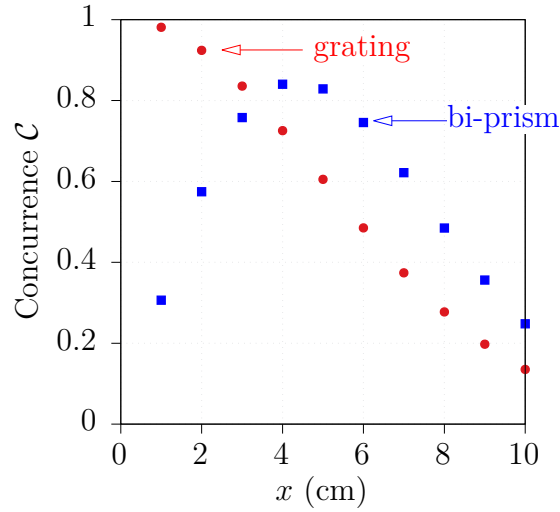


Figure 6.5 – Numerical simulation of the concurrence as a function of the distance x between the source and the grating (red circle) or the source and the bi-prism (blue square). The simulations are performed for the real structure on a spectral window of ± 2.95 nm around the degeneracy wavelength $2 \times \lambda_p$. The initial pump beam has a waist $w_p = 600$ μm , a pulse duration $\tau_p = 3.5$ ps and central wavelength $\lambda_p = 759.4$ nm. The spatial profile of the pump beam on the ridge is obtained with Fresnel diffraction.

Other mechanisms than the spatial shape of the pump beam can be detrimental for the entanglement quality of the produced state; for example the slightly different transverse profiles of the TE and TM modes. Nevertheless, in the experiment [86] and in this work, the photons are coupled in single mode fibers which act like spatial filters and cancel this effect. We note that in the absence of mode filtering we may have to consider SPDC processes which involve photons with higher order spatial modes.

Another phenomenon, which we considered in the calculation of the JSAs, is the timing difference between TE and TM photons at the output of the source because of the difference in group velocities of the photons and the length of the sample. This is negligible in our case since the group velocities of the TE and TM modes are almost identical (for degenerate photons) and the length of our sample is rather short ($L \approx 2$ mm). With other sources of polarization Bell states however, such as the ones based on Periodically Poled Lithium Niobate (PPLN) waveguides and whose typical lengths reach several centimeters, a stage of compensation is necessary to prevent which-path information to deteriorate the entanglement in polarization [194, 195].

Up to now in this analysis, we have neglected the reflectivity of the facets of the waveguide. The following section is devoted to their influence on the entanglement in polarization.

6.4 Influence of the reflectivities of the facets

We resume the treatment of section 2.3 where we assumed the presence of polarizers on each side of the source, so that we could look at only one polarization on each arm. Relaxing this hypothesis, the creation operator of the signal mode is transformed, after n round-trips in the sample, into:

$$\begin{aligned} \hat{a}_{s,\sigma}^\dagger(\omega) \rightarrow & e^{ik_\sigma L/2} \left(r_\sigma^{2n+1} e^{ik_\sigma 2nL} \hat{a}_{i,\sigma}^\dagger(\omega) \right. \\ & + t_\sigma \sum_{j=0}^n \left[r_\sigma^2 e^{ik_\sigma 2L} \right]^j \hat{b}_{s,\sigma}^\dagger(\omega) \\ & \left. + t_\sigma r_\sigma e^{ik_\sigma L} \sum_{j=0}^n \left[r_\sigma^2 e^{ik_\sigma 2L} \right]^j \hat{b}_{i,\sigma}^\dagger(\omega) \right) \end{aligned} \quad (6.16)$$

The first two terms are unchanged compared to the treatment of section 2.3. The additional last term describes the photons emitted in the device in a given direction but leaving the source on the opposite side. After a sufficient number of round-trips ($n \rightarrow \infty$), all the energy will be extracted from the cavity, *i.e.* the term in $\hat{a}_{i,\sigma}^\dagger(\omega)$ in the previous equation becomes negligible. The original creation operator then reads:

$$\hat{a}_{s,\sigma}^\dagger(\omega) = f_\sigma^\rightarrow(\omega) \hat{b}_{s,\sigma}^\dagger(\omega) + f_\sigma^\leftarrow(\omega) \hat{b}_{i,\sigma}^\dagger(\omega) \quad (6.17)$$

with f_σ^\rightarrow and f_σ^\leftarrow , the transmission and reflection Fabry-Perot functions:

$$f_\sigma^\rightarrow(\omega) = e^{ik_\sigma L/2} \frac{t_\sigma}{1 - r_\sigma^2 e^{ik_\sigma 2L}} \quad (6.18)$$

$$f_\sigma^\leftarrow(\omega) = r_\sigma e^{ik_\sigma L} f_\sigma^\rightarrow(\omega) \quad (6.19)$$

In the perspective of producing Bell states in polarization we cannot neglect anymore the second term of equation (6.17). Applying the scheme described in the previous sections with two suitable pumping angles and the spectral filtering of non-degenerate photons, and expressing the occupation of the modes with kets of the form $|sH, sV, iH, iV\rangle$, the general state reads:

$$\begin{aligned} |\psi\rangle = & \frac{1}{\sqrt{2}} \iint d\omega_H d\omega_V \left(\phi_{HV}^{+\theta_{\text{deg}}}(\omega_H, \omega_V) f_H^\rightarrow(\omega_H) f_V^\rightarrow(\omega_V) |\omega_H, 0, 0, \omega_V\rangle \right. \\ & + \phi_{VH}^{-\theta_{\text{deg}}}(\omega_V, \omega_H) f_H^\rightarrow(\omega_H) f_V^\rightarrow(\omega_V) |0, \omega_V, \omega_H, 0\rangle \\ & + \phi_{HV}^{+\theta_{\text{deg}}}(\omega_H, \omega_V) f_H^\leftarrow(\omega_H) f_V^\leftarrow(\omega_V) |0, \omega_V, \omega_H, 0\rangle \\ & + \phi_{VH}^{-\theta_{\text{deg}}}(\omega_V, \omega_H) f_H^\leftarrow(\omega_H) f_V^\leftarrow(\omega_V) |\omega_H, 0, 0, \omega_V\rangle \\ & + \phi_{HV}^{+\theta_{\text{deg}}}(\omega_H, \omega_V) f_H^\leftarrow(\omega_H) f_V^\rightarrow(\omega_V) |0, 0, \omega_H, \omega_V\rangle \\ & + \phi_{VH}^{-\theta_{\text{deg}}}(\omega_V, \omega_H) f_H^\rightarrow(\omega_H) f_V^\leftarrow(\omega_V) |0, 0, \omega_H, \omega_V\rangle \\ & + \phi_{HV}^{+\theta_{\text{deg}}}(\omega_H, \omega_V) f_H^\rightarrow(\omega_H) f_V^\leftarrow(\omega_V) |\omega_H, \omega_V, 0, 0\rangle \\ & \left. + \phi_{VH}^{-\theta_{\text{deg}}}(\omega_V, \omega_H) f_H^\leftarrow(\omega_H) f_V^\rightarrow(\omega_V) |\omega_H, \omega_V, 0, 0\rangle \right) \end{aligned} \quad (6.20)$$

The first two terms of this expression correspond to the situation where both photons are directly transmitted by the facets and are thus closely related to the general expression we have obtained ignoring the facets (see equation (6.7)). The next two terms describe photons which are both subject to an odd number of reflections before being transmitted. They can thus contribute to the entanglement in polarization of the states depending on their spectral and temporal overlap. The last four terms of the expression correspond to photons that leave the device by the same side.

In the following we assume a perfect detection and collection in order to focus on the direct implications of the Fabry-Perot on the state. Doing so, we discard the last four terms of the former equation to reach a simpler expression of the state, similar to equation (6.7):

$$|\psi\rangle = \frac{1}{\sqrt{2}} \iint d\omega_s d\omega_i \left[\phi_{HV}(\omega_s, \omega_i) \hat{b}_H^\dagger(\omega_s) \hat{b}_V^\dagger(\omega_i) + \phi_{VH}(\omega_s, \omega_i) \hat{b}_V^\dagger(\omega_s) \hat{b}_H^\dagger(\omega_i) \right] |\text{vac}\rangle \quad (6.21)$$

where ϕ_{HV} and ϕ_{VH} are effective JSAs for the production of a $|HV\rangle$ or $|VH\rangle$ pair, respectively, which are expressed:

$$\phi_{HV}(\omega_s, \omega_i) = \phi_{HV}^{+\theta_{\text{deg}}}(\omega_s, \omega_i) f_H^\rightarrow(\omega_s) f_V^\rightarrow(\omega_i) + \phi_{VH}^{-\theta_{\text{deg}}}(\omega_i, \omega_s) f_H^\leftarrow(\omega_s) f_V^\leftarrow(\omega_i) \quad (6.22)$$

$$\phi_{VH}(\omega_s, \omega_i) = \phi_{VH}^{-\theta_{\text{deg}}}(\omega_s, \omega_i) f_V^\rightarrow(\omega_s) f_H^\rightarrow(\omega_i) + \phi_{HV}^{+\theta_{\text{deg}}}(\omega_i, \omega_s) f_V^\leftarrow(\omega_s) f_H^\leftarrow(\omega_i) \quad (6.23)$$

The reduced density matrix of this state takes an identical form to the one we have computed for perfectly transmissive facets – see equation (6.8) – with:

$$\alpha_{HV} = \iint d\omega_s d\omega_i |\phi_{HV}(\omega_s, \omega_i)|^2 \quad (6.24)$$

$$\alpha_{VH} = \iint d\omega_s d\omega_i |\phi_{VH}(\omega_s, \omega_i)|^2 \quad (6.25)$$

as the diagonal elements, and:

$$\beta = \iint d\omega_s d\omega_i \phi_{HV}(\omega_s, \omega_i) \phi_{VH}^*(\omega_s, \omega_i) \quad (6.26)$$

as the anti-diagonal term characterizing the overlap between the two effective processes. The target state is again obtained when $\alpha_{HV} = \alpha_{VH} = |\beta| = 1$ and in particular the best entanglement in polarization is achieved by maximizing the value of the concurrence $\mathcal{C} = |\beta|$. We saw in section 5.1 that the visibility of the Hong-Ou-Mandel (HOM) dip was not necessarily reduced by the partially reflective facets, as long as the TE and TM Fabry-Perot resonances coincide where the JSI takes a significant value. This is also the case for the production of Bell states in polarization, the concurrence \mathcal{C} reaching 1 when these resonances are in phase since the JSAs in equations (6.22) and (6.23) are then indistinguishable apart from polarization. With the Fabry-Perot transmissions we measured with our sample at room temperature [148], the overlap of the Fabry-Perot combs is

not optimal, and assuming a pump made of two Gaussian beams impinging with $+\theta_{\text{deg}}$ and $-\theta_{\text{deg}}$ and overlapping perfectly at the center of the waveguide with a waist $w_p = 600 \mu\text{m}$, the concurrence saturates at $\mathcal{C} = 80.4\%$.

If the source is to belong to a fully integrated photonic circuit, with production, processing and detection of the photons in a single integrated chip, the absence of facets implies that we should not suffer from any reduction of the entanglement due to such Fabry-Perot mechanisms. Nevertheless, even if the source is used as a single element, means exist to prevent the degradation of the concurrence. Our team is collaborating with Xavier Lafosse (LPN, Marcoussis) to deposit mirrors on waveguide facets [196]. A work is currently ongoing to adapt this technique for the deposition of anti-reflection coatings on the facets of our samples in order to suppress any Fabry-Perot effect. Preliminary simulations suggest that reflectivities as low as 0.01% can be expected.

6.5 Conclusion

In this chapter we have detailed the production of Bell states in polarization with the counterpropagating phase-matching scheme. In particular we have shown that a frequency-degenerate $|\Psi^+\rangle$ Bell states can be produced by pumping the device with two opposite angles of incidence and with a suitable frequency filtering on the photons. We have linked the level of entanglement in polarization to the overlap of the JSAs describing the two processes HV and VH occurring in the source and have proposed a pumping scheme to optimize it with a spatial shearing grating. Finally, we have studied the influence of the facets' reflectivities.

A part of the work presented in this chapter has been published in [197].

Perspectives

The variety of topics treated in this work allow to open several perspectives. We have already presented in section 4.4 a proposal to extend the technique of reconstruction of the photons' joint spectrum in order to include the phase. In section 5.2, we presented methods to generate more exotic states. We mentioned the deposition of anti-reflective coatings on the facets in order to suppress their potentially undesired reflectivity. If reflective coatings are deposited instead, the comb structure due to the Fabry-Perot cavity would be reinforced. A theoretical work is in progress with the theory team to clarify the question of whether such states would correspond to the proposal of Gottesman, Kitaev and Preskill [198], with a strong potential for fault-tolerant quantum computing. Hereafter we present three promising perspectives under study in our team.

Photonics Circuits The control of the biphoton state as well as the techniques for characterizing it pave the way towards the use of our source in more complex photonic circuits. Manipulation of photons on chip is already well established on glass [34] and silicon [199, 55] platforms. More recently this issue started to be tackled also on the III-V platform. These efforts have led to an integrated HOM interferometer [46] and to antibunching experiments with embedded quantum dots sources [200, 201]. Our team has also started to work on this hot topic with the development of integrated beam-splitters, one of the fundamental building blocks for on-chip generation and manipulation of photons. Different strategies can be adopted to implement this operation. We have chosen the Multi-Mode Interferometers (MMIs) because of their strong tolerance to fabrication inaccuracies. Figure 6.6 reports a Scanning Electron Microscope (SEM) picture of one of our devices. The MMI has two long input arms which can be pumped with beams of different spatial profiles, allowing the generation of photon pairs with the desired properties. Photons impinging on the splitter are heralded by the detection of their twins on the opposite side. The deposition of electrodes or a shift of the pump beam spots on the input arms would allow to implement the optical path delay required for the HOM experiment. After classical characterizations meant to characterize the optical losses and splitting ratio of the sample, experiments are now in progress to check the behavior of the device in the single photon regime. Indeed, an integrated Hanbury Brown and Twiss experiment [202] can be performed by pumping only one input arm and recording counts on the output arms.

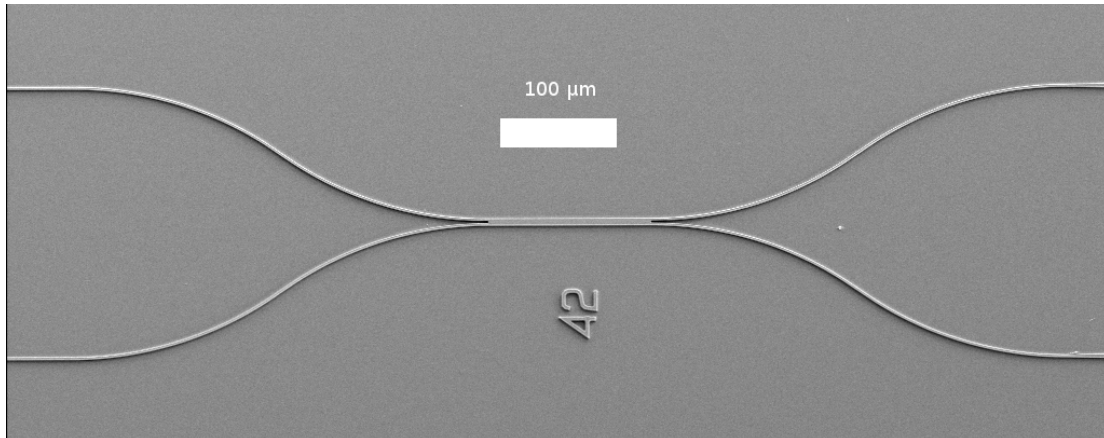


Figure 6.6 – Integrated beam-splitter observed with a scanning electron microscope. The MMI can be seen in the center at the junction of all four arms. The length of the coupling region is suitably chosen to obtain a 50/50 coupling ratio at the wavelengths of interest.

Integration of the pump laser Our current pumping procedure with an external Ti:sapphire laser does not allow yet for a compact device. We thus do not exploit the optoelectronic capabilities of the III-V platform. Indeed our team has recently demonstrated a *monolithic* source of photon pairs in a collinear geometry (the photon pairs and the pump beam are emitted in the same direction), the device being electrically injected to lase on the pump mode and consequently generate photon pairs by SPDC [58].

With our phase-matching geometry however, an edge emitting laser is not suitable and the natural route leads to Vertical-Cavity Surface-Emitting Lasers (VCSELs). In those lasers, active layers formed by quantum dots or quantum wells are sandwiched in a microcavity delimited by two (top and bottom) Bragg mirrors. An aperture for the optical field and the charge carriers is defined by the controlled oxidation of an AlAs layer so that the laser beam is emitted from the surface (towards the top). In electrically injected versions, this configuration allows to get very efficient lasers with a low threshold and high optical power, especially when VCSELs are combined in arrays.

In particular, the devices presented in [203] with their large rectangular apertures are of great interest to compact our source. Electrically pumped VCSELs emitting at 850 nm are demonstrated with extreme aspect ratio apertures such as $5 \times 125 \mu\text{m}^2$ or $10 \times 200 \mu\text{m}^2$. This fits our needs concerning the pump beam profile to pump the nonlinear waveguide over a long length and a narrow width. The devices even seem to perform better than VCSELs with identical active area but with square or circular apertures shapes, due to a better heat management and carrier transport.

In a subsequent article [204], the same authors showed that a coherent emission can also occur at two symmetric angles, a situation comparable to our scheme to generate polarization entangled states. The accurate control of the angle of emission might be an issue.

While these results are encouraging, the advantages of our source are only unveiled when we can control both spatial and temporal properties of the pump beam which is a great challenge, notably with compact semiconductor devices [205]. A compromise between a fully monolithic device and one with an external laser could be provided by Vertical-External-Cavity Surface-Emitting Lasers (VECSELs) that are related to VCSELs with no top Distributed Bragg Reflector (DBR) so that the cavity extends in free space, giving an extra control on the laser emission.

From our experience with the collinear source, we also know that the doping is responsible for additional losses in the telecom band. It is thus very likely that the active layers and the nonlinear interaction volume will not coincide. In essence, keeping the versatility of the source of counterpropagating photons and improving its compacity will be a great challenge.

Bridging single photons and optomechanics A last perspective of this work is the study of the interaction of optical and mechanical resonances in our devices. This will be done in the framework of a collaboration with I. Favero, expert in optomechanics, working in MPQ. Indeed, it has been shown that for the GaAs/AlAs family of materials, a resonator structure based on distributed Bragg reflectors and designed to confine photons can also efficiently confine acoustic phonons [206]. Following these ideas, it has recently been shown that a picosecond strain pulse injected into a vertical-cavity surface-emitting laser induces a modulation of the lasing intensity at frequencies up to 40 GHz, corresponding to the frequency of confined phonons [207]. Preliminary numerical simulations show very similar properties on our ridge-microcavity, making this device a promising candidate to explore quantum state transfer between optical photons and micro-mechanical phonons. We could envision using the phonons to store information, create optical delays or implement logic gates, opening the way to a new class of on-chip processors of optical information.

Conclusion

Polarization has certainly been the most used degree of freedom for quantum optics. The exploration and control of other properties of light is now a major axis of development along with the miniaturization of quantum technologies.

The source at the heart of this work presents many advantages which make it a very convenient device to demonstrate new techniques and a serious competitor in quantum photonics. Indeed, its room temperature operation does not necessitate cumbersome cryogenic systems; the emission of photons at wavelengths compatible with the telecommunication networks allows the transmission of the photons over long distance; finally, III-V semiconductor materials presents a strong potential for miniaturization, integrating the pump laser to get a monolithic device, thanks to their direct bandgap, or nesting the source in a fully functional photonic circuits. The most interesting aspect of our device is certainly its versatility for frequency-correlations engineering. Indeed the control of the frequency-time properties of photon pairs is of paramount importance especially for integrated devices where the addition of spectral filtering is not necessarily practical: on one hand for applications such as heralded single photon sources, correlations between the signal and idler frequencies may be undesired. On the other hand, the accurate engineering of these properties can be very beneficial for dense coding applications taking advantage of the high-dimensional frequency Hilbert space of the photon pairs. To verify this, fast, reliable and high resolution spectral characterization techniques are needed. This is a difficult task, requiring the characterization of the chronocyclic properties of pulses as with classical beams and of the correlations existing between the signal and the idler, both at a very low power regime.

In this thesis, we have developed a theoretical description of light generation with our device. We have highlighted the originality of the counterpropagating phase-matching scheme with a transverse pump, where all the fields involved in the SPDC process are separated outside the source. In particular we have developed an analytic description of the Joint Spectral Amplitude (JSA), the biphoton wavefunction describing all the spectral and temporal properties of the photons. Supported by numerical simulations, this analytic development takes into account the properties of the pump beam, and those of the device, especially the influence of the microcavity and the facets of the waveguide. We have also shown how to derive, from the expression of the JSA, the Joint Temporal Amplitude and the Chronocyclic Wigner Functions (CWFs), which can be more adapted to the description of the biphoton depending on the context of the study. Most importantly, this theoretical development leads to the identification of the parameters of the

pump beam allowing to engineer the frequency properties of the photons. With this source, the degree of frequency correlations can be modified by changing the spot size of the pump beam on the waveguide. Modifying the angle of incidence of the pump beam on the other hand allows to control the central wavelengths of the photons. Moreover, correlating the wavevectors of the pump with the frequency components of the pump pulse enables the production of uncorrelated photons with different bandwidths. Expressing the photon pairs' time-frequency properties in terms of CWFs, we have developed a general framework to describe states with arbitrary complexity which may be obtained with modifications of the spatial profile of the pump beams. In particular we have given examples of Schrödinger cat-like states and compass states.

The demonstration of the frequency-engineering with our device was made possible by the implementation of reliable characterization techniques. Compared to techniques where the JSI is reconstructed by recording coincidences between photons filtered by monochromators, the single-photon fiber spectrograph reconstructs the JSI over the full spectral window. This reduces the integration time required to get enough photons statistics and this allowed us check the degree of frequency correlations of our photons. Nevertheless, the duration of the experiment is still significant due to limitations imposed by the single-photon detection and to the strong losses induced by the fiber. Moreover this technique is not highly resolved because of the electronic jitters in the detection chains. We have thus introduced a new method based on the stimulation of the SPDC process. A monochromatic seed beam injected in the device acting as specific vacuum fluctuations in the signal mode, stimulates the emission of idler photons corresponding to a given slice of the JSA at the wavelength of the seed. Indeed the JSA plays the role of a response function, even for this stimulated nonlinear process. The idler power that is produced is sufficient to be detected and spectrally characterized with classical instruments. It is thus possible to reconstruct the JSI, slice by slice, in a shorter integration time, and with more resolution than previous techniques. This allowed us to resolve features in the JSI so far inaccessible. Our current implementation is limited to the norm the biphoton wavefunction, but we have analyzed the feasibility of a scheme sensitive to both phase and intensity of the JSA. Alternatively, we have theoretically shown that a generalized Hong-Ou-Mandel interferometer, where both the photons' frequency and arrival time difference are manipulated, is particularly suitable to reconstruct the generated biphoton state. We note that this technique is also accessible to non-parametric sources.

Finally, we have theoretically analyzed the production of Bell states in polarization. We have shown how entanglement between polarization *and* frequency can be detrimental to the quality of such state. Indeed the Fresnel bi-prism used in our first experimental demonstration introduced temporal which-path information, responsible for a level of entanglement lower than expected. We have proposed a solution based on a grating used in wavefront reconstruction technique to get an ideal situation where the entanglement is not limited by the pumping procedure itself and can thus be maximal in theory. We have also identified that the central

position of the spot of the pump beam is responsible for the phase φ in the maximally entangled state produced with our source: $|\Psi\rangle = \frac{1}{\sqrt{2}}(|HV\rangle + e^{i\varphi}|VH\rangle)$. We have finally shown the importance of the facets reflectivity on the level of entanglement in polarization.

The results of this work have pushed forward the comprehension of the generation of light with our sources and give means to characterize and engineer the states they generate. This thesis has allowed to develop many fruitful collaborations with theoreticians, leading to measurement tools already adopted by several groups and opening perspectives to engineer interesting states for quantum information.

Appendix A

Source sample

In this appendix, we give the nominal structure of our samples. Fourier-Transform Infra-Red (FTIR) measurements performed on the wafers allow to deduce the real structure through numerical simulations of the reflectivity with thicknesses h corrected according to $h_{\text{real}} = h_{\text{nominal}} \times (1 + \Delta h)$.

Number of periods	Role	Al content (%)	Thickness h (nm)
1	Substrate	0	
36	Bottom	90	70.8
	Bragg	35	50.1
1	Buffer	90	125.1
4	Core	25	129.1
	Core	80	104.3
1	Core	25	129.1
1	Buffer	90	125.1
14	Top	35	50.1
	Bragg	90	70.8
1	Cap	0	46.2

Nominal epitaxial structure for the wafers **88P14** (or 89P14) (January 2009) and **F3W083** (April 2015). Unless stated otherwise, the samples used in this thesis have been processed from the wafer 88P14.

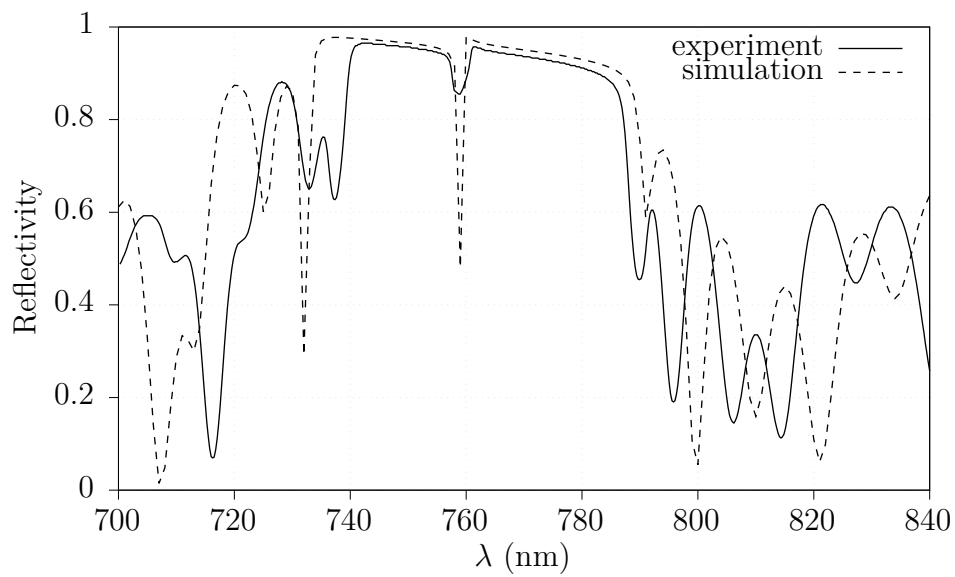


Figure A.1 – Reflectivity spectrum measured with the FTIR on wafer **88P14** (solid line) and numerically simulated with an adjustment $\Delta h = -2.4\%$ of the nominal thicknesses (dashed line).

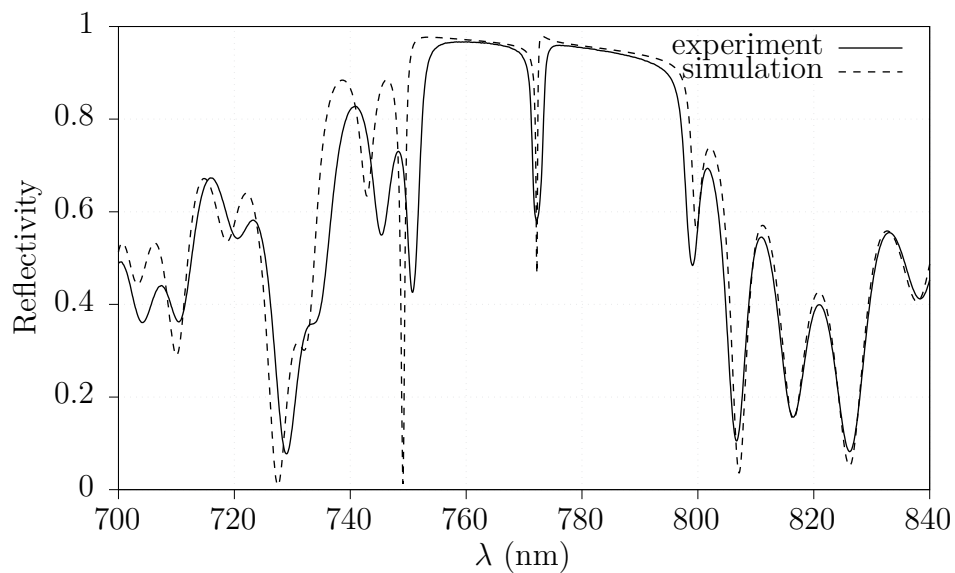


Figure A.2 – Reflectivity spectrum measured with the FTIR on wafer **F3W084** (solid line) and numerically simulated with an adjustment $\Delta h = -0.41\%$ of the nominal thicknesses (dashed line).

Appendix B

Characteristics of the Dispersion Compensating Fibers

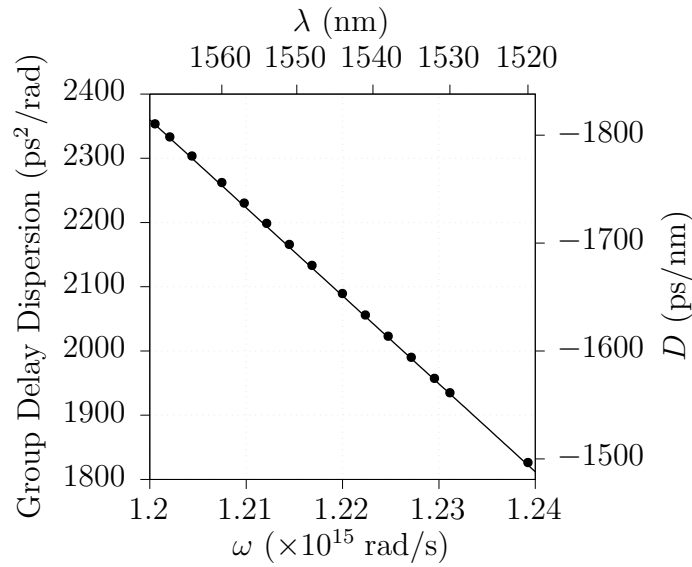


Figure B.1 – Group delay dispersion $\frac{\partial^2 k}{\partial \omega^2} \times l$ of the dispersion compensating fiber spool **DMV1000907** – with l the length of the fibers – measured (black dots) and linear fit to the experimental data (solid line): $\frac{\partial^2 k}{\partial \omega^2} \times l = 1.37 \times 10^{-35} \omega + 1.88 \times 10^{-20}$.

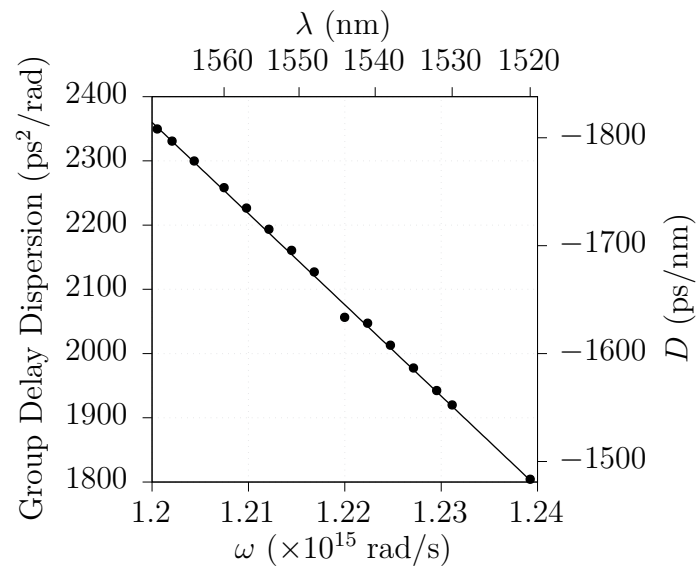


Figure B.2 – Group delay dispersion $\frac{\partial^2 k}{\partial \omega^2} \times l$ of the dispersion compensating fiber spool **DMV1000908** – with l the length of the fibers – measured (black dots) and linear fit to the experimental data (solid line): $\frac{\partial^2 k}{\partial \omega^2} \times l = 1.42 \times 10^{-35} \omega + 1.94 \times 10^{-20}$.

Appendix C

Concurrence and Joint Spectral overlap

We show in this appendix the equivalence between the Concurrence \mathcal{C} and the overlap $|\beta|$ between the JSAs of the processes HV and VH used in the production of Bell states in polarization (see chapter 6).

To give the definition of the concurrence $\mathcal{C}(\hat{\rho})$ of a given density matrix $\hat{\rho}$, we must construct the matrix:

$$\hat{R} = \hat{\rho}(\hat{\sigma}_y \otimes \hat{\sigma}_y)\hat{\rho}^*(\hat{\sigma}_y \otimes \hat{\sigma}_y) \quad (\text{C.1})$$

where $(\hat{\sigma}_y \otimes \hat{\sigma}_y)\hat{\rho}^*(\hat{\sigma}_y \otimes \hat{\sigma}_y)$ is the “spin-flipped” density matrix. Here $(\hat{\sigma}_y \otimes \hat{\sigma}_y)$ are Pauli matrices applied on both qubits, giving:

$$(\hat{\sigma}_y \otimes \hat{\sigma}_y) = \begin{pmatrix} & |HH\rangle & |HV\rangle & |VH\rangle & |VV\rangle \\ \left(\begin{array}{cccc} 0 & 0 & 0 & -1 \\ 0 & 0 & 1 & 0 \\ 0 & 1 & 0 & 0 \\ -1 & 0 & 0 & 0 \end{array} \right) & & & & \end{pmatrix} \quad (\text{C.2})$$

The concurrence is then obtained according to [191, 192]:

$$\mathcal{C}(\hat{\rho}) = \max\{0; \sqrt{r_1} - \sqrt{r_2} - \sqrt{r_3} - \sqrt{r_4}\} \quad (\text{C.3})$$

where $\sqrt{r_1} \geq \sqrt{r_2} \geq \sqrt{r_3} \geq \sqrt{r_4}$ are the square roots of the eigenvalues r_i of \hat{R} .

We recall the general form of the density matrix in our Bell states production scheme given by equation (6.8):

$$\hat{\rho} = \frac{1}{2} \begin{pmatrix} & |HH\rangle & |HV\rangle & |VH\rangle & |VV\rangle \\ \left(\begin{array}{cccc} 0 & \dots & \dots & 0 \\ \vdots & \alpha_+ & \beta & \vdots \\ \vdots & \beta^* & \alpha_- & \vdots \\ 0 & \dots & \dots & 0 \end{array} \right) & & & & \end{pmatrix} \quad (\text{C.4})$$

A few steps of calculation lead to the expression of \hat{R} :

$$\hat{R} = \frac{1}{4} \begin{pmatrix} |HH\rangle & |HV\rangle & |VH\rangle & |VV\rangle \\ 0 & \dots & \dots & 0 \\ \vdots & \alpha_+\alpha_- + |\beta|^2 & 2\alpha_+\beta & \vdots \\ \vdots & 2\alpha_-\beta^* & \alpha_+\alpha_- + |\beta|^2 & \vdots \\ 0 & \dots & \dots & 0 \end{pmatrix} \quad (\text{C.5})$$

whose eigenvalues are given by $r_{\pm} = \left(\frac{\sqrt{\alpha_+\alpha_-} \pm |\beta|}{2} \right)^2$. If the two processes HV and VH have equal strength, then $\alpha_+ = \alpha_- = 1$. The concurrence is then obtained by taking $\mathcal{C} = \sqrt{r_+} - \sqrt{r_-}$, leading to:

$$\boxed{\mathcal{C} = |\beta|} \quad (\text{C.6})$$

Appendix D

A note on softwares

Most of the graphs presented in this thesis have been plotted with Gnuplot. Concerning this tool, I am particularly indebted to Dr. Hagen Wierstorf and his website gnuplotting.org. The diverging colormap has been devised by Kenneth Moreland [208] providing an elegant alternative to the problematic jet/rainbow colormap. For sketches, I made an extensive use of The Gimp and Inkscape. The bibliography is managed with JabRef [209].

Appendix E

List of Publications and Conferences

Publications

- [1] G. BOUCHER, A. ECKSTEIN, A. ORIEUX, I. FAVERO, G. LEO, T. COUDREAU, A. KELLER, P. MILMAN and S. DUCCI, “Polarization-entanglement generation and control in a counterpropagating phase-matching geometry”, *Physical Review A*, vol. 89, p. 033815, March 2014.
- [2] A. ECKSTEIN, G. BOUCHER, A. LEMAÎTRE, P. FILLOUX, I. FAVERO, G. LEO, J. E. SIPE, M. LISCIDINI and S. DUCCI, “High-resolution spectral characterization of two photon states via classical measurements”, *Laser & Photonics Reviews*, vol. 8, p. L76–L80, June 2014.
- [3] C. AUTEBERT, G. BOUCHER, F. BOITIER, A. ECKSTEIN, I. FAVERO, G. LEO and S. DUCCI, “Photon pair sources in AlGaAs: from electrical injection to quantum state engineering”, *Journal of Modern Optics*, vol. 62, no. 20, p. 1739–1745, 2015.
- [4] G. BOUCHER, T. DOUCE, D. BRESTEAU, S. P. WALBORN, A. KELLER, T. COUDREAU, S. DUCCI and P. MILMAN, “Toolbox for continuous-variable entanglement production and measurement using spontaneous parametric down-conversion”, *Physical Review A*, vol. 92, p. 023804, August 2015.

Communications

- [1] **A. Orieux**, G. BOUCHER, A. ECKSTEIN, E. GALOPIN, A. LEMAÎTRE, C. MANQUEST, I. FAVERO, G. LEO and S. DUCCI, “A laser diode for integrated photon pair generation at telecom wavelength”, in *EOS Annual Meeting*, (Aberdeen, UK), September 2012.
- [2] A. ORIEUX, G. BOUCHER, A. ECKSTEIN, E. GALOPIN, A. LEMAÎTRE, C. MANQUEST, I. FAVERO, G. LEO and **S. Ducci**, “Semiconductor source

- of entangled photons at room temperature”, in *EOS Annual Meeting*, (Aberdeen, UK), September 2012. Invited.
- [3] A. ORIEUX, **G. Boucher**, A. ECKSTEIN, A. LEMAÎTRE, P. FILLOUX, I. FAVERO, G. LEO, T. COUDREAU, A. KELLER, P. MILMAN and S. DUCCI, “A semiconductor source of entangled photons at room temperature”, in *GDR - IQFA, third Colloquium*, (Grenoble (France)), November 2012. Poster.
- [4] A. ORIEUX, **G. Boucher**, A. ECKSTEIN, A. LEMAÎTRE, P. FILLOUX, C. MANQUEST, T. COUDREAU, I. FAVERO, G. LEO, A. KELLER, P. MILMAN and S. DUCCI, “Entangled photon generation on III-V semiconductor chip at room temperature”, in *SPIE Optics & Optoelectronics*, (Prague, Czech Republic), April 2013.
- [5] A. ORIEUX, G. BOUCHER, **A. Eckstein**, A. LEMAÎTRE, P. FILLOUX, I. FAVERO, G. LEO, T. COUDREAU, A. KELLER, P. MILMAN and S. DUCCI, “Bell states generation on a III-V semiconductor chip at room temperature”, in *CLEO/IQEC Europe*, (Munich, Germany), May 2013.
- [6] A. ORIEUX, **G. Boucher**, A. ECKSTEIN, A. LEMAÎTRE, P. FILLOUX, I. FAVERO, G. LEO, T. COUDREAU, A. KELLER, P. MILMAN and S. DUCCI, “Direct bell states generation on a III-V semiconductor chip at room temperature”, in *CLEO US*, (San Jose, USA), June 2013.
- [7] A. ORIEUX, G. BOUCHER, A. ECKSTEIN, A. LEMAÎTRE, P. FILLOUX, I. FAVERO, G. LEO and **S. Ducci**, “Sources semiconductrices de photons intriqués a temperature ambiante”, in *Journées Nationales d’Optique Guidée (JNOG 33)*, (Villetaneuse, France), July 2013. Invited.
- [8] **G. Boucher**, A. ORIEUX, A. ECKSTEIN, A. LEMAÎTRE, P. FILLOUX, I. FAVERO, G. LEO, T. COUDREAU, A. KELLER, P. MILMAN and S. DUCCI, “Génération directe d’états de Bell sur une puce semiconductrice III-V à température ambiante”, in *Coloq 2013*, (Villetaneuse, France), July 2013. Poster.
- [9] A. ORIEUX, G. BOUCHER, A. ECKSTEIN, A. LEMAÎTRE, P. FILLOUX, I. FAVERO, G. LEO and **S. Ducci**, “Semiconductor sources of quantum light at room temperature”, in *Workshop on Quantum Manipulation of Atoms and Photons (QMAP 2013)*, (Palaiseau, France), September 2013. Invited.
- [10] **A. Eckstein**, G. BOUCHER, A. LEMAÎTRE, P. FILLOUX, I. FAVERO, G. LEO, J. E. SIPE, M. LISCIDINI and S. DUCCI, “Classical difference frequency generation as a tool to characterize a quantum light source”, in *GDR-IQFA*, (Paris, France), November 2013. Poster.
- [11] G. BOUCHER, A. ECKSTEIN, A. LEMAÎTRE, M. LISCIDINI, J. SIPE, I. FAVERO, G. LEO and **S. Ducci**, “Quantum frequency correlation engineer-

- ing with a semiconductor cavity at room temperature”, in *SPIE Photonics West 2014*, (San Francisco, USA), February 2014. Invited.
- [12] **G. Boucher**, A. ECKSTEIN, A. LEMAÎTRE, M. LISCIDINI, J. SIPE, I. FAVERO, G. LEO and S. DUCCI, “High-resolution characterization of quantum bi-photon sources with classical difference frequency generation”, in *SPIE Photonics Europe 2014*, (Brussels, Belgium), April 2014.
- [13] G. BOUCHER, C. AUTEBERT, **F. Boitier**, A. ECKSTEIN, A. ORIEUX, A. LEMAÎTRE, E. GALOPIN, C. MANQUEST, C. SIRTORI, I. FAVERO, G. LEO and S. DUCCI, “Photon pair sources in AlGaAs : from state engineering to electrical injection”, in *Quantum 2014*, (Torino, Italy), May 2014.
- [14] **G. Boucher**, C. AUTEBERT, F. BOITIER, A. ECKSTEIN, A. LEMAÎTRE, C. MANQUEST, C. SIRTORI, I. FAVERO, G. LEO and S. DUCCI, “Integrated AlGaAs sources of quantum correlated photon pairs”, in *ECOC 2014*, (Cannes, France), September 2014.
- [15] **C. Autebert**, G. BOUCHER, F. BOITIER, A. ECKSTEIN, A. LEMAÎTRE, I. FAVERO, G. LEO and S. DUCCI, “Photon pair sources in AlGaAs : from electrical pumping to quantum state engineering”, in *PICQUE Workshop*, (Oxford, United-Kingdom), January 2015.
- [16] **G. Boucher**, T. DOUCE, A. ECKSTEIN, I. FAVERO, G. LEO, T. COUDREAU, P. MILMAN and S. DUCCI, “Engineering time-frequency properties of photon pairs generated by a transversally pumped semiconductor device”, in *CLEO/Europe-EQEC*, (Munich, Germany), June 2015.
- [17] G. BOUCHER, C. AUTEBERT, Y. HALIOUA, Q. YAO, A. LEMAÎTRE, C. GOMEZ, I. FAVERO, G. LEO and **S. Ducci**, “Photon pair sources in AlGaAs: from electrical injection to quantum state engineering”, in *Single Photon Workshop*, (Geneva, Switzerland), July 2015. Invited.
- [18] **G. Boucher**, T. DOUCE, A. ECKSTEIN, A. LEMAÎTRE, I. FAVERO, G. LEO, T. COUDREAU, P. MILMAN and S. DUCCI, “Engineering time-frequency properties of photon pairs with a transversally pumped semiconductor source”, in *Single Photon Workshop*, (Geneva, Switzerland), July 2015. Poster.
- [19] **Y. Halioua**, C. AUTEBERT, G. BOUCHER, Q. YAO, J. BELHASSEN, A. LEMAÎTRE, C. G. CARBONELL, I. FAVERO, G. LEO and S. DUCCI, “AlGaAs devices generating non-classical states of light”, in *QLIMS*, (Barcelona, Spain), November 2015.

Articles

In the following pages we include the papers reporting on the work presented in this doctoral thesis.

Polarization-entanglement generation and control in a counterpropagating phase-matching geometry

G. Boucher,¹ A. Eckstein,¹ A. Orioux,^{1,*} I. Favero,¹ G. Leo,¹ T. Coudreau,¹ A. Keller,² P. Milman,¹ and S. Ducci^{1,†}

¹*Laboratoire Matériaux et Phénomènes Quantiques, Université Paris Diderot, Sorbonne Paris Cité, CNRS-UMR 7162, Case courrier 7021, 75205 Paris Cedex 13, France*

²*Université Paris Sud, Institut des Sciences Moléculaires d'Orsay, CNRS - UMR 8214 Bâtiment 210 Université Paris-Sud 91405 Orsay Cedex*
(Received 27 September 2013; published 10 March 2014)

We present a theoretical model to describe polarization-entanglement generation by spontaneous parametric down conversion in a transverse pump configuration. It takes into account the effect of a resonant microcavity for the pump beam and gives a direct link between the level of generated entanglement and the spatial profile of the pump beam. A pumping scheme leading to the generation of high quality Bell states is proposed.

DOI: [10.1103/PhysRevA.89.033815](https://doi.org/10.1103/PhysRevA.89.033815)

PACS number(s): 42.65.Lm, 42.50.Ct, 42.82.Et, 42.65.Wi

I. INTRODUCTION

The process of spontaneous parametric down conversion (SPDC) is a key ingredient for a large number of applications in the domain of quantum communication and information including quantum teleportation [1], quantum cloning [2,3], quantum cryptography [4], and quantum computation [5]. As the proposals for quantum information protocols with SPDC become more numerous and sophisticated, the requirements on SPDC sources become more varied and stringent. For example, polarization-entanglement based protocols require the violation of Bell inequalities of tens of standard deviations [6], implying a high degree of control on the two biphoton amplitudes; optical quantum computation demands indistinguishable single photons implying a complete control of their properties. For instance, the linear optical implementation of the ubiquitous CNOT gate relies on Hong-Ou-Mandel interference [7], requiring a very high wave function overlap between photons. Photon pairs produced by SPDC are often entangled in several degrees of freedom (direction, momentum, frequency, polarization, etc.); on one hand, this can allow the production of hyperentangled states [8] that have been shown to be beneficial both in quantum communications, e.g., to increase the bit rate [9], and in quantum computation, e.g., to reduce the number of necessary gates to perform a logic operation [10]. On the other hand, the existence of correlations on several degrees of freedom can destroy the requisite indistinguishability by enabling one to learn about one photon state by performing measurements on its twin.

For all these reasons, the availability of sources able to generate versatile two-photon states according to a particular quantum information protocol requires a deep understanding of the entanglement generation process and the ability to control it. A great deal of attention has been devoted to the generation of two-photon states with specific spectral properties; different schemes have been proposed based on group velocity matching [11,12], on noncollinear phase-matching geometries [13–17], or on the shaping of the pump beam [18].

Among these possibilities, a phase-matching scheme with a transverse pump beam impinging on a nonlinear waveguide allows us to generate counterpropagating twin photons [19]. This configuration presents the advantage of a complete control on the frequency degree of entanglement regardless of the dispersion relation of the waveguide, thus providing extreme versatility [20,21]. This opens the possibility to generate a very large variety of two-photon states spanning the two-dimensional Hilbert space of polarization and the infinite-dimensional space of frequency.

Starting from the recent experimental demonstration of Bell states generation in a semiconductor microcavity [22] based on this phase-matching scheme [23], this paper presents a theoretical model of such a source taking into account the pertinent physical parameters having an impact on the generated entanglement. In particular, we study the effect of the microcavity on the SPDC spectrum, we link the level of generated entanglement to the joint spectral amplitude of the biphoton state, consider the impact of imperfect detection on state tomography, and we show how to optimize the pumping scheme to get a maximum entanglement.

Figure 1 presents the working principle of the source: A pump beam impinges on top of an AlGaAs ridge microcavity generating two counterpropagating, orthogonally polarized wave guided SPDC photons. The frequencies of the emitted photons are fixed by energy and momentum conservation; since the photons are emitted in opposite directions, two type II interactions take place. In interaction (1) the signal is TE (H) polarized and the idler is TM (V); in interaction (2), the opposite occurs. Momentum conservation in the epitaxial direction is satisfied through a quasiphase-matching (QPM) structure of AlGaAs layers with alternating refractive indices. In order to enhance the conversion efficiency, a resonant cavity for the pump beam is implemented with two Bragg mirrors surrounding the core of the waveguide [24]. Central frequencies for the signal and idler are given by the phase-matching conditions for interactions

$$(1): \begin{cases} \Delta\omega_1 = \omega_p - \omega_s - \omega_i = 0 \\ c\Delta k_1 = \omega_p \sin \theta - \omega_s n_H(\omega_s) + \omega_i n_V(\omega_i) = 0 \end{cases} \quad (1)$$

and

$$(2): \begin{cases} \Delta\omega_2 = \omega_p - \omega_s - \omega_i = 0 \\ c\Delta k_2 = \omega_p \sin \theta - \omega_s n_V(\omega_s) + \omega_i n_H(\omega_i) = 0 \end{cases} \quad (2)$$

*Present address: Dipartimento di Fisica, Sapienza Università di Roma, Piazzale Aldo Moro, 5, I-00185 Roma, Italy.

†sara.ducci@univ-paris-diderot.fr

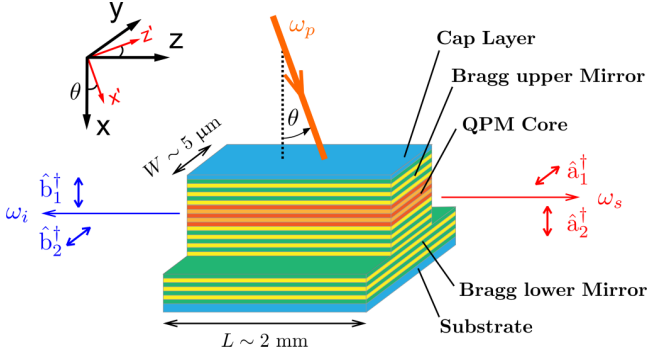


FIG. 1. (Color online) Counterpropagating phase-matching scheme implemented in a semiconductor microcavity waveguide. The waveguide is etched from an epitaxially grown AlGaAs layer structure with alternating Al content, deposited on a GaAs chip (the substrate). The cap layer on top of the sample protects the lower structures from chemical degradation through contact with the environment. Both the upper and the lower Bragg mirror have a higher layer density than the QPM core, which is responsible for quasiphase matching of the SPDC processes.

The tunability curves of the source are presented in Fig. 2.

The paper is organized as follows: In Sec. II we derive the expression of the generated state taking into account a Gaussian profile for the pump beam as well as the microcavity structure. In Sec. III we consider polarization state tomography and derive the expression of the concurrence, an entanglement monotone, as a function of the source parameters and pumping configuration. Section IV describes the treatment of noise in the reconstructed density matrix, while Sec. V shows

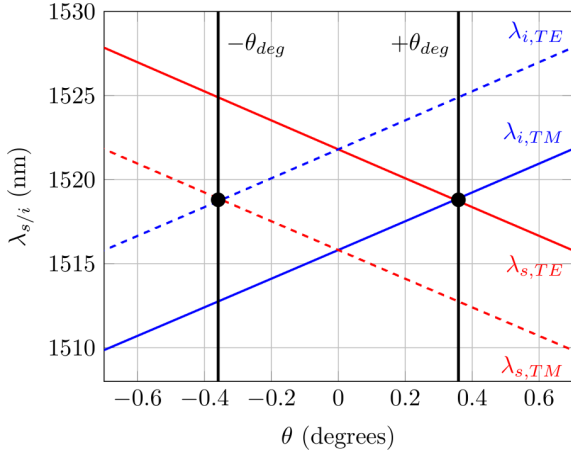


FIG. 2. (Color online) Angular dependence of the signal and idler wavelength of interactions 1 (solid lines) and 2 (slashed lines). The black slashed lines correspond to pump beams at $+\theta_{deg}$ and $-\theta_{deg}$ such that each process generates a frequency degenerate photon pair. The birefringence $\Delta n = 6.1 \times 10^{-3}$ between TE and TM mode induced by the structuring of the waveguide device breaks the complete symmetry of phase matching where the blue and the red curves respectively coincide with each other. Black circles mark the creation of photons at the intersections of the tuning curves and the pump beam markers. Nondegenerate photon pairs are rejected through filtering.

the impact of the pumping scheme on the quality of the entanglement. Two cases are studied in detail: In the first one the pump beam is engineered with a Fresnel biprism, while in the second one a lateral-shearing grating is used. Finally, Sec. VI presents the conclusions and perspectives of this work.

II. SPDC IN THE TRANSVERSE PUMP CONFIGURATION

If we consider a frequency-broadband SPDC process in a collinear, spatially single-mode case in a monomode waveguide, we can describe it with an effective Hamiltonian

$$\hat{H} \propto \int dt \hat{H}(t) = \int_{-\frac{1}{2}L}^{\frac{1}{2}L} dz \iint d\omega_s d\omega_i \times \hat{a}^\dagger(\omega_s) \hat{b}^\dagger(\omega_i) \hat{c}(\omega_s + \omega_i) e^{i\Delta k z} + \text{H.c.}, \quad (3)$$

where L is the length of the interaction volume in the direction of the interacting beams, and Δk is their phase mismatch. Integration over the waveguide width and height to compute the spatial mode overlap between pump, signal, and idler are routinely neglected, as they result in a constant factor that can be dealt with in the normalization of the output state.

In a transverse pump configuration with a beam impinging with a small, variable angle of incidence θ , the Hamiltonian must be modified to reflect this new degree of freedom [14]:

$$\begin{aligned} \hat{H}_j &= \int dt \hat{H}_j(t) \\ &\propto \iint d\omega_s d\omega_i \int_{-\frac{1}{2}L}^{\frac{1}{2}L} dz e^{i\Delta k_j z} S(z, \theta) \\ &\times \int dx d_{\text{eff}}(x) u_s^*(x) u_i^*(x) u_p(x) e^{ik_p(\omega_s + \omega_i)x} \\ &\times \hat{a}_j^\dagger(\omega_s) \hat{b}_j^\dagger(\omega_i) \hat{c}(\omega_s + \omega_i) + \text{H.c.} \end{aligned} \quad (4)$$

$j \in \{1, 2\}$ indicates interaction 1 or 2. Both phase-mismatch functions Δk_1 and Δk_2 from Eqs. (1) and (2) result in spectrally close counterpropagating, cross-polarized photon pairs, but with switched polarizations relative to each other. The transversal spatial distribution S of the pump field now defines the interaction region together with the waveguide boundaries at $z = \pm \frac{L}{2}$ and thus enters the equation under the integral in the z direction. The x integral tests the overlap between the transversal signal and idler modes u_s and u_i with the longitudinal pump field amplitude $u_p(x) e^{ik_p(\omega_s + \omega_i)x}$. An appropriate variation of the effective nonlinear coefficient $d_{\text{eff}}(x)$ with period Λ leads to QPM in the x direction: $k_p \approx \frac{2\pi}{\Lambda}$.

Let us consider an incident Gaussian beam with a spatial field amplitude S' in “beam coordinates” (x' is the beam propagation axis and z' its transverse axis, see Fig. 1) close to focus $x' = 0$ so we can neglect phase front curvature. The transverse amplitude is given by

$$S'(z') = S_0 e^{-\frac{z'^2}{w_p^2}} \rightarrow S(z, \theta) = S_0 e^{-\frac{(z \cos \theta)^2}{w_p^2}}, \quad (5)$$

where S is the function transformed into the waveguide coordinate system, with w_p the pump beam’s waist. Since the waveguide thickness is typically much smaller than the pump beam waist, we assume it to be constant in the x direction.

We assume a coherent pump beam, and a SPDC source producing with high probability only single photon pairs, so that higher order events are negligible. It is then justified to substitute the pump mode operator $\hat{c}(\omega)$ with the c -number valued spectral amplitude function $\gamma(\omega)$ of the pump state $|\gamma\rangle$:

$$\hat{c}(\omega)|\gamma\rangle = \gamma(\omega)|\gamma\rangle. \quad (6)$$

However, within the integrated microcavity, the SPDC process acts on the intracavity field rather than the original pump field. We therefore first replace the operator \hat{c} in the Hamiltonians \hat{H}_j with the intracavity operator \hat{c}_{cav} defined in Appendix A and find

$$\hat{c}_{\text{cav}}(\omega)|\gamma\rangle = f_+(\omega)\gamma(\omega)|\gamma\rangle, \quad (7)$$

with f_+ the transfer function between extra- and intracavity pump spectrum.

With this substitution, we define from Eq. (4) the joint spectral amplitude $\mathcal{A}^{(j)}$ of the output photon pair of interaction $j \in \{1, 2\}$ via

$$\begin{aligned} \hat{H}_j|0\rangle &\propto |\psi_{\text{pair},j}\rangle \\ &= \frac{1}{\sqrt{\mathcal{N}_j}} \iint d\omega_s d\omega_i \mathcal{A}^{(j)}(\omega_s, \omega_i, \theta) \hat{a}_j^\dagger(\omega_s) \hat{b}_j^\dagger(\omega_i) |0\rangle, \end{aligned} \quad (8)$$

with

$$\begin{aligned} \mathcal{A}^{(j)}(\omega_s, \omega_i, \theta) &= f_+(\omega_s + \omega_i) \gamma(\omega_s + \omega_i) \\ &\times \int_{-\frac{1}{2}L}^{\frac{1}{2}L} dz e^{i\Delta k_j(\omega_s, \omega_i, \theta)z} S(z, \theta) \\ &\times \int dx d_{\text{eff}}(x) u_s^*(x) u_i^*(x) u_p(x) e^{ik_p(\omega_s + \omega_i)x}, \end{aligned} \quad (9)$$

giving the probability amplitude of an emitted photon pair emerging in the modes $\hat{a}_H(\omega_s)$ and $\hat{b}_V(\omega_i)$ ($j = 1$), or $\hat{a}_V(\omega_s)$ and $\hat{b}_H(\omega_i)$ ($j = 2$). \mathcal{N}_j is a normalization constant.

We now introduce a second pump beam, mirror symmetric to the first one with respect to the z axis, at angle $-\theta$ and at the same frequency. This too will pump two possible SPDC processes, making for a total of up to four distinct photon pairs generated in the perturbative approximation. For the proper choice of pump beam angle $\pm\theta_{\text{deg}}$, as a consequence of the symmetry around $\theta = 0$ (see Fig. 2), each beam pumps one frequency-degenerate process. By filtering out the additional nonfrequency-degenerate photons, we create the superposition state

$$\begin{aligned} &|\Psi(\theta_{\text{deg}}, -\theta_{\text{deg}})\rangle \\ &= \frac{1}{\sqrt{\mathcal{N}_{12}}} \iint d\omega_s d\omega_i [\mathcal{A}^{(1)}(\omega_s, \omega_i, \theta_{\text{deg}}) \hat{a}_H^\dagger(\omega_s) \hat{b}_V^\dagger(\omega_i) \\ &\quad + \mathcal{A}^{(2)}(\omega_s, \omega_i, -\theta_{\text{deg}}) \hat{a}_V^\dagger(\omega_s) \hat{b}_H^\dagger(\omega_i)] |0\rangle, \end{aligned} \quad (10)$$

which—for sufficiently overlapping joint spectral amplitudes $\mathcal{A}^{(1)}$ and $\mathcal{A}^{(2)}$ —constitutes a polarization entangled Bell state with a normalization constant \mathcal{N}_{12} .

III. BELL STATE GENERATION AND TOMOGRAPHY

The generation of polarization Bell states is obtained by impinging with two pump beams at signal and idler frequency degeneracy angles $\pm\theta_{\text{deg}}$ (cf. Fig. 2), such that a superposition of two spectrally overlapping photon pairs with reversed polarizations is created.

A complete reconstruction of the produced polarization state is usually done by a state tomography [25]. If only polarization measurements are performed and frequencies are not measured, it is convenient to work with the reduced state obtained by taking the trace over frequencies of the produced state $\hat{\rho}(\theta_{\text{deg}}, -\theta_{\text{deg}})$. We can thus calculate the reduced state and then evaluate how its purity is linked to the parameters of the system. Starting from

$$\hat{\rho}(\theta_{\text{deg}}, -\theta_{\text{deg}}) = |\Psi(\theta_{\text{deg}}, -\theta_{\text{deg}})\rangle \langle\Psi(\theta_{\text{deg}}, -\theta_{\text{deg}})| \quad (11)$$

and taking the trace over frequencies, we obtain the reduced state

$$\begin{aligned} \hat{\rho} &= \alpha_1 |HV\rangle \langle HV| + \alpha_2 |VH\rangle \langle VH| \\ &\quad + \beta^* |VH\rangle \langle HV| + \beta |HV\rangle \langle VH|, \end{aligned} \quad (12)$$

with

$$\begin{aligned} \alpha_1 &= \frac{1}{\mathcal{N}_{12}} \iint d\omega_s d\omega_i |\mathcal{A}^{(1)}(\omega_s, \omega_i, \theta_{\text{deg}})|^2, \\ \alpha_2 &= \frac{1}{\mathcal{N}_{12}} \iint d\omega_s d\omega_i |\mathcal{A}^{(2)}(\omega_s, \omega_i, -\theta_{\text{deg}})|^2, \quad \text{and} \\ \beta &= \frac{1}{\mathcal{N}_{12}} \iint d\omega_s d\omega_i \mathcal{A}^{(1)}(\omega_s, \omega_i, \theta_{\text{deg}}) \mathcal{A}^{(2)*}(\omega_s, \omega_i, -\theta_{\text{deg}}). \end{aligned} \quad (13)$$

While the squared ratio of α_1 and α_2 gives the relative strength of both SPDC interactions, β quantifies the overlap between their output photon pairs in time and frequency.

The reduced state is then represented as a 2×2 density matrix, in the basis ($|HV\rangle, |VH\rangle$). The two eigenvalues λ_- and λ_+ are

$$\begin{aligned} \lambda_{\pm} &= \frac{1}{2}[\alpha_1 + \alpha_2 \pm \sqrt{(\alpha_1 - \alpha_2)^2 + 4|\beta|^2}] \\ &= \frac{1}{2}\{1 \pm \sqrt{1 + 4[|\beta|^2 - \alpha_1(1 - \alpha_1)]}\}, \end{aligned} \quad (14)$$

where the normalization condition $\alpha_1 + \alpha_2 = 1$ has been used. Purity and the entanglement in polarization can now be computed and linked to α_1 and $|\beta|^2$. We note that these integrals depend on frequency correlation amplitudes and their overlap, which in turn depend on the spatial degrees of freedom of the pump.

The matrix $\hat{\rho}$ is pure if and only if $\text{Tr}[\hat{\rho}^2] = 1$, or $\lambda_-^2 + \lambda_+^2 = 1$. Using $\lambda_- + \lambda_+ = 1$, this is equivalent to $\lambda_- = 0$, that is

$$|\beta|^2 = \alpha_1(1 - \alpha_1) \quad (15)$$

[see Eq. (14)]. Since $\alpha_1 \leq 1$, the relation $|\beta|^2 \leq \frac{1}{4}$ always holds. In that case $\lambda_+ = 1$ and the corresponding eigenvectors are

$$\begin{aligned} \lambda_+ = 1 &\rightarrow \frac{1}{\sqrt{1 - \alpha_1}} \begin{pmatrix} \beta \\ 1 - \alpha_1 \end{pmatrix}, \\ \lambda_- = 0 &\rightarrow \frac{1}{\sqrt{\alpha_1}} \begin{pmatrix} \beta \\ -\alpha_1 \end{pmatrix}. \end{aligned} \quad (16)$$

$\hat{\rho}$ can thus be written as $\hat{\rho} = |\phi\rangle\langle\phi|$ with

$$|\phi\rangle = \frac{1}{\sqrt{1-\alpha_1}} [\beta |H, V\rangle + (1-\alpha_1) |V, H\rangle]. \quad (17)$$

The pure state is maximally entangled in polarization if the two, orthogonal, contributions have an equal weight, that is

$$|\beta|^2 = (1-\alpha_1)^2. \quad (18)$$

To satisfy both conditions of purity [Eq. (15)] and maximum entanglement [Eq. (18)] at the same time, the relevant elements of the reduced density matrix $\hat{\rho}$ too must have equal weight, that is

$$\alpha_1 = \alpha_2 = \frac{1}{2} = |\beta|. \quad (19)$$

The equality $\alpha_1 = \alpha_2$ translates the fact that both interactions have equal contributions: This is a necessary but nonsufficient condition. Indeed, the two interactions must also be indistinguishable to suppress which-path information in the frequencies of the photons. This condition is obtained when the joint spectral amplitudes $\mathcal{A}^{(1)}$ and $\mathcal{A}^{(2)}$ characterizing interactions 1 and 2 perfectly overlap, therefore when the value of $|\beta| = \iint d\omega_s d\omega_i |\mathcal{A}^{(1)} \mathcal{A}^{(2)*}|$ is equal to 1/2. Note that this joint spectrum overlap $|\beta|$ is directly linked to the *concurrence* \mathcal{C} , a commonly used entanglement estimator, via $\mathcal{C} = 2|\beta|$ [22,26].

In conclusion, to obtain a maximally entangled state in polarization, we need to set up the two laser pumps such that $\alpha_1 = \alpha_2$ in order to excite the two processes with the same strength, and at the same time make them as indistinguishable as possible to maximize the value of $|\beta|$ (or alternatively of \mathcal{C}) by minimizing the distinguishability of the frequency-degenerate photon pairs from interactions 1 and 2. We note that the existence of spectral correlations between signal and idler does not necessarily result in a degradation of the produced entanglement. This can be seen in the definition of β : Like the HOM interference between the photons from a single SPDC process, it depends on the spectral symmetry between signal and idler, which does not preclude spectral correlation. A practical solution to realize this will be described in Sec. V.

IV. DETECTOR DARK COUNTS AND BACKGROUND LIGHT

The theoretical model presented in the previous sections gives a direct link between entanglement and controllable parameters involved in the experiment, and has been used to analyze the results reported in the polarization state tomography experiment described in [22]. The fact that the fidelity to the Bell state $|\psi^+\rangle$ is $F_{\text{raw}} = \langle\psi^+|\hat{\rho}_{\text{exp}}|\psi^+\rangle = 0.83$ rather than 1 is—according to this model—partly due to residual distinguishability between both nonlinear processes. This is equivalent to the loss of coherence between the two possible polarization states of the entangled photon pair, but background light and detector dark count events also have this effect.

With p_B the detection probability of a background event (from either background light or dark counts), the measurement operator for a single photon detector with quantum efficiency η (measuring behind a polarizer transmitting only

vertically polarized light) takes the form

$$\mu_{\text{SPDC}} = p_B |0\rangle\langle 0| + (\eta + p_B - \eta p_B) |V\rangle\langle V|. \quad (20)$$

The term $p_B |0\rangle\langle 0|$ reflects the possibility of a detection event when there is no input photon, while the factor to the vertical term accounts for the possibility of detecting an incoming photon, or a background event, or the occurrence of both. Plugging this measurement operator into the state tomography method after [25], we find the reconstructed polarization entangled two-photon state of an ideal input state $(1-p_{\text{PDC}})|0\rangle\langle 0| + p_{\text{PDC}}\hat{\rho}$. For $\hat{\rho}$ an input state according to Eq. (12), the result of the tomography method is well approximated by

$$\hat{\rho}_r \approx \frac{1}{N} \eta^2 (1-p_B)^2 p_{\text{PDC}} \hat{\rho} + \frac{1}{N} [\eta p_B (1-p_B) p_{\text{PDC}} + p_B^2] \mathbb{1} \quad (21)$$

as long as $|\alpha_2 - \alpha_1| \ll 1$, that is if SPDC interaction 1 is as strong as interaction 2. p_{PDC} is the probability for an entangled photon pair to be emitted. The first summand of $\hat{\rho}_r$ represents the “real” coincidence events. The second term is caused by coincidence events that stem partly or fully from (incoherent) background events, and thus is proportional to the completely mixed state $\frac{1}{4}\mathbb{1}$. $N = p_{\text{PDC}}\eta^2(1-p_B)^2 + 4 + p_{\text{PDC}}\eta p_B(1-p_B) + 4p_B^2$ is a normalization constant.

We apply this noise model by comparing the expected fidelity $F_{\text{noise}} = \langle\psi^+|\hat{\rho}_r|\psi^+\rangle$ with the experimental fidelity $F_{\text{raw}} = 0.83 \pm 0.04$ demonstrated in [22]. Taking from there a theoretical optimal value for $|\beta| = 0.43$, its phase (according to experiment) $\arg(\beta) = -0.17$, the background coincidence event probability $p_B^2 = 3.5 \times 10^{-7}$ (from dark counts and background light), and absolute detection efficiency of $\eta = 0.13 \times 0.25$ (consisting of photon losses both in the experimental setup and in the detection, respectively) we find $F_{\text{noise}} = 0.79$.

Since the calculated fidelity is compatible with the error interval of the experimental value, we conclude that the treatment of systematic errors presented here, which takes into account imperfect overlap of the SPDC pump beams as well as background light and detector dark counts, adequately models our experiment.

V. POLARIZATION-ENTANGLEMENT OPTIMIZATION

Different mechanisms can be detrimental for the entanglement quality of the produced state; for example the slightly different transverse profiles of the TE and TM modes. Nevertheless, in the experiment of Ref. [22] and in this work, the photons are coupled through single mode fibers which act like spatial filters and cancel this effect. Another phenomenon which often requires a compensation stage is the timing difference between TE and TM photons at the output of the source. In our case the birefringence of the device is very weak and the length of the waveguide sufficiently small such that the delay acquired by orthogonally polarized photons (88 fs) is well below their coherence time (typically 10 ps). This mechanism is nevertheless taken into account in our analysis of the overlap of the joint spectral amplitudes of the two possible interactions. In this section we compare the impact of two

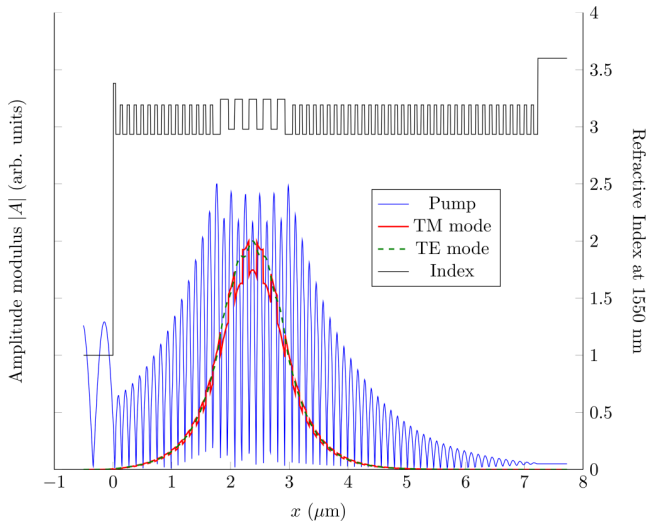


FIG. 3. (Color online) Waveguide refractive index structure and the amplitude modulus $|A|$ of the guided transversal signal (bold dashed line) and idler (bold solid line) modes and the longitudinal pump field (thin solid line) in the medium.

different pumping configurations on the quality of polarization entanglement; we will show that the main contribution in our case comes from the spatial profile of the pump beam.

Starting from the amplitude distribution of the pump beam on top of the waveguide, the joint spectral amplitudes associated with the two interactions can be numerically evaluated, taking into account the epitaxial structure of the device through a standard transfer-matrix method [27]. This allows us to determine the transversal signal and idler mode profiles (Fig. 3). The resonant longitudinal pump mode was obtained with a scattering matrix method [28].

The necessary parameters can be found in Appendix B. From this we can calculate the parameter β presented in Sec. III, which is directly related to the amount of entanglement generated by the source.

A very simple way to produce two coherent pump beams impinging at $\pm\theta_{deg}$ is passing the pump beam through the center of a Fresnel biprism (see Fig. 4). The angle of each prism can be chosen such that it deviates the pump beam entering the first face with a normal incidence by θ_{deg} . This

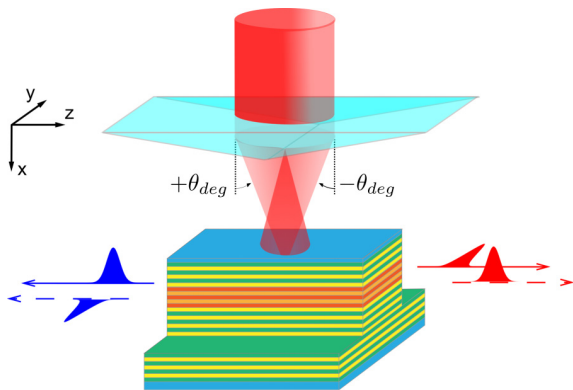


FIG. 4. (Color online) Bell state generation with a Fresnel biprism.

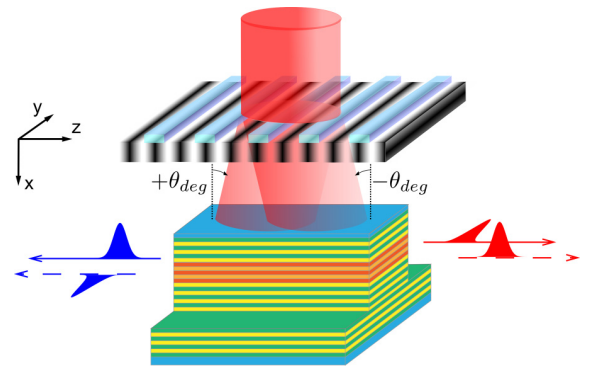


FIG. 5. (Color online) Bell state generation with a grating.

solution has been adopted in Ref. [22]. A second possibility consists of shearing the incident pump beam into two replicas with a specific type of grating (see Fig. 5), designed to diffract the incident intensity only into its first order with an angle $\pm\theta_{deg}$. This is possible if the grating transmission function $t_d(z)$ is

$$t_d(z) = \cos\left(\frac{2\pi z}{d}\right), \quad (22)$$

where $d \sim \frac{\lambda}{\theta_{deg}}$ is the period of the grating.

In this case a normally incident Gaussian beam with amplitude $S(z, \theta = 0)$ and waist w_p is transformed into two beams:

$$S^\pm(x, z) = \frac{1}{2}S(z - z_\pm, \pm\theta_{deg}), \quad (23)$$

with

$$z_\pm = \pm\tan(\theta_{deg})(x - x_G) = \pm\frac{\lambda}{d}(x - x_G), \quad (24)$$

where x_G is the position of the grating.

We thus create two copies of the incident Gaussian beam impinging onto the waveguide with opposite angles $\pm\theta_{deg}$. This kind of grating can be realized with an intensity mask corresponding to the absolute value of the sinusoidal transmission factor and a phase mask to account for the alternating sign [29].

To achieve a perfect entanglement in polarization, the joint spectral amplitudes of the two interactions must be identical: In this way, no which-path information is associated to the frequency degree of freedom. Their absolute difference

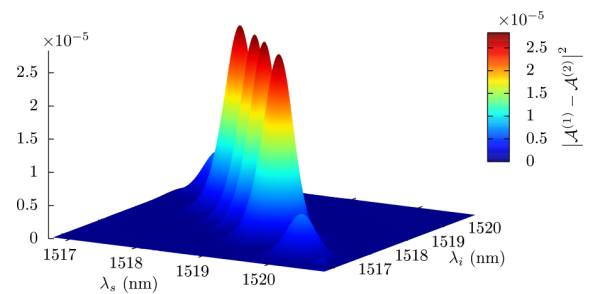


FIG. 6. (Color online) Absolute value of the difference between $\mathcal{A}^{(1)}$ and $\mathcal{A}^{(2)}$ in the case of the biprism. The degeneracy angles for the two pumping beams are obtained for a biprism angle $\alpha = 41'10''$.

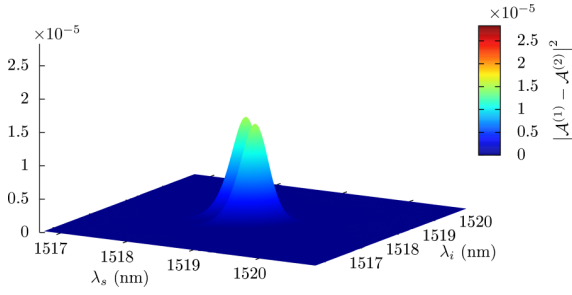


FIG. 7. (Color online) Absolute value of the difference between $\mathcal{A}^{(1)}$ and $\mathcal{A}^{(2)}$ in the case of the grating. The degeneracy angles for the two pumping beams are obtained for a grating period $d = 125 \mu\text{m}$.

$|\mathcal{A}^{(1)}(\theta_{\text{deg}}) - \mathcal{A}^{(2)}(-\theta_{\text{deg}})|$ can be used to visualize the possible entanglement degradation of the generated Bell states, since we find

$$\begin{aligned} & \iint d\omega_s d\omega_i |\mathcal{A}^{(1)}(\theta_{\text{deg}}) - \mathcal{A}^{(2)}(-\theta_{\text{deg}})|^2 \\ &= \alpha_1 + \alpha_2 - 2|\beta| = 1 - \mathcal{C} \end{aligned} \quad (25)$$

using the definitions and results of Sec. III. As expected, the concurrence \mathcal{C} tends towards unity when the integral of Eq. (25) tends to zero, namely when the two processes are indistinguishable.

Figures 6 and 7 show this for the two cases of biprism and grating; we assume a pulsed, Gaussian pump beam with waist $w_p = 0.6 \text{ mm}$ at $\lambda_{\text{pump}} = 759 \text{ nm}$ and with temporal width $\tau_{\text{pump}} = 3.5 \text{ ps}$, optimized for the generation of frequency-uncorrelated states [22]. The biprism is placed at a distance of 4 cm where the obtained concurrence \mathcal{C} is optimal and the grating at a distance of 1 cm. It is clear that the overlap of the two joint spectral amplitudes is higher when the grating solution is used: The smaller the volume below the represented surface, the higher is the obtained entanglement.

For a quantitative analysis, Fig. 8 reports the value of the concurrence and $|\beta|$ obtained in the two cases as a function of the distance between the optical element producing the

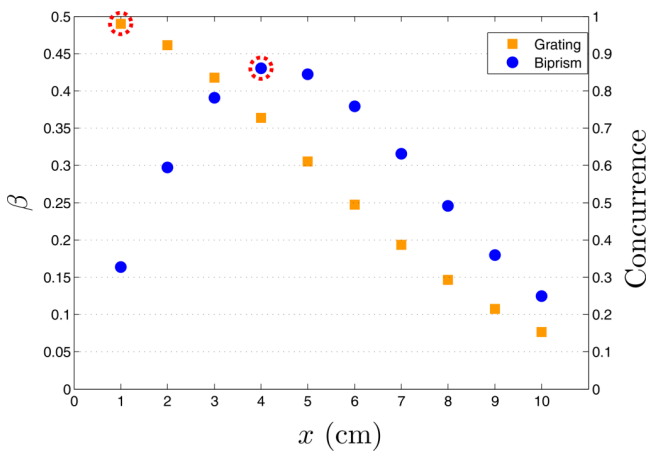


FIG. 8. (Color online) β and concurrence as a function of the distance between biprism (circles) or the grating (squares) and the waveguide. The conditions of Figs. 6 and 7 are indicated by dashed circles.

two pumping beams and the waveguide. In the case of the biprism, the concurrence saturates at 0.86, corresponding to the optimal overlap between the two *half-Gaussians* emerging from it. The situation is different with the grating since we can obtain almost unity concurrence simply by moving it towards the waveguide, as the overlap between both pump beams monotonically decreases with increasing distance. Even if due to space constraints in an experimental setup it may be difficult to reduce the distance to less than 1 cm, this already results in a photon pair concurrence of 0.97, or an improvement of 13% with respect to the optimal biprism configuration.

VI. CONCLUSION

We have provided an extensive theoretical model to describe the generation of polarization entanglement by SPDC in a semiconductor waveguide with a transversal pump configuration. We have analyzed the effect of the resonant cavity for the pump beam, of its spatial profile, and of the background noise on the level of generated entanglement, comparing our model with the experimental results of Ref. [22]. Finally, we have proposed a pumping scheme based on a lateral-shearing grating, to improve the entanglement level by at least 13%. These results open the way to fully exploit the versatility of the transversal pump configuration for SPDC: The ability to adapt the interaction volume within the waveguide by modulating the transversal pump field affords a spectral control of the process far beyond that of a typical collinear scheme, allowing for the creation of more exotic, spectral and polarization hyperentangled photon pair states [6], with a quantum information density surpassing that of the purely polarization entangled state [30,31].

ACKNOWLEDGMENTS

This work was partly supported by the French Brazilian ANR HIDE project and by Region Ile de-France in the framework of C Nano IdF with the TWILIGHT project and SESAME Project “Communications quantiques.” A.E. and S.D. thank Jean-Philippe Karr for helpful discussions. S.D. is member of Institut Universitaire de France.

APPENDIX A: FABRY-PEROT CAVITY

A convenient way to enhance the conversion efficiency of the source is the implementation of a resonant microcavity for the pump beam. However, there is also an effect on the SPDC biphoton spectrum, which we will consider in this Appendix. For the sake of simplicity, let us assume a very simple plane two-mirror cavity, enveloping the waveguide in epitaxial direction x . The medium inside the cavity shall only affect the incoming pump beam by dispersion, we neglect nonlinear effects and absorption. The sketch in Fig. 9 depicts the elements involved: Each semitransmissive mirror is described as a beam splitter BS_1 and BS_2 and we choose imaginary transmission coefficients it_1, it_2 and real reflection coefficients r_1, r_2 , respectively. A coherent, monochromatic laser beam with linear polarization in the y direction at frequency ω in mode $\hat{c}_0^+(\omega)$ enters the system with an incidence angle θ . This angle shall be small enough not to significantly reduce the

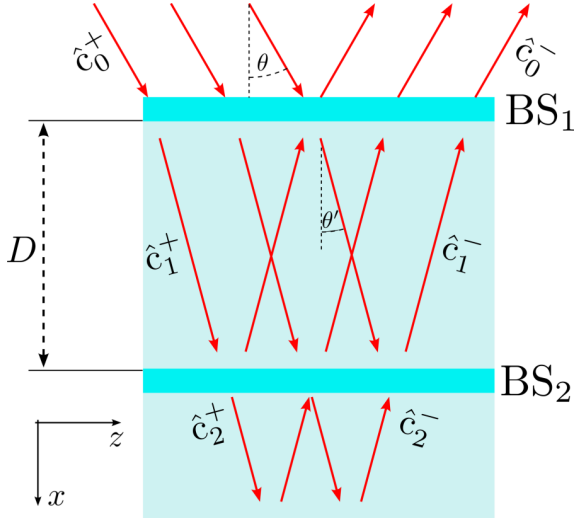


FIG. 9. (Color online) Simple cavity model with two parallel, plane semitransparent mirrors BS₁ and BS₂ separated by a distance D and refractive index n_p inside the medium between them and beneath BS₂ in the substrate. The pump beam's incidence angle is θ , and θ' inside the medium. The operators \hat{c}_i^\pm are the monochromatic, plane wave mode operators of the system.

spatial overlap between the counterpropagating cavity modes so as to let us assume plane wave modes. Inside the cavity, the beam travels under the refracted angle θ' , populating two counterpropagating modes $\hat{c}_1^\pm(\omega)$. Finally, \hat{c}_2^+ and \hat{c}_2^- are the cavity's output modes. Mode \hat{c}_2^- can also act as input mode, but in our case it faces the waveguide sample's substrate and thus can be said to be unpopulated. During one round trip an intracavity beam picks up a phase difference $2\varphi = \frac{2n_p D \cos\theta' \omega}{c_{\text{light}}} = \frac{\omega \cos\theta'}{\Delta\nu}$ with respect to the incident beam, where n_p is the pump refractive index of the medium and $\Delta\nu$ is the free spectral range of the cavity at normal incidence. To accurately predict the SPDC output states, we now define the intracavity field modes [32] for our setting.

Since the cavity consists only of linear optical elements (discounting the effects of the $\chi^{(2)}$ -nonlinear medium as negligible), we can determine its effect on each spectral component at a sharp frequency ω one at a time, even for a short, broadband pump pulse. A monochromatic beam is completely delocalized in time, so we look for a steady-state solution of the coupled beam splitter input and output relations of the system:

$$\begin{pmatrix} \hat{c}_1^+ \\ \hat{c}_0^- \end{pmatrix} = \begin{pmatrix} it_1 & r_1 \\ r_1 & it_1 \end{pmatrix} \begin{pmatrix} 1 & 0 \\ 0 & e^{i\varphi} \end{pmatrix} \begin{pmatrix} \hat{c}_0^+ \\ \hat{c}_1^- \end{pmatrix} \quad (\text{A1})$$

and

$$\begin{pmatrix} \hat{c}_2^+ \\ \hat{c}_1^- \end{pmatrix} = \begin{pmatrix} it_2 & r_2 \\ r_2 & it_2 \end{pmatrix} \begin{pmatrix} e^{i\varphi} & 0 \\ 0 & 1 \end{pmatrix} \begin{pmatrix} \hat{c}_1^+ \\ \hat{c}_2^- \end{pmatrix}. \quad (\text{A2})$$

The right matrix in Eqs. (A1) and (A2) applies a phase shift by φ to intracavity mode \hat{c}_1^\pm for having completed half a round trip, and the left matrix applies the respective beam splitter operation. Solving for the intracavity modes \hat{c}_1^\pm yields

expressions depending on the cavity input modes \hat{c}_0^+ and \hat{c}_2^- ,

$$\begin{aligned} \hat{c}_1^+ &= i \frac{t_1 \hat{c}_0^+ + t_2 r_1 e^{i\varphi} \hat{c}_2^-}{1 - r_1 r_2 e^{2i\varphi}}, \\ \hat{c}_1^- &= i \frac{t_1 r_2 e^{i\varphi} \hat{c}_0^+ + t_2 \hat{c}_2^-}{1 - r_1 r_2 e^{2i\varphi}}. \end{aligned} \quad (\text{A3})$$

We can now define an overall cavity mode operator as the superposition of the directional intracavity operators:

$$\begin{aligned} \hat{c}_{\text{cav}}(\omega) &= \hat{c}_1^+(\omega) + \hat{c}_1^-(\omega) \\ &= f_+(\omega) \hat{c}_0^+(\omega) + f_-(\omega) \hat{c}_2^-(\omega), \end{aligned} \quad (\text{A4})$$

with

$$f_+(\omega) = \frac{it_1(1 + r_2 e^{i\varphi})}{1 - r_1 r_2 e^{2i\varphi}} \quad (\text{A5})$$

the cavity's transfer function for a pump beam entering through BS₁. The expression for f_- can be gained by swapping t_1 with t_2 , and r_1 with r_2 . Replacing $\hat{c} \rightarrow \hat{c}_{\text{cav}}$ in the definition of the SPDC Hamiltonians \hat{H}_j and applying it to a two coherent beam input state $|\gamma_0^+\rangle \otimes |\gamma_2^-\rangle$ with field amplitude $\gamma_2^- \rightarrow 0$ (i.e., no input beam from "below") will result in a modulation of the SPDC biphoton spectral amplitudes by the transfer function f_+ only:

$$\mathcal{A}^{(j)}(\omega_s, \omega_i, \theta) \rightarrow \mathcal{A}^{(j)}(\omega_s, \omega_i, \theta) \times f_+(\omega_s + \omega_i). \quad (\text{A6})$$

Since we assumed input mode c_2^- to be unpopulated, the respective transfer function f_- does not feature here.

APPENDIX B: WAVEGUIDE DEVICE AND SIMULATION PARAMETERS

Table I shows the aluminum content and the thicknesses of the different layers in the heterostructure of the waveguide source. AlGaAs refractive indices are then calculated according to [33]. To calculate the frequency dependent effective indices of the TE and TM modes, we use a standard transfer matrix method [27]. At degeneracy, for example, $n_{\text{TE}} = 3.0987$ and $n_{\text{TM}} = 3.0865$. This allows us to determine the phase mismatch Δk for both interactions [Eqs. (1) and (2)].

TABLE I. Composition of the heterostructure of the counterpropagating source used in the simulation and experiments of [22] and [24].

Number of cycles	Role	xAl (%)	Thickness h (nm)
1	Substrate	0	
36	Lower Bragg	90	70.8
		35	50.1
1	Buffer	90	125.1
4	Core	25	129.1
	Core	80	104.3
1	Core	25	129.1
1	Buffer	90	125.1
14	Upper Bragg	35	50.1
		90	70.8
1	Cap	0	46.2

We assume a hyperbolic secant shape for the pump spectrum:

$$\gamma(\omega) = \operatorname{sech}\left[0.891\left(\omega - \frac{2\pi c}{\lambda_p}\right)\Delta\tau_p\right], \quad (\text{B1})$$

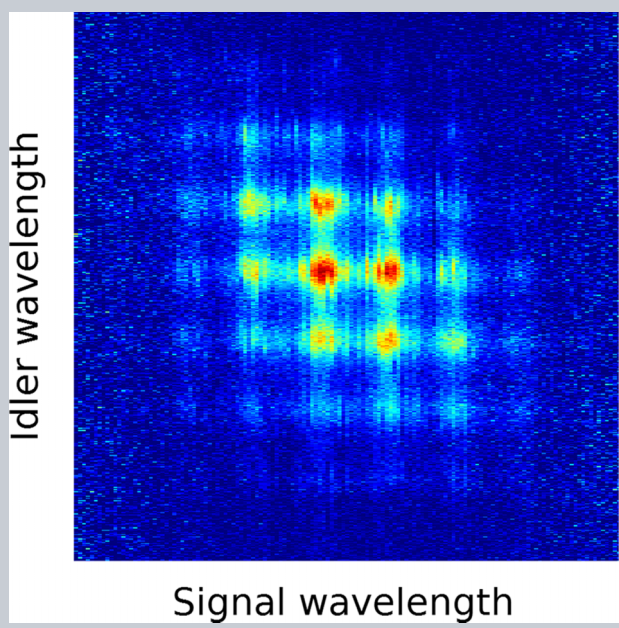
with pulse duration $\Delta\tau_p = 3.5$ ps and central wavelength $\lambda_p = 759.4$ nm. The pump spatial shape is a Gaussian $S(z) = e^{-\frac{z^2}{w_p^2}}$

with waist $w_p = 0.6$ mm, incident on the waveguide with an angle $\theta_{\text{deg}} = 0.349^\circ$. The microcavity is treated according to Eq. (A5). The phase is adjusted so that the resulting Airy peak is centered at $\lambda_p = 759.4$ nm. This peak has a full width half maximum of 0.4 nm.

With these parameters we can then calculate $\mathcal{A}^{(j)}(\omega_s, \omega_i, \theta)$ for both interactions according to Eq. (9).

-
- [1] D. Bouwmeester, J.-W. Pan, K. Mattle, M. Eibl, H. Weinfurter, and A. Zeilinger, *Nature (London)* **390**, 575 (1997).
- [2] V. Bužek and M. Hillery, *Phys. Rev. A* **54**, 1844 (1996).
- [3] A. Lamas-Linares, C. Simon, J. C. Howell, and D. Bouwmeester, *Science* **296**, 712 (2002).
- [4] A. K. Ekert, *Phys. Rev. Lett.* **67**, 661 (1991).
- [5] E. Knill, R. Laflamme, and G. J. Milburn, *Nature (London)* **409**, 46 (2001).
- [6] J. T. Barreiro, N. K. Langford, N. A. Peters, and P. G. Kwiat, *Phys. Rev. Lett.* **95**, 260501 (2005).
- [7] S. Gasparoni, J.-W. Pan, P. Walther, T. Rudolph, and A. Zeilinger, *Phys. Rev. Lett.* **93**, 020504 (2004).
- [8] P. G. Kwiat, *J. Mod. Opt.* **44**, 2173 (1997).
- [9] J. T. Barreiro, T.-C. Wei, and P. G. Kwiat, *Nat. Phys.* **4**, 282 (2008).
- [10] K. Chen, C.-M. Li, Q. Zhang, Y.-A. Chen, A. Goebel, S. Chen, A. Mair, and J.-W. Pan, *Phys. Rev. Lett.* **99**, 120503 (2007).
- [11] A. B. U'Ren, C. Silberhorn, K. Banaszek, I. A. Walmsley, R. Erdmann, W. P. Grice, and M. G. Raymer, *Laser Phys.* **15**, 146 (2005).
- [12] J. Svozilik, M. Hendrych, A. S. Helmy, and J. P. Torres, *Opt. Express* **19**, 3115 (2011).
- [13] A. De Rossi and V. Berger, *Phys. Rev. Lett.* **88**, 043901 (2002).
- [14] M. C. Booth, M. Atatüre, G. Di Giuseppe, B. E. A. Saleh, A. V. Sergienko, and M. C. Teich, *Phys. Rev. A* **66**, 023815 (2002).
- [15] S. Carrasco, J. P. Torres, L. Torner, A. Sergienko, B. E. A. Saleh, and M. C. Teich, *Phys. Rev. A* **70**, 043817 (2004).
- [16] J. Peřina, *Phys. Rev. A* **77**, 013803 (2008).
- [17] A. Christ, A. Eckstein, P. J. Mosley, and C. Silberhorn, *Opt. Express* **17**, 3441 (2009).
- [18] A. Valencia, A. Ceré, X. Shi, G. Molina-Terriza, and J. P. Torres, *Phys. Rev. Lett.* **99**, 243601 (2007).
- [19] L. Lanco, S. Ducci, J.-P. Likforman, X. Marcadet, J. A. W. van Houwelingen, H. Zbinden, G. Leo, and V. Berger, *Phys. Rev. Lett.* **97**, 173901 (2006).
- [20] Z. D. Walton, A. V. Sergienko, B. E. A. Saleh, and M. C. Teich, *Phys. Rev. A* **70**, 052317 (2004).
- [21] X. Caillet, V. Berger, G. Leo, and S. Ducci, *J. Mod. Opt.* **56**, 232 (2009).
- [22] A. Orioux, A. Eckstein, A. Lemaître, P. Filloux, I. Favero, G. Leo, T. Coudreau, A. Keller, P. Milman, and S. Ducci, *Phys. Rev. Lett.* **110**, 160502 (2013).
- [23] X. Caillet, Ph.D. thesis, Université Paris Diderot, 2009.
- [24] A. Orioux, X. Caillet, A. Lemaître, P. Filloux, I. Favero, G. Leo, and S. Ducci, *J. Opt. Soc. Am. B* **28**, 45 (2011).
- [25] D. F. V. James, P. G. Kwiat, W. J. Munro, and A. G. White, *Phys. Rev. A* **64**, 052312 (2001).
- [26] V. Coffman, J. Kundu, and W. K. Wootters, *Phys. Rev. A* **61**, 052306 (2000).
- [27] J. Chilwell and I. Hodgkinson, *J. Opt. Soc. Am. A* **1**, 742 (1984).
- [28] L. Li, *J. Opt. Soc. Am. A* **13**, 1024 (1996).
- [29] P. Bon, G. Maucort, B. Watellier, and S. Monneret, *Opt. Express* **17**, 13080 (2009).
- [30] T.-C. Wei, J. T. Barreiro, and P. G. Kwiat, *Phys. Rev. A* **75**, 060305 (2007).
- [31] B. P. Lanyon, M. Barbieri, M. P. Almeida, T. Jennewein, T. C. Ralph, K. J. Resch, G. J. Pryde, J. L. O'Brien, A. Gilchrist, and A. G. White, *Nat. Phys.* **5**, 134 (2008).
- [32] D. F. Walls and G. G. J. Milburn, *Quantum Optics* (Springer, Berlin, 2008).
- [33] S. Gehrsitz, F. K. Reinhart, C. Gourgon, N. Herres, A. Vonlanthen, and H. Sigg, *J. Appl. Phys.* **87**, 7825 (2000).

Abstract Quantum optics plays a central role in the study of fundamental concepts in quantum mechanics, and in the development of new technological applications. Typical experiments employ sources of photon pairs generated by parametric processes such as spontaneous parametric down-conversion and spontaneous four-wave-mixing. The standard characterization of these sources relies on detecting the pairs themselves and thus requires single photon detectors, which limit both measurement speed and accuracy. Here it is shown that the two-photon quantum state that would be generated by parametric fluorescence can be characterised with unprecedented spectral resolution by performing a classical experiment. This streamlined technique gives access to hitherto unexplored features of two-photon states and has the potential to speed up design and testing of massively parallel integrated nonlinear sources by providing a fast and reliable quality control procedure. Additionally, it allows for the engineering of quantum light states at a significantly higher level of spectral detail, powering future quantum optical applications based on time-energy photon correlations.



High-resolution spectral characterization of two photon states via classical measurements

Andreas Eckstein¹, Guillaume Boucher¹, Aristide Lemaître², Pascal Filloux¹, Ivan Favero¹, Giuseppe Leo¹, John E. Sipe³, Marco Liscidini⁴, and Sara Ducci^{1,*}

1. Introduction

One of most utilized strategies to generate quantum correlated photons is exploiting spontaneous parametric down-conversion (SPDC), the spontaneous fission of a “pump” photon into a pair of photons, “signal” and “idler”, in a nonlinear medium (see Fig. 1a). In general, the probability of such an event is very small. Thus the quantum state describing the radiation field in the frequency regime of signal and idler is mostly the vacuum state $|0\rangle$, but it also contains a normalized two-photon component

$$|\psi_{\text{pair}}\rangle = \frac{1}{\sqrt{2}} \sum_{\nu,\eta} \iint d\omega_1 d\omega_2 \phi_{\nu,\eta}(\omega_1, \omega_2) \times \hat{a}_{\nu}^{\dagger}(\omega_1) \hat{a}_{\eta}^{\dagger}(\omega_2) |0\rangle. \quad (1)$$

with a small probability amplitude γ ; here $|\gamma|^2$ is the probability with which a photon pair is emitted, ν and

η label the modes into which the photons are generated, and ω_1 and ω_2 indicate their frequencies. The biphoton wavefunction $\phi_{\nu,\eta}(\omega_1, \omega_2)$ characterizes all properties of the two-photon state, and it describes any quantum correlation between the two emitted photons; $\phi_{\nu,\eta}(\omega_1, \omega_2)$ is determined by the medium in which SPDC occurs, as well as the pumping scheme [1]. In particular, $|\phi_{\nu,\eta}(\omega_1, \omega_2)|^2$ is known as the joint spectral density (JSD), with $|\phi_{\nu,\eta}(\omega_1, \omega_2)|^2 d\omega_1 d\omega_2$ being the probability of generating “photon 1” in the mode ν with frequency within $d\omega_1$ of ω_1 , and “photon 2” in the mode η with frequency within $d\omega_2$ of ω_2 .

So far, the JSD has been obtained by performing spectrally resolved single photon coincidence measurements [2–4]. In practice this strategy is constrained by the pair generation probability, which must be much smaller than unity within the time resolution of the single photon detector; otherwise an error would be introduced in the measured spectral correlations by the detection of multiple photon

¹ Laboratoire Matériaux et Phénomènes Quantiques, Université Paris Diderot, Sorbonne Paris Cité, CNRS-UMR 7162, Case courrier 7021, 75205 Paris Cedex 13, France

² Laboratoire de Photonique et Nanostructures, CNRS-UPR20, Route de Nozay, 91460 Marcoussis, France

³ Department of Physics and Institute for Optical Sciences, University of Toronto, 60 St. George Street, Ontario M5S 1A7, Canada

⁴ Department of Physics, University of Pavia, Via Bassi 6, I-27100 Pavia, Italy

*Corresponding author: e-mail: sara.ducci@univ-paris-diderot.fr

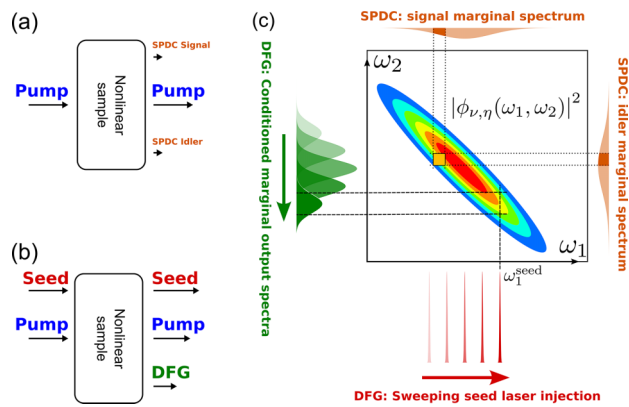


Figure 1 Working principle: (a) In a sample with a second order optical nonlinearity, SPDC converts a photon from the coherent pump pulse into a signal and idler photon pair with some probability. (b) If a coherent “seed” beam is introduced into the nonlinear sample in the mode of either the signal or the idler photon, a DFG process takes place and the conversion rate of pump photons is stimulated and increased by a factor proportional to the seed beam power. (c) Reconstruction of a typical JSD, shared by the SPDC and the DFG process for the same nonlinear sample and the same pump configuration. In the SPDC case, the emitted signal and idler photons are analyzed with spectrometers. By single photon coincidence detection of each spectrometer’s transmission, the intensity of a “pixel”, corresponding to the joint transmission of both spectrometers’ filter characteristics, is measured. The whole JSD can be reconstructed after collecting a sufficient number of events. In the DFG case, a narrow-band seed laser beam at frequency ω_1^{seed} stimulates the emission of a spectrally pre-conditioned coherent output beam in the idler mode. This spectrum is proportional to a “slice” of the JSD corresponding to the injected wavelength (see Eq. 2). Sweeping the seed wavelength allows the reconstruction of the JSD.

pairs. Moreover, after the detection event each single photon detector has to be re-set to an operational state; this results in a deadtime τ_D , which limits the maximally detectable coincidence rate to τ_D^{-1} . These constraints lead to unavoidable limitations in the spectral resolution with which the JSD can be determined. On one hand, a large number of coincidences is required for reasonably low relative errors, demanding long integration times. On the other hand, short experimental runs are desirable to minimize any drift in the experimental conditions and to allow the characterization of a large number of sources. Both of these requirements cannot be satisfied simultaneously, and so the development of convenient characterization strategies for quantum correlated photons, necessary for the emergence of advanced quantum optical applications in integrated devices [5–10], remains an outstanding technological challenge.

An alternative approach can be envisioned by recalling that, while SPDC can be described only in the framework of quantum theory, it can be viewed as difference frequency generation (DFG) in the quantum limit. Indeed, in DFG the conversion of pump photons to signal and idler pairs is stimulated by a seed beam, so SPDC can be considered as a DFG process stimulated by vacuum power fluctuations

[11]. The existence of a corresponding classical process naturally prompts one to question if it is possible to gain information about the quantum process by investigating only its classical analog. In the past, DFG has been used to determine the phase-matching function of SPDC sources [12, 13]. It has also been experimentally demonstrated that seeded four-wave mixing (FWM) can be used to directly determine the number of pairs that would be generated by spontaneous FWM in ring resonators [14]. Theoretical studies have shown that DFG can be similarly used to determine the number of pairs that would be generated by SPDC, both in ring resonators and in other structures such as waveguides [11]. In another context, DFG has been exploited for the realization of quantum cloning [15].

In this letter we extend this classical-quantum connection even further, and demonstrate experimentally that quantum correlations of photon pairs that would be generated by SPDC can be investigated through measurements of the corresponding DFG process [16]. Besides the intriguing fundamental aspect of this result, we show that our approach makes it possible to achieve an outstanding spectral resolution and increase data acquisition rates well beyond the state-of-the-art for spectrally resolved coincidence measurements [17, 18]. Finally, as one moves from SPDC to DFG, the increase of the generated output beam intensity by several orders of magnitude allows the replacement of single photon detectors with an optical spectrum analyzer (OSA), a widely available general purpose instrument.

The strategy we employ is based on the fact that, provided the same pumping scheme, the biphoton wavefunction $\phi_{\nu,\eta}(\omega_1, \omega_2)$ that *would be relevant* in SPDC plays the role of the response function of the structure that characterizes the generation of the stimulated light by DFG [16]. This is due to the fact that SPDC and DFG share the same phasematching configuration and pump spectrum and thus the same spectral correlation function, as indicated in Fig. 1. In particular, the average number of photons stimulated in the mode η with energy between ω_2 and $\omega_2 + \delta\omega_2$ by a coherent seeding beam exiting the system in mode ν and having energy centered at ω_1 with a width of $\delta\omega_1$ can be written as

$$\begin{aligned} & \langle \hat{a}_\eta^\dagger(\omega_2) \hat{a}_\eta(\omega_2) \rangle_{B_\nu(\omega_1)} \delta\omega_2 \\ & \approx 2 |B_\nu(\omega_1)|^2 |\gamma|^2 |\phi_{\nu,\eta}(\omega_1, \omega_2)|^2 \delta\omega_2 \delta\omega_1 \\ & \equiv |B_\nu(\omega_1)|^2 \langle \hat{a}_\eta^\dagger(\omega_2) \hat{a}_\eta(\omega_2) \hat{a}_\nu^\dagger(\omega_1) \hat{a}_\nu(\omega_1) \rangle \delta\omega_2 \delta\omega_1 \quad (2) \end{aligned}$$

where $|B_\nu(\omega_1)|^2$ is the average number of photons in the coherent seeding beam, and $\langle \hat{a}_\eta^\dagger(\omega_2) \hat{a}_\eta(\omega_2) \hat{a}_\nu^\dagger(\omega_1) \hat{a}_\nu(\omega_1) \rangle \delta\omega_2 \delta\omega_1$ is the average number of pairs generated within $\delta\omega_2$ and $\delta\omega_1$, by SPDC. Hence, Eq. 2 links the intensity of the signal stimulated via DFG (shown in Fig. 3) to the number of coincidences given by the photon pairs generated via SPDC in the corresponding experiment (Fig. 2). Thus, by scanning the coherent seeding beam over the full spectrum in a DFG experiment (see Fig. 1), it is possible to obtain the JSD, $|\phi_{\nu,\eta}(\omega_1, \omega_2)|^2$, that one would extract from

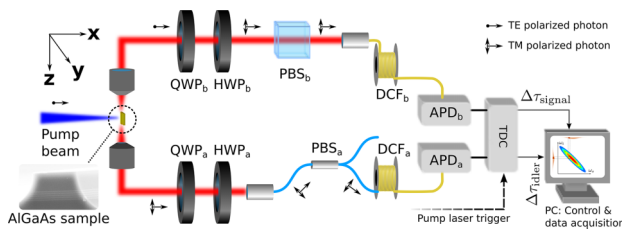


Figure 2 Sketch of the experimental setup for SPDC-based spectral correlation measurements. A pump pulse incident from the top of the semiconductor device leads to the creation of counterpropagating pairs of signal and idler photons in the waveguide. One of the two possible type II phase-matched processes is selected with polarization optics (HWP_{a/b}, PBS_{a/b}) and two fiber single photon spectrometers [4] are used to analyze signal and idler photon. By introducing high group velocity dispersion with the fiber spools DCF_{a/b}, the arrival time of each photon at the avalanche photo-diodes APD_{a/b} relative to the pump laser's electrical trigger signal reveals the photon frequency and is recorded by a personal computer via a time-to-digital converter (TDC).

coincidence measurements in the corresponding SPDC experiment (i.e., without seed). Finally, Eq. 2 tells us that the signal measured in the DFG experiments will be essentially $|B_V(\omega_1)|^2$ times the one measured in the corresponding coincidence measurement, and thus several orders of magnitude larger.

2. Experimental results

To demonstrate the advantages of our characterization technique, we experimentally compared SPDC and DFG-based frequency correlation characterizations of an integrated quantum light source: a picosecond-pulse-pumped AlGaAs ridge waveguide in a transverse pump configuration, in which an integrated microcavity with a resonance at the frequency of the pump pulse enhances [13] the emission of counterpropagating photon pairs from two simultaneously phase-matched type II SPDC processes [19]. Integrated sources are attracting a considerable interest for their flexibility and the possibility of mass production, but these sources are also particularly challenging to investigate.

In the SPDC experiment (Fig. 2) we use a fiber spectrometer [4] to reconstruct the JSD by collecting one photon pair at a time. When the detectors indicate the arrival of both a signal and idler photon originating from the same trigger pulse, the corresponding pair of signal/idler arrival times is added to a joint histogram. With a sufficiently large number of collected events this procedure yields the JSD, which is proportional to the coincidence counts plotted in Fig. 4a. Here the spectral resolution is $\Delta\lambda_{\text{SPDC}} = 224$ pm, limited by the temporal jitter of the single photon detection signal relative to the pump trigger signal.

In the DFG experiment (see Fig. 3) we collect the idler spectrum generated, under the same pumping condition, by sweeping a CW seed beam over the signal bandwidth of the spontaneous process. In accordance with Eq. 2, each pre-conditioned idler spectrum is proportional to the “slice” of

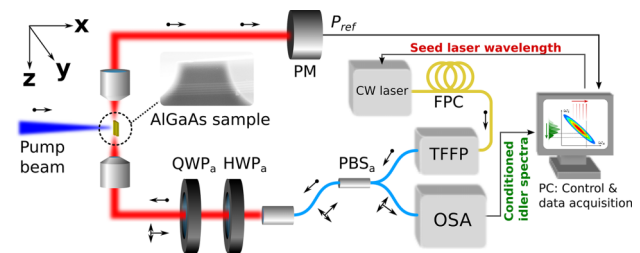


Figure 3 Sketch of the experimental setup for DFG-based spectral correlation measurements. Besides the pump pulse injected as in the SPDC experiment shown in Fig. 2, we inject a CW seed laser beam into the signal mode of the waveguide. Its polarization, adjusted by fiber polarization controller FPC and filtered by PBS_a, is used to select the same type II process as in the SPDC experiment. The transmitted seed laser power P_{ref} is measured by the powermeter PM. The tunable, fibered Fabry-Perot filter TFFP is used for spectral clean-up of the seed laser line. The backward emitted DFG beam has the same beam path as the seed beam, but has opposite polarization and propagation direction. The fiber integrated PBS_a is therefore used as a combiner/splitter for both beams to retrieve the DFG output and guide it to an optical spectrum analyzer (OSA).

the JSD corresponding to the pairs generated with the signal photon at the wavelength of the CW seed. The measurement result is presented in Fig. 4b. The spectral resolution along the signal axis is determined by the accuracy of the seed laser wavelength (20 pm), while along the idler axis it is given by the OSA resolution (20 pm).

From a simple visual comparison of Fig. 4a and 4b, it is hard to believe that the two pictures correspond to the same JSD. This is due to the extremely high resolution offered by our technique: for each pixel of the SPDC graph we have more than 100 pixels in the DGF measurement. Thus, to verify that the difference in the two measurements is simply determined by the spectral resolution, we calculated the expected JSD in the two cases (see Fig. 4c and d and Supplementary Information I).

When we assume a resolution of 224 pm of the SPDC experiment, the calculated JSD (Fig. 4c) corresponds to the blurred blob obtained from the coincidence measurement (Fig. 4a). On the contrary, if the resolution is increased, the calculated JSD (Fig. 4d) is in excellent agreement with that revealed by the DFG measurements (Fig. 4b). It should be noted that the characteristic grid pattern is the result of interferences within the waveguide due to the high index mismatch at the waveguide facets. The resulting high reflectivity creates a Fabry-Perot cavity situation for both output modes, so that the final two-photon spectrum is shaped by the characteristic transmission functions of the signal and idler cavities (see Supplementary Information I). Interestingly, this effect was theoretically predicted for resonant SPDC devices four years ago [20], but it has *never* been observed, due to the limitations on the resolution of measurements made with single photon detectors. The high resolution JSD measurement presented here boosts the pixel count over the SPDC results by two orders of magnitude, while taking less than half as long to collect.

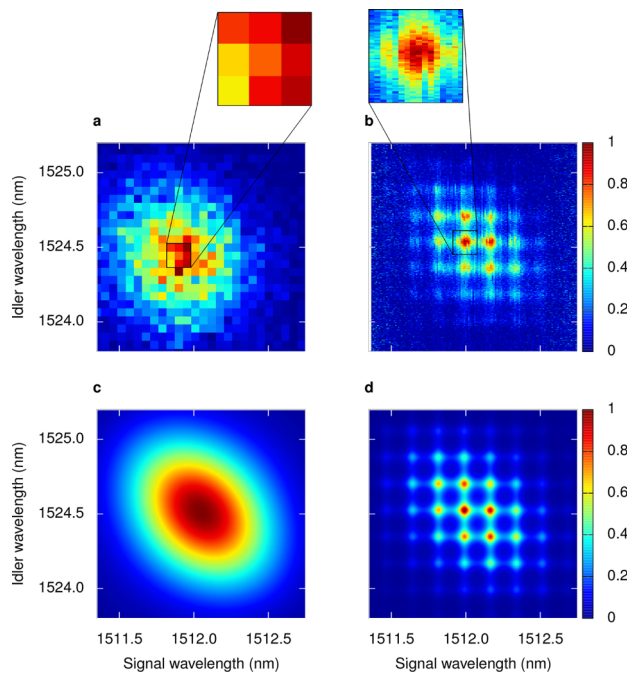


Figure 4 Results: (a) Experimental JSD obtained by SPDC-based measurements (see Fig. 2) with a sampling rate of 25×25 pixels over $1.4 \text{ nm} \times 1.4 \text{ nm}$, an integration time of 120 min, and a spectral resolution of 224 pm. The pixel pitch of $56 \text{ pm} \times 56 \text{ pm}$ is determined by the group velocity dispersion of the DCF coils and the temporal resolution of the TDC to measure photon arrival times. (b) Experimental JSD obtained by DFG-based measurements (see Fig. 3) with a sampling rate of 141×501 pixels over $1.4 \text{ nm} \times 1.4 \text{ nm}$, an integration time of 45 min, and a spectral resolution of 20 pm. The pixel pitch of $10 \text{ pm} \times 2.8 \text{ pm}$ corresponds to the scanning steps of the seed laser on the x-axis and to the spectral span over the number of data points of the OSA on the y-axis. The raw spectral data has been normalized to account for varying seed power (see Methods), leading to increased noise levels towards the left and the right edge of the plot. The visible offset between SPDC and DFG central wavelengths is caused by a shift of the central pump wavelength by 0.1 nm when re-locking the pump laser. (c) The figure c) is the convolution of figure d) with a Gaussian of FWHM 224 pm, corresponding to the resolution of the SPDC measurement. (d) Numerical calculation of the SPDC photon pairs' JSD generated by the device under study.

Thanks to this dramatic increase in data acquisition rate, it becomes possible to fully exploit the spectral resolution of the seed laser and the detector, and at the same time minimize statistical errors within realistic measurement durations.

Assuming a pure pump state, the Schmidt number $K = 1.05$ (obtained from simulations) quantifies the spectral entanglement of SPDC photon pairs emitted by the sample [21, 22]. From the measured high resolution JSD (Fig. 4b), we can under this assumption estimate an experimental lower boundary [23] at $K_{\min}^{\text{exp}} = 1.04$ after noise suppression, corresponding to a theoretical value of

$K_{\min} = 1.03$ extracted from (Fig. 4d) (see Supplementary Information II).

3. Experimental parameters

Figures 2 and 3 depict the measurement set-ups for the direct reconstruction of the JSD for SPDC and DFG-based methods, respectively. In each experiment, the sample is pumped by a mode-locked Coherent Mira Ti:Sapphire picosecond pulse laser at 759.1 nm, with a 0.4 nm spectral FWHM. Its repetition rate is reduced from 76 MHz to 3.8 MHz with an APE Pulse Select acousto-optical pulse picker, introducing a temporal jitter of up to $\tau_{\text{PP}} = 200 \text{ ps}$ into the pump laser's trigger signal. The beam power in front of the waveguide is 46 mW.

The sample is a chemically-etched ridge AlGaAs waveguide grown by molecular-beam epitaxy. The employed phasematching scheme is non-collinear with a pump pulse impinging on top of the waveguide at almost perpendicular incidence [13]. Signal and idler beam are emitted in cross-polarized, counterpropagating modes from either of two simultaneously phase-matched type II SPDC processes [19] (see Supplementary Information I for details).

In SPDC measurements, both signal and idler photons are collected on either side of the source with X40 microscope objectives. A set of wave plates and a polarizer allow us to select the correct polarization mode for each photon. Both photons then travel through DCF spools with a dispersion of $D_{\text{DCF}} = -1475 \text{ ps/nm}$. Free-running idQuantique id220 avalanche photo diodes (APD) act as single photon detectors at the end of each fiber. Detection efficiency is set to 20%, the timing jitter of the electrical detection signal is $\tau_{\text{APD}} = 250 \text{ ps}$ and the dead time $\tau_p = 10 \text{ }\mu\text{s}$. A quTools quTau TDC, connected to the APDs, measures the photons' arrival times relative to the pump laser's electrical trigger pulse with a $\tau_{\text{TDC}} = 81 \text{ ps}$ mean temporal bin size. The spectral resolution of the fiber spectrometer assembly is given by the joint temporal jitter of the pulse picker and the APD, as well as the TDC time resolution over DCF dispersion, resulting in $\Delta\lambda_{\text{SPDC}} = \sqrt{\tau_{\text{PP}}^2 + \tau_{\text{APD}}^2 + \tau_{\text{TDC}}^2} / D_{\text{DCF}} = 224 \text{ pm}$. The brightest "pixel" contains exactly 100 coincidence counts, so that detector saturation or multiple photon pair events distorting the result spectrum are not an issue.

In DFG measurements, we use a Yokogawa 6730C OSA with a resolution of 20 pm for spectral analysis of the idler beam. We employ a Tunic-Plus CW laser with a line-width of 100 kHz at an output power level of 8 mW to stimulate downconversion. The tunable fibered Fabry-Perot filter TFFP from ozOptics was used to clean the seed laser line; it has a Gaussian transmission profile with a 1.1 nm FWHM set to be centered at 1512.1 nm. At the output facet of the waveguide less than 10% of the nominal seed power exits, mainly due to losses in the filter and coupling losses. With the help of the OSA, we detected a deviation from the nominal output wavelength by -0.33 nm and verified its relative wavelength accuracy to be within the OSA resolution. The

filter causes a variable seed laser power during the seed laser's wavelength sweep, which we monitored by recording the power P_{ref} of the seed beam exiting the waveguide and accounted for in Fig. 4b by dividing the experimental value for each data point by the corresponding seed beam power. The maximal total DFG power measured with the OSA was 290 nW.

4. Conclusion and outlook

We have implemented a novel technique to reconstruct the joint spectral density of biphoton states that would be emitted by spontaneous parametric processes, using a completely classical difference frequency generation experiment. It significantly out-performs spectrally resolved single photon coincidence measurements, both in measurement time and resolution, and constitutes a fast, accurate, and reliable tool for the characterization of photon pair sources. Even in the first implementation performed here it provides a qualitative advance over previous methods, and reveals details of the biphoton joint spectral density that have never been observed before. Further enhancements can easily be achieved, as the 20 pm spectral resolution in our experiments could be improved by an order of magnitude using state-of-the-art spectrum analyzers and lasers. Adapting our method to explore polarization or spatial degrees of freedom would allow the complete characterization of biphoton states generated by parametric processes, opening the way to a new generation of experiments to explore hitherto unstudied aspects of nonclassical states of light.

Acknowledgement. M.L. was supported by the Italian Ministry of University and Research, FIRB Contract No. RBFR08XMVY, by the Foundation Alma Mater Ticinensis. J.S. was supported by the Natural Sciences and Engineering Research Council of Canada. This work was partly supported by the French Brazilian ANR HIDE project and by Région Ile de-France in the framework of C'Nano IdF with the TWILIGHT project. S.D acknowledges the Institut Universitaire de France.



Supporting Information: for this article is available free of charge under <http://dx.doi.org/10.1002/lpor.201400057>

Received: 13 March 2014, **Revised:** 7 May 2014,

Accepted: 20 May 2014

Published online: 25 June 2014

Key words: Photon pair sources, nonlinear optics, spectral correlations, semiconductor photonics.

References

- [1] Z. Yang, M. Liscidini, and J. E. Sipe, *Phys. Rev. A* **77**(3), 033808 (2008).
- [2] Y. H. Kim and W. P. Grice, *Optics Letters* **30**(8), 908 (2005).
- [3] W. Wasilewski, P. Wasylczyk, P. Kolenderski, K. Banaszek, and C. Radzewicz, *Optics Letters* **31**(8), 1130 (2006).
- [4] M. Avenhaus, A. Eckstein, P. J. Mosley, and C. Silberhorn, *Opt. Lett.* **34**(18), 2873–2875 (2009).
- [5] J. L. O'Brien, A. Furusawa, and J. Vučković, *Nature Photon.* **3**(12), 687 (2009).
- [6] E. Martín-López, A. Laing, T. Lawson, R. Alvarez, X. Q. Zhou, and J. L. O'Brien, *Nature Photon.* **6**(11), 773 (2012).
- [7] W. J. Munro, A. M. Stephens, S. J. Devitt, K. A. Harrison, and K. Nemoto, *Nature Photon.* **6**(11), 777 (2012).
- [8] M. A. Broome, A. Fedrizzi, S. Rahimi-Keshari, J. Dove, S. Aaronson, T. C. Ralph, and A. G. White, *Science* **339**(6121), 794 (2013).
- [9] A. Crespi, R. Osellame, R. Ramponi, D. Brod, E. Galvão, N. Spagnolo, C. Vitelli, E. Maiorino, P. Mataloni, and F. Sciarrino, *Nature Photon.* **7**(7), 545–549 (2013).
- [10] M. Collins, C. Xiong, I. Rey, T. Vo, J. He, S. Shahnia, C. Reardon, T. Krauss, M. Steel, A. Clark, and B. Eggleton, *Nature Communications* **4**, 2582 (2013).
- [11] L. G. Helt, M. Liscidini, and J. E. Sipe, *J. Opt. Soc. Am. B* **29**(8), 2199 (2012).
- [12] E. J. Mason, M. A. Albota, F. König, and F. N. C. Wong, *Opt. Lett.* **27**(23), 2115 (2002).
- [13] X. Caillet, V. Berger, G. Leo, and S. Ducci, *J. Mod. Opt.* **56**(2–3), 232–239 (2009).
- [14] S. Azzini, D. Grassani, M. Galli, L. C. Andreani, M. Sorel, M. J. Strain, L. G. Helt, J. E. Sipe, M. Liscidini, and D. Bajoni, *Opt. Lett.* **37**(18), 3807 (2012).
- [15] F. De Martini, V. Bužek, F. Sciarrino, and C. Sias, *Nature* **419**(6909), 815–818 (2002).
- [16] M. Liscidini and J. E. Sipe, *Phys. Rev. Lett.* **111**(Nov), 193602 (2013).
- [17] J. Chen, A. J. Pearlman, A. Ling, J. Fan, and A. L. Migdall, *Opt. Express* **17**(8), 6727 (2009).
- [18] T. Gerrits, M. J. Stevens, B. Baek, B. Calkins, A. Lita, S. Glancy, E. Knill, S. W. Nam, P. R. Mirin, R. H. Hadfield, R. S. Bennink, W. P. Grice, S. Dorenbos, T. Zijlstra, T. Klapwijk, and V. Zwiller, *Opt. Express* **19**(24), 24434 (2011).
- [19] A. Orioux, A. Eckstein, A. Lemaître, P. Filloux, I. Favero, G. Leo, T. Coudreau, A. Keller, P. Milman, and S. Ducci, *Phys. Rev. Lett.* **110**(16), 160502 (2013).
- [20] Y. Jeronimo-Moreno, S. Rodriguez-Benavides, and A. U'Ren, *Laser Phys.* **20**(5), 1221–1233 (2010).
- [21] R. Grobe, K. Rzazewski, and J. H. Eberly, *J. Phys. B* **27**(16), L503 (1994).
- [22] C. K. Law, I. A. Walmsley, and J. H. Eberly, *Phys. Rev. Lett.* **84**(Jun), 5304–5307 (2000).
- [23] G. Harder, V. Ansari, B. Brecht, T. Dirmeier, C. Marquardt, and C. Silberhorn, *Opt. Express* **21**(12), 13975 (2013).

Photon pair sources in AlGaAs: from electrical injection to quantum state engineering

C. Autebert, G. Boucher, F. Boitier, A. Eckstein¹, I. Favero, G. Leo and S. Ducci*

Laboratoire Matériaux et Phénomènes Quantiques, Université Paris Diderot, Paris Cedex 13, France

(Received 27 October 2014; accepted 11 December 2014)

Integrated quantum photonics is a very active field of quantum information, communication, and processing. One of the main challenges to achieve massively parallel systems for complex operations is the generation, manipulation, and detection of many qubits within the same chip. Here, we present our last achievements on AlGaAs quantum photonic devices emitting nonclassical states of light at room temperature by spontaneous parametric down conversion (SPDC). The choice of this platform combines the advantages of a mature fabrication technology, a high nonlinear coefficient, a SPDC wavelength in the C-telecom band and the possibility of electrical injection.

Keywords: integrated quantum photonics; semiconductor devices; electrical injection; parametric down conversion; entanglement; frequency correlations

1. Introduction

In the field of integrated quantum photonics, semiconductor materials have a strategic position to achieve extremely compact and massively parallel devices. In these last years, many efforts have been devoted to the development of biphoton sources of photonic circuits to manipulate correlated photon pairs and of chips including several functionalities (generation and manipulation or manipulation and detection). In the context of entangled photon sources, the efforts are focused on three main types of systems: quantum dots, silicon waveguides/resonators, and AlGaAs waveguides/resonators. Quantum dots-based photon pair sources exploit the radioactive decay of a biexciton state; entangled photon generation has been demonstrated both under optical [1] and electrical [2] pumping. This approach allows obtaining almost deterministic sources taking into account that a quantum dot can emit a photon pair per exciting pulse, and the recent progress in the efficiency of photon pairs extraction. However, since the exploitation of this physical process requires that the thermal energy of the system be inferior to the biexciton energy, these sources have to be cooled to typical temperatures of some Kelvin. Optical parametric conversion offers an alternative approach. Despite its nondeterministic nature, this process is the most widely used to produce photon pairs for quantum information and communications protocols. The spectacular progress made in silicon photonics has recently led to the demonstration of entangled photon sources with integrated devices having different geometries (waveguides,

nanowires, whispering-gallery mode resonators, etc.) [3–5]. Since Silicon doesn't present naturally a second-order nonlinearity, the main physical process used in this case is four-wave mixing. Sources emitting in the telecom band at room temperature have thus been demonstrated as making use of the SOI (Silicon-On-Insulator) platform, compatible with the CMOS technology. However, the indirect band gap of silicon hinders the demonstration of electrically driven devices. Conversely, the parametric down-conversion in direct band gap semiconductors is a process allowing to achieve devices working at room temperature, keeping the door open to the integration of the pump laser and the nonlinear medium. Several advances have recently been reported by exploiting the process of three-wave mixing on the AlGaAs platform which combines high conversion efficiencies (χ^2 of GaAs around 110 pm/V at 1550 nm) with the emission of photons in the near infrared. Since this material is not birefringent, different solutions have been proposed to satisfy the phase-matching condition among which form birefringence (consisting in inducing an artificial birefringence by alternating GaAs and AlOx layers [6]), quasi-phase-matching (by fabricating devices presenting a periodical inversion of the nonlinearity [7]), modal phase-matching (in which phase velocity mismatch is compensated by multimode waveguide dispersion [8,9]), and counterpropagating phase-matching (with a pump beam transverse to the generated photons [10]). In this paper, we address two main aspects: the pair production by electrical injection, leading to extremely compact sources

*Corresponding author. Email: sara.ducci@univ-paris-diderot.fr

¹Present address: Clarendon Laboratory, University of Oxford U.K

directly compatible with the existing telecom network, and the biphoton state engineering with a device in a transverse pump configuration, opening the way to dense coding of information.

2. Photon pair production by electrical injection at room temperature

As mentioned before, the direct band gap of AlGaAs presents an evident interest for the realization of electrically injected devices. Among the above mentioned phase-matching strategies, modal phase matching is the most promising to monolithically integrate the laser source and the nonlinear medium into a single device [11,12]. In this scheme, the interacting modes can either be confined by homogeneous claddings [13] or by photonic band gap [14], this latter option avoiding aging problems via the reduction in the total aluminum content.

Our device consists of a multilayer AlGaAs ridge waveguide: two Bragg mirrors provide both a photonic band gap confinement for a TE Bragg mode at 780 nm and total internal reflection claddings for TE and TM modes at 1.56 μm . The structure has been optimized for efficient type-II SPDC and lasing on the TE Bragg mode at room temperature. The spatial profile of the three interacting modes is shown in Figure 1. The details of the epitaxial structure can be found in [15].

The sample was grown by molecular beam epitaxy on a (100) *n*-doped GaAs substrate. Waveguides are fabricated using wet chemical etching to define 5.5–6 μm wide and 2 μm deep ridges along the (011) crystalline axis, in order to exploit the maximum nonzero nonlinear coefficient and a natural cleavage plane. Processing is completed by sample thinning and contact metallization with Au alloys; finally, samples are cleaved into 2 mm long stripes. Figure 2 shows the main processing steps used to fabricate the devices.

The simulated tuning curves of the source are given in Figure 3; the strong dispersion of the Bragg mode arising from the proximity to the energy band gap of the core

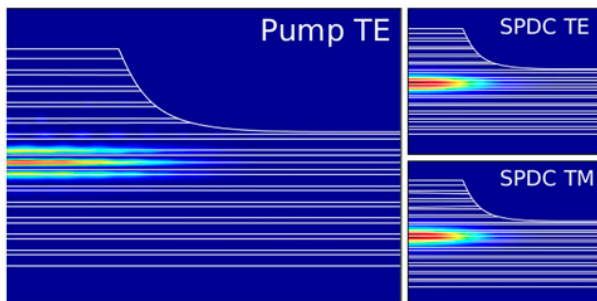


Figure 1. Simulated intensity profiles of the TE Bragg mode (pump beam at 775 nm), and the TE and TM fundamental modes (twin photons modes in the telecom range). (The colour version of this figure is included in the online version of the journal.)

induces a great sensibility of the signal and idler wavelength on the pump wavelength. This means that the spectral sensitivity range of the single-photon avalanche detectors will limit the window, in which both photons of a pair can be detected; the tunability of the laser wavelength will thus be a key issue for our device. The internal peak power and the voltage characteristics of the device as a function of the injected current are tested with a standard characterization bench allowing a temperature control between 15 and 40°C with a Peltier module. In the first devices, in order to avoid unwanted thermal drifts, we have employed current pulses of duration 120 ns and a repetition rate of 10 KHz. Figure 4 (a) reports the laser emission intensity spectra as a function of heat sink temperature, for an injected current of 422 mA; the general trend corresponds to the theoretical temperature dependence of the QW band gap (0.23 nm/°C) plotted in the same graph. Since the operation temperature of the device sets at the same time the laser and the phase-matching wavelength [15], we have checked the possibility to have an additional degree of freedom to control the laser emission; Figure 4 (b) displays the laser wavelength dependence on the injected current for a heat sink temperature of 14°C. The data demonstrate the presence of a stark effect shifting the gain spectrum (and thus the laser wavelength emission) of the device [16]; this effect, presenting much shorter response times than a temperature tuning, could indeed be exploited to set the working point of our devices.

In order to check the possibility to drive the device in continuous wave operation, we have measured the output power as a function of the duty cycle; Figure 5 reports our results for a device working at $T = 20^\circ\text{C}$. The observation of a constant peak output power for a duty cycle up to 66% indicates that a CW operation is possible, showing the technological maturity of the device.

The demonstration of photon pair emission in the telecom range is done by performing time correlation measurements under electrical injection in pulsed regime; the emerging TE and TM photons are detected with two InGaAs single-photon avalanche photodiodes having 20% detection efficiency and 50 ns gate, synchronized with the current pulses. A time-to-digital converter is used to analyze the time correlations between detected photons. Figure 6 reports the zero delay time coincidence value as a function of injected current for a typical device; for a current value below the laser threshold, no ‘true coincidences’ peak emerges from noise. For a current value between 570 and 780 mA, a peak appears and increases linearly with the injected current as expected from the typical diode behavior of the device.

Taking into account the overall transmission along the optical path, the internal generation of the device is $\sim 7 \times 10^{-11}$ pairs per injected electron above the threshold, corresponding to a SPDC efficiency $\sim 10^{-9}$ pairs/pump photon. The maximum signal-to-noise ratio (SNR) measured up to now in our devices is 15, mainly limited by the

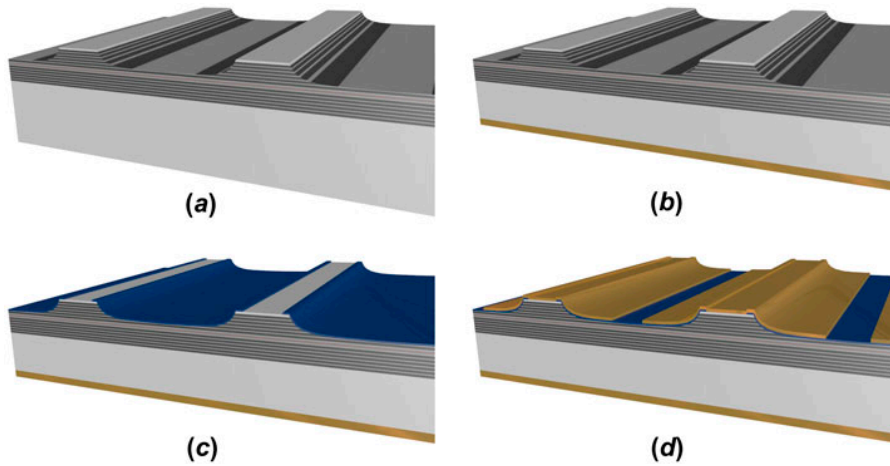


Figure 2. Main processing steps for the fabrication of the electrically pumped device: (a) ridge definition by wet etching; (b) lower contact deposition; (c) insulator deposition for independent addressing of each source; (d) upper contact deposition. (The colour version of this figure is included in the online version of the journal.)

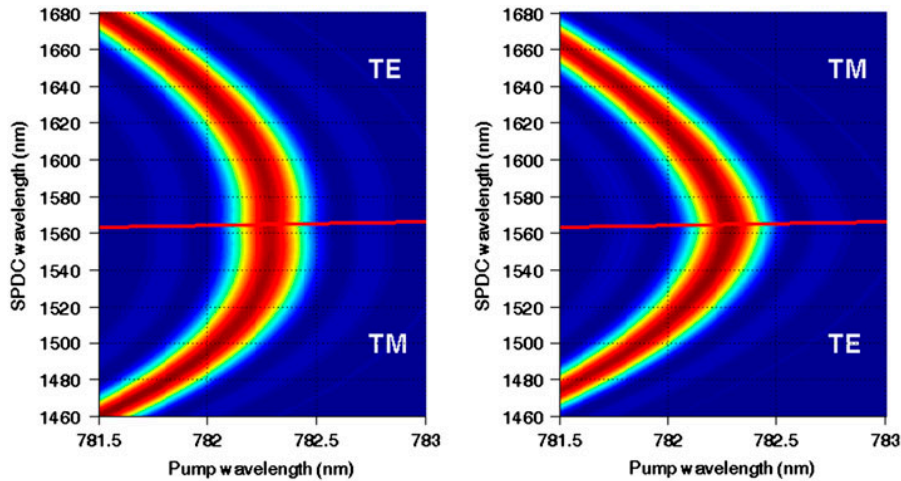


Figure 3. Numerical simulation of the type-II phase-matching resonance giving the twin photons wavelength as a function of the pump wavelength. (The colour version of this figure is included in the online version of the journal.)

luminescence noise; an optimization work on both sample design and technological processing is under progress to reduce spurious luminescence. Assuming that the source emits a Werner state, our result allows to estimate the fidelity F to the Bell state $|\psi_+\rangle$ that can be produced with the present value of SNR: F would be given by $(1 + 3P)/4$ with $P = SNR/(2 + SNR)$ leading to a value $\sim 91\%$, which is compliant with future experimental violation of Bell's inequality.

3. Quantum state engineering in a transverse pump configuration

The control of frequency correlations of photon pairs is a key issue for quantum information processing since different kinds of correlations are needed depending on

the specific application (linear optics quantum computation, clocks synchronization, long-distance communication in optical fibers, etc.). Indeed, their existence can either be an advantage for protocols based on hyperentangled states, or a drawback when, for example, the frequency of a photon must not reveal that of its twin. In this section, we present a source, based on a transverse pump configuration, allowing for a great versatility in the quantum state of the emitted biphoton. This device is based on the scheme of Figure 7: a pump beam at 775 nm impinging on top of a multilayer AlGaAs waveguide with an incidence angle θ generates by SPDC two orthogonally polarized signal/idler guided modes around 1.55 μm . Two Bragg mirrors provide a vertical microcavity for the pump beam increasing the conversion efficiency of the device [17,18].

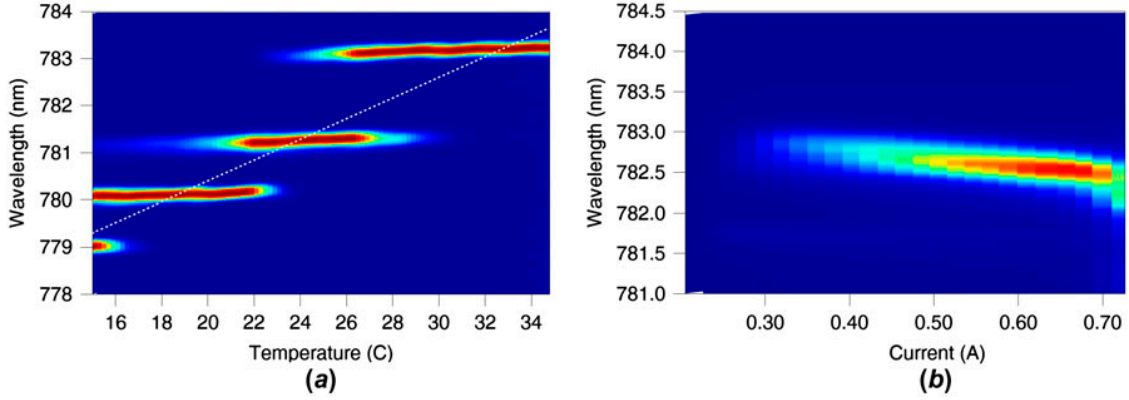


Figure 4. (a) Laser emission intensity as a function of wavelength and heat sink temperature. The dashed line shows the theoretical temperature variation of the QW band gap. (b) Laser wavelength dependence on the injected current demonstrating the presence of stark effect. (The colour version of this figure is included in the online version of the journal.)

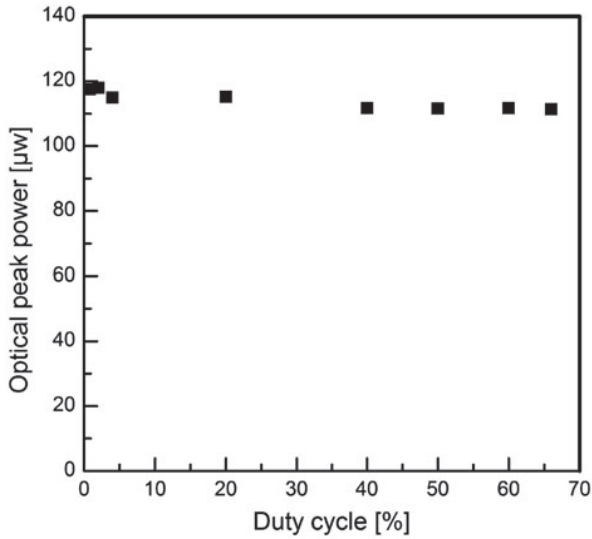


Figure 5. Laser output power as a function of the duty cycle of the injected current having a value of 755 mA.

As a consequence of the opposite propagation directions for signal and idler modes, two simultaneously phase-matched processes occur: one where the signal (which we will consider copropagating with the horizontal component of the pump beam) is horizontally polarized and the idler (which we will consider counterpropagating with the horizontal component of the pump beam) is vertically polarized (interaction 1), and the other where the signal is vertically polarized and the idler horizontally (interaction 2). The frequencies of the emitted fields are fixed by the energy conservation of the interacting modes ; Figure 8 reports the maximum values of the signal and idler wavelengths as a function of the angle of incidence of the pump beam. The black slashed lines correspond to pump beams at $+\theta_{deg}$ and $-\theta_{deg}$ such that each process generates a frequency degenerate photon pair.

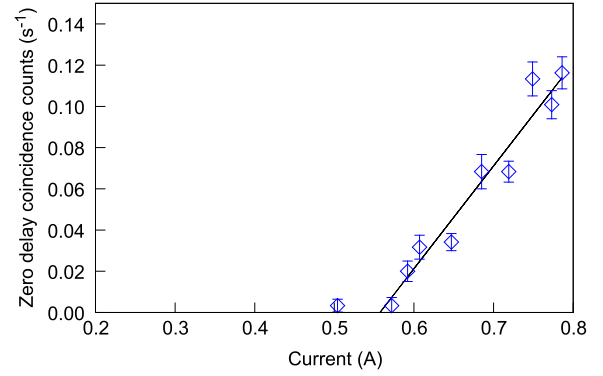


Figure 6. Zero delay time coincidence value as a function of the applied current. (The colour version of this figure is included in the online version of the journal.)

By simultaneously pumping the device with the angle $+\theta_{deg}$ and the angle $-\theta_{deg}$ and filtering out the additional frequency nondegenerate photons, we create the superposition state [19]

$$\begin{aligned}
 & |\Psi(\theta_{deg}, -\theta_{deg})\rangle \\
 &= \frac{1}{\sqrt{2}} \iint d\omega_s d\omega_i \left[\mathcal{A}^{(1)}(\omega_s, \omega_i, \theta_{deg}) \hat{a}_H^\dagger(\omega_s) \hat{b}_V^\dagger(\omega_i) \right. \\
 & \quad \left. + \mathcal{A}^{(2)}(\omega_s, \omega_i, -\theta_{deg}) \hat{a}_V^\dagger(\omega_s) \hat{b}_H^\dagger(\omega_i) \right] |0\rangle \quad (1)
 \end{aligned}$$

with

$$\begin{aligned}
 \mathcal{A}^{(j)}(\omega_s, \omega_i, \theta) &= \frac{1}{\sqrt{\mathcal{N}_j}} \Gamma_{ovl} f_M(\omega_s + \omega_i) \alpha(\omega_s + \omega_i) \\
 & \quad \times \int_{-\frac{1}{2}L}^{\frac{1}{2}L} dz e^{i\Delta k_j(\omega_s, \omega_i, \theta)z} S(z, \theta) \quad (2)
 \end{aligned}$$

Here, \mathcal{N}_j is a normalization constant, Γ_{ovl} is the nonlinear overlap integral between the interacting modes, L is the length of the illuminated region on the top of the waveguide, $f_M(\omega_s + \omega_i)$ is a function describing the Fabry–Perot effect

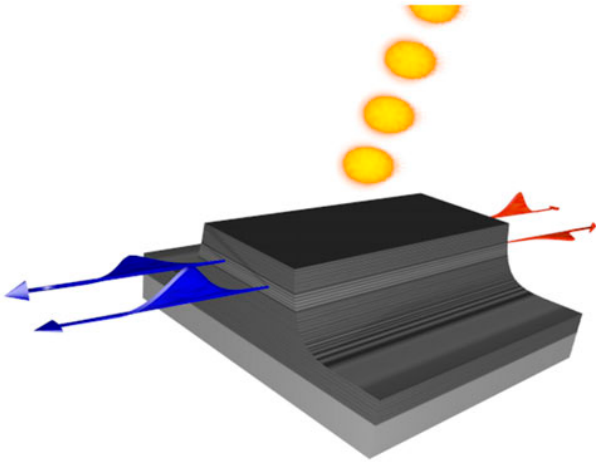


Figure 7. Operation principle of the device: a pump beam impinging on top of a waveguide with an angle θ produces twin photons via two possible interactions. Phase-matching is obtained automatically along the waveguide direction and through a periodic modulation of the waveguide core in the epitaxial direction. (The colour version of this figure is included in the online version of the journal.)

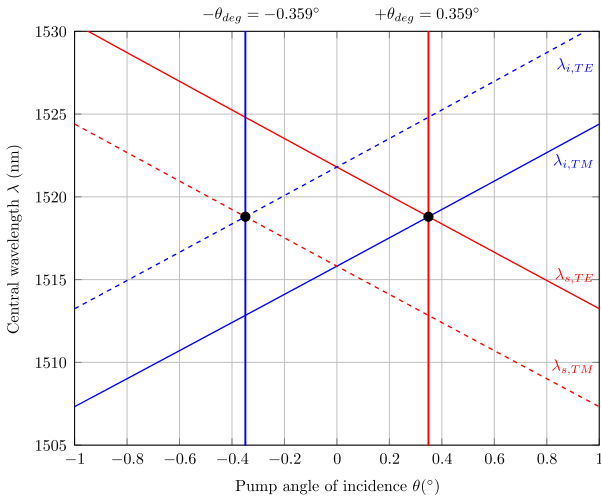


Figure 8. Simulated signal and idler tuning curves as a function of the angle of incidence of the pump beam. Polarization entangled photons can be generated by simultaneously pumping interaction 1 (solid line) at $+\theta_{deg}$ and 2 (dashed line) at $-\theta_{deg}$. (The colour version of this figure is included in the online version of the journal.)

of the microcavity on the pump beam, α is the spectral amplitude of the pump beam given by $\alpha_p(\omega) = \text{sech}\left(\frac{\omega - \omega_p}{\Delta\omega}\right)$, with ω_p the pump central frequency and $\Delta\omega$ its bandwidth, $\Delta k_j(\omega_s, \omega_i, \theta)$ are the phase-mismatch functions and $S(z, \theta)$ is the transverse spatial distribution of the pump beam.

$\mathcal{A}^{(j)}(\omega_s, \omega_i, \theta)$ are usually called joint spectral amplitudes and give the probability amplitude of an emitted

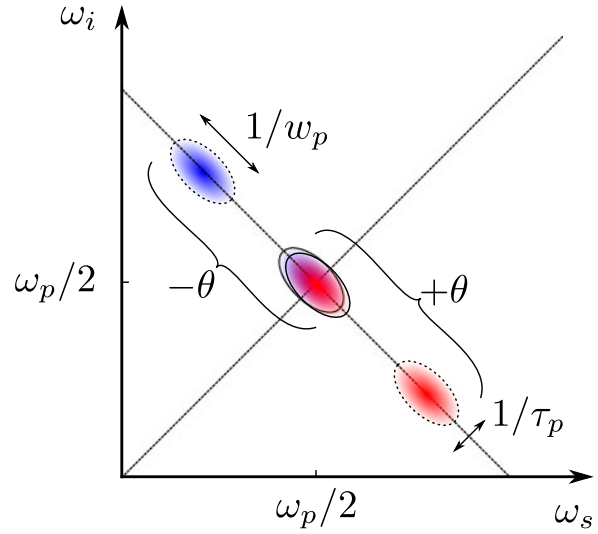


Figure 9. Sketch of the joint spectral amplitude obtained by pumping the device in the vicinity of $+\theta_{deg}$. The dimensions of the spectral distributions are determined by the spatial and spectral properties of the pump beam having a waist w_p and a pulse duration τ_p . (The colour version of this figure is included in the online version of the journal.)

photon pair emerging in the modes $\hat{a}_H(\omega_s)$ and $\hat{b}_V(\omega_i)$ ($j = 1$), or $\hat{a}_V(\omega_s)$ and $\hat{b}_H(\omega_i)$ ($j = 2$).

In Figure 9, we have sketched the joint spectral amplitudes corresponding to the two interactions, when the device is pumped in the vicinity of $+\theta_{deg}$ with a pulsed beam.

A complete reconstruction of the produced polarization state when the device is simultaneously pumped at $\pm\theta_{deg}$ has been done by a state tomography [20,21]. If only polarization measurements are performed and frequencies are not measured, it is convenient to work with the reduced state obtained by taking the trace over frequencies. We can, thus, calculate the reduced state and evaluated how its purity is linked to the parameters of the system [19]. In particular, we can link the *concurrence* \mathcal{C} , a commonly used entanglement estimator, to the joint spectral amplitudes of the two interactions by $\mathcal{C} = \iint d\omega_s d\omega_i \mathcal{A}^{(1)}(\omega_s, \omega_i, \theta_{deg}) \mathcal{A}^{(2)*}(\omega_s, \omega_i, -\theta_{deg})$.

A maximally entangled state will be obtained only if the two interactions are excited with the same strength and if the joint spectral amplitudes characterizing interaction 1 and 2 perfectly overlap. Figure 10 illustrates this point with two examples; case (a) corresponds to the experimental situation of [21], in which the two pumping beams are obtained by passing a Gaussian pump beam through the center of a Fresnel biprism. The angle of each prism can be chosen such that it deviates the pump beam entering the first face with a normal incidence by θ_{deg} . Case (b) corresponds to a situation in which the two incident pumping beams are obtained by producing two replicas of a Gaussian beam with a specific type of grating designed to diffract the incident

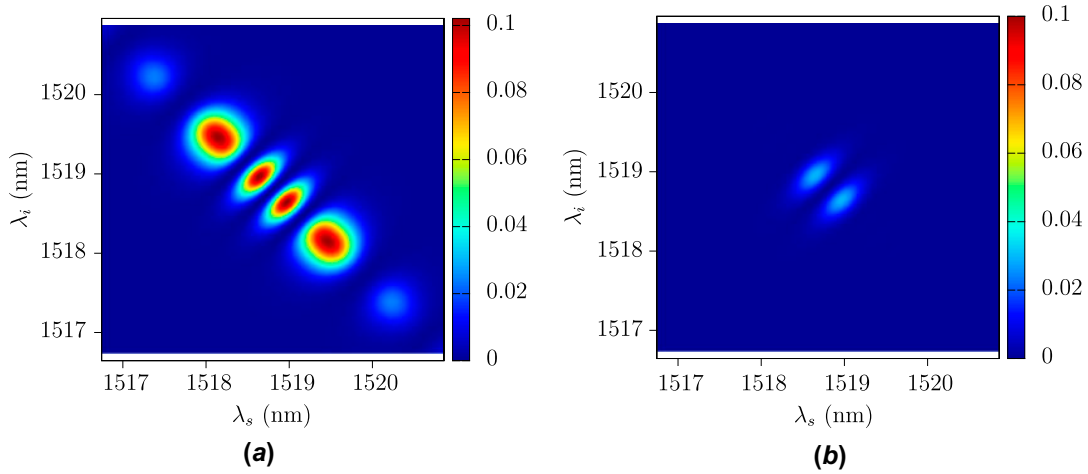


Figure 10. Squared absolute value of the difference between $\mathcal{A}^{(1)}(\omega_s, \omega_i, \theta_{deg})$ and $\mathcal{A}^{(2)*}(\omega_s, \omega_i, -\theta_{deg})$ using a biprism (a) or a lateral shear grating (b) to produce the two pumping beams to generate polarization entanglement. The concurrence value is 0.86 for case (a) and 0.97 for case (b). (The colour version of this figure is included in the online version of the journal.)

intensity only into its first order with an angle $\pm\theta_{deg}$. For each case, concurrence is calculated: the use of the grating allows to almost 'erase' the which-path information in the frequencies of the photons, and obtain a very high degree of entanglement ($C = 0.97$).

Another interesting feature of this device is its versatility in the control of the degree of frequency correlations between the two photons of the pair by an appropriate choice of the spatial and spectral pump beam profiles [22,23].

Taking into account, also the effect of the facets' reflectivities, which is around 25–30% due to the index contrast between semiconductor and air [24], the expression of the

joint spectral amplitude given above modifies in:

$$\mathcal{A}^{(j)}(\omega_s, \omega_i, \theta) \rightarrow \mathcal{A}^{(j)}(\omega_s, \omega_i, \theta) f_{TE}(\omega_i) f_{TM}(\omega_s)$$

where $f_{TE}(\omega_i)$ and $f_{TM}(\omega_s)$ describe the effect of the reflection on the waveguide facets for the generated TE and TM polarized photons. In order to experimentally characterize frequency correlations, we have recently demonstrated a technique based on difference frequency generation [25,26]. When the structure is stimulated with a CW signal beam, while it is subject to the same pumping scheme of interest for SPDC, the biphoton wavefunction relevant for the spontaneous experiment plays the role of the response function of the structure that characterizes the idler generated. Thus, by scanning the full spectrum of the signal photons, it is possible to obtain the joint spectral density that one would derive in a SPDC experiment. This method allows reconstructing the joint spectral density of a biphoton state with an unprecedented resolution (20 pm) giving access to features that were theoretically predicted but never observed (Figure 11). This streamlined technique has the potential to speed up design and testing of massively parallel integrated nonlinear sources and opens the way to a new generation of experiments to explore hitherto unstudied aspects of nonclassical states of light [27].

All these results demonstrate that III-V semiconductors are a viable platform to develop integrated components for future applications in quantum communications and information. Note that the small birefringence associated to these devices together with small footprint avoid the necessity of additional steps (such as walk off compensation or interferometric schemes) to convert the correlated photons into highly entangled states thus, facilitating the implementation of large-scale architectures.

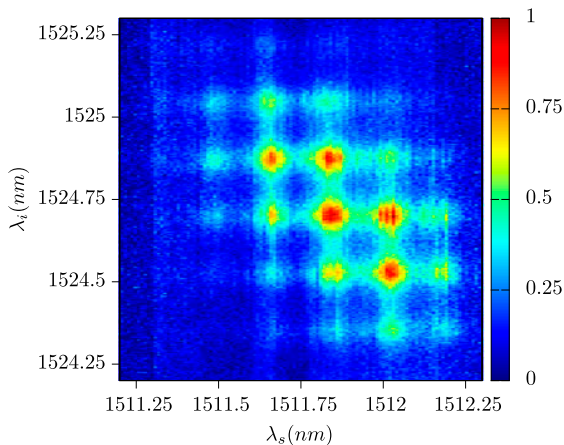


Figure 11. High resolution joint spectral intensity of the biphoton state emitted by our device pumped with a beam having a waist of 0.22 mm and a pulse duration of 3.5 ps. The observed intensity modulation is due to the multiple reflections of the twin photons on the waveguide facets. (The colour version of this figure is included in the online version of the journal.)

Acknowledgements

C.A. acknowledges the Délégation Générale de l'Armement (DGA) for financial support. F.B. acknowledges the Labex SEAM Program N°ANR-11-LABX-086 for financial support in the framework of the Program N°ANR-11-IDEX-0005-02. This work was partly supported by the French Brazilian ANR HIDE project. S. Ducci acknowledges the Institut Universitaire de France.

References

- [1] Dousse, A.; Suffczynski, J.; Beveratos, A.; Krebs, O.; Lemaître, A.; Sagnes, I.; Bloch, J.; Voisin, P.; et al. *Nature London*. **2010**, *466*, 217–220.
- [2] Salter, C.L.; Stevenson, R.M.; Farrer, I.; Nicoll, C.A.; Ritchie, D.A.; Shields, A.J. *Nature London*. **2010**, *465*, 594–597.
- [3] Takesue, H.; Matsuda, N.; Kuramochi, E.; Munro, W.J.; Notomi, M. *Nat. Commun.* **2013**, *4*, 2725-1–2725-7.
- [4] Azzini, S.; Grassani, D.; Strain, M.; Sorel, M.; Helt, L.; Sipe, J.; Liscidini, M.; Galli, M.; Bajoni, D. *Opt. Express*. **2012**, *20*, 23100–23107.
- [5] O'Brien, J.L.; Furusawa, A.; Vučković, J. *Nat. Photonics*. **2009**, *3*, 687–695.
- [6] Fiore, A.; Berger, V.; Rosencher, E.; Bravetti, P.; Nagle, J. *Nature London*. **1998**, *391*, 463–466.
- [7] Vodopyanov, K.L.; Levi, O.; Kuo, P.S.; Pinguet, T.J.; Harris, J.S.; Fejer, M.M.; Gerard, B.; Becouarn, L.; Lallier, E. *Opt. Lett.* **2004**, *29*, 1912–1914.
- [8] Ducci, S.; Lanco, L.; Berger, V.; de Rossi, A.; Ortiz, V.; Calligaro, M. *Appl. Phys. Lett.* **2004**, *84*, 2974–2976.
- [9] Helmy, A. *Opt. Express*. **2006**, *14*, 1243–1252.
- [10] Rossi, A.D.; Berger, V. *Phys. Rev. Lett.* **2002**, *88*, 043901-1–043901-4.
- [11] Orioux, A.; de Souza, C.E.R.; Lemaître, A.; Galopin, E.; Manquest, C.; Favero, I.; Leo, G.; Ducci, S.A. *A Laser diode for Integrated Photon Pair Generation at Telecom Wavelength*. Conference on Lasers and Electro-Optics, San José, CA, **2012**. pp JW4A.114.
- [12] Bijlani, B.J.; Abolghasem, P.; Helmy, A.S. *Appl. Phys. Lett.* **2013**, *103*, 091103-091105.
- [13] Rossi, A.D.; Ortiz, V.; Calligaro, M.; Vinter, B.; Nagle, J.; Ducci, S.; Berger, V. *Semicond. Sci. Technol.* **2004**, *19*, L99–L102.
- [14] Bijlani, B.J.; Helmy, A.S. *Opt. Lett.* **2009**, *34*, 3734–3736.
- [15] Boitier, F.; Orioux, A.; Autebert, C.; Lemaître, A.; Galopin, E.; Manquest, C.; Sirtori, C.; Favero, I.; Leo, G.; Ducci, S. *Phys. Rev. Lett.* **2014**, *112*, 183901–183904.
- [16] Le Thomas, N.; Pelekanos, N.; Hatzopoulos, Z. *Appl. Phys. Lett.* **2003**, *83*, 1304–1306.
- [17] Lanco, L.; Ducci, S.; Likforman, J.P.; Marcadet, X.; van Houwelingen, J.A.W.; Zbinden, H.; Leo, G.; Berger, V. *Phys. Rev. Lett.* **2006**, *97*, 173901–173904.
- [18] Orioux, A.; Caillet, X.; Lemaître, A.; Filloux, P.; Favero, I.; Leo, G.; Ducci, S. *J. Opt. Soc. Am. B: Opt. Phys.* **2011**, *28*, 45–51.
- [19] Boucher, G.; Eckstein, A.; Orioux, A.; Favero, I.; Leo, G.; Coudreau, T.; Keller, A.; Milman, P.; Ducci, S. *Phys. Rev. A*. **2014**, *89*, 033815-1–033815-8.
- [20] James, D.F.V.; Kwiat, P.G.; Munro, W.J.; White, A.G. *Phys. Rev. A*. **2001**, *64*, 052312-1–052312-15.
- [21] Orioux, A.; Eckstein, A.; Lemaître, A.; Filloux, P.; Favero, I.; Leo, G.; Coudreau, T.; Keller, A.; Milman, P.; Ducci, S. *Phys. Rev. Lett.* **2013**, *110*, 160502–160505.
- [22] Walton, Z.D.; Sergienko, A.V.; Saleh, B.E.A.; et al. *Phys. Rev. A*. **2004**, *70*, 052317-1–052317-5.
- [23] Caillet, X.; Berger, V.; Leo, G.; Ducci, S. *J. Mod. Opt.* **2009**, *56*, 232–239.
- [24] Jeronimo-Moreno, Y.; Rodriguez-Benavides, S.; U'Ren, A.B. *Laser Phys.* **2010**, *20*, 1221–1233.
- [25] Liscidini, M.; Sipe, J.E. *Phys. Rev. Lett.* **2013**, *111*, 193602–193605.
- [26] Eckstein, A.; Boucher, G.; Lemaître, A.; Filloux, P.; Favero, I.; Leo, G.; Sipe, J.E.; Liscidini, M.; et al. *Laser Photon. Rev.* **2014**, *8*, L76–L80.
- [27] Douce, T.; Eckstein, A.; Walborn, S.P.; Khoury, A.Z.; Ducci, S.; Keller, A.; Coudreau, T.; Milman, P. *Sci. Rep.* **2013**, *3*, 3530-1–3530-6.

Toolbox for continuous-variable entanglement production and measurement using spontaneous parametric down-conversion

G. Boucher,^{1,*} T. Douce,¹ D. Bresteau,^{1,†} S. P. Walborn,² A. Keller,³ T. Coudreau,¹ S. Ducci,¹ and P. Milman¹

¹Laboratoire Matériaux et Phénomènes Quantiques, Université Paris Diderot, CNRS UMR 7162, 75013, Paris, France

²Instituto de Física, Universidade Federal do Rio de Janeiro, Caixa Postal 68528, 21941-972 Rio de Janeiro, RJ, Brazil

³Institut de Sciences Moléculaires d'Orsay (CNRS), Université Paris-Sud 11, Bâtiment 350–Campus d'Orsay, 91405 Orsay Cedex, France

(Received 9 April 2015; published 4 August 2015)

We provide a toolbox for continuous-variable quantum-state engineering and characterization of biphoton states produced by spontaneous parametric down-conversion in a transverse pump configuration. We show that the control of the pump beam's incidence spot and angle corresponds to phase-space displacements of conjugate collective continuous variables of the biphoton. In particular, we illustrate with numerical simulations on a semiconductor device how this technique can be used to engineer and characterize arbitrary states of the frequency and time degrees of freedom.

DOI: [10.1103/PhysRevA.92.023804](https://doi.org/10.1103/PhysRevA.92.023804)

PACS number(s): 42.50.Dv, 03.67.Bg, 42.65.Lm, 42.65.Wi

I. INTRODUCTION

Spontaneous parametric down-conversion (SPDC) experiments play a prominent role in the field of quantum information and communications. Single and multiple photon pairs generated through SPDC display entanglement in multiple degrees of freedom (DOF) which are fundamentally different from each other. When combined or independently accessed, they constitute a powerful platform for experimental demonstrations of quantum protocols. Discrete DOF, such as polarization and orbital angular momentum, are currently used to implement quantum logic gates and protocols [1], test the nonlocal properties of quantum mechanics [2–5], and realize quantum cryptography [6–8] and teleportation [9,10]. DOF associated with observables with a continuous spectrum, like the quadratures of the electromagnetic field, potentially offer the same versatility as discrete ones in the field of quantum information. Continuous DOF in the single-photon regime, such as frequency, transverse momentum, or position, display a perfect analogy with a multiphoton single-mode continuous variable (CV) [11,12]. Consequently, they constitute an attractive platform to realize CV quantum information protocols [13] that are usually associated with the single-mode multiphoton configuration. For example, an appealing aspect of using a single photon's transverse coordinates in this field is their relatively easy manipulation with readily available optical devices, such as spatial light modulators (SLMs) and lenses [12], circumventing the difficulties encountered in multiphoton CV strategies to implement non-Gaussian operations, which are essential ingredients of universal quantum computation [13]. For these reasons, the study of entanglement in CVs in the single-photon regime is a valuable strategy to demonstrate CV-based quantum gates [14], quantum key distribution [15,16], error correcting codes [17,18], and quantum metrology protocols [19] and to study quantum-to-classical transitions [20,21]. Finally, we can

mention that continuous DOF can be combined with discrete ones to implement conditional operations [22–24].

CV entanglement in photon pairs can be generated in different DOF via SPDC; one example is the spatial transverse DOF of photon pairs produced in nonlinear bulk crystals. Tailoring the spatial properties of the pump beam has been previously employed to engineer [25,26] and detect quantum states of photon pairs with different properties: in [27] it was shown that controlling the transverse phase properties of the pump beam could lead to bunching or antibunching of a photon pair. References [22] and [28] demonstrate that the use of SLMs placed in the arms of an interferometer can lead to the measurement of arbitrary momenta of the quantum state associated with the transverse photonic DOF.

Using frequency as a CV degree of freedom instead of the transverse coordinates presents a series of potential advantages: in general, the transverse variables of a propagating field are entangled in the two-dimensional orthogonal spatial coordinates x and y or, equivalently, the momentum coordinates p_x and p_y ; this renders arbitrary state production and measurement more challenging and limits the applications of such DOF in quantum information tasks, since the quantum state associated with each spatial direction is entangled and can be cross-correlated between the x and the y directions. Moreover, this spatial entanglement is jeopardized when coupling into optical fibers or waveguides, while frequency states remain robust in such devices. For all these reasons, we illustrate our ideas focusing on the spectral degree of freedom. Indeed, the characterization of arbitrary frequency entangled states of photon pairs draws a lot of attention as illustrated by recent works on frequency-dependent intensity correlation measurements of the photon pair [29], the reconstruction of biphoton wave functions generated with a monochromatic pump [30], and amplitude-sensitive tomography techniques in the time-energy space [31].

In the waveguided regime, frequency-correlated, uncorrelated, and anticorrelated photon pairs can be produced by modifying the spectral properties of the pump beam [32,33]. Nevertheless, even if the nature of correlations can be controlled, pump bandwidth modification alone cannot lead to arbitrary CV-state engineering, an essential tool for CV

*guillaume.boucher@univ-paris-diderot.fr

†Current address: Laboratoire Aimé Cotton, Bâtiment 505–Campus d'Orsay, Université Paris-Sud 11, 91405 Orsay Cedex, France.

quantum information and communications, fundamental tests of quantum mechanics and quantum metrology.

In this paper, we provide a toolbox to exploit the capabilities of SPDC to create, measure, and characterize entanglement in the CV DOF of a photon pair. Our strategy is based on the combination of pump spatial engineering with the possibility of characterizing a Wigner function of the photon pair using a Hong-Ou-Mandel (HOM)–type [34] experiment [35].

In order to clarify these concepts, we present the case study of a transversally pumped semiconductor waveguide [36,37] potentially having great versatility in the control of the biphoton frequency correlations [29]. Indeed it has been shown that the pumping configuration allows one to modify the phase matching conditions by simply changing the spatial properties of the pump beam [38–40], e.g., its waist or angle of incidence. However, more complex quantum-state engineering has not been explored so far.

II. DESCRIPTION OF THE BIPHOTON STATE WITH CHRONOCYCLIC WIGNER FUNCTIONS

The properties of the photon pair are described by the biphoton wave function, which takes a complex form due to the constraints imposed by momentum and energy conservation. By neglecting group velocity dispersion (which is justified in the spectral range of the generated photon pairs) and in the narrow-bandwidth limit for the pump beam, we can write the state of the pair in the form

$$|\Psi\rangle = \chi_\Gamma \iint d\omega_s d\omega_i f_+(\omega_s + \omega_i) f_-(\omega_s - \omega_i) |\omega_s, \omega_i\rangle, \quad (1)$$

where $\omega_{s,i}$ represent the signal and idler frequencies, respectively, and χ_Γ is a normalization constant [41]. The function f_+ corresponds to the spectrum of the pump beam reflecting the condition of energy conservation ($\omega_p = \omega_s + \omega_i \equiv \omega_+$). The phase of this function is affected by the presence of a microcavity formed by two Bragg mirrors as shown in the nonflat phase profile in Fig. 1(c). The narrow-band assumption allows us to consider the phase-matching-dependent part of the biphoton state as a strictly antidiagonal function f_- ,

$$f_-(\omega_- \equiv \omega_s - \omega_i) = \int_{-L/2}^{L/2} dz \varphi(z) e^{i \frac{(\omega_s - \omega_i)z}{\bar{v}_g}}, \quad (2)$$

where L is the length of the sample, \bar{v}_g is the average group velocity of the signal and idler photons at frequency degeneracy, and $\varphi(z) = \Phi(z) e^{-ik_{\text{deg}}z}$. The function $\Phi(z)$ is the spatial profile of the pump beam and $k_{\text{deg}} = \sin(\theta_{\text{deg}}) \frac{\omega_p^{(0)}}{c} = \frac{(n_s - n_i) \omega_p^{(0)}}{2c}$, where $n_{s,i}$ corresponds to the signal and idler effective refractive indices at degeneracy, $\omega_p^{(0)}$ is the central frequency of the pump beam, and θ_{deg} is the pumping incidence angle for which degeneracy occurs.

If the dimensions of the waveguide are large with respect to the pump waist, i.e., the limit where $L \rightarrow \infty$, f_- can be approximated by the Fourier transform of the spatial profile of the pump beam:

$$f_-(\omega_-) \approx \tilde{\varphi}\left(\frac{\omega_-}{\bar{v}_g}\right). \quad (3)$$

We start by considering the situation depicted in Fig. 1(a), where a Gaussian pump beam with waist w_p impinges onto the source at an angle θ and position z_0 . The field distribution along the axis z is $\Phi(z) \propto e^{-(z-z_0)^2 \cos^2 \theta / w_p^2} e^{i(k \sin \theta)z}$ and therefore f_- reads

$$f_-(\omega_-) \propto e^{i\omega_- \tau_0} e^{-\frac{(\omega_- - \omega_-^{(0)})^2}{\Delta\omega^2}}, \quad (4)$$

with $\tau_0 = z_0/\bar{v}_g$, $\Delta\omega = \bar{v}_g/2w_p$, and $\omega_-^{(0)} = (k \sin \theta - k_{\text{deg}})\bar{v}_g \approx \delta\theta \bar{v}_g \omega_p/c$ [42]. Figures 1(b) and 1(c) represent the biphoton wave-function norm and phase distribution numerically simulated for a pump impinging at the degeneracy angle θ_{deg} at $z_0 = 0$ with waist $w_p = 200 \mu\text{m} \ll L = 2 \text{ mm}$, central wavelength $\lambda_p = 775 \text{ nm}$, and pulse duration $\tau_p = 3.2 \text{ ps}$ [43].

Instead of the complex-valued biphoton wave function, a more convenient representation is given by chronocyclic Wigner functions, which are the time-energy analogs of the phase-space Wigner functions. With this approach, the time and energy properties of the single photons of the pairs are illustrated with real quantities [44,45], in the same way that pulses of light are depicted in the domain of ultrafast optics [46]. In this work, we describe, instead of the properties of the isolated photons of the pair, their correlations along the antidiagonal part f_- of the biphoton wave function. This represents the quasiprobability distribution of the biphoton as a function of the detuning Ω between signal and idler frequencies and the time-delay-conjugated variable τ . The corresponding Wigner function W_- is given by

$$W_-(\tau, \Omega) = \int_{-\infty}^{\infty} d\omega_- f_-(\Omega - \omega_-) f_-^*(\Omega + \omega_-) e^{i2\tau\omega_-}. \quad (5)$$

Using the expression obtained in (4), we see that this corresponds to a Gaussian Wigner function centered at point $\tau = \tau_0$, $\Omega = \omega_-^{(0)}$, of widths $\Delta\Omega = 1/\Delta\tau = \Delta\omega = \bar{v}_g/2w_p$, which is equivalent to the representation of a coherent state [see Fig. 1(d)]. Thus, in this situation, shifting the pumping spot z_0 is equivalent to realizing displacements in the τ axis of the phase space, while changing the angle of incidence θ of the pump beam corresponds to shifting the state along the Ω axis.

III. ENGINEERING AND MEASUREMENT OF BIPHOTON STATES

More complex states can be obtained by engineering the pump beam. Indeed two identical beams impinging at z_a and z_b will generate a superposition of two coherent states displaced along the τ axis. In the limit $|z_a - z_b| \gg 2w_p$ such states are almost orthogonal, representing a superposition of two distinct quasiclassical states (Schrödinger cat-like states). An analog superposition is obtained along axis Ω by using two angles of incidence, θ_a and θ_b , impinging at the same point z_0 . Quasiorthogonality is obtained for $|\theta_a - \theta_b| \gg \frac{c}{2\omega_p w_p}$. We can generalize these Schrödinger cat-like states using more complex configurations of pump beams. As an illustration, we choose a compass state (see Fig. 2), a superposition of four coherent states presenting interesting applications in quantum metrology, as pointed out in [47] and [48]. In order to obtain this state, a set of four different pump beam configurations is required: two pairs of beams impinging at two different points

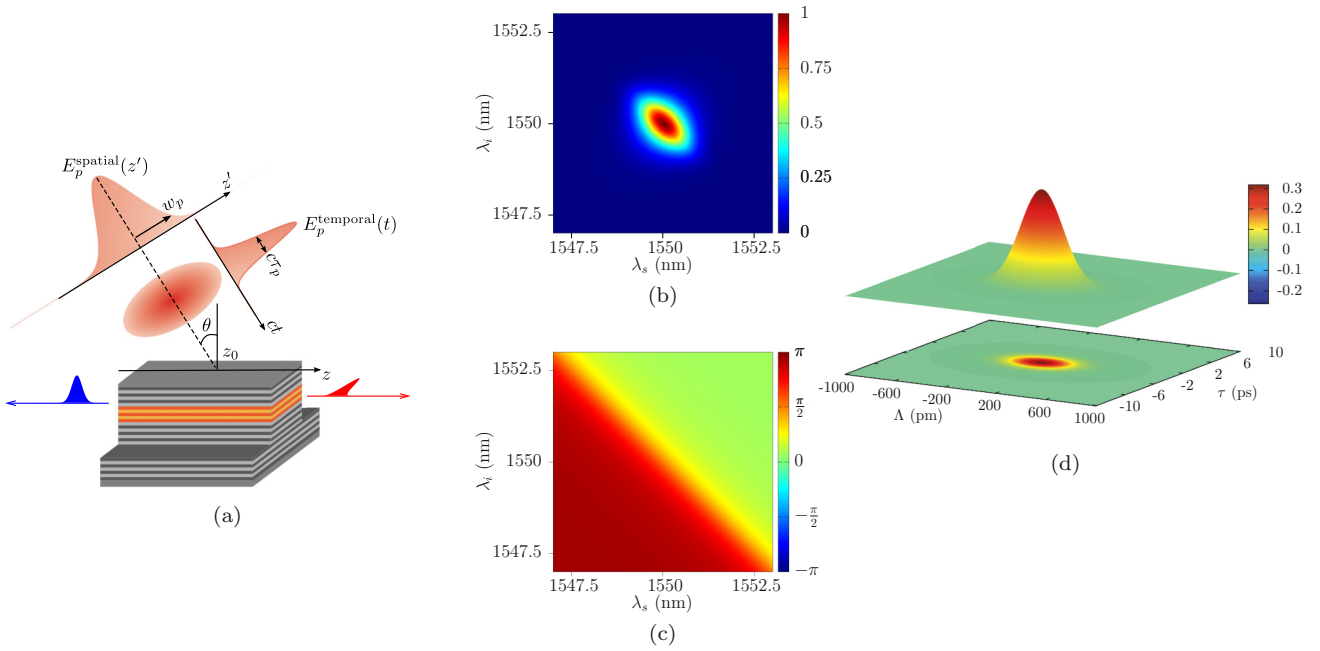


FIG. 1. (Color online) (a) Counter-propagating phase-matching scheme implemented in a semiconductor microcavity waveguide. The characteristics of the pump pulses allow us to tune the time-energy properties of the biphoton. (b) Norm and (c) phase of the biphoton wave function for $w_p = 200 \mu\text{m}$, $\lambda_p = 775 \text{ nm}$, $\tau_p = 3.2 \text{ ps}$, and $\theta = \theta_{\text{deg}}$. The phase pattern in (c) is due to the resonance of the pump in the microcavity. (d) Corresponding Wigner function. The Ω axis is given in units of $\Lambda = \frac{8\pi c}{\omega_p} \Omega$.

separated by a distance Δz , each pair consisting of two beams tilted symmetrically with respect to the degeneracy angle as shown in Fig. 2(a).

The procedure detailed above to generate quantum states with different properties and applications can be generalized, leading to the creation of arbitrary CV quantum states, since

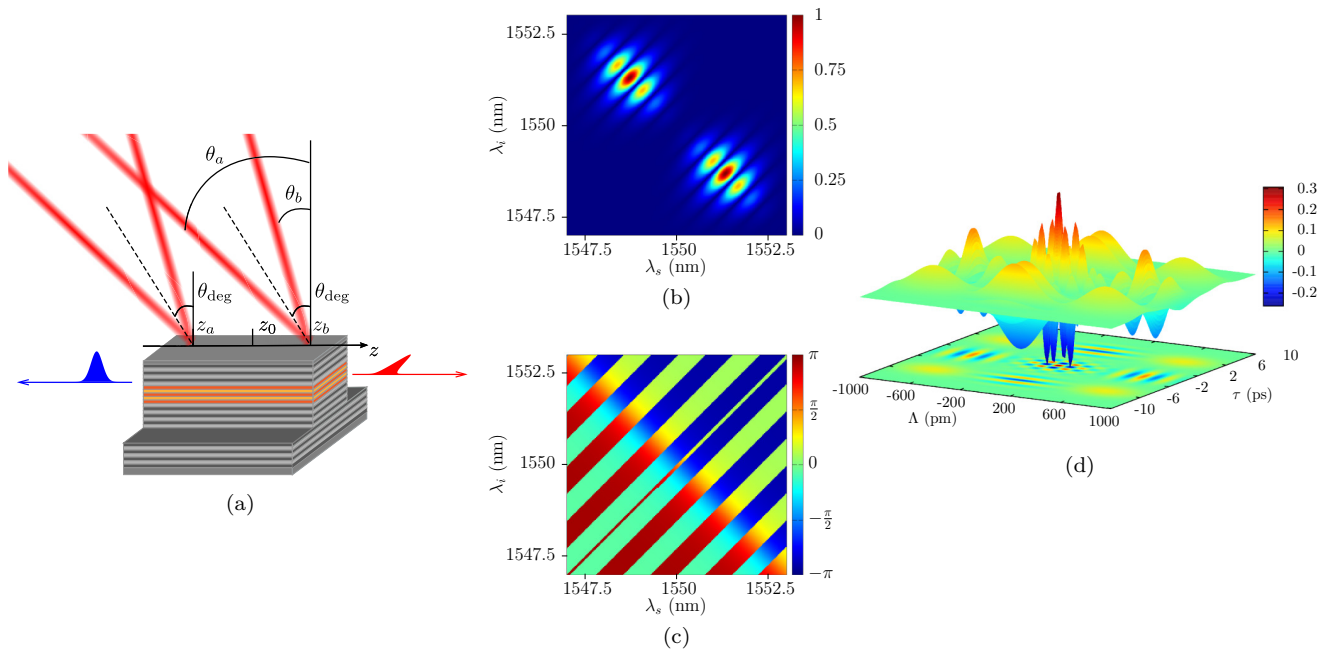


FIG. 2. (Color online) (a) Pump illumination scheme to generate a compass state: two pairs of beams impinge onto the waveguide at two spots, z_a and z_b , equidistant from the center of the source, each pair consisting of two beams tilted symmetrically with respect to the degeneracy angle ($\theta_{a,b} = \theta_{\text{deg}} \pm \delta\theta$). (b) Norm and (c) phase of the biphoton wave function of the corresponding cat state with $\delta\theta = 9.37'$, $|z_a - z_b| = 1 \text{ mm}$ and for each beam $w_p = 200 \mu\text{m}$, $\lambda_p = 775 \text{ nm}$, $\tau_p = 3.2 \text{ ps}$, and $\theta = \theta_{\text{deg}}$. (d) Corresponding Wigner function with $\Delta\Lambda = 1.37 \text{ nm}$ and $\Delta\tau = 10.8 \text{ ps}$. The Ω axis is given in units of $\Lambda = \frac{8\pi c}{\omega_p} \Omega$.

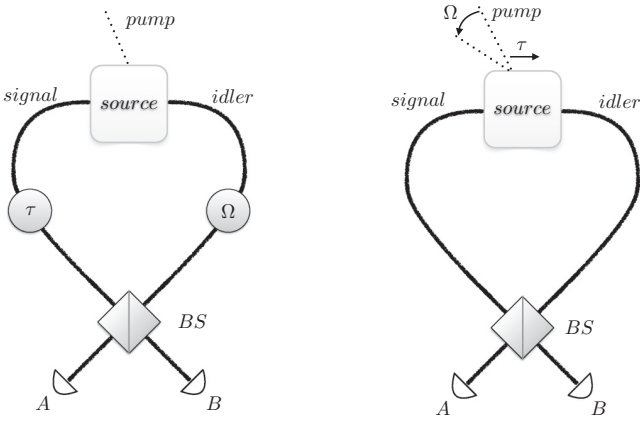


FIG. 3. Two possible strategies to realize the modified HOM experiment leading to the measurement of the Wigner function. Left: Displacements in time and frequency are realized in each arm of the interferometer after the production of the photon pair. Right: In a completely analogous setup, displacements in time and frequency are realized by pump engineering. While modifying the incidence angle of the pump beam, and, consequently, the phase matching condition, corresponds to displacements in frequency, modifying the pump's incidence spot corresponds to displacements in time.

any state can be constructed from the overcomplete basis of coherent states.

We now discuss how pump engineering can be used to characterize arbitrary CV states using the direct measurement of the Wigner function in all points of phase space. In [35], it was shown how a generalization of the HOM experiment leads to direct measurement of the Wigner function in the Ω, τ phase space. This generalization consists of considering displacements in the frequency degree of freedom of the photons, in addition to time displacements. Of course, displacing either one of these parameters modifies the distinguishability between the photons in each arm of the HOM interferometer, as depicted in Fig. 3. Time displacements can be realized relatively straightforwardly by simply modifying the optical path in each arm of the HOM interferometer. However, the frequency displacements required to reconstruct the Wigner function are quite broad with respect to the performances of currently available optical modulators [49]. Pump engineering provides an alternative solution to realize both time and frequency displacements, dramatically simplifying the direct measurement of the Wigner function and the CV state characterization.

As discussed previously, modification of the pump beam's incidence angle corresponds to displacing the central frequency of the symmetric part of the wave function associated with the photon pairs, while modification of the incidence point corresponds to time displacements. Using these ingredients, one can devise a procedure for the complete Wigner function measurement as follows: in the first step, an initial state is engineered. This state is the one to be characterized. Running the HOM experiment with no frequency or time displacement leads directly to the value of $W_-(0,0)$, the Wigner function at the origin [35]. Then tilting the incident pump beams by

a given amount and repeating the same HOM experiment is equivalent to displacing the original state in frequency and measuring its Wigner function, leading to the value of $W_-(\Omega,0)$. Analogously, displacing the pump beam in the z axis and repeating the HOM strategy leads to the value of $W_-(0,\tau)$. It is clear that, by combining different tilting angles and displacements, one can obtain an arbitrary point of the Wigner function and reconstruct $W_-(\Omega,\tau)$ for all values of Ω and τ . In order to characterize the quantum state, the magnitude of the displacements in both axes of phase space should cover the region where $|f_-(\omega_-)|^2$ has a significant value. This corresponds to realizing the pump's angular displacements in an interval $\Delta\theta \approx \theta_a - \theta_b = 18.7^\circ$, while its impinging position is displaced by an amount $\Delta z \approx z_a - z_b = 1$ mm (see Fig. 2). Note that, as shown in [50], the proposed strategy presents the advantage of not being limited by the detector's response time for measuring highly oscillating fringes or phase-space structures associated with sub-Planck scales [47]. Note that the resolution required for displacements along the z axis is easily achieved; as far as the angular displacement is concerned, since $\Delta\theta$ is of the order of 2.7 mrad, a resolution of 100 μrad is sufficient to resolve the fringes. This is also achievable with thermal stabilization and stable mechanical mountings.

One may argue that modifying the pump, in reality, modifies the state to be measured instead of the measuring apparatus that is probing different points of the phase space; but this is common practice in quantum measurement strategies, where the modification of the settings of the measurement apparatus is formally equivalent to that of the state to be measured. This equivalency was used, for instance, in the context of cavity quantum electrodynamics in [21]. There, the Wigner function is directly measured using a Rydberg atom interacting dispersively for a fixed time interval with the field of a high-quality microwave cavity. The setup is kept the same for all points in phase space and the quantum state of the field in the cavity to be measured is displaced, and consequently modified, through the application of a coherent field. Also in [30], the use of a monochromatic pump generating pairs of photons through SPDC is combined with modification of the pump frequency (or shifts in the temperature of the crystal) to circumvent the difficulty of broad frequency displacements. In the present case, changing the pump spatial configuration is equivalent to displacing the state to be measured.

IV. CONCLUSION

In conclusion, we have shown how spatial pump engineering can be used to generate arbitrary CV frequency states of a photon pair and directly characterize it through a HOM-like experiment. The combination of the variety of pumping geometries with that of the possible design of integrated photonic circuits [51] will allow the realization of complex and versatile quantum photonic chips [40]. The generalization of this technique to prepare quantum states with higher photon numbers, as well as to simulate the dynamics of CV states and the application of different quantum operations to it, is an interesting open perspective that will be investigated.

ACKNOWLEDGEMENTS

This work was partly supported by the ANR project Semi-QuantRoom ANR-14-CE26-0029 and by Region Ile de France

in the framework of C’Nano IdF with the GENESIS project. S.D. acknowledges the Institut Universitaire de France.

G.B. and T.D. contributed equally to this work.

-
- [1] J. L. O’Brien, *Science* **318**, 1567 (2007).
- [2] J. S. Bell, *Physics* **1**, 195 (1964).
- [3] J. F. Clauser, M. A. Horne, A. Shimony, and R. A. Holt, *Phys. Rev. Lett.* **23**, 880 (1969).
- [4] A. Aspect, P. Grangier, and G. Roger, *Phys. Rev. Lett.* **49**, 91 (1982).
- [5] R. Ursin, F. Tiefenbacher, T. Schmitt-Manderbach, H. Weier, T. Scheidl, M. Lindenthal, B. Blauensteiner, T. Jennewein, J. Perdigues, P. Trojek, B. Omer, M. Furst, M. Meyenburg, J. Rarity, Z. Sodnik, C. Barbieri, H. Weinfurter, and A. Zeilinger, *Nature Phys.* **3**, 481 (2007).
- [6] T. Jennewein, C. Simon, G. Weihs, H. Weinfurter, and A. Zeilinger, *Phys. Rev. Lett.* **84**, 4729 (2000).
- [7] D. S. Naik, C. G. Peterson, A. G. White, A. J. Berglund, and P. G. Kwiat, *Phys. Rev. Lett.* **84**, 4733 (2000).
- [8] N. Gisin, G. Ribordy, W. Tittel, and H. Zbinden, *Rev. Mod. Phys.* **74**, 145 (2002).
- [9] C. H. Bennett, G. Brassard, C. Crépeau, R. Jozsa, A. Peres, and W. K. Wootters, *Phys. Rev. Lett.* **70**, 1895 (1993).
- [10] D. Bouwmeester, J.-W. Pan, K. Mattle, M. Eibl, H. Weinfurter, and A. Zeilinger, *Nature (London)* **390**, 575 (1997).
- [11] A. F. Abouraddy, T. Yarnall, B. E. A. Saleh, and M. C. Teich, *Phys. Rev. A* **75**, 052114 (2007).
- [12] D. S. Tasca, R. M. Gomes, F. Toscano, P. H. Souto Ribeiro, and S. P. Walborn, *Phys. Rev. A* **83**, 052325 (2011).
- [13] S. L. Braunstein and P. van Loock, *Rev. Mod. Phys.* **77**, 513 (2005).
- [14] S. Lloyd and S. L. Braunstein, *Phys. Rev. Lett.* **82**, 1784 (1999).
- [15] F. Grosshans and P. Grangier, *Phys. Rev. Lett.* **88**, 057902 (2002).
- [16] F. Grosshans, G. Van Assche, J. Wenger, R. Brouri, N. J. Cerf, and P. Grangier, *Nature* **421**, 238 (2003).
- [17] D. Gottesman, A. Kitaev, and J. Preskill, *Phys. Rev. A* **64**, 012310 (2001).
- [18] O. J. Farfás, F. de Melo, P. Milman, and S. P. Walborn, *Phys. Rev. A* **91**, 062328 (2015).
- [19] V. Giovannetti, S. Lloyd, and L. Maccone, *Phys. Rev. Lett.* **96**, 010401 (2006).
- [20] W. Zurek, *Phys. Today* **44**, 36 (1991).
- [21] S. Deléglise, I. Dotsenko, C. Sayrin, J. Bernu, M. Brune, J.-M. Raimond, and S. Haroche, *Nature (London)* **455**, 510 (2008).
- [22] M. Hor-Meyll, J. O. de Almeida, G. B. Lemos, P. H. S. Ribeiro, and S. P. Walborn, *Phys. Rev. Lett.* **112**, 053602 (2014).
- [23] P. Vernaz-Gris, A. Ketterer, A. Keller, S. P. Walborn, T. Coudreau, and P. Milman, *Phys. Rev. A* **89**, 052311 (2014).
- [24] J. Anders, D. K. L. Oi, E. Kashefi, D. E. Browne, and E. Andersson, *Phys. Rev. A* **82**, 020301 (2010).
- [25] C. H. Monken, P. H. S. Ribeiro, and S. Pádua, *Phys. Rev. A* **57**, 3123 (1998).
- [26] A. Valencia, A. Ceré, X. Shi, G. Molina-Terriza, and J. P. Torres, *Phys. Rev. Lett.* **99**, 243601 (2007).
- [27] S. P. Walborn, A. N. de Oliveira, S. Pádua, and C. H. Monken, *Phys. Rev. Lett.* **90**, 143601 (2003).
- [28] S. Machado, P. Milman, and S. P. Walborn, *Phys. Rev. A* **87**, 053834 (2013).
- [29] A. Eckstein, G. Boucher, A. Lemaître, P. Filloux, I. Favero, G. Leo, J. E. Sipe, M. Liscidini, and S. Ducci, *Laser Photon. Rev.* **8**, L76 (2014).
- [30] N. Tischler, A. Buese, L. G. Helt, M. L. Juan, N. Piro, J. Ghosh, M. J. Steel, and G. Molina-Terriza, [arXiv:1503.08629](https://arxiv.org/abs/1503.08629).
- [31] M. Avenhaus, B. Brecht, K. Laiho, and C. Silberhorn, [arXiv:1406.4252](https://arxiv.org/abs/1406.4252).
- [32] A. Eckstein, A. Christ, P. J. Mosley, and C. Silberhorn, *Phys. Rev. Lett.* **106**, 013603 (2011).
- [33] Y.-W. Cho, K.-K. Park, J.-C. Lee, and Y.-H. Kim, *Phys. Rev. Lett.* **113**, 063602 (2014).
- [34] C. K. Hong, Z. Y. Ou, and L. Mandel, *Phys. Rev. Lett.* **59**, 2044 (1987).
- [35] T. Douce, A. Eckstein, S. P. Walborn, A. Z. Khoury, S. Ducci, A. Keller, T. Coudreau, and P. Milman, *Sci. Rep.* **3**, 3530 (2013).
- [36] A. Orioux, X. Caillet, A. Lemaître, P. Filloux, I. Favero, G. Leo, and S. Ducci, *J. Opt. Soc. Am. B* **28**, 45 (2011).
- [37] A. Orioux, A. Eckstein, A. Lemaître, P. Filloux, I. Favero, G. Leo, T. Coudreau, A. Keller, P. Milman, and S. Ducci, *Phys. Rev. Lett.* **110**, 160502 (2013).
- [38] X. Caillet, V. Berger, G. Leo, and S. Ducci, *J. Mod. Opt.* **56**, 232 (2009).
- [39] J. Peřina, *Phys. Rev. A* **77**, 013803 (2008).
- [40] Z. D. Walton, A. V. Sergienko, B. E. A. Saleh, and M. C. Teich, *Phys. Rev. A* **70**, 052317 (2004).
- [41] The overlap between the field in the transverse and that in the epitaxial direction of the waveguide is contained in this term. The variations of χ_{Γ} with the pump, signal, and idler frequencies are negligible in the range of this study.
- [42] The transverse size of the pump beam will change with the incidence angle. However, the range of angles considered here is small enough to approximate $\sin \theta \rightarrow \theta$ and $\cos \theta \rightarrow 1$.
- [43] This choice of parameters corresponds to typical experimental conditions for the device illustrating our method. In particular, the generation of frequency-uncorrelated biphoton states is achievable by modifying the size pump beam so that f_+ and f_- have similar widths. Note that the technique remains valid for other pumping regimes since the pulse duration only impacts the positively correlated part f_+ of the biphoton wave function.
- [44] B. Brecht and C. Silberhorn, *Phys. Rev. A* **87**, 053810 (2013).
- [45] X. Sanchez-Lozano, A. B. U’Ren, and J. L. Lucio, *J. Opt.* **14**, 015202 (2012).
- [46] J. Paye, *IEEE J. Quantum Electron.* **28**, 2262 (1992).
- [47] W. H. Zurek, *Nature (London)* **412**, 712 (2001).
- [48] F. Toscano, D. A. R. Dalvit, L. Davidovich, and W. H. Zurek, *Phys. Rev. A* **73**, 023803 (2006).
- [49] L. Olislager, I. Mbodji, E. Woodhead, J. Cussey, L. Furfaro, P. Emplit, S. Massar, K. P. Huy, and J.-M. Merolla, *New J. Phys.* **14**, 043015 (2012).
- [50] Z. Y. Ou and L. Mandel, *Phys. Rev. Lett.* **61**, 54 (1988).
- [51] J. L. O’Brien, A. Furusawa, and J. Vučković, *Nature Photon.* **3**, 687 (2009).

Bibliography

- [1] N. GISIN, G. RIBORDY, W. TITTEL and H. ZBINDEN, “Quantum cryptography”, *Reviews of Modern Physics*, vol. 74, no. 1, pp. 145–195, 2002. (cited on pages 1 and 100).
- [2] M. BORN, *The Born-Einstein Letters*. Walker, New York, 1971. (cited on page 1).
- [3] N. GISIN, *Quantum Chance: Nonlocality, Teleportation and Other Quantum Marvels*. Springer, 2014. (cited on page 1).
- [4] S. J. FREEDMAN and J. F. CLAUSER, “Experimental test of local hidden-variable theories”, *Physical Review Letters*, vol. 28, pp. 938–941, Apr 1972. (cited on page 1).
- [5] E. S. FRY and R. C. THOMPSON, “Experimental test of local hidden-variable theories”, *Physical Review Letters*, vol. 37, pp. 465–468, Aug 1976. (cited on page 1).
- [6] A. ASPECT, P. GRANGIER and G. ROGER, “Experimental tests of realistic local theories via Bell’s theorem”, *Physical Review Letters*, vol. 47, pp. 460–463, 1981. (cited on pages 1, 3, and 99).
- [7] A. ASPECT, P. GRANGIER and G. ROGER, “Experimental realization of Einstein-Podolsky-Rosen-Bohm gedankenexperiment: a new violation of Bell’s inequalities”, *Physical Review Letters*, vol. 49, pp. 91–94, 1982. (cited on pages 1 and 99).
- [8] A. ASPECT, J. DALIBARD and G. ROGER, “Experimental test of Bell’s inequalities using time-varying analyzers”, *Physical Review Letters*, vol. 49, pp. 1804–1807, 1982. (cited on pages 1 and 99).
- [9] J. S. BELL, “On the Einstein-Podolsky-Rosen paradox”, *Physics*, vol. 1, no. 3, pp. 195–200, 1964. (cited on pages 1 and 99).
- [10] J. F. CLAUSER, M. A. HORNE, A. SHIMONY and R. A. HOLT, “Proposed experiment to test local hidden-variable theories”, *Physical Review Letters*, vol. 23, pp. 880–884, Oct. 1969. (cited on pages 1 and 99).

- [11] R. P. FEYNMAN, “Simulating physics with computers”, *International Journal of Theoretical Physics*, vol. 21, no. 6, pp. 467–488, 1982. (cited on page 1).
- [12] P. W. SHOR, “Polynomial-time algorithms for prime factorization and discrete logarithms on a quantum computer”, *SIAM Journal on Computing*, vol. 26, no. 5, pp. 1484–1509, 1997. (cited on pages 1 and 100).
- [13] L. K. GROVER, “Quantum mechanics helps in searching for a needle in a haystack”, *Physical Review Letters*, vol. 79, no. 2, pp. 325–328, 1997. (cited on page 1).
- [14] L. M. K. VANDERSYPEN, M. STEFFEN, G. BREYTA, C. S. YANNONI, M. H. SHERWOOD and I. L. CHUANG, “Experimental realization of Shor’s quantum factoring algorithm using nuclear magnetic resonance”, *Nature, London*, vol. 414, pp. 883–887, 2001. (cited on page 1).
- [15] E. LUCERO, R. BARENDTS, Y. CHEN, J. KELLY, M. MARIANTONI, A. MEGRANT, P. O’MALLEY, D. SANK, A. VAINSENER, J. WENNER, T. WHITE, Y. YIN, A. N. CLELAND and J. M. MARTINIS, “Computing prime factors with a Josephson phase qubit quantum processor”, *Nature Physics*, vol. 8, pp. 719–723, Oct. 2012. (cited on page 1).
- [16] A. DEWES, R. LAURO, F. R. ONG, V. SCHMITT, P. MILMAN, P. BERTET, D. VION and D. ESTEVE, “Quantum speeding-up of computation demonstrated in a superconducting two-qubit processor”, *Physical Review B*, vol. 85, p. 140503, Apr. 2012. (cited on page 1).
- [17] T. CHANELIERE, D. MATSUKEVICH, S. JENKINS, S.-Y. LAN, T. KENNEDY and A. KUZMICH, “Storage and retrieval of single photons transmitted between remote quantum memories”, *Nature*, vol. 438, no. 7069, pp. 833–836, 2005. (cited on page 1).
- [18] J. P. HOME, D. HANNEKE, J. D. JOST, J. M. AMINI, D. LEIBFRIED and D. J. WINELAND, “Complete methods set for scalable ion trap quantum information processing”, *Science*, vol. 325, no. 5945, pp. 1227–1230, 2009. (cited on page 1).
- [19] T. D. LADD, F. JELEZKO, R. LAFLAMME, Y. NAKAMURA, C. R. MONROE and J. L. O’BRIEN, “Quantum computers”, *Nature, London*, vol. 464, no. 7285, pp. 45–53, 2010. (cited on page 1).
- [20] E. KNILL, R. LAFLAMME and G. MILBURN, “A scheme for efficient quantum computation with linear optics”, *Nature, London*, vol. 409, pp. 46–52, 2001. (cited on pages 1 and 2).
- [21] C. H. BENNETT and G. BRASSARD, “Quantum cryptography: Public key distribution and coin tossing”, in *Proceedings of IEEE International Conference on Computers, Systems and Signal Processing*, vol. 175, p. 8, New York, 1984. (cited on page 1).

- [22] A. K. EKERT, “Quantum cryptography based on Bell’s theorem”, *Physical Review Letters*, vol. 67, pp. 661–663, 1991. (cited on page 1).
- [23] A. V. SERGIENKO, M. ATATÜRE, Z. WALTON, G. JAEGER, B. E. A. SALEH and M. C. TEICH, “Quantum cryptography using femtosecond-pulsed parametric down-conversion”, *Physical Review A*, vol. 60, pp. R2622–R2625, Oct 1999. (cited on page 1).
- [24] T. JENNEWEIN, C. SIMON, G. WEIHS, H. WEINFURTER and A. ZEILINGER, “Quantum cryptography using entangled photons”, *Physical Review Letters*, vol. 84, p. 4729, 2000. (cited on page 1).
- [25] W. TITTEL, J. BRENDEL, H. ZBINDEN and N. GISIN, “Quantum cryptography using entangled photons in energy-time Bell states”, *Physical Review Letters*, vol. 84, p. 4737, 2000. (cited on page 1).
- [26] D. BOUWMEESTER, J.-W. PAN, K. MATTLE, M. EIBL, H. WEINFURTER and A. ZEILINGER, “Experimental quantum teleportation”, *Nature, London*, vol. 390, pp. 575–579, 1997. (cited on pages 2 and 100).
- [27] A. FURUSAWA, J. L. SØRENSEN, S. L. BRAUNSTEIN, C. A. FUCHS, H. J. KIMBLE and E. S. POLZIK, “Unconditional quantum teleportation”, *Science*, vol. 282, no. 5389, pp. 706–709, 1998. (cited on page 2).
- [28] J. NILSSON, R. M. STEVENSON, K. H. A. CHAN, J. SKIBA-SZYMANSKA, M. LUCAMARINI, M. B. WARD, A. J. BENNETT, C. L. SALTER, I. FARRER, D. A. RITCHIE and A. J. SHIELDS, “Quantum teleportation using a light-emitting diode”, *Nature Photonics*, vol. 7, pp. 311–315, 2013. (cited on page 2).
- [29] J.-W. PAN, D. BOUWMEESTER, H. WEINFURTER and A. ZEILINGER, “Experimental entanglement swapping: entangling photons that never interacted”, *Physical Review Letters*, vol. 80, pp. 3891–3894, 1998. (cited on page 2).
- [30] T. JENNEWEIN, G. WEIHS, J.-W. PAN and A. ZEILINGER, “Experimental nonlocality proof of quantum teleportation and entanglement swapping”, *Physical Review Letters*, vol. 88, p. 017903, 2001. (cited on page 2).
- [31] J. B. SPRING, B. J. METCALF, P. C. HUMPHREYS, W. STEVEN KOLTHAMMER, X.-M. JIN, M. BARBIERI, A. DATTA, N. THOMAS-PETER, N. K. LANGFORD, D. KUNDYS, J. C. GATES, B. J. SMITH, P. G. R. SMITH and I. A. WALMSLEY, “Boson sampling on a photonic chip”, *Science*, vol. 339, no. 6121, pp. 798–801, 2013. (cited on page 2).
- [32] M. A. BROOME, A. FEDRIZZI, S. RAHIMI-KESHARI, J. DOVE, S. AARONSON, T. C. RALPH and A. G. WHITE, “Photonic boson sampling in a tunable circuit”, *Science*, vol. 339, no. 6121, pp. 794–798, 2013. (cited on page 2).

- [33] M. TILLMANN, B. DAKIĆ, R. HEILMANN, S. NOLTE, A. SZAMEIT and P. WALTHER, “Experimental boson sampling”, *Nature Photonics*, vol. 7, pp. 540–544, 2013. (cited on page 2).
- [34] A. CRESPI, R. OSELLAME, R. RAMPONI, D. J. BROD, E. F. GALVÃO, N. SPAGNOLO, C. VITELLI, E. MAIORINO, P. MATALONI and F. SCARRINO, “Integrated multimode interferometers with arbitrary designs for photonic boson sampling”, *Nature Photonics*, vol. 7, p. 545, 2013. (cited on pages 2 and 111).
- [35] C. K. HONG, Z. Y. OU and L. MANDEL, “Measurement of subpicosecond time intervals between two photons by interference”, *Physical Review Letters*, vol. 59, pp. 2044–2046, 1987. (cited on pages 2, 50, 81, and 82).
- [36] P. G. KWIAT, K. MATTLE, H. WEINFURTER, A. ZEILINGER, A. V. SERGIENKO and Y. SHIH, “New high-intensity source of polarization-entangled photon pairs”, *Physical Review Letters*, vol. 75, pp. 4337–4341, Dec. 1995. (cited on pages 2, 3, 9, and 101).
- [37] M. JOHNSON, M. AMIN, S. GILDERT, T. LANTING, F. HAMZE, N. DICKSON, R. HARRIS, A. BERKLEY, J. JOHANSSON, P. BUNYK *et al.*, “Quantum annealing with manufactured spins”, *Nature*, vol. 473, no. 7346, pp. 194–198, 2011. (cited on page 2).
- [38] S. BOIXO, T. F. RØNNOW, S. V. ISAKOV, Z. WANG, D. WECKER, D. A. LIDAR, J. M. MARTINIS and M. TROYER, “Evidence for quantum annealing with more than one hundred qubits”, *Nature Physics*, vol. 10, no. 3, pp. 218–224, 2014. (cited on page 2).
- [39] W. HANSEL, P. HOMMELHOFF, T. W. HANSCH and J. REICHEL, “Bose-Einstein condensation on a microelectronic chip”, *Nature, London*, vol. 413, pp. 498–501, Oct. 2001. (cited on page 2).
- [40] D. J. WINELAND, “Quantum information processing and quantum control with trapped atomic ions”, *Physica Scripta*, vol. T137, p. 014007, Dec. 2009. (cited on page 2).
- [41] J. L. O’BRIEN, A. FURUSAWA and J. VUČKOVIĆ, “Photonic quantum technologies”, *Nature Photonics*, vol. 3, no. 12, pp. 687–695, 2009. (cited on page 2).
- [42] Z. D. WALTON, A. V. SERGIENKO, B. E. A. SALEH and M. C. TEICH, “Generation of polarization-entangled photon pairs with arbitrary joint spectrum”, *Physical Review A*, vol. 70, no. 5, p. 052317, 2004. (cited on pages 2, 17, and 31).
- [43] P. YEH, *Optical waves in layered media*, vol. 95. Wiley New York, 1988. (cited on page 2).

- [44] J. M. HEATON, R. M. JENKINS, D. R. WIGHT, J. T. PARKER, J. C. H. BIRBECK and K. P. HILTON, “Novel 1-to-n way integrated optical beam splitters using symmetric mode mixing in GaAs/AlGaAs multimode waveguides”, *Applied Physics Letters*, vol. 61, no. 15, pp. 1754–1756, 1992. (cited on page 2).
- [45] R. M. JENKINS, J. M. HEATON, D. R. WIGHT, J. T. PARKER, J. C. H. BIRBECK, G. W. SMITH and K. P. HILTON, “Novel $1 \times n$ and $n \times n$ integrated optical switches using self-imaging multimode GaAs/AlGaAs waveguides”, *Applied Physics Letters*, vol. 64, no. 6, pp. 684–686, 1994. (cited on page 2).
- [46] J. WANG, A. SANTAMATO, P. JIANG, D. BONNEAU, E. ENGIN, J. W. SILVERSTONE, M. LERMER, J. BEETZ, M. KAMP, S. HOFLING, M. G. TANNER, C. M. NATARAJAN, R. H. HADFIELD, S. N. DORENBOS, V. ZWILLER, J. L. O’BRIEN and M. G. THOMPSON, “Gallium arsenide (GaAs) quantum photonic waveguide circuits”, *Optics Communications*, Mar. 2014. (cited on pages 2 and 111).
- [47] D. DAI and J. E. BOWERS, “Novel ultra-short and ultra-broadband polarization beam splitter based on a bent directional coupler”, *Optics Express*, vol. 19, pp. 18614–18620, Sep 2011. (cited on page 2).
- [48] D. DAI, Y. TANG and J. E. BOWERS, “Mode conversion in tapered submicron silicon ridge optical waveguides”, *Optics Express*, vol. 20, pp. 13425–13439, Jun 2012. (cited on page 2).
- [49] J. P. SPRENGERS, A. GAGGERO, D. SAHIN, S. JAHANMIRINEJAD, G. FRUCCI, F. MATTIOLI, R. LEONI, J. BEETZ, M. LERMER, M. KAMP, S. HOFLING, R. SANJINES and A. FIORE, “Waveguide superconducting single-photon detectors for integrated quantum photonic circuits”, *Applied Physics Letters*, vol. 99, no. 18, pp. 181110–181110, 2011. (cited on page 2).
- [50] D. SAHIN, A. GAGGERO, Z. ZHOU, S. JAHANMIRINEJAD, F. MATTIOLI, R. LEONI, J. BEETZ, M. LERMER, M. KAMP, S. HÖFLING and A. FIORE, “Waveguide photon-number-resolving detectors for quantum photonic integrated circuits”, *Applied Physics Letters*, vol. 103, p. 111116, 2013. (cited on page 2).
- [51] A. DOUSSE, J. SUFFCZYŃSKI, A. BEVERATOS, O. KREBS, A. LEMAÎTRE, I. SAGNES, J. BLOCH, P. VOISIN and P. SENELLART, “Ultrabright source of entangled photon pairs”, *Nature, London*, vol. 466, pp. 217–220, 2010. (cited on page 2).
- [52] Y.-M. HE, Y. HE, Y.-J. WEI, D. WU, M. ATATÜRE, C. SCHNEIDER, S. HÖFLING, M. KAMP, C.-Y. LU and J.-W. PAN, “On-demand semiconductor single-photon source with near-unity indistinguishability”, *Nature Nanotechnology*, vol. 8, pp. 213–217, Mar. 2013. (cited on page 2).

- [53] C. L. SALTER, R. M. STEVENSON, I. FARRER, C. A. NICOLL, D. A. RITCHIE and A. J. SHIELDS, “An entangled-light-emitting diode”, *Nature, London*, vol. 465, no. 7298, pp. 594–597, 2010. (cited on page 2).
- [54] H. TAKESUE, H. FUKUDA, T. TSUCHIZAWA, T. WATANABE, K. YAMADA, Y. TOKURA and S. ichi ITABASHI, “Generation of polarization entangled photon pairs using silicon wire waveguide”, *Optics Express*, vol. 16, no. 8, pp. 5721–5727, 2008. (cited on page 3).
- [55] J. W. SILVERSTONE, R. SANTAGATI, D. BONNEAU, M. J. STRAIN, M. SOREL, J. L. O’BRIEN and M. G. THOMPSON, “Qubit entanglement between ring-resonator photon-pair sources on a silicon chip”, *Nature Communications*, vol. 6, p. 7948, Aug 2015. (cited on pages 3, 70, and 111).
- [56] S. AZZINI, D. GRASSANI, M. STRAIN, M. SOREL, L. HELT, J. SIPE, M. LISCIDINI, M. GALLI and D. BAJONI, “Ultra-low power generation of twin photons in a compact silicon ring resonator”, *Optics Express*, vol. 20, no. 21, pp. 23100–23107, 2012. (cited on page 3).
- [57] A. D. ROSSI, V. ORTIZ, M. CALLIGARO, B. VINTER, J. NAGLE, S. DUCCI and V. BERGER, “A third-order-mode laser diode for quantum communication”, *Semiconductor Science and Technology*, vol. 19, no. 10, pp. L99–L102, 2004. (cited on page 3).
- [58] F. BOITIER, A. ORIEUX, C. AUTEBERT, A. LEMAÎTRE, E. GALOPIN, C. MANQUEST, C. SIRTORI, I. FAVERO, G. LEO and S. DUCCI, “Electrically injected photon-pair source at room temperature”, *Physical Review Letters*, vol. 112, p. 183901, May 2014. (cited on pages 3, 11, and 112).
- [59] E. GUILLOTTEL, M. RAVARO, F. GHIgliENO, C. LANGLOIS, C. RICOLLEAU, S. DUCCI, I. FAVERO and G. LEO, “Parametric amplification in GaAs/AlOx waveguide”, *Applied Physics Letters*, vol. 94, no. 17, p. 171110, 2009. (cited on page 3).
- [60] R. HORN, P. ABOLGHASEM, B. J. BIJLANI, D. KANG, A. S. HELMY and G. WEIHS, “Monolithic source of photon pairs”, *Physical Review Letters*, vol. 108, no. 15, p. 153605, 2012. (cited on page 3).
- [61] K. L. VODOPYANOV, O. LEVI, P. S. KUO, T. J. PINGUET, J. S. HARRIS, M. M. FEJER, B. GERARD, L. BECOUARN and E. LALLIER, “Optical parametric oscillation in quasi-phase-matched GaAs”, *Optics Letters*, vol. 29, no. 16, pp. 1912–1914, 2004. (cited on page 3).
- [62] J. OTA, W. NARITA, I. OHTA, T. MATSUSHITA and T. KONDO, “Fabrication of periodically-inverted AlGaAs waveguides for quasi-phase-matched wavelength conversion at 1.55 μm ”, *Japanese Journal of Applied Physics*, vol. 48, no. 4, p. 04C110, 2009. (cited on page 3).

- [63] P. S. KUO and G. S. SOLOMON, “On-and off-resonance second-harmonic generation in GaAs microdisks”, *Optics Express*, vol. 19, no. 18, pp. 16898–16918, 2011. (cited on page 3).
- [64] S. MARIANI, A. ANDRONICO, A. LEMAÎTRE, I. FAVERO, S. DUCCI and G. LEO, “Second-harmonic generation in AlGaAs microdisks in the telecom range”, *Optics Letters*, vol. 39, pp. 3062–3065, May 2014. (cited on page 3).
- [65] M. A. SOLÍS-PROSSER, A. ARIAS, J. J. M. VARGA, L. REBÓN, S. LEDESMA, C. IEMMI and L. NEVES, “Preparing arbitrary pure states of spatial qudits with a single phase-only spatial light modulator”, *Optics Letters*, vol. 38, pp. 4762–4765, Nov. 2013. (cited on page 4).
- [66] O. J. FARÍAS, F. de MELO, P. MILMAN and S. P. WALBORN, “Quantum information processing by weaving quantum talbot carpets”, *Physical Review A*, vol. 91, p. 062328, Jun 2015. (cited on page 4).
- [67] G. GIBSON, J. COURTIAL, M. J. PADGETT, M. VASNETSOV, V. PAS’KO, S. M. BARNETT and S. FRANKE-ARNOLD, “Free-space information transfer using light beams carrying orbital angular momentum”, *Optics Express*, vol. 12, pp. 5448–5456, Nov 2004. (cited on page 4).
- [68] M. PADGETT and L. ALLEN, “Light with a twist in its tail”, *Contemporary Physics*, vol. 41, no. 5, pp. 275–285, 2000. (cited on page 4).
- [69] M. MIRHOSSEINI, O. S. MAGAÑA-LOAIZA, M. N. O’SULLIVAN, B. RODENBURG, M. MALIK, M. P. J. LAVERY, M. J. PADGETT, D. J. GAUTHIER and R. W. BOYD, “High-dimensional quantum cryptography with twisted light”, *New Journal of Physics*, vol. 17, no. 3, p. 033033, 2015. (cited on page 4).
- [70] E. KARIMI, F. CARDANO, M. MAFFEI, C. de LISIO, L. MARRUCCI, R. W. BOYD and E. SANTAMATO, “Hardy’s paradox tested in the spin-orbit Hilbert space of single photons”, *Physical Review A*, vol. 89, pp. 032122–7, Mar. 2014. (cited on page 4).
- [71] A. C. DADA, J. LEACH, G. S. BULLER, M. J. PADGETT and E. ANDERSSON, “Experimental high-dimensional two-photon entanglement and violations of generalized bell inequalities”, *Nature Physics*, vol. 7, pp. 677–680, May 2011. (cited on page 4).
- [72] L. OLISLAGER, J. CUSSEY, A. T. NGUYEN, P. EMPLIT, S. MASSAR, J.-M. MEROLLA and K. P. HUY, “Frequency-bin entangled photons”, *Physical Review A*, vol. 82, p. 013804, Jul. 2010. (cited on page 4).
- [73] L. OLISLAGER, I. MBODJI, E. WOODHEAD, J. CUSSEY, L. FURFARO, P. EMPLIT, S. MASSAR, K. P. HUY and J.-M. MEROLLA, “Implementing two-photon interference in the frequency domain with electro-optic phase

- modulators”, *New Journal of Physics*, vol. 14, no. 4, p. 043015, 2012. (cited on pages 4 and 91).
- [74] L. OLISLAGER, E. WOODHEAD, K. PHAN HUY, J.-M. MEROLLA, P. EMPPLIT and S. MASSAR, “Creating and manipulating entangled optical qubits in the frequency domain”, *Physical Review A*, vol. 89, p. 052323, May 2014. (cited on pages 4 and 91).
- [75] A. HAYAT, X. XING, A. FEIZPOUR and A. M. STEINBERG, “Multidimensional quantum information based on single-photon temporal wavepackets”, *Optics Express*, vol. 20, pp. 29174–29184, Dec 2012. (cited on page 4).
- [76] B. BRECHT, A. ECKSTEIN, R. RICKEN, V. QUIRING, H. SUCHE, L. SANSONI and C. SILBERHORN, “Demonstration of coherent time-frequency schmidt mode selection using dispersion-engineered frequency conversion”, *Physical Review A*, vol. 90, p. 030302, Sep. 2014. (cited on page 4).
- [77] B. BRECHT, D. V. REDDY, C. SILBERHORN and M. G. RAYMER, “Photon temporal modes: A complete framework for quantum information science”, *Physical Review X*, vol. 5, p. 041017, Oct 2015. (cited on page 4).
- [78] W. P. GRICE, A. B. U’REN and I. A. WALMSLEY, “Eliminating frequency and space-time correlations in multiphoton states”, *Physical Review A*, vol. 64, no. 6, p. 063815, 2001. (cited on page 4).
- [79] A. B. U’REN, C. SILBERHORN, R. ERDMANN, K. BANASZEK, W. P. GRICE, I. A. WALMSLEY and M. G. RAYMER, “Generation of pure-state single-photon wavepackets by conditional preparation based on spontaneous parametric downconversion”, *Laser Physics*, vol. 15, p. 146, 2005. (cited on pages 4 and 31).
- [80] A. PE’ER, B. DAYAN, A. A. FRIESEM and Y. SILBERBERG, “Temporal shaping of entangled photons”, *Physical Review Letters*, vol. 94, p. 073601, Feb. 2005. (cited on page 4).
- [81] B. DAYAN, Y. BROMBERG, I. AFEK and Y. SILBERBERG, “Spectral polarization and spectral phase control of time-energy entangled photons”, *Physical Review A*, vol. 75, no. 4, p. 043804, 2007. (cited on page 5).
- [82] C. BERNHARD, B. BESSIRE, T. FEURER and A. STEFANOV, “Shaping frequency-entangled qudits”, *Physical Review A*, vol. 88, pp. 032322–4, Sep. 2013. (cited on page 5).
- [83] A. ECKSTEIN, A. CHRIST, P. J. MOSLEY and C. SILBERHORN, “Highly efficient single-pass source of pulsed single-mode twin beams of light”, *Physical Review Letters*, vol. 106, p. 013603, Jan. 2011. (cited on pages 5 and 30).
- [84] A. VALENCIA, A. CERÉ, X. SHI, G. MOLINA-TERRIZA and J. P. TORRES, “Shaping the waveform of entangled photons”, *Physical Review Letters*, vol. 99, p. 243601, Dec. 2007. (cited on pages 5, 9, 17, 30, and 49).

- [85] M. AVENHAUS, A. ECKSTEIN, P. J. MOSLEY and C. SILBERHORN, “Fiber-assisted single-photon spectrograph”, *Optics Letters*, vol. 34, no. 18, pp. 2873–2875, 2009. (cited on pages 5, 51, and 53).
- [86] A. ORIEUX, A. ECKSTEIN, A. LEMAÎTRE, P. FILLOUX, I. FAVERO, G. LEO, T. COUDREAU, A. KELLER, P. MILMAN and S. DUCCI, “Direct bell states generation on a III-V semiconductor chip at room temperature”, *Physical Review Letters*, vol. 110, pp. 160502–5, Apr. 2013. (cited on pages 6, 11, 99, 101, 104, and 107).
- [87] A. D. ROSSI and V. BERGER, “Counterpropagating twin photons by parametric fluorescence”, *Physical Review Letters*, vol. 88, no. 4, p. 043901, 2002. (cited on page 9).
- [88] L. LANCO, S. DUCCI, J.-P. LIKFORMAN, X. MARCADET, J. A. W. van HOUWELINGEN, H. ZBINDEN, G. LEO and V. BERGER, “Semiconductor waveguide source of counterpropagating twin photons”, *Physical Review Letters*, vol. 97, no. 17, p. 173901, 2006. (cited on pages 9 and 12).
- [89] L. LANCO, *Sources semiconductrices de photons jumeaux*. Ph.D. dissertation, Université Paris-Diderot, 2006. (cited on page 9).
- [90] A. ORIEUX, X. CAILLET, A. LEMAÎTRE, P. FILLOUX, I. FAVERO, G. LEO and S. DUCCI, “Efficient parametric generation of counterpropagating two-photon states”, *Journal of the Optical Society of America B: Optical Physics*, vol. 28, pp. 45–51, Jan. 2011. (cited on pages 9, 13, 41, and 69).
- [91] X. CAILLET, *Une microcavité semiconductrice source de photons jumeaux contrapropageants à température ambiante*. Ph.D. dissertation, Université Paris-Diderot, 2009. (cited on pages 9, 23, and 29).
- [92] J. CHILWELL and I. HODGKINSON, “Thin-films field-transfer matrix theory of planar multilayer waveguides and reflection from prism-loaded waveguides”, *Journal of the Optical Society of America A: Optics, Image Science, and Vision*, vol. 1, no. 7, pp. 742–753, 1984. (cited on pages 11, 35, and 69).
- [93] S. GEHRITZ, F. K. REINHART, C. GOURGON, N. HERRES, A. VONLANTHEN and H. SIGG, “The refractive index of $\text{Al}_x\text{Ga}_{1-x}\text{As}$ below the band gap: Accurate determination and empirical modeling”, *Journal of Applied Physics*, vol. 87, pp. 7825–7837, 2000. (cited on pages 11 and 15).
- [94] S. J. B. YOO, R. BHAT, C. CANEAU and M. A. KOZA, “Quasi-phase-matched second-harmonic generation in AlGaAs waveguides with periodic domain inversion achieved by wafer-bonding”, *Applied Physics Letters*, vol. 66, no. 25, pp. 3410–3412, 1995. (cited on page 14).
- [95] M. OHASHI, T. KONDO, R. ITO, S. FUKATSU, Y. SHIRAKI, K. KUMATA and S. S. KANO, “Determination of quadratic nonlinear optical coefficient of $\text{Al}_x\text{Ga}_{1-x}\text{As}$ system by the method of reflected second harmonics”, *Journal*

- of Applied Physics*, vol. 74, no. 1, pp. 596–601, 1993. (cited on pages 14 and 27).
- [96] S. ADACHI, “GaAs, AlAs, and $\text{Al}_x\text{Ga}_{1-x}\text{As}$ material parameters for use in research and device applications”, *Journal of Applied Physics*, vol. 58, pp. R1–R29, Aug. 1985. (cited on page 15).
- [97] Z. D. WALTON, M. C. BOOTH, A. V. SERGIENKO, B. E. A. SALEH and M. C. TEICH, “Controllable frequency entanglement via auto-phase-matched spontaneous parametric down-conversion”, *Physical Review A*, vol. 67, p. 053810, May 2003. (cited on pages 17 and 35).
- [98] T. E. KELLER and M. H. RUBIN, “Theory of two-photon entanglement for spontaneous parametric down-conversion driven by a narrow pump pulse”, *Physical Review A*, vol. 56, pp. 1534–1541, Aug. 1997. (cited on pages 17 and 34).
- [99] J. PEŘINA, “Quantum properties of counterpropagating two-photon states generated in a planar waveguide”, *Physical Review A*, vol. 77, no. 1, p. 013803, 2008. (cited on pages 17, 20, and 34).
- [100] C. COHEN-TANNOUDJI, J. DUPONT-ROC and G. GRYNBERG, *Photons et atomes: introduction à l’électrodynamique quantique*. EDP Sciences, 2001. (cited on pages 18 and 19).
- [101] D. P. CRAIG and T. THIRUNAMACHANDRAN, *Molecular quantum electrodynamics: an introduction to radiation-molecule interactions*. Courier Corporation, 1998. (cited on page 18).
- [102] L. LANDAU and E. LIFSHITZ, *Mechanics, vol. 1*. Course of theoretical physics, third edition éd., 1976. (cited on page 18).
- [103] G. GRYNBERG, A. ASPECT and C. FABRE, *Introduction to quantum optics: from the semi-classical approach to quantized light*. Cambridge University Press, 2010. (cited on pages 18 and 21).
- [104] R. LOUDON, *The quantum theory of light*. Oxford University Press, 2000. (cited on pages 18, 21, 22, 34, and 82).
- [105] B. HUTTNER and S. M. BARNETT, “Quantization of the electromagnetic field in dielectrics”, *Physical Review A*, vol. 46, pp. 4306–4322, Oct 1992. (cited on page 19).
- [106] K. J. BLOW, R. LOUDON, S. J. D. PHOENIX and T. J. SHEPHERD, “Continuum fields in quantum optics”, *Physical Review A*, vol. 42, pp. 4102–4114, Oct 1990. (cited on page 19).
- [107] S. M. DUTRA, *Cavity quantum electrodynamics: the strange theory of light in a box*. John Wiley & Sons, 2005. (cited on page 19).

- [108] Z. YANG, M. LISCIDINI and J. E. SIPE, “Spontaneous parametric down-conversion in waveguides: A backward heisenberg picture approach”, *Physical Review A*, vol. 77, p. 033808, Mar. 2008. (cited on pages 19 and 21).
- [109] M. LISCIDINI, L. G. HELT and J. E. SIPE, “Asymptotic fields for a hamiltonian treatment of nonlinear electromagnetic phenomena”, *Physical Review A*, vol. 85, p. 013833, Jan. 2012. (cited on page 19).
- [110] G. BREIT and H. A. BETHE, “Ingoing waves in final state of scattering problems”, *Physical Review*, vol. 93, pp. 888–890, Feb 1954. (cited on page 19).
- [111] P. T. KRISTENSEN and S. HUGHES, “Modes and mode volumes of leaky optical cavities and plasmonic nanoresonators”, *ACS Photonics*, vol. 1, no. 1, pp. 2–10, 2014. (cited on page 19).
- [112] L. HELT, M. LISCIDINI and J. SIPE, “How does it scale? Comparing quantum and classical nonlinear optical processes in integrated devices”, *Journal of the Optical Society of America B: Optical Physics*, vol. 29, no. 8, pp. 2199–2212, 2012. (cited on page 19).
- [113] M. LISCIDINI and J. E. SIPE, “Stimulated emission tomography”, *Physical Review Letters*, vol. 111, pp. 193602–5, Nov. 2013. (cited on pages 19, 65, and 72).
- [114] R. GHOSH, C. K. HONG, Z. Y. OU and L. MANDEL, “Interference of two photons in parametric down conversion”, *Physical Review A*, vol. 34, pp. 3962–3968, Nov. 1986. (cited on page 19).
- [115] Z. Y. OU, L. J. WANG and L. MANDEL, “Vacuum effects on interference in two-photon down conversion”, *Physical Review A*, vol. 40, pp. 1428–1435, Aug 1989. (cited on page 19).
- [116] M. C. BOOTH, M. ATATÜRE, G. DI GIUSEPPE, B. E. A. SALEH, A. V. SERGIENKO and M. C. TEICH, “Counterpropagating entangled photons from a waveguide with periodic nonlinearity”, *Physical Review A*, vol. 66, p. 023815, Aug. 2002. (cited on page 20).
- [117] A. MESSIAH, *Quantum Mechanics Vol. I*. 1958. (cited on page 20).
- [118] R. W. BOYD, *Nonlinear Optics*. San Diego: Academic Press, third edition éd., 2008. (cited on page 22).
- [119] B. BRECHT, *Engineering ultrafast quantum frequency conversion*. Ph.D. dissertation, Paderborn, Universität Paderborn, Diss., 2014, 2014. (cited on page 23).
- [120] I. SHOJI, T. KONDO, A. KITAMOTO, M. SHIRANE and R. ITO, “Absolute scale of second-order nonlinear-optical coefficients”, *Journal of the Optical Society of America B: Optical Physics*, vol. 14, no. 9, pp. 2268–2294, 1997. (cited on page 27).

- [121] M. H. RUBIN, D. N. KLYSHKO, Y. H. SHIH and A. V. SERGIENKO, “Theory of two-photon entanglement in type-II optical parametric down-conversion”, *Physical Review A*, vol. 50, pp. 5122–5133, Dec. 1994. (cited on page 34).
- [122] W. P. GRICE, *Interference and Indistinguishability in Ultrafast Spontaneous Parametric*. Ph.D. dissertation, University of Rochester, 1997. (cited on pages 34 and 38).
- [123] L. LI, “Formulation and comparison of two recursive matrix algorithms for modeling layered diffraction gratings”, *Journal of the Optical Society of America A: Optics, Image Science, and Vision*, vol. 13, no. 5, pp. 1024–1035, 1996. (cited on page 35).
- [124] D. I. BABIC and S. W. CORZINE, “Analytic expressions for the reflection delay, penetration depth, and absorptance of quarter-wave dielectric mirrors”, *IEEE Journal of Quantum Electronics*, vol. 28, pp. 514–524, Feb. 1992. (cited on page 35).
- [125] L. R. BROVELLI and U. KELLER, “Simple analytical expressions for the reflectivity and the penetration depth of a Bragg mirror between arbitrary media”, *Optics Communications*, vol. 116, no. 4-6, pp. 343–350, 1995. (cited on page 35).
- [126] X. SANCHEZ-LOZANO, A. B. U’REN and J. L. LUCIO, “On the relationship between pump chirp and single-photon chirp in spontaneous parametric downconversion”, *Journal of Optics*, vol. 14, no. 1, p. 015202, 2012. (cited on pages 37 and 39).
- [127] E. WIGNER, “On the quantum correction for thermodynamic equilibrium”, *Physical Review*, vol. 40, pp. 749–759, Jun 1932. (cited on page 37).
- [128] J. PAYE, “The chronocyclic representation of ultrashort light pulses”, *Quantum Electronics, IEEE Journal of*, vol. 28, no. 10, pp. 2262–2273, 1992. (cited on page 38).
- [129] I. A. WALMSLEY and C. DORRER, “Characterization of ultrashort electromagnetic pulses”, *Advances in Optics and Photonics*, vol. 1, pp. 308–437, Apr. 2009. (cited on pages 38, 49, and 72).
- [130] B. BRECHT and C. SILBERHORN, “Characterizing entanglement in pulsed parametric down-conversion using chronocyclic wigner functions”, *Physical Review A*, vol. 87, pp. 053810–6, May 2013. (cited on page 39).
- [131] X. CAILLET, A. ORIEUX, A. LEMAÎTRE, P. FILLOUX, I. FAVERO, G. LEO and S. DUCCI, “Two-photon interference with a semiconductor integrated source at room temperature”, *Optics Express*, vol. 18, no. 10, pp. 9967–9975, 2010. (cited on pages 41 and 85).

- [132] Y. JERONIMO-MORENO, S. RODRIGUEZ-BENAVIDES and A. B. U'REN, "Theory of cavity-enhanced spontaneous parametric downconversion", *Laser physics*, vol. 20, no. 5, pp. 1221–1233, 2010. (cited on page 41).
- [133] A. D. ROSSI, V. ORTIZ, M. CALLIGARO, L. LANCO, S. DUCCI, V. BERGER and I. SAGNES, "Measuring propagation loss in a multimode semiconductor waveguide", *Journal of Applied Physics*, vol. 97, no. 7, pp. 073105–7, 2005. (cited on page 43).
- [134] P. J. MOSLEY, J. S. LUNDEEN, B. J. SMITH, P. WASYLCHYK, A. B. U'REN, C. SILBERHORN and I. A. WALMSLEY, "Heralded generation of ultrafast single photons in pure quantum states", *Physical Review Letters*, vol. 100, p. 133601, Apr. 2008. (cited on pages 49 and 91).
- [135] N. BRUNO, A. MARTIN, T. GUERREIRO, B. SANGUINETTI and R. T. THEW, "Pulsed source of spectrally uncorrelated and indistinguishable photons at telecom wavelengths", *Optics Express*, vol. 22, pp. 17246–17253, Jul 2014. (cited on page 49).
- [136] Y.-W. CHO, K.-K. PARK, J.-C. LEE and Y.-H. KIM, "Engineering frequency-time quantum correlation of narrow-band biphotons from cold atoms", *Physical Review Letters*, vol. 113, p. 063602, Aug. 2014. (cited on page 49).
- [137] C. POLYCARPOU, K. N. CASSEMIRO, G. VENTURI, A. ZAVATTA and M. BELLINI, "Adaptive detection of arbitrarily shaped ultrashort quantum light states", *Physical Review Letters*, vol. 109, pp. 053602–5, Aug. 2012. (cited on page 50).
- [138] Z. Y. J. OU, *Multi-photon quantum interference*. Springer Verlag, 2007. (cited on page 50).
- [139] A. F. ABOURADDY, T. M. YARNALL and G. DI GIUSEPPE, "Phase-unlocked hong-ou-mandel interferometry", *Physical Review A*, vol. 87, p. 062106, Jun. 2013. (cited on page 50).
- [140] T. DOUCE, A. ECKSTEIN, S. P. WALBORN, A. Z. KHOURY, S. DUCCI, A. KELLER, T. COUDREAU and P. MILMAN, "Direct measurement of the biphoton wigner function through two-photon interference", *Scientific Reports*, vol. 3, p. 3530, Dec. 2013. (cited on pages 50, 86, and 91).
- [141] F. BOITIER, A. GODARD, N. DUBREUIL, P. DELAYE, C. FABRE and E. ROSENCHER, "Two-photon-counting interferometry", *Physical Review A*, vol. 87, no. 1, p. 013844, 2013. (cited on page 50).
- [142] R. PASCHOTTA, *Encyclopedia of laser physics and technology*, vol. 1. Wiley-vch Berlin, 2008. (cited on pages 50 and 59).

- [143] M. CHEKHOVA, “Two-photon spectron”, *Journal of Experimental and Theoretical Physics Letters*, vol. 75, no. 5, pp. 225–226, 2002. (cited on page 51).
- [144] G. BRIDA, V. CARICATO, M. CHEKHOVA, M. GENOVESE, M. GRAMEGNA and T. S. ISKHAQOV, “Testing ultrafast two-photon spectral amplitudes via optical fibres”, *Optics Express*, vol. 18, no. 12, pp. 12915–12922, 2010. (cited on page 51).
- [145] A. VALENCIA, M. V. CHEKHOVA, A. TRIFONOV and Y. SHIH, “Entangled two-photon wave packet in a dispersive medium”, *Physical Review Letters*, vol. 88, p. 183601, Apr 2002. (cited on page 51).
- [146] A. ECKSTEIN, *Mastering quantum light pulses with nonlinear waveguide interactions*. Ph.D. dissertation, Erlangen, Universität Erlangen-Nürnberg, Diss., 2012, 2012. (cited on page 56).
- [147] F. TREPANIER, G. BROCHU, M. MORIN and A. MAILLOUX, “High-end FBG design and manufacturing for industrial lasers, sensing and telecommunications”, in *Bragg Gratings, Photosensitivity, and Poling in Glass Waveguides*, pp. BM4D–1, Optical Society of America, 2014. (cited on page 56).
- [148] A. ECKSTEIN, G. BOUCHER, A. LEMAÎTRE, P. FILLOUX, I. FAVERO, G. LEO, J. E. SIPE, M. LISCIDINI and S. DUCCI, “High-resolution spectral characterization of two photon states via classical measurements”, *Laser & Photonics Reviews*, vol. 8, pp. L76–L80, Jun. 2014. (cited on pages 57, 79, 85, and 109).
- [149] F. MARSILI, V. B. VERMA, J. A. STERN, S. HARRINGTON, A. E. LITA, T. GERRITS, I. VAYSHENKER, B. BAEK, M. D. SHAW, R. P. MIRIN and S. W. NAM, “Detecting single infrared photons with 93% system efficiency”, *Nature Photonics*, vol. 7, pp. 210–214, Feb. 2013. (cited on page 62).
- [150] B. FANG, O. COHEN, M. LISCIDINI, J. E. SIPE and V. O. LORENZ, “Fast and highly resolved capture of the joint spectral density of photon pairs”, *Optica*, vol. 1, pp. 281–284, Nov. 2014. (cited on page 70).
- [151] R. KUMAR, J. R. ONG, M. SAVANIER and S. MOOKHERJEA, “Controlling the spectrum of photons generated on a silicon nanophotonic chip”, *Nature Communications*, vol. 5, p. 5489, Nov 2014. (cited on page 70).
- [152] D. GRASSANI, A. SIMBULA, M. GALLI, S. PIROTTA, T. BAEHR-JONES, M. HOCHBERG, N. C. HARRIS, C. GALLAND, M. LISCIDINI and D. BAJONI, “Joint spectral density measurement of energy correlations of photon pairs generated by a silicon microring resonator”, in *2015 European Conference on Lasers and Electro-Optics - European Quantum Electronics Conference*, pp. EA–7–6, Optical Society of America, 2015. (cited on page 70).
- [153] A. MONMAYRANT, S. WEBER and B. CHATEL, “A newcomer’s guide to ultrashort pulse shaping and characterization”, *Journal of Physics B: Atomic,*

- Molecular and Optical Physics*, vol. 43, no. 10, p. 103001, 2010. (cited on page 72).
- [154] V. WONG and I. A. WALMSLEY, “Analysis of ultrashort pulse-shape measurement using linear interferometers”, *Optics Letters*, vol. 19, no. 4, p. 287, 1994. (cited on page 73).
- [155] B. J. CUSACK, B. S. SHEARD, D. A. SHADDOCK, M. B. GRAY, P. K. LAM and S. E. WHITCOMB, “Electro-optic modulator capable of generating simultaneous amplitude and phase modulations”, *Applied Optics*, vol. 43, pp. 5079–5091, Sep 2004. (cited on page 73).
- [156] A. MOTTET, N. BOURRIOT and J. HAUDEN, “Tunable frequency shifter based on LiNbO₃- I&Q modulators”, tech. rep., Photline Technologies, 2013. (cited on page 74).
- [157] J. CVIKLINSKI, *Interface quantique atomes-champ en régime de variables continues*. Theses, Université Pierre et Marie Curie - Paris VI, May 2008. (cited on page 74).
- [158] A. L. CAMPILLO, “Orthogonally polarized single sideband modulator”, *Optics Letters*, vol. 32, pp. 3152–3154, Nov 2007. (cited on page 74).
- [159] A. SERGIENKO, Y. SHIH and M. RUBIN, “Experimental evaluation of a two-photon wave packet in type-II parametric downconversion”, *Journal of the Optical Society of America B: Optical Physics*, vol. 12, no. 5, pp. 859–862, 1995. (cited on page 84).
- [160] C. AUTEBERT, N. BRUNO, A. MARTIN, A. LEMAITRE, C. G. CARBONELL, I. FAVERO, G. LEO, H. ZBINDEN and S. DUCCI, “Integrated AlGaAs source of highly indistinguishable and energy-time entangled photons”, *Optica*, vol. 3, pp. 143–146, Feb 2016. (cited on page 84).
- [161] S. WALBORN, A. de OLIVEIRA, S. PÁDUA and C. MONKEN, “Multimode hong-ou-mandel interference”, *Physical Review Letters*, vol. 90, p. 143601, Apr. 2003. (cited on page 84).
- [162] W. ZUREK, “Decoherence and the transition from quantum to classical”, *Physics Today*, vol. 44, no. 10, pp. 36–44, 1991. (cited on page 89).
- [163] S. DELÉGLISE, I. DOTSENKO, C. SAYRIN, J. BERNU, M. BRUNE, J.-M. RAIMOND and S. HAROCHE, “Reconstruction of non-classical cavity field states with snapshots of their decoherence”, *Nature, London*, vol. 455, pp. 510–514, Sep. 2008. (cited on page 89).
- [164] A. ECKSTEIN and C. SILBERHORN, “Broadband frequency mode entanglement in waveguided parametric downconversion”, *Optics Letters*, vol. 33, no. 16, pp. 1825–1827, 2008. (cited on pages 89 and 91).

- [165] E. SCHMIDT, “Zur theorie der linearen und nichtlinearen integralgleichungen”, *Mathematische Annalen*, vol. 63, no. 4, pp. 433–476, 1907. (cited on page 89).
- [166] T. B. PITTMAN, D. V. STREKALOV, A. MIGDALL, M. H. RUBIN, A. V. SERGIENKO and Y. H. SHIH, “Can two-photon interference be considered the interference of two photons?”, *Physical Review Letters*, vol. 77, pp. 1917–1920, Sep. 1996. (cited on page 89).
- [167] Z. Y. OU and L. MANDEL, “Observation of spatial quantum beating with separated photodetectors”, *Physical Review Letters*, vol. 61, pp. 54–57, Jul. 1988. (cited on page 90).
- [168] W. H. ZUREK, “Sub-Planck structure in phase space and its relevance for quantum decoherence”, *Nature, London*, vol. 412, no. 6848, pp. 712–717, 2001. (cited on page 91).
- [169] F. TOSCANO, D. DALVIT, L. DAVIDOVICH and W. ZUREK, “Sub-Planck phase-space structures and heisenberg-limited measurements”, *Physical Review A*, vol. 73, p. 023803, Feb. 2006. (cited on page 91).
- [170] H. d. RIEDMATTEN, I. MARCIKIC, W. TITTEL, H. ZBINDEN and N. Gisin, “Quantum interference with photon pairs created in spatially separated sources”, *Physical Review A*, vol. 67, p. 022301, Feb. 2003. (cited on page 91).
- [171] O. KUZUCU, M. FIORENTINO, M. A. ALBOTA, F. N. C. WONG and F. X. KÄRTNER, “Photon coincident-frequency entanglement via extended phase matching”, *Physical Review Letters*, vol. 94, p. 083601, Mar. 2005. (cited on page 91).
- [172] M. B. NASR, S. CARRASCO, B. E. A. SALEH, A. V. SERGIENKO, M. C. TEICH, J. P. TORRES, L. TORNER, D. S. HUM and M. M. FEJER, “Ultrabroadband biphotons generated via chirped quasi-phase-matched optical parametric down-conversion”, *Physical Review Letters*, vol. 100, p. 183601, May 2008. (cited on page 91).
- [173] N. TISCHLER, A. BÜSE, L. G. HELT, M. L. JUAN, N. PIRO, J. GHOSH, M. J. STEEL and G. MOLINA-TERRIZA, “Measurement and shaping of biphoton spectral wave functions”, *Physical Review Letters*, vol. 115, p. 193602, Nov 2015. (cited on page 92).
- [174] E. BOLDUC, N. BENT, E. SANTAMATO, E. KARIMI and R. W. BOYD, “Exact solution to simultaneous intensity and phase encryption with a single phase-only hologram”, *Optics Letters*, vol. 38, pp. 3546–3549, Sep. 2013. (cited on pages 92 and 94).
- [175] J. LIESENER, M. REICHERTER, T. HAIST and H. TIZIANI, “Multi-functional optical tweezers using computer-generated holograms”, *Optics Communications*, vol. 185, no. 1, pp. 77–82, 2000. (cited on page 92).

- [176] T. SHIRAI and T. H. BARNES, “Adaptive restoration of a partially coherent blurred image using an all-optical feedback interferometer with a liquid-crystal device”, *Journal of the Optical Society of America A: Optics, Image Science, and Vision*, vol. 19, pp. 369–377, Feb 2002. (cited on page 92).
- [177] A. MONMAYRANT and B. CHATEL, “New phase and amplitude high resolution pulse shaper”, *Review of Scientific Instruments*, vol. 75, no. 8, pp. 2668–2671, 2004. (cited on page 92).
- [178] Z. ZHANG, G. LU and T. FRANCIS, “Simple method for measuring phase modulation in liquid crystal televisions”, *Optical Engineering*, vol. 33, no. 9, pp. 3018–3022, 1994. (cited on page 93).
- [179] V. CARRAT, *Correction dynamique d’un SLM pour une holographie de haute fidélité. Réalisation d’un MOT-2D pour l’application de modes de Laguerre-Gauss*. Ph.D. dissertation, Université Paris Sud-Paris XI, 2012. (cited on page 94).
- [180] J. OTÓN, P. AMBS, M. S. MILLÁN and E. PÉREZ-CABRÉ, “Multipoint phase calibration for improved compensation of inherent wavefront distortion in parallel aligned liquid crystal on silicon displays”, *Applied Optics*, vol. 46, pp. 5667–5679, Aug. 2007. (cited on page 94).
- [181] G. BOUCHER, T. DOUCE, D. BRESTEAU, S. P. WALBORN, A. KELLER, T. COUDREAU, S. DUCCI and P. MILMAN, “Toolbox for continuous-variable entanglement production and measurement using spontaneous parametric down-conversion”, *Physical Review A*, vol. 92, p. 023804, Aug. 2015. (cited on page 96).
- [182] A. EINSTEIN, B. PODOLSKY and N. ROSEN, “Can quantum-mechanical description of physical reality be considered complete?”, *Physical Review*, vol. 47, pp. 777–780, May 1935. (cited on page 99).
- [183] N. BOHR, “Can quantum-mechanical description of physical reality be considered complete? (2)”, *Physical Review*, vol. 48, pp. 696–702, Oct. 1935. (cited on page 99).
- [184] S. L. BRAUNSTEIN, A. MANN and M. REVZEN, “Maximal violation of bell inequalities for mixed states”, *Physical Review Letters*, vol. 68, pp. 3259–3261, Jun 1992. (cited on page 99).
- [185] D. DEUTSCH and R. JOZSA, “Rapid solution of problems by quantum computation”, *Proceedings of the Royal Society of London A: Mathematical, Physical and Engineering Sciences*, vol. 439, no. 1907, pp. 553–558, 1992. (cited on page 100).
- [186] D. F. V. JAMES, P. G. KWIAT, W. J. MUNRO and A. G. WHITE, “Measurement of qubits”, *Physical Review A*, vol. 64, no. 5, p. 052312, 2001. (cited on page 101).

- [187] M. PARIS and J. ŘEHÁČEK, *Quantum state estimation*, vol. 649. Springer Verlag, 2004. (cited on page 101).
- [188] C. SCHWEMMER, L. KNIPS, D. RICHART, H. WEINFURTER, T. MORODER, M. KLEINMANN and O. GÜHNE, “Systematic errors in current quantum state tomography tools”, *Physical Review Letters*, vol. 114, p. 080403, Feb. 2015. (cited on page 101).
- [189] A. ORIEUX, *Sources semiconductrices d’états à deux photons à température ambiante*. Ph.D. dissertation, Université Paris-Diderot, 2012. (cited on page 101).
- [190] S. HILL and W. K. WOOTTERS, “Entanglement of a pair of quantum bits”, *Physical Review Letters*, vol. 78, pp. 5022–5025, Jun 1997. (cited on page 103).
- [191] W. K. WOOTTERS, “Entanglement of formation of an arbitrary state of two qubits”, *Physical Review Letters*, vol. 80, no. 10, pp. 2245–2248, 1998. (cited on pages 103 and 123).
- [192] V. COFFMAN, J. KUNDU and W. K. WOOTTERS, “Distributed entanglement”, *Physical Review A*, vol. 61, no. 5, p. 052306, 2000. (cited on pages 103 and 123).
- [193] P. BON, G. MAUCORT, B. WATTELLIER and S. MONNERET, “Quadriwave lateral shearing interferometry for quantitative phase microscopy of living cells”, *Optics Express*, vol. 17, no. 15, pp. 13080–13094, 2009. (cited on page 105).
- [194] A. MARTIN, A. ISSAUTIER, H. HERRMANN, W. SOHLER, D. B. OSTROWSKY, O. ALIBART and S. TANZILLI, “A polarization entangled photon-pair source based on a type-II PPLN waveguide emitting at a telecom wavelength”, *New Journal of Physics*, vol. 12, p. 103005, Oct. 2010. (cited on page 107).
- [195] W. UENO, F. KANEDA, H. SUZUKI, S. NAGANO, A. SYOUJI, R. SHIMIZU, K. SUIZU and K. EDAMATSU, “Entangled photon generation in two-period quasi-phase-matched parametric down-conversion”, *Optics Express*, vol. 20, no. 5, pp. 5508–5517, 2012. (cited on page 107).
- [196] M. SAVANIER, C. OZANAM, L. LANCO, X. LAFOSSE, A. ANDRONICO, I. FAVERO, S. DUCCI and G. LEO, “Near-infrared optical parametric oscillator in a III-V semiconductor waveguide”, *Applied Physics Letters*, vol. 103, p. 261105, Dec. 2013. (cited on page 110).
- [197] G. BOUCHER, A. ECKSTEIN, A. ORIEUX, I. FAVERO, G. LEO, T. COUDREAU, A. KELLER, P. MILMAN and S. DUCCI, “Polarization-entanglement generation and control in a counterpropagating phase-matching geometry”, *Physical Review A*, vol. 89, p. 033815, Mar. 2014. (cited on page 110).

- [198] D. GOTTESMAN, A. KITAEV and J. PRESKILL, “Encoding a qubit in an oscillator”, *Physical Review A*, vol. 64, pp. 012310–21, Jun. 2001. (cited on page 111).
- [199] A. POLITI, M. J. CRYAN, J. G. RARITY, S. YU and J. L. O’BIEN, “Silicon-silicon waveguide quantum circuits”, *Science*, vol. 320, no. 5876, pp. 646–649, 2008. (cited on page 111).
- [200] K. D. JÖNS, U. RENGSTL, M. OSTER, F. HARGART, M. HELDMAIER, S. BOUNOUAR, S. M. ULRICH, M. JETTER and P. MICHLER, “Monolithic on-chip integration of semiconductor waveguides, beamsplitters and single-photon sources”, *Journal of Physics D: Applied Physics*, vol. 48, no. 8, p. 085101, 2015. (cited on page 111).
- [201] U. RENGSTL, M. SCHWARTZ, T. HERZOG, F. HARGART, M. PAUL, S. L. PORTALUPI, M. JETTER and P. MICHLER, “On-chip beamsplitter operation on single photons from quasi-resonantly excited quantum dots embedded in GaAs rib waveguides”, *Applied Physics Letters*, vol. 107, no. 2, 2015. (cited on page 111).
- [202] R. HANBURY BROWN and R. Q. TWISS, “Correlation between photons in two coherent beams of light”, *Nature, London*, vol. 177, pp. 27–29, 1956. (cited on page 111).
- [203] S. GRONENBORN, J. POLLMANN-RETSCH, P. PEKARSKI, M. MILLER, M. STRÖSSER, J. KOLB, H. MÖNCH and P. LOOSEN, “High-power VCSELs with a rectangular aperture”, *Applied Physics B: Lasers and Optics*, vol. 105, pp. 783–792, Dec. 2011. (cited on page 112).
- [204] S. GRONENBORN, T. SCHWARZ, P. PEKARSKI, M. MILLER, H. MONCH and P. LOOSEN, “Optical modes in a rectangular VCSEL resonator with properties of both Gaussian and Fourier modes”, *IEEE Journal of Quantum Electronics*, vol. 48, pp. 1040–1044, Aug. 2012. (cited on page 112).
- [205] I. N. DULING III, *Compact sources of ultrashort pulses*, vol. 18. Cambridge University Press, 2006. (cited on page 113).
- [206] A. FAINSTEIN, N. D. LANZILLOTTI-KIMURA, B. JUSSERAND and B. PER-RIN, “Strong optical-mechanical coupling in a vertical GaAs/AlAs micro-cavity for subterahertz phonons and near-infrared light”, *Physical Review Letters*, vol. 110, p. 037403, Jan 2013. (cited on page 113).
- [207] T. CZERNIUK, C. BRÜGGEMANN, J. TEPPER, S. BRODBECK, C. SCHNEIDER, M. KAMP, S. HÖFLING, B. A. GLAVIN, D. R. YAKOVLEV, A. V. AKIMOV and M. BAYER, “Lasing from active optomechanical resonators”, *Nature Communications*, vol. 5, Jul 2014. (cited on page 113).
- [208] K. MORELAND, “Diverging color maps for scientific visualization”, in *Advances in Visual Computing*, pp. 92–103, Springer, 2009. (cited on page 125).

- [209] JABREF DEVELOPMENT TEAM, *JabRef*, 2016. (cited on page 125).

Résumé

Ce travail porte sur l'ingénierie et la caractérisation des propriétés temps-fréquence de paires de photons générées par une source semiconductrice. Ce dispositif utilise la conversion paramétrique à température ambiante pour émettre des paires de photons se propageant dans des directions opposées et aux longueurs d'onde télécom. Une microcavité intégrée à la source permet d'augmenter l'efficacité de l'interaction nonlinéaire par résonance du champ de pompe transverse.

Nous présentons la théorie de la conversion paramétrique dans cette source et nous montrons comment les propriétés spatiales et spectrales du faisceau de pompe influencent les propriétés des photons, en particulier leur degré d'intrication en fréquence, permettant une ingénierie souple. La variété d'états pouvant être produits est illustrée à l'aide de l'amplitude spectrale jointe.

Deux techniques permettant la caractérisation de l'intensité spectrale jointe ont été implémentées. La première est un spectrographe à photons uniques ; la seconde, basée sur la stimulation du processus de conversion paramétrique, a permis une amélioration dramatique de la résolution et du temps d'intégration. Les deux approches ont permis la démonstration de l'ingénierie des corrélations en fréquences en variant la taille et la courbure du faisceau de pompe. Des exemples d'états plus exotiques et une méthode pour caractériser leur fonction de Wigner chronocyclique sont étudiés théoriquement. La relation entre les propriétés temps-fréquence et le degré d'intrication en polarisation de la paire est aussi explorée.

Summary

This work is focused on the engineering and characterization of the frequency-time properties of photon pairs generated with a semiconductor source. This device emits photons propagating in opposite directions at telecom wavelengths using spontaneous parametric down-conversion at room temperature. A microcavity integrated in the source allows the resonance of the transverse pump beam, enhancing the efficiency of the nonlinear interaction.

We give a theoretical description of the down-conversion process in the source and we show how the spatial and spectral properties of the pump beam impact the properties of the photons, in particular their degree of entanglement in frequency, allowing a versatile engineering. The variety of states that can be produced is illustrated using the Joint Spectral Amplitude.

Two techniques allowing the characterization of the Joint Spectral Intensity have been implemented. The first one is a single photon spectrograph. The second one, based on the stimulation of the down-conversion process showed a dramatic improvement in terms of resolution and integration time. Both techniques allowed the demonstration of the frequency correlation engineering by varying the waist and curvature radius of the pump beam. Examples of more exotic states and a technique to characterize their chronocyclic Wigner function are theoretically investigated. The relationship between time-frequency properties and degree of entanglement in polarization of the biphoton is also explored.